Building and Controlling Fluidically Actuated Soft Robots: From Open Loop to Model-based Control

by

Robert Kevin Katzschmann

Dipl.-Ing., Karlsruhe Institute of Technology (2013)

Submitted to the Department of Mechanical Engineering
in partial fulfillment of the requirements for the degree of

Doctor of Philosophy in Mechanical Engineering

at the

MASSACHUSETTS INSTITUTE OF TECHNOLOGY

June 2018

Author .....
Department of Mechanical Engineering
May 4, 2018

Certified by .....
Professor Daniela L. Rus
Professor of Electrical Engineering and Computer Science
Thesis Supervisor

Accepted by .....
Professor Rohan Abeyaratne
Chairman, Department Committee on Graduate Theses

Building and Controlling Fluidically Actuated Soft Robots: From Open Loop to Model-based Control

by

Robert Kevin Katzschmann

Submitted to the Department of Mechanical Engineering
on May 4, 2018, in partial fulfillment of the
requirements for the degree of
Doctor of Philosophy in Mechanical Engineering

Abstract

This thesis describes the creation and control of soft robots made of deformable elastomer materials and powered by fluidics. We embed soft fluidic actuators into self-contained soft robotic systems, such as fish for underwater exploration or soft arms for dynamic manipulation. We present models describing the physical characteristics of these continuously deformable and fully soft robots, and then leverage these models for motion planning and closed-loop feedback control in order to realize quasi-static manipulation, dynamic arm motions, and dynamic interactions with an environment.

The design and fabrication techniques for our soft robots include the development of soft actuator morphologies, soft casting techniques, and closed-circuit pneumatic and hydraulic powering methods. With a modular design approach, we combine these soft actuator morphologies into robotic systems. We create a robotic fish for underwater locomotion, as well as multi-finger hands and multi-segment arms for use in object manipulation and interaction with an environment. The robotic fish uses a soft hydraulic actuator as its deformable tail to perform open-loop controlled swimming motions through cyclic undulation. The swimming movement is achieved by a custom-made displacement pump and a custom-made buoyancy control unit, all embedded within the soft robotic fish. The fish robot receives high-level control commands via acoustic signals to move in marine environments.

The control of the multi-segment arms is enabled by models describing the geometry, kinematics, impedance, and dynamics. We use the models for quasi-static closed-loop control and dynamic closed-loop control. The quasi-static controllers work in combination with the kinematic models and geometric motion planners to enable the soft arms to move in confined spaces, and to autonomously perform object grasping. Leveraging the models for impedance and dynamics, we also demonstrate dynamic arm motions and end-effector interactions of the arm with an environment. Our dynamic model allows the application of control techniques developed for rigid robots to the dynamic control of soft robots. The resulting model-based closed-loop controllers enable dynamic curvature tracking as well as surface tracing in Cartesian space.

Thesis Supervisor: Professor Daniela L. Rus
Title: Professor of Electrical Engineering and Computer Science

Acknowledgments

A great number of people helped me throughout my PhD and made it possible for me to write this thesis. First of all, I would like to thank my advisor, Prof. Daniela Rus, for providing me with excellent daily advice, many resources, and an exceptional environment to work in a field we both share a deep passion for: soft autonomous robots. Daniela is unique in her ability to motivate and encourage to move our research forward; she always has good advice when things do not look like they are going to work out. Looking back at the past five years, we worked on a large variety of problems, many of which I was not able to capture in this thesis. We went through many great adventures, went on expeditions to try our robots, both underwater and in direct contact with humans. I will miss being a PhD student in your lab, and I hope we will have many mutual fruitful future collaborations. I would also greatly like to thank my thesis committee consisting of Prof. Russ Tedrake, Prof. John Leonard, and Prof. Peko Hosoi for all their advice and for their eagerness in supporting me through the main portion of my PhD. I remember some great conversations and discussions, and with some of you I actively collaborated during my PhD and hope to continue doing so in the future. My gratitude also goes to my past supervisors Prof. Torsten Kröger, Prof. Oussama Khatib, and Prof. Tamim Asfour, who provided me with great advice during my master thesis (Diplomarbeit) and encouraged me to stay on the academic track and pursue a PhD.

I would like to thank all my direct collaborators during the PhD, including Brandon Araki, Prof. Antonio Bicchi, Cosimo Della Santina, Youbin Kim, Dr. Shuguang Li, Austin de Maille, Joseph DelPreto, Prof. Mehmet Dogar, David Dorhout, Bianca Homberg, Prof. Robert MacCurdy, Dr. Andrew Marchese, Dr. Santani Teng, and Prof. Hsueh-Cheng Wang. I learned many things from each of you while we were making and controlling new robots together.

Without all the members of our lab, the Distributed Robotics Laboratory, this journey would have been much harder and more difficult. I would also like to thank all of my current lab members: Alexander Amini, Brandon Araki, Thomas Balch, Cenk

Baykal, Lillian Chin, Cosimo Della Santina, Joseph DelPreto, Dr. Igor Gilitschenski, Dr. Shuguang Li, Dr. Jeffrey Lipton, Lucas Liebenwein, Mieke Moran, Felix Naser, Teddy Ort, Dr. Alyssa Pierson, John Romanishin, Wilko Schwarting, Dr. Hayim Shaul, Andrew Spielberg, Dr. Cristian Vasile, and Alexander Wallar. I am lucky to be in a lab environment that is very supportive and collaborative. The atmosphere of the lab is always warm and welcoming, it provides for great discussions, both in terms of science and just about anything else. I will always remember our daily lunches altogether, our yearly lab outings to the mountains for hiking or rafting, and our regular celebrations with lots of coffee and cake. I would like to thank our lab admin Mieke Moran, who ensures on a daily basis that everyone in the lab has everything needed and that we always stay well-fed.

I also want to mention all my previous lab members that have already graduated or finished their assignments, all of you also helped to create a great PhD journey for me, and I enjoyed it very much working with all of you: Prof. Javier Alonso-Mora, Byoungkwon An, Stuart Baker, Thomas Bertossi, Dr. Stephane Bonardi, Prof. Changhyun Choi, Sebastian Claici, Prof. Mehmet Dogar, Dr. Marek Doniec, David Dorhout, Prof. Daniel Feldman, Prof. Stephanie Gil, Dr. Kyle Gilpin, Bianca Homberg, Prof. Ross Knepper, Prof. Robert MacCurdy, Dr. Andrew Marchese, Prof. Ankur Mehta, Prof. Shuhei Miyashita, Tobias Nägli, Dr. Sedat Ozer, Prof. Liam Paull, Dr. Guy Rosman, Dr. Andrés Salazar-Gómez, Jenny Shen, Daniel Soltero, Prof. Cynthia Sung, Prof. Michael Tolley, Dr. Mikhail Volkov, and Prof. Jingjin Yu.

Many thanks also go to all the other CSAIL staff, including Ron Wiken, Adam Conner-Simons, Rachel Gordon, and Lauralyn Smith. I want to acknowledge all the help I received from everyone in The-Infrastructure-Group, Human Resources and Headquarters.

A big thank you goes out to all my friends for always standing by my side and supporting me for all those years. I especially would like to express gratitude to my friends Alex, Mikhail, Joao, Affi, Sara, Uyanga, Felix, Joseph, Philipp, Christian, Gregor and everyone else I forgot to mention. You all were amazing, you were there for me during different phases of my life, thank you for all the fun times, great

conversations, and special adventures we had together.

I would like to thank all my family members back in Germany. I miss our regular family gatherings with lots of cakes, fun conversations, and just hanging out together on the weekends. I am very proud of my family for holding together so strongly and being there for each other. I always received so much support and encouragement from everyone.

To my love Grace, thank you so much for your support, advice, and encouragement. You stood by me during success and failure, tirelessly encouraging and supporting me every day. Thank you for all the inspiring discussions and all the loving words. I am looking forward to many more fun times of creating things together and going on new adventures with you.

To my son Colin, you have always borne with a father still in graduate school, happily accompanying me to work when a deadline was close or just because I really wanted to finish building something. Thank you for always cheering me up with your deep curiosity and strong interest in learning new things. I am looking forward to continue instilling your desire to make things. Together we will create many more robots in the future!

To my brother Philip, thank you for all the advice and support you have given me since I was born. I could not have wished for a more supportive and encouraging brother than what I found in you. You are my rock in the ocean, whenever I call you up, you have time and patience for me, thank you so much!

To Tanti and Onkel Heinz, I miss both of you very much and would wish to be closer to home so we could spend more time together. I learned many things from you, especially a great outlook on life. I admire the cordiality and sincerity that you both live and taught me. I happily remember all the care and love I received from both of you.

Finally, my deepest gratitude goes to my mother Wilhelmina and my father Ulrich, who have always encouraged me to follow my dreams. I could not have wished for more loving and caring parents than what I found in both of you. I admire you greatly for all you have shown and taught me in my life so far, and I am looking forward to

many more years of joyful adventures together.

Contents

List of Figures

List of Tables

List of Algorithms

List of Processes

List of Notations

DOF	degree(s) of freedom
SMA	Shape Memory Alloy
FEA	Fluidic Elastomer Actuator
L_0	length (unstrained)
ΔL	length (difference)
p_c	pressure of entrapped fluid in cavity
$\bar{h}$	undeformed diameter of cylindrical elastomer channel
$\bar{t}$	undeformed wall thickness of cylindrical elastomer channel
$\hat{h}$	deformed diameter of cylindrical elastomer channel
$\hat{t}$	deformed wall thickness of cylindrical elastomer channel
$\Delta\mathbf{p}_c$	vector of all consecutive incremental pressure increases
$p_c^{\max}$	maximum channel pressure
σ_{el}	stress in elastomer
ϵ_{el}	strain in elastomer
$\bar{c}$	undeformed circumference of channel
p_{atm}	atmospheric pressure
$\hat{c}$	deformed circumference of channel
$\Delta p_{c,i}$	incremental pressure increases i
θ	bend angle of a segment's neutral axis

$\mathbb{V}_c$	supplied volume
$V_{Elastic}$	potential energy
$\mathbb{V}$	volume
SoFi	soft robotic fish
κ	curvature
ϑ	orientation of base of soft robot
s	point along constant curvature arc
x	x position in Cartesian space
y	y position in Cartesian space
w	position and orientation of end-effector or other controlled point along arm
IK	inverse kinematics
A	point describing base of arc
B	point describing tip of arc
ϖ	weighting vector
$*$	optimal
error	error
$\mathbf{h}$	point on the robot's envelope
$\mathbb{H}$	all points on the robot's envelope
$\mathbf{e}$	point on the surrounding environment
$\mathbb{E}$	all points on the surrounding environment
α	angle
r_o	radius of object
n	total number of constant curvature segments within soft arm
PCC	piecewise constant curvature
CC	constant curvature
S	reference frame attached to end of segment
i	i-th reference segment or frame
T	homogeneous transformation

μ	mass of a soft fluidic actuator
τ	torque by fluidic actuator
q	generalized coordinates, for planar case it is degree of curvatures
L	length of segment
$\mathbb{R}$	real numbers
ρ	radius of curvature
ξ	state space of equivalent rigid robot, the augmented state
h	number of joints per constant curvature segment
m	nonlinear map constraining end points and point masses between rigid and soft robot
DH	Denavit Hartenberg
θ_{DH}	angle about previous z axis, from old x axis to new x axis (classic DH parametrization)
d_{DH}	offset along previous z axis to the common normal (classic DH parametrization)
a_{DH}	length of the common normal (classic DH parametrization)
α_{DH}	angle about common normal, from old z axis to new z axis (classic DH parametrization)
R	revolute joint or rotation
P	prismatic joint or translation
T	transpose
B	inertia matrix
C	Coriolis and centrifugal matrix
G	gravitational forces
J	Jacobian
f	wrenches or forces
ext	external

ct	contact
x	coordinates of set of contact positions
k	number of contact points
Δ	thickness of segment section
δ	small distance/displacement
imp	impedance
E	energy
ϱ	infinitesimal stiffness
ς	infinitesimal damping
k	stiffness vector
d	damping vector
K	stiffness matrix
D	damping matrix
ν	vector of length n
R	matrix that has as column space the Range of B_ξ
N	matrix that has as column space the Kernel of B_ξ
d_r	rank of B_ξ
U	diagonal matrix collecting all the non-null eigenvalues B_ξ
M	matrix containing R and N
$\bar{q}$	desired evolution in generalized coordinates q
t	time
e	error variable defined by q - $\bar{q}$
V	Lyapunov candidate
K_C	Cartesian stiffness matrix of impedance attached to end-effector
D_C	Cartesian damping matrix of impedance attached to end-effector
d	desired (subscript)
η	Cartesian Coriolis and centrifugal matrix

Λ	Cartesian inertia matrix
v_{n}	nullspace velocity in operational space
N	nullspace Jacobian $\mathbb{R}^{(n-k)\times n}$
Z	opportunely defined matrix
N	nullspace
n	vector with parallel or perpendicular direction to the environment
$\parallel$	parallel to the environment
$\perp$	perpendicular to the environment
t	target
ϵ	manually defined threshold
I_{ct}	integral gain for tangential motion along environment
FEM	finite element model
meas	measured
in	input
kn	known
f	final
SIMC	Skogestad Internal Model Control (tuning rule)
PID	proportional-integral-derivative
k_{P}	proportional gain
k_{I}	integral gain
k_{D}	derivative gain
ω	frequency
p_{L2}	L_2 norm
mag	absolute magnitude
a_{Gain}	exponential gain of sigmoidal force field
δ_{pen}	penetration depth relative to surface
l	placement of the piston within pneumatic cylinder
ζ	linear actuation gain from fluidic pressure to torque

α	amplitude of sinusoidal trajectory
c	number of potential contacts

Chapter 1

Introduction

1.1 Vision

For millions of years biological organisms have exploited their continuous body deformation or undulation in various forms for manipulation and mobility tasks. Elephants use their trunks to explore the environment or to pick up objects. Exploration is achieved by undulating and extending their trunk, either to sweep over a surface while staying in supporting contact with that surface or to swing the trunk dynamically to reach somewhere. An elephant can reach with its trunk backwards to spray wash its body, move adaptively through narrow openings, follow a smell and pick up food, or even fend off predators and fight back. Similarly, octopuses use their tentacles to elegantly walk, swim, and grasp underwater. The undulation of a soft body as a means of animal underwater locomotion is prevalent within nature and has proven to be highly advantageous throughout evolution. This incredibly successful evolutionary development can be found everywhere in nature, from microscopic flagella on bacteria to the body of a whale as it swims.

However, despite the near ubiquitous existence of these natural systems, little progress has been made in robotics to create similar artificial organisms. The infancy of muscle-like actuators and the high complexity of modeling and controlling continuously deforming soft structures are some of the key challenges of creating artificial organisms. It is typical that engineers compare the performance of their designs,

no matter how crude those might be, to natural counterparts that are somewhat similar. Researchers do this by metrics such as the level of biomimicry or the degree of success in achieving tasks that natural systems would typically do. However, animals move very differently from rigid robots: they perform dynamic tasks efficiently, and interact robustly, compliantly, and continuously with the external world through their body's elasticity [Roberts and Azizi, 2011, Roberts, 2016]. Robots were traditionally developed to move with greater precision, higher forces and power, and have longer endurance than natural systems like human workers or animals; but traditional robotic systems are still greatly lacking in aspects of adaptability to the environment, compliant interactions with humans and objects, and the flexibility to achieve multiple tasks with the same robotic mechanism.

Within the area of robotics, an emerging field called *soft robotics* seeks to explore the design, actuation, and control of soft and flexible bodies to achieve greater flexibility and adaptability when compared to the more traditional field of rigid robotic structures. Soft robots are a type of robot that is partially or fully made of highly compliant materials, similar to those found in living organisms. Soft robots are inspired by the movement of living organisms and the way they adapt to their surroundings. The bodies of living organisms are to a great extent compliant and easily adaptable, which inspires the design of soft robots. Research on soft robots especially targets the aspects of flexibility, adaptability, and agility needed in robotic tasks while providing for safer interactions with humans [Rus and Tolley, 2015, Laschi et al., 2016, Polygerinos et al., 2017].

Soft robotic technologies not only enhance traditionally rigid locomotion and manipulation approaches, but actually provide innovative solutions where there were none available before. The field of robotic locomotion studies systems that can crawl, walk, swim, fly, or use other modalities to move about in space. The field of robotic manipulation investigates systems that can handle and change objects or interact with living beings by picking up, moving, and placing them. Locomotion and manipulation can be greatly enhanced when compared to approaches with rigid robots by new actuation functions such as bending, stretching, or undulation of

continuously deforming structures. Soft continuum robots have the advantage of being more compliant and are equipped with a higher degree of freedom than rigid robots consisting of the same number of parts. This attribute should allow soft robots to autonomously execute tasks that require high dexterity and have substantial uncertainties within the task.

There have been great advances in developing soft robotic hardware architectures [Laschi et al., 2012, Seok et al., 2013, Holland et al., 2017]. However, rigid robots still outperform their soft counterparts in many regards of locomotion and manipulation, such as adaptable motions in unstructured terrain, higher flexibility for manipulation tasks, and better grasping performance [Wilson et al., 2013, Seok et al., 2015] – all the features we believe soft robots should comparatively excel at. Current approaches to design, motion planning, inverse kinematics, and control are still limited and do not exploit the full capacity of soft locomotors and soft manipulators. Soft robotic research is primarily focused on the structure, including actuators and sensors, which is the body of the system. Equally important, however, is the capability of the controller that is the brain of the robot to enable even more functionalities and allow soft robots to achieve their full potential. While high-resolution actuators and sensors that can be embedded within the compliant bodies are required for further development, we also need better models and controllers to deliver the promise of soft-bodied machines. One of the main motivations for building soft robots is the hope to become better with respect to dynamic movements and compliant interactions with the environment. We need to improve the controlled actuations of soft structures by designing appropriate and comprehensive models. Just like biological organisms, which have a brain and nervous system containing lifelong trained motor skills and experienced memories, the models we develop for soft robots should have a capacity to adapt and learn. We are also motivated and inspired by the many advances in modeling and controlling rigid robots [Andersson, 1989, Leidner et al., 2014, Kuindersma et al., 2016, Hong et al., 2017, Haddadin et al., 2017], and would like to see those applied to soft robots.

We are inspired by the potential of soft robots to do more for people than currently

possible – for example, by providing a biomimetic swimming underwater observatory or by the creation of compliant manipulator systems that can dynamically and safely interact with the world. Therefore, the objective of this thesis is to advance and innovate in both the creation and the control of soft robots. We use soft fluidic actuators to create controllable robots with compact actuation and useful endurance. We intentionally incorporate and leverage the natural softness of the compliant elements of the robots when solving locomotion and manipulation tasks through new designs, fabrication methods, models and controllers. We are enabling new capabilities of soft robots by developing algorithms and models for the control of both quasi-static and dynamic motions.

1.2 New Capabilities

A set of new capabilities is enabled through the theoretical and experimental work presented in this thesis. Trivedi et al. [2008], Kim et al. [2013], Rus and Tolley [2015], and Laschi et al. [2016] have highlighted many of the possible advantages of deformable bodies for robotic systems. Soft robots have many potential capabilities – for example, safe interactions, controlled continuous deformation, dexterity through compliance, simplification of mechanisms, and biomimicry. Safer interaction between robots and humans is attained by the structural softness and decreased weight of the robots. Continuous flexing and deformation of robotic limbs in a controlled manner permits complex locomotion with a minimum of parts, reaching into tight spaces and compliant manipulation of objects. More dexterity is also achieved through this added compliance: for example, a compliant prosthetic hand can handle a variety of objects with only a single actuator driving it. Traditional robotic designs have a larger part count than their soft counterpart; a single body fulfills several functions at the same time. Biomimicry through continuously deforming motions achieves motion behaviors that are practically impossible to recreate with a set of discrete joints and links.

1.2.1 Safe Interactions

We believe that in the future humans and machines will be working side by side, collaborating and interacting. In a human-centered environment, safety becomes an immediate concern. Traditional robots are often considered too rigid for human-centered environments where the tasks are unpredictable and the robots have to ensure that their interaction with the environment and with humans is safe. The majority of commercially deployed industrial robots are still isolated from humans, confined to operating behind screens. During the design of new robots, the competing goals of safety and performance have to be taken into account [Wyrobek et al., 2008]. Much research is aimed at equipping rigid robots with soft capabilities [De Santis et al., 2008]. For example, the inclusion of compliant elements within transmissions has the function of decoupling actuator and link inertia when necessary to minimize collision forces [Bicchi and Tonietti, 2004]. Common approaches to variable-impedance actuation, reviewed by Vanderborght et al. [2013], include series elastic actuators [Pratt and Williamson, 1995] and variable stiffness actuators [Tonietti et al., 2005, Wolf and Hirzinger, 2008]. However, despite these safer design morphologies, robots are still fundamentally composed of rigid components and rely on control software to guarantee safety if collisions with humans or environments occur. Soft robots are the natural progression in robotic design towards inherent safety. Soft robots, with their highly deformable body components, offer the potential for better mechanical compatibility between robots and humans [Lipson, 2014]. A rigid robot has rigid links which act as impactful weights during a collision, applying a concentrated momentum onto the object or person in the way. In contrast to this, a soft robot of similar size would typically be lighter and more deformable. Because of that, the soft robot will not apply a strong impact during an accidental collision. The compliant contact surface will gradually deform around the object or person the robot is colliding with and only over some finite time, not instantaneously, transfer a momentum via a larger area, not just a few contact points.

1.2.2 Controlled Continuous Deformation

Traditionally, robots are composed of rigid links and revolute or prismatic joints, but not of soft materials. Kinematic and dynamic modeling and control solutions and their applications to commercial or industrial tasks require repetitive and reliable operations with high precision. Continuously deforming soft and compliant bodies were not available for a long time, in part due to lack of materials and fabrication techniques, and also due to the lack of understanding of how these bodies can be properly modeled and controlled. In this thesis, we show to we enable controlled continuous deformation of soft bodies for use in the construction of new robotic systems that can approach tasks differently, leveraging their compliance and their conforming deformations for enveloping objects and interacting with the world. Although robots with finite degrees of freedom and electro-mechanical actuators show promising capabilities, especially for repetitive industrial tasks, they often cannot match the speed nor the dexterity of biological organisms. Traditional robotic designs can only approximate naturally continuous body motion with multiple discrete links separated by fixed joints. Soft robots offer the potential to lift the limitations imposed by rigid-body kinematics, as their bodies can deform continuously under actuation. These features make soft robots well-suited to emulate the kinematics and dexterity displayed by some natural systems. The continuous deformation of the soft robotic bodies not only allows for an actively actuated bending, contracting or extending, but whether the body is actuated or not, it always allows for a compliant interaction with the environment or living beings from all directions.

1.2.3 Dexterity Through Compliance

A robot which can deform its body continuously is able to envelop an object and build up a surface contact, unlike a rigid-bodied robot which is only able to make discrete contact with the object while enveloping it. Soft robots can work with unstructured environments and manipulate unknown objects by conforming to those environments or objects while following the same control strategy for each object. The uncertainty

in the shape of an unstructured object or environment is mitigated through the compliance of the soft robot. By comparison, rigid robots have to be extremely precise in their motion and measure the contact forces accurately in order to successfully achieve a task. Therefore the ability to conform to an environment or to envelop an object is already increased by moving from a finite-degrees-of-freedom system to an infinite-degrees-of-freedom system: a soft, compliant robot. Therefore, the dexterity of a soft manipulator in picking up and placing objects is already made possible to some extent just by the soft body's inherent compliance. The soft body also brings its own challenges in terms of how to model its deformation: dealing with the infinite dimensionality is a challenge. This thesis presents models, planners, and controllers – all of which are specifically designed to enable the dexterity of actuated compliant bodies.

1.2.4 Simplification of Mechanisms

The dream of engineers to create machines inspired by natural systems goes back a long way [Hirose et al., 1993], and includes humanoids [Hirai et al., 1998, Kaneko et al., 2008, Kuindersma et al., 2016], snake-like robots [Dowling, 1996, Buckingham, 2002], four-legged robots [Raibert, 1986], insects [Wood, 2008], and hands [Cutkosky and Kao, 1989]. The robotic mechanisms designed to imitate natural motions such as undulation (for example, the swimming motion of a fish) were traditionally built heterogeneously out of a number of links and actuated joints, surrounded by some artificial skin, and all was held together by fasteners or glue [Anderson and Chhabra, 2002]. The soft robot body approach advances the body of a system by replacing these links and joints with a small set of continuously deformable bodies that are designed to mimic the deformation behavior intrinsically [Suzumori et al., 2007]. These new designs are built out of soft rubber-like materials, which are either cast or printed, allowing for new advantages during fabrication with low part counts and less assembly time [Marchese et al., 2014c]. Soft materials can also couple sensing, actuation, computation, and communication [McEvoy and Correll, 2015]. Rapid prototyping allows quick iteration of those designs [Cho et al., 2009, Kim et al., 2014]. The mechanisms are low-cost in

production and can easily be replaced and duplicated.

1.2.5 Biomimicry

Biomimicry is the design and production of materials, structures, and systems that are modeled on biological entities and processes. Biomimetic systems seek to reproduce the capabilities of natural systems through copying motions, appearance, and behaviors. In the process of developing biomimetic systems, new technologies are developed that enable the imitation of natural systems. The biomimicry of the deforming movements of soft robots enables the imitation of natural systems such as snakes [Luo et al., 2014], elephant trunks [Hannan and Walker, 2003], or fish [Marchese et al., 2014c]. Biomimicry plays an important role in the emerging field of "ethorobotics" [Krause et al., 2011]. For this emerging field, biomimetic robots are useful for the study of biological systems through imitation, disguised observation, and intended interaction. Initial experiments have shown that observed biomimicry causes animals to react differently to robots, allowing for new types of animal-robot interactions [Miklósi and Gerencsér, 2012].

1.3 Applications

There are many areas of application for soft robots. We will focus on two particular applications for which this thesis will offer contributions. These areas are dynamic manipulations with soft arms as well as the observation of marine life through a biomimetic robotic fish.

1.3.1 Manipulation

The capabilities of soft robots also enable more adaptable and compliant manipulation compared to rigid systems. Much work has focused on making soft grippers. Dollar and Howe [2006, 2010] presented one of the earliest examples of underactuated and flexible grippers, a hand made of soft and rigid elements and actuated by cables. This hand

was able to easily grasp a wide array of objects. In order to make the fingers softer, a puncture-resistant soft pneumatic gripper was developed by Shepherd et al. [2013b]. Deimel and Brock [2016] developed a pneumatically actuated anthropomorphic soft hand capable of dexterous grasps. All these soft hands were standalone, which means that they were either moved manually by a human operator or were mounted to a rigid robot arm. The actuation of these systems is basic open-loop control. New applications add such soft fingers or hands to soft robotic arms and allow for autonomous manipulation and interaction with inherently safe and compliant systems. In particular, the lack of models for controlling multi-segment soft structures has limited this development. Dynamic controllers have the potential to enable a wide range of dynamic tasks. These tasks range from exploring three-dimensional spaces through contact, learning the geometry of the world, swiftly picking up delicate objects, and moving heavy objects. Dynamic controllers leverage models to enable these dynamic interactions with the world.

1.3.2 Observation of Marine Life

One area of application studied in this thesis is the use of soft robotic fish for observations in marine life environments. Traditionally, this has only been done with rigid, propeller-driven underwater robots. With these rigid systems, there has been much technological progress in regards to nature filmmaking, but it can still be very hard to document sea animals up close without disturbing them. Close-up and minimally disruptive observations of marine life are particularly useful when studying animals' behaviors, swim patterns, and interactions within their habitats [Krause et al., 2011, Miklósi and Gerencsér, 2012]. A biomimetic underwater observatory for long-term studies could facilitate deeper understanding of marine life, especially their social behaviors and how environmental changes affect the delicate balance within the marine world. One possibility to achieve this is using underwater vehicles which can swim alongside marine life to allow close-up observations. Current systems for the study of the underwater world are typically built out of a rigid shell and propelled by fast spinning propellers. These so-called remotely operated vehicles (ROVs) or autonomous

underwater vehicles (AUVs) typically use propellers or jet-based propulsion systems [Bogue, 2015]. However, these propulsion systems generate substantial turbulence and have the potential to scare marine life and prevent close-up observations [Southall et al., 2007]. In addition, the mere appearance of these vehicles, typically large and rigid like a submarine, does not integrate well into the marine environment. The complexity of most traditional ROVs also requires costly fabrication and intricate control strategies, and their large bulk restricts their tethered deployment to deeper water using specially equipped vessels. Smaller ROVs also generally require tethers, which can be cumbersome and restricts operation.

Controlled soft robots have the potential to enable observations of marine life with less disruption of the animals. A small and agile soft robot, swimming with its continuously deforming and undulating tail, appears more biomimetic and has shown first successes in preliminary studies [Halloy et al., 2007, Bonnet et al., 2016]. Using such a robot enables researchers to swim closer alongside marine animals. In the future, similar soft robots enabling this capability in other fields of biology are now conceivable.

1.4 Challenges

1.4.1 Why are Soft Robots Hard to Model and Control?

Performing manipulation or underwater locomotion with soft robots poses several challenges. Since robots are highly compliant, their motions are not necessarily as precise as the motions of rigid-bodied manipulators. Rigid robots are intentionally built stiff so that the kinematics of the robot can be defined by the readings of positional encoders embedded in the joints and the dynamics can be determined by torque sensors also embedded in the joints. Rigid robots are usually fully-actuated, that means each degree of freedom (DOF) of the robot is confined to the rotation joint axes and all these joint axes can be controlled individually. Soft robots are not available for purchase, so each soft robot has to be built from scratch, including the

ways of powering these bodies, sensing their deformations, and sensing forces. There is only limited literature in existence on how to design and fabricate soft robots, so part of the challenge is to develop design and fabrication principles that allow for easy, repeatable, and reliable fabrication of soft robots.

The structural compliance within soft robots introduces degrees of freedom that are not actuated; soft robots are underactuated systems. It is a challenge to precisely steer a soft robot into a particular configuration without knowing how impedance, dynamics, gravity, and external forces will affect the robot's body. The lack in modeling these behaviors leads to uncertainty in positioning. We require therefore an approach to modeling that takes the physical behavior of the robot into account and mitigates the uncertainty. The uncertainty in the modeling of these soft bodies requires intelligent ways of simplifying just enough to make the modeling computationally tractable while not loosing too much fidelity and control. The limited strength and actuation power of these systems further add to the underactuatedness of these soft mechanisms and limit controllability. Similarly, the nonlinear deformation behavior of soft bodies negatively affects the overall controllability of soft robots. Rapid prototyping of those systems can lead to large tolerances and variability after manufacturing. The models have to be re-identified for each prototype instance. In addition, soft robots change their properties over time due to external influences, for example heat, sunlight, moisture, and contacting chemicals. This creates an additional challenge of time-variability of the parameters of soft robots. This also needs to be accounted for when modeling the system and needs to be addressed with repeated calibrations. Another challenge is the relatively low puncture resistance of soft robots that have interior balloon-like chambers and are actuated through air or water. These pneumatically or hydraulically actuated systems are sensitive to punctures and ruptures in their bodies, caused by sharp objects or over-actuation.

Each soft robot needs a power source that converts energy into actuation. Such actuation can be achieved by having a motor pull on cables embedded within the soft robot; or by applying a voltage to an electroactive polymer that makes up the soft robot; or by applying a fluidic pressure in internal chambers of the soft body. The fluidic

pressure is produced by a fluidic supply, such as a pneumatic cylinder or a compressor pump. In this thesis, we will focus on fluidic supplies as the source of actuation for soft robots. The body elements of soft robots powered by a fluidic pressure source are called fluidic elastomer actuators. The bulkiness of the fluidic supplies as well as the bulkiness of the connected power source pose challenges concerning portability, wearability, and accessibility of theses soft robotic systems.

1.4.2 Why are Current Solutions Inadequate?

Current approaches to design, fabrication, motion planning, inverse kinematics, and control are still limited and do not exploit the full capacity of soft locomotors and soft manipulators. Recent reviews [Trimmer, 2014, Lipson, 2014, Majidi, 2014, Rus and Tolley, 2015, Laschi et al., 2016, Polygerinos et al., 2017] provide an overview of what current soft robotic solutions can and cannot provide. As these reviews show, soft robotic research is primarily focused on the structure, including actuators and sensors, but equally important is the modelling and control of the robot to enable more functionalities and allow soft robots to achieve their full potential. In the following, we will discuss the shortcomings by separately addressing the areas of design and fabrication as well as modeling and control.

1.4.2.1 Current Design and Fabrication

Current engineering tools for the design and fabrication of robots are well-suited for rigid-bodied robots, but when elastic materials are introduced as building blocks, the common engineering tools do not provide a solution on how to design and integrate these blocks. As explained in Section 1.4.1, only during the last few years researchers have started to report on how to design and fabricate soft robots. While there is a large variety of possible material choices and powering sources, there are barely any studies on the effectiveness of certain materials and power combinations. While for rigid robots there are many design recommendations on what combinations of actuators work best for which application, these recommendations do not readily

apply to soft robots, requiring new investigations and studies. IN addition, methods for repeatable production of soft robots do not yet exist, an important feature when developing model-based control approaches which to a large degree rely on the time-invariance of the system's parameters. Therefore, in order to create soft robots made of fluidic elastomer actuators, we must overcome many technical challenges. The most important challenges are as follows:

1. We need new methods for the construction of robots. We advocate for modularity as a design principle for the composition of complex structures out of components with well defined functions. That is, we need to identify and develop appropriate functional modules as well as provide ways of assembling these into multi-body robots.

2. Consistently reproducing the crucial properties of soft robots, for example their elasticity or internal channel geometry, is difficult when using current fabrication techniques. Accordingly, we must develop fabrication techniques that allow for repeatability and scalability without limiting the complexity of possible features and shape profiles.

1.4.2.2 Current Modeling and Control

A recent review by Polygerinos et al. [2017] describes the state of the art in modeling and control, covering morphologicial control, kinematic closed-loop control, and dynamic feedforward control solutions. Model-based closed-loop control, that is the control of a soft robot using a model when closing the control loop, has not been addressed yet. Soft robots cannot just be approximated by rigid links and revolute or prismatic joints to describe their kinematics and dynamics, this approach done naively does not match the motions of a soft robot. Taking it to the other extreme, modeling the deformations through a high-dimensional finite element model makes this control problem almost intractable and challenging to implement. For further explanations on why the modeling and control is hard, see Section 1.4.1. Therefore, we need to improve on how we perform controlled actuations of the soft structures

by designing appropriate and comprehensive models. We are motivated and inspired by the advances in modeling and controlling of articulated robots with embedded compliance [Andersson, 1989, Leidner et al., 2014, Kuindersma et al., 2016, Hong et al., 2017, Haddadin et al., 2017]. These articulated robots are rigid robots with added spring-damper elements at the discrete joints. We would like to see the advances of the research on articulated robots with embedded compliance applied to continuously deforming soft robots. Falkenhahn et al. [2015] and Marchese et al. [2016] propose feedforward controllers that account for the dynamics of a soft robot. Model-free quasi-static control of soft robots was shown in Katzschmann et al. [2015], Marchese et al. [2014a] and is further elaborated in this thesis in Section 5. The state of current modeling and control can be summarized as follows:

1. Soft robots do not have a predictable way of positioning themselves, while this is typically a fundamental ingredient to manipulation with rigid robots. The challenge in controlling the configuration of soft limbs such as arms and fingers for manipulation is due to the limb's inherent elasticity, the sensing of the limb's state, and the compliance of its fluidic power system. Models accounting for these aspects and controllers leveraging these resulting models are needed.

2. Planning for soft robots is a relatively unexplored field with people only very recently starting to publish on. In order to autonomously complete manipulation tasks, we need to develop algorithms for motion and manipulation planning.

3. The task of manipulation not only necessitates the development of new hardware but also requires control structures which enable model-based closed-loop control. To the best of our knowledge, these model-based methods for controlling the deformation of fluidic elastomer robots have not been proposed yet. Instead, current robots primarily rely on the concept of morphological control [Nakajima et al., 2014, Cheney et al., 2013] or feedforward control [Falkenhahn et al., 2015, Marchese et al., 2016]. In particular, when dynamic manipulation or interaction with the world is required, we need to develop dynamic models to allow for model-based control. Without a model, we can not predict the behavior of a

soft manipulator and realize reasonably precise motions.

1.5 Our Approach

This thesis addresses some of the challenges described in Section 1.4 by innovating in design, fabrication, modeling and control. Those innovations are validation in applications for locomotion and manipulation. An overview of our approach to the challenges is given in Figure 1-1.

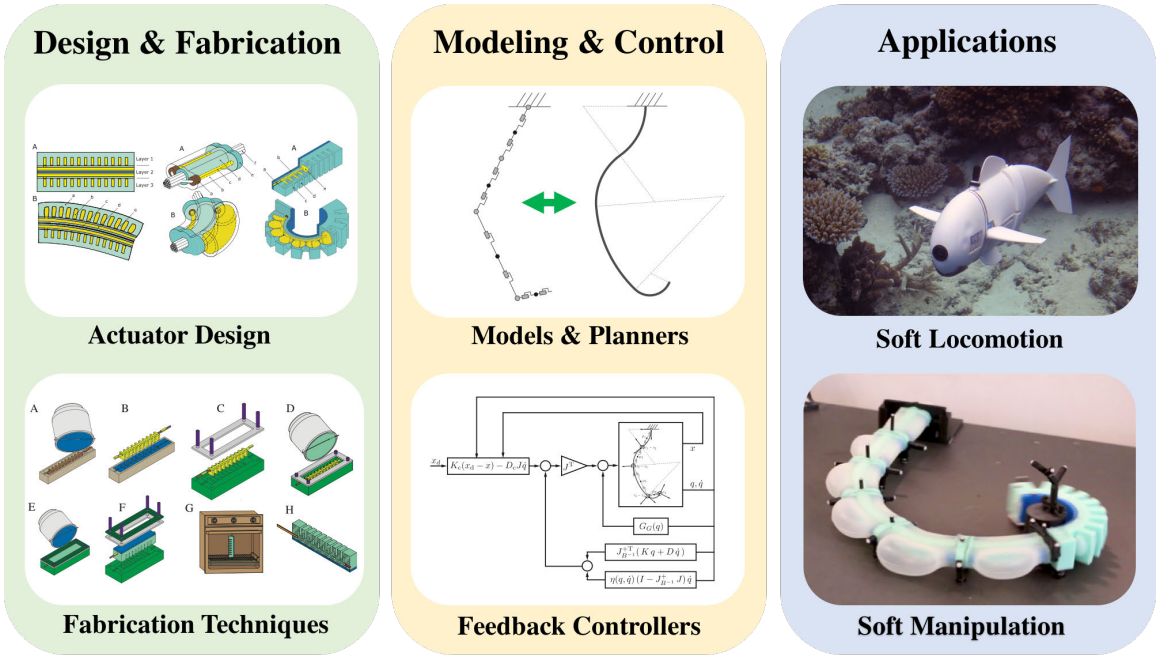

Figure 1-1: Overview of the thesis and our approach: The design and fabrication the soft robotic systems enables the creation of soft robots, for which we then develop models and controls specific to locomotion and manipulation tasks.

1.5.1 Overview of Our Approach

Our approach starts by understanding and describing the morphologies of soft actuators and the use of soft elastomer materials in the design and fabrication of these fluidically-driven soft actuators. Fluidically-driven actuators are bodies made of soft rubber-like materials that have interior chambers for pressurization through fluids, such as air or

water. Under pneumatic or hydraulic pressurization, these chambers deform in a pre-designed manner to create desired deformations and motions. The fluidically-driven actuators are treated as combinable modules and can be embedded into self-contained, multi-module systems to bring them to practical use and test out models and controllers for such soft robots. We develop models for the actuation, kinematics, impedance, and dynamic characteristics of these continuously deformable soft systems. We leverage these models in the algorithms of motion planners as well as in the formulations of closed-loop feedback controllers. The closed-loop feedback controllers achieve dynamic motions and interactions with an environment. We create systems to apply the models and controllers to systems such as a soft robotic fish for underwater locomotion and an autonomously controlled soft manipulator for dynamic motions, surface tracing and grasping. In the following, we describe our approach for design, fabrication, modeling, and control. We then detail how we approach the experimental validation within soft applications.

1.5.2 Design and Fabrication

We study the design and fabrication of these soft robots and develop soft actuator morphologies, soft casting techniques, as well as pneumatic and hydraulic powering methods under closed-circuit fluid control [Marchese et al., 2015]. With a modular design approach we combine soft actuator morphologies into robotic systems [Marchese et al., 2014a, Katzschmann et al., 2015, Homberg et al., 2015, 2018, Katzschmann et al., 2018b]. We create a robotic fish for underwater locomotion, and soft manipulators, such as multi-finger hands and multi-segment arms, for the use in object manipulation and interaction with the environment. To enable the use of the soft actuator morphologies in underwater locomotion, we make robotic fish that uses a soft actuator as its tail to perform cyclic undulating swimming motion. The open-loop controlled swimming movement of the robotic fish prototype is enabled by a custom-made displacement pump and a custom-made buoyancy control unit, all embedded within a self-contained design mimicking a fish-like underwater robot [Katzschmann et al., 2014, 2016]. This underwater robot receives high-level control commands via acoustic signals in order to

move in coral reef environments and to film marine life [Katzschmann et al., 2018b].

1.5.3 Modeling and Control

To improve the use of the soft actuator morphologies for manipulation tasks and interactions with an environment, we develop models describing the geometry, kinematics, structural impedance, and the full dynamics. We make use of these insights for both model-free feedback control [Katzschmann et al., 2015, Marchese et al., 2014a] and model-based feedback control of the developed soft manipulators [Della Santina et al., 2018, Katzschmann et al., 2018c].

The model-free feedback controllers only use kinematics models and work in combination with geometric motion planners. The model-free feedback controllers enable a soft manipulator arm to move in confined spaces [Marchese et al., 2014a] and enable a soft arm with a gripper attached to it to autonomously perform pick-and-place operations of objects [Katzschmann et al., 2015].

Leveraging the models describing the impedance and dynamics of soft multi-segment arms, we propose controllers that are designed for performing dynamic arm motions and end-effector interactions with an environment [Della Santina et al., 2018]. The first controller aims to achieve dynamic trajectory following of curvatures. Curvatures are the deformations of each segment of a multi-segment arm. The second controller is an impedance controller that allows to control the position of the end effector in free space and to move along a surface, while staying in contact with that surface. Both controllers rely on a model linking the soft robot to a classic rigid serial manipulator with a parallel elastic mechanism. This model makes use of an augmented formulation that allows the application of control techniques developed for rigid robots to the use in the dynamic control of soft robots. Prior tools developed for the models of rigid robots [Ott, 2008, Sciavicco and Siciliano, 2012] can be exploited under this model formulation. We also evaluate the effectiveness of both dynamic controllers by assessing the characteristics of the controllers theoretically within the modeling hypotheses.

1.5.4 Control Demonstrated in Applications

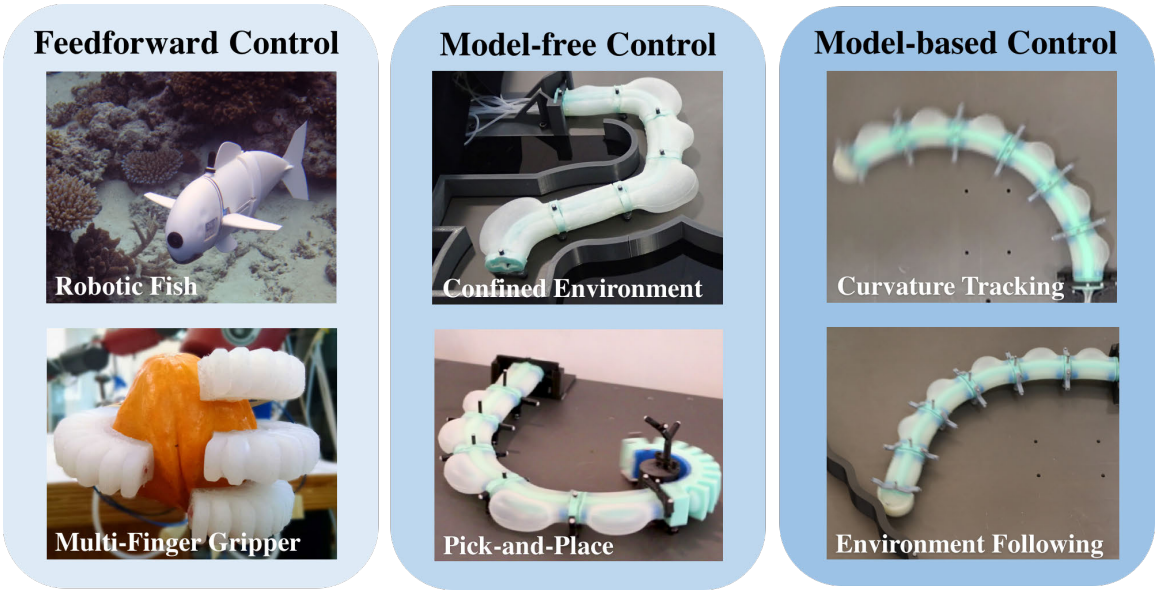

Figure 1-2: Applications of the soft robotic systems developed in this thesis. The systems are sorted by the control approach taken: Feedforward control, model-free control, and model-based control.

We demonstrate the developed soft systems, models and controllers in applications for locomotion underwater and manipulation on a plane. We depict these applications, sorted by their level of control complexity, in Figure 1-2. We design experiments with each system to demonstrate the successful use of the theoretical insights of this thesis. The soft robotic fish [Katzschmann et al., 2014, 2018b] and the soft hand [Homberg et al., 2015, 2018] perform feedforward control to achieve the task of swimming or object grasping, respectively. The model-free control and planning approaches are validated in experiments on a multi-segment arm for motions in a planar maze [Marchese et al., 2014a] and grasping on a plane [Katzschmann et al., 2015]. Finally, for a multi-segment arm, we show that we can dynamically control the arm's deformations with minimal error and also control the same arm to interact with an environment by tracing along its surface without getting stuck [Della Santina et al., 2018].

1.6 Thesis Contributions

1.6.1 Overview of Contributions

Our key technical insights and contributions with this thesis are (i) a systematic description of the design, fabrication, powering, and use of soft elastomer materials in the design of fluidically-driven actuators; (ii) an approach for embedding fluidically-driven actuators into fully self-contained systems for applications such as a soft robotic fish or soft manipulator arms; (iii) computationally tractable modeling approaches, describing the kinematics, impedance, and dynamic characteristics of continuously deformable soft manipulators; and (iv) validated motion planners and closed-loop feedback controllers for the performance of motions in confined environments, grasping objects, achieving dynamic motions, and interacting dynamically with environments.

Parts of the work on the design and fabrication and the work on the model-free quasi-static control in confined environments was developed in collaboration with Marchese [Marchese et al., 2014a, 2015]. This work is now documented in [Marchese, 2015] and the thesis here at hand. The work on the dynamic model-based control of multi-segment soft arms was developed with equal contributions by Della Santina and Katzschmann.

1.6.2 Contributions in Detail

In the following, we list out the detailed contributions, in order of the general structure of this thesis work.

1.6.2.1 Design and Fabrication

We contribute to the design and fabrication techniques of soft robots through the development and presentation of viable morphologies of soft fluidic actuator, soft fabrication techniques with focus on casting, as well as fluidic powering methods under closed-circuit control. We cover both pneumatics and hydraulics as fluidic powering methods. With a modular design approach we combine these soft actuator

morphologies into robotic systems. To be specific, the contributions are as follows:

- We classify three viable fluidic elastomer actuator (FEA) morphologies. That is, an FEA with a (i) ribbed channel structure and embedded transmission lines, (ii) cylindrical channel structure and hollow interior, (iii) seamless pleated channel structure.

- We present three fabrication processes to reliably manufacture these FEAs. These are (i) a lamination-based casting process with heterogeneous embedded components, (ii) a retractable-pin-based casting process, (iii) a lost-wax-based casting process.

- We further present the design, powering and fluidic control of soft robots built for locomotion and manipulation using these design and fabrication approaches.

- The resulting soft robots are (i) a soft robotic fish with an undulating soft tail and custom pump mechanism for cyclic undulation of the tail for underwater locomotion; (ii) a modular, proprioceptive soft hand that has integrated bend and force sensors; and (iii) a set of soft multi-segment manipulator arms for reaching in confined spaces, pick-and-place, and dynamic interaction tasks.

1.6.2.2 Applications for Biomimetic Swimming

We present the full integration of an end-to-end system that locomotes in a biomimetic manner underwater, is remote controlled, and can serve as an underwater observatory for the study of marine life. This biomimetic soft robotic fish is able to swim along three-dimensional trajectories with the use of its soft tail and a buoyancy control system. The application is to observe the biocenosis of coral reefs in the ocean. The key contributions of this robotic fish prototype are:

- 3D controllable motion for prolonged operation underwater;

- autonomous depth control via dive planes and a miniaturized piston-based buoyancy control unit;

- underwater remote control via a miniaturized end-to-end acoustic communication system;
- performing at depths of 0 to 18 m, as evidenced by ocean experiments.

1.6.2.3 Model-Free Control

We show that planar manipulation with a completely soft fluidic elastomer manipulator is possible and provide an approach for the planning and model-free closed-loop control of the arm's motion:

- A planner for whole body continuous motion of a soft planar manipulator that considers the tasks of controlling the pose of the end effector while avoiding collisions between the soft arm's bulging skin and a confined environment.
- A planning algorithm to grasp-and-place randomly positioned objects on a planar surface using a seven-DOF soft manipulator.
- A closed-loop configuration control for a soft fluidic elastomer robot consisting of (i) a kinematic model and an algorithm for estimating the manipulator's configuration in real-time, (ii) a novel device for providing continuous, closed-circuit adjustment of the manipulator's fluid, and (iii) a cascaded curvature controller for the execution of the motion plans.

1.6.2.4 Model-Based Control

We realize dynamic, model-based control of soft robots. We contribute a closed loop dynamic feedback controller for a continuous soft robot capable of:

- dynamically tracking desired segment deformations over time;
- moving in Cartesian space and compliantly tracking a surface.

This is enabled by a dynamic model we call the *augmented formulation*. The augmented formulation links a soft robot to a classic rigid-bodied serial manipulator and enables the application of classical control techniques and insights to the control of soft robots.

1.6.2.5 Applications of Models and Controllers

We successfully deploy our models and controllers to our soft multi-segment arms. We perform autonomous manipulation experiments

- demonstrating the end-effector control of a soft finger attached to a soft arm using a motion tracking system;
- showing the quasi-static control of the pose of an end effector pose while minimizing collisions between the soft arm's bulging skin and a confined environment;
- grasping-and-placing of various objects of unknown geometry placed randomly in the work space without requiring force sensing or accurate positioning;
- performing dynamic motions with minimal tracking error (in simulations and real experiments); and
- moving in Cartesian space and compliantly tracking a long curvy-shaped surface.

1.7 Thesis Outline

The thesis first introduces the related work in Chapter 2. We then begin by presenting the design, fabrication, and actuation of fluidic soft robots in Chapter 3. This chapter also introduces the soft systems (Section 3.6) we have developed. These systems for underwater locomotion (Section 3.6.1) and manipulation (Sections 3.6.6 to 3.6.9) are used in the remainder of the thesis for developing and validating our models, planners and controllers. Chapter 4 shows the application of the design and fabrication to a feedforward controlled soft robotic fish for underwater swimming and exploration. Next, we describe our modeling and control techniques for soft multi-segment arm robots, divided by model-free feedback control in Chapter 5 and model-based feedback control in Chapter 6. Chapter 5 on the model-free control describes the algorithms we developed for quasi-static feedback control. Chapter 6 describes the models and algorithms used to achieve model-based feedback control. In that chapter, we start by describing a dynamic model that uses insights from models for serial rigid robots

and applies those to serial soft manipulators. We propose two model-based controllers for multi-segment soft robots. The experimental validation of the model and control approaches is presented in Chapter 7. To conclude this thesis in Chapter 8, we offer a final discussion by providing a summary of the thesis, list contributions, discuss the limitations, report on the lessons learned, mention the supplementary material online[1], introduce the related projects by the author, and mention possible future extensions to this thesis work.

[1] http://people.csail.mit.edu/rkk/phdthesis/

Chapter 2

Related Work

Animals move very differently from rigid robots: they perform dynamic tasks efficiently and interact robustly, compliantly, and continuously with the external world through their body's elasticity [Roberts and Azizi, 2011]. Inspired by biology, and with the aim of reaching a higher level of agility and compliance, researchers are designing soft robots with elastic bodies. Creating robots with soft bodies to imitate natural systems has the promise of providing us one day with robotic machines with unheard-of agility in motion and excellent dexterity. During the last few years, there has been some progress in the design and fabrication of soft machines. Softness not only provides inherent safety for a human working alongside the robot, but also has the potential of providing better adaptability for manipulation and locomotion tasks. Soft robots exhibit continuous body motion, large scale deformation, and relatively high compliance compared to traditional rigid-bodied robots [Trivedi et al., 2008]. Such characteristics give this class of robots advantages like the ability to mitigate uncertainty with passive compliance [McMahan et al., 2006], perform highly dexterous tasks [Deimel and Brock, 2014], and exhibit resiliency [Tolley et al., 2014b]. Recently, several review articles have appeared on this topic [Kim et al., 2013, Trimmer, 2014, Lipson, 2014, Rus and Tolley, 2015, Laschi et al., 2016], but dynamic modeling and control design for these machines continue to be an outstanding challenge [Polygerinos et al., 2017]. In this chapter, we introduce the relevant related works in the areas of design, fabrication, control, and applications.

2.1 Design

We will discuss the related work on actuation design and sensing modalities, and then cover computational tools for designing soft robots. This review is mostly based on the review we presented in Marchese et al. [2015].

2.1.1 Actuation

There are various approaches to actuating the body of a soft robot. One distinguishing feature of many soft robots is that actuators and/or power transmission systems are integrated within and distributed throughout the body. We will review four common actuator types as follows:

2.1.1.1 Shape Memory Alloy Actuators

The basic operating principle behind Shape Memory Alloy (SMA) technology is that nickel titanium (NiTi) wire contracts under Joule heating. This heating is typically produced by passing electrical current through the wire. The contracting wire can be used as an agonist actuator, similar to the way one's biceps muscle pulls the forearm towards the body. Kim et al. [2009b] model, design, and fabricate these actuators and show their viability in soft robot applications. Additionally, the elastomer-based bio-inspired octopus arms developed in Laschi et al. [2012] and Cianchetti et al. [2014a] use SMA actuation to emulate a muscular hydrostat. Further, Seok et al. [2010] use SMA spring actuators to generate peristaltic locomotion in a worm-like robot, Koh and Cho [2013] developed SMA coil-spring actuators to generate two-anchor crawling in an inchworm-like robot, and Umedachi et al. [2013] use SMA actuators to produce both crawling and inching in a 3D-printed soft robot.

2.1.1.2 Thermal Actuation

Actuation can also be achieved through heating and cooling of materials other than SMA. These thermally active materials substantially deform or change their rigidity due to thermal energy. These materials typically need to be used in combination with

other actuation modalities such as cables. McEvoy and Correll [2014a] and McEvoy and Correll [2014b] thermally actuated a programmable stiffness spine and used it in conjunction with tendons to achieve a change of shape in a soft rubber arm. A thermally tunable and self-healing composite, namely a flexible open-cell foam coated in wax, can achieve significant ranges of stiffness, strength, and volume for the use in soft robotic applications [Cheng et al., 2014]. A soft mobile robot is composed of multiple thermally activated joints driven by a single actuator [Cheng et al., 2010]. Shan et al. [2013] demonstrate electrically tunable rigidity by using a phase-changing metal alloy to reversibly tune the elastic rigidity of an elastomer composite.

2.1.1.3 Cable Actuators

So far, the design of existing so-called "soft" manipulators, which are position-controlled and have multiple degrees of freedom, actually are not soft. Originally, many hard hyper redundant and hard continuum robots [Cieslak and Morecki, 1999, Buckingham, 2002, Gravagne and Walker, 2002, Hannan and Walker, 2003, McMahan et al., 2005, Camarillo et al., 2009] used an array of servomotors or linear actuators to pull cables that move rigid connecting plates located between body segments. Some softer robots have adopted a similar actuation scheme consisting of tendons pulling rigid fixtures embedded within an elastomer body, for example, the soft-bodied fish [Valdivia y Alvarado and Youcef-Toumi, 2006] and the soft octopus-inspired arms [Calisti et al., 2010, 2011]. There is an example of a position-controlled soft rubber arm using cables without rigid plates developed by Wang et al. [2013], but the arm consists of only one actuated segment and therefore does not require internal fixtures.

2.1.1.4 Pneumatic Artificial Muscles

Another common actuation scheme for soft robots involves distributed Pneumatic Artificial Muscle (PAM) actuators, also known as McKibben actuators. A PAM actuator is fundamentally composed of an inflatable elastic tube surrounded by a braided mesh. Depending on the weave pattern of the braided mesh, the actuator can be designed to contract or extend under internal pressurization. Typically, these

actuators are operated with driving pressures between 3.4 bar to 6.9 bar. These actuators have been used and studied extensively in Chou and Hannaford [1996], Tondu and Lopez [2000], Caldwell et al. [2000], Daerden and Lefeber [2002], Reynolds et al. [2003]. Notable examples for semi-soft robots using PAMs include McMahan et al. [2006], Pritts and Rahn [2004], Kang et al. [2013]. McMahan et al. [2006] uses 18 air muscle actuators distributed throughout four arm segments. Pritts and Rahn [2004] uses 14 McKibben actuators within two body segments. Kang et al. [2013] uses 24 PMAs within 6 body segments. Again, these designs are not entirely soft, because rigid plates are included between the segments for actuator mounting and as kinematic constraints.

2.1.1.5 Fluidic Elastomer Actuators

A softer alternative is the Fluidic Elastomer Actuator (FEA), which is predominantly used throughout this thesis. The FEA is an actuator composed of low Shore durometer[1] rubber ranging from 30 Shore OO to 30 Shore A and driven by fluid with relatively low pressure in the range of 0 bar to 1 bar. Although many motion primitives are achievable with a FEA (e.g., extending, contracting, twisting, and bending) in this work, we primarily focus on actuators designed for bending. Its basic structure consists of two soft elastomer layers separated by a flexible, but relatively inextensible constraint. The inextensible constraint is typically created by using cloth, paper, plastics, and even stiffer rubbers. Each of these elastomer layers contains embedded fluidic channels. By pressurizing the fluid entrapped in these channels, stress is induced within the elastic material producing localized strain. This strain, in combination with the relative inextensibility of the constraint, produces body segment bending. FEAs can be powered pneumatically or hydraulically.

As the review by Rus and Tolley [2015] discusses, perhaps the earliest application of pneumatically actuated elastomer bending segments to robotics was by Suzumori et al. [1992]. Here, fiber-reinforced Flexible Microactuators were developed and shown to be viable in a manipulator and multi-fingered hand. Recently, these concepts have been

[1] ASTM D2240-00

extended and developed into the FEA and used to build a variety of soft mechanisms [Shepherd et al., 2011, Ilievski et al., 2011, Morin et al., 2012, Martinez et al., 2013, Roche et al., 2014] and soft robotic systems [Onal et al., 2011, Marchese et al., 2011, Onal and Rus, 2013, Marchese et al., 2014c,b,a, Katzschmann et al., 2014, 2015, Tolley et al., 2014a,b, Marchese and Rus, 2016, Marchese et al., 2016, Katzschmann et al., 2018b]. Furthermore, Polygerinos et al. [2013], Mosadegh et al. [2014], and Katzschmann et al. [2015] have investigated more elaborate channel designs in order to reduce elastomer strain on the outer layer of the actuator, allowing for higher bending curvatures. Additionally, Cianchetti et al. [2014b] developed a fluidically actuated bending arm with a jamming spine. Jamming actuators were proposed by Liu and Nagel [1998] as well as Brown et al. [2010]. Volder and Reynaerts [2010] provide a detailed review of micro-actuators using pneumatics or hydraulics. Wehner et al. [2014] reviewed existing pneumatic energy sources for the actuation of FEAs.

There are also less flexible, fiber-reinforced FEAs that occupy the soft actuator space between purely elastomer FEAs and PAMs. While these actuators have to be operated with comparably higher driving pressures of up to 1.7 bar to 2.4 bar, they can apply higher forces accordingly, which is advantageous when higher loads have to be handled or gravity needs to be overcome. There are several notable examples of fiber-reinforced FEAs in the literature by Suzumori et al. [1992, 2007], Bishop-Moser et al. [2012], Galloway et al. [2013], Deimel and Brock [2013, 2014], Park et al. [2014], Polygerinos et al. [2015] and Connolly et al. [2017].

2.1.2 Sensing

Configuration estimates of soft robots are typically acquired through exteroceptive means, for example motion tracking systems [Marchese et al., 2014b] or RGB cameras [Marchese et al., 2014c]. Various sensor types that can measure curvature and bending have been studied, but few have been integrated into a soft robot. Park et al. [2010, 2012] have shown that an artificial skin made of multi-layered embedded microchannels filled up with liquid metals can be used to detect multi-axis strain and pressure. Danisch et al. [1999] described a fiber optic curvature sensor, called

Shape Tape, that could sense bend and twist. Weiß and Worn [2005] have reported on the working principle of resistive tactile sensor cells to sense applied loads. Biddiss and Chau [2006] described the use of electroactive polymeric sensors to sense bend angles and bend rates in protheses. Kusuda et al. [2007] developed a bending sensor for flexible micro structures like pneumatic balloon actuators. Their sensor used the fluid resistance change of the structure during bending. Other recent work in this area include that by Vogt et al. [2013] and Chossat et al. [2014]. Chuah and Kim [2014] presented a new force sensor design approach that mapped the local sampling of pressure inside a composite polymeric footpad to forces in three axes.

2.1.3 Design Tools

Design tools for soft robots are limited with respect to the availability of design tools for more traditional rigid-body robots. Suzumori et al. [2007] use finite element modeling to analyze the bending of fiber re-inforced pneumatic tube-like actuators. Specifically, hyper-elastic material models are used to capture the nonlinear material properties of rubber, line elements are used to represent radial inextensibility constraints due to fiber reinforcement, and the simulation is performed using the software MARC. Outside of this example, the community has generally found that iterative nonlinear finite element solvers are limited to small deformations and offer limited use when modeling very soft nonlinear materials [Lipson, 2014]. VoxCAD and the Voxelyze physics engine, as used in Cheney et al. [2013] and Lehman and Stanley [2011] and reviewed by Lipson [2014], are simulation tools for very soft nonlinear materials. These tools use the concept of nonlinear relaxation to effectively perform physically correct particle-based material simulation. They have the advantage of allowing the user to individually set the local material properties of each particle. The disadvantage is that many physical parameters of active and passive material types must be derived experimentally. More recently, Duriez et al. [2016] as well as Duriez and Bieze [2017] proposed a framework for the simulation of soft robots using an optimization-based inverse model.

2.2 Fabrication

There have been various design and fabrication techniques proposed for fluidic elastomer actuators. This review on fabrication techniques is based on our review in Marchese et al. [2015].

Cho et al. [2009], Rus and Tolley [2015], Polygerinos et al. [2017] review several manufacturing processes for soft biomimetic robots. The vast majority of soft elastomer robots rely on the processes of soft lithography [Xia and Whitesides, 1998], shape deposition manufacturing [Cham et al., 2002], and/or thread-reinforced pneumatic chambers [Deimel and Brock, 2013]. For soft fluidic elastomer robots, the soft lithography fabrication process generally consists of three steps: (1) Two elastomer layers are molded through a casting process using pourable silicone rubber. The mold used for the outer layer contains a model of the desired channel structure. When cast, the outer layer contains a negative of this channel structure. The mold used for the constraint layer may contain fiber, paper, or a plastic film to produce the property of inextensibility required for actuation. When the elastomer is poured, this material is effectively embedded within the constraint layer. (2) The two layers are cured, removed from their molds, and their joining faces are dipped into a thin layer of uncured elastomer. (3) Finally, the two layers are joined and cured together. The primary limitation of this soft lithography fabrication process is that it is fundamentally 2.5D, meaning that the robots are largely constrained to a planar morphology and limited in the ability to achieve amorphous, three-dimensional forms. Retractable pin casting [Marchese et al., 2015] is another fabrication method to realize soft fluid actuators. Umedachi et al. [2013] provide the first SMA-actuated soft robot fabricated using 3D printing. However, although 3D printing allows printing of flexible materials in amorphous forms, these materials are relatively brittle with respect to cast rubbers and are therefore not well-suited for FEAs, which rely on pressurization of the rubber. 3D printing of soft actuators using a method called Printable Hydraulics [MacCurdy et al., 2016] has shown that fine-grained control of various materials allows for the automated fabrication of heterogeneous structures with embedded liquids as functional

actuation or passive damping channels. While 3D printing opens previously unknown dimensions in heterogeneous actuator design, the materials available for most printing techniques are typically not deformable enough and also not robust enough to undergo strong cyclical flexing. Direct printing of a silicone elastomer mix [Morrow et al., 2017] addresses this limitation in material properties: the proposed method allows the use of two-part silicone elastomers within a 3D printer for fused deposition manufacturing. However, none of these methods allow for the repeatable fabrication of soft fluidic actuators without weakening seams and integrated functional structures such as backbones or tubing. Steltz et al. [2009] proposes the use of wax for the fabrication of jammable skin chambers, which stiffen by vacuuming them. Motivated by this use of wax, monolithic casting using a lost-wax fabrication technique [Katzschmann et al., 2014] is a reliable and easily reproducible way to fabricate soft actuators with complex inner cavities and without seams that may compromise structural integrity.

2.3 Control

Highly compliant robots, whose bodies are made of soft rubber, and distributed pneumatic actuators are usually open-loop controlled. Prior works in this field focused on open-loop control, that is the actuation of the soft robotic body without measuring the deformation or other states of the system, and feed those back to regulate the actuation. This approach is not sufficient for providing accurate control of the curvature of a body segment during the execution of tasks. Closed-loop control is closing the loop from state measurements to actuation to allow for more accurate control. Closed-loop control for soft robots was shown in our works [Marchese et al., 2014b,a, Katzschmann et al., 2015, Della Santina et al., 2018], and the following review on the control of soft robots is based on the reviews presented in these works.

Most fluid-powered soft robots use open-loop valve sequencing to control the bending of a body segment. Valve sequencing means that a valve is turned on for a duration of time to pressurize the actuator and then turned off to either hold or deflate it. For instance, there are soft rolling robots developed by Correll et al. [2010], Onal

et al. [2011], and Marchese et al. [2011] made of Fluidic Elastomer Actuators (FEAs) and controlled through the sequencing of valves. Also a soft snake-like robot developed by Onal and Rus [2013] uses this open-loop scheme to control eight distributed FEAs in four body segments to enable serpentine locomotion. Shepherd et al. [2011] use an open-loop valve controller to drive body segment bending in an entirely soft multi-gait robot and then passive control in an explosive, jumping robot [Shepherd et al., 2013a]. Martinez et al. [2013] developed manually operated elastomer tentacles containing nine PneuNet actuators embedded in three body segments. There is also an example of controlling a soft pneumatic inchworm-like robot using servo-controlled pressure described in Lianzhi et al. [2010]. Here, a pulse-width modulation is used to drive rapid valve-switching to continuously vary the airflow.

Open-loop control is also common for soft rubber robots that do not use pneumatic actuation. For example, previous work on soft bio-inspired octopus-like arms developed by Calisti et al. [2010] demonstrate open-loop capabilities like grasping and locomotion [Laschi et al., 2012, Calisti et al., 2011]. Umedachi et al. [2013] developed a soft crawling robot that uses an open-loop SMA driver to control body bending.

2.3.1 Kinematics

Despite variability in the design of soft continuum robots [Gravagne and Walker, 2002, Pritts and Rahn, 2004, McMahan et al., 2005, 2006, Chen et al., 2006, Camarillo et al., 2009, Kang et al., 2013, Wang et al., 2013], their kinematics are often represented using a piecewise constant curvature (PCC) model. The PCC assumption means that each body segment of a multi-segment arm is assumed to deform with constant curvature. This representation for continuum robots is reviewed by Webster and Jones [2010]. Hannan and Walker [2003] provide one of the first examples of the PCC model. As Webster's review discusses, the generality of this modeling assumption is due to the physics behind the deformation. Specifically, Gravagne et al. [2003] and Li and Rahn [2002] show that a moment applied by a guided cable fixed to the end of a continuum backbone produces constant curvature along the backbone. Jones and Walker [2006b] show that the constant curvature concept also applies to pneumatic muscle actuators

bending a continuum backbone. Recently, Onal et al. [2011] showed that rectangular fluidic elastomer actuators with serpentine channels deform along an arc of constant curvature. Marchese et al. [2014b] demonstrate closed-loop positioning of a soft and highly compliant inextensible planar arm under the PCC modeling assumption.

2.3.2 Planning

A limitation of existing approaches in solving the inverse kinematics problem for soft continuum arms is that the whole arm, in addition to the end effector's pose, is not considered in the solution. Autonomous obstacle avoidance and movement through a confined environment is difficult without a computational solution for the inverse kinematics problem that is aware of the robot's whole arm in space. Buckingham [2002] articulates as a distinguishing advantage of a snake-like arm, that it can potentially achieve the primary task of tip control, while meeting the secondary task of shaping the whole arm. Neppalli et al. [2009] provide a closed-form inverse kinematics solution for continuum arms, but the Jacobian-based solution only considers the endpoint of the final body segment and obstacle avoidance requires manual planning. Jones and Walker [2006a] control Air-OCTOR and OctArm using real-time Jacobian-based control over task-space, but rely on joystick control for whole arm tasks like manipulation and grasping [Csencsits et al., 2005]. Local optimization has shown promising results for rigid-bodied redundant manipulators [Nenchev, 1989], but this kind of technique has not been used to solve the whole body manipulation problem for a soft robot. Xiao and Vatcha [2010] presented simulation results using an online motion planner for a planar hard continuum manipulator. This work was extended by Li and Xiao [2015] to present a more general formulation to a constrained hard continuum manipulation. Soft-bodied fluidic robots with highly deformable exterior envelopes [Correll et al., 2010, Onal et al., 2011, Onal and Rus, 2013, Marchese et al., 2011, 2014b, Shepherd et al., 2011, 2013a, Martinez et al., 2013] should consider whole body manipulation when moving in task-space. With fewer kinematic constraints, the envelopes of these soft robots expand or radially bulge at locations along the body under actuation. Accordingly, whole body planning for soft and highly compliant robots must take this

dynamic envelope into consideration.

2.3.3 Closed-Loop Grasping Control

There are several examples of soft fluidic grippers described in recent literature. Deimel and Brock [2013] developed a pneumatically actuated three-fingered hand made of reinforced silicone that is mounted to a hard robot and capable of robust grasping. More recently, they have developed an anthropomorphic soft pneumatic hand capable of dexterous grasps [Deimel and Brock, 2014]. Ilievski et al. [2011] created a pneumatic starfish-like gripper composed of silicone membranes and demonstrated how it can grasp an egg. Stokes et al. [2014] use a soft elastomer quadrupedal robot to grasp objects on a hard-soft hybrid robotic platform. A puncture-resistant soft pneumatic gripper is developed in Shepherd et al. [2013b]. An alternative to positive pressure-actuated soft grippers is the robotic gripper based on the jamming of granular material developed in Brown et al. [2010]. Perhaps the soft pneumatic actuator designs most related to our work are the Pneu-net designs by Mosadegh et al. [2014] and by Polygerinos et al. [2013]. These finger-like actuators can deform with minimal volume change and leverage a pleated channel morphology.

2.3.4 Dynamic Model-Based Feedback Control

Despite the emergence of several soft robotic hardware architectures [Laschi et al., 2012, Seok et al., 2013, Holland et al., 2017, Katzschmann et al., 2018b, Homberg et al., 2018], we are still missing examples that show the execution of dynamic movements and controlled compliant interaction with the environment. One of the main motivations for building soft robots is to become better at dynamic movements and compliant interactions, but robots with rigid structures still outperform their soft counterparts in these tasks [Andersson, 1989, Leidner et al., 2014, Kuindersma et al., 2016, Hong et al., 2017, Haddadin et al., 2017]. To a large degree, this limitation has to be attributed to the lack of a *soft robotic brain* exploiting the *embodied intelligence* which the elastic body of a soft robot provides [Pfeifer et al., 2012]. Both tasks, dynamic movements

and compliant interactions, are indeed inherently dynamical, while most of the existing control algorithms for soft robots rely only on static modeling [Webster and Jones, 2010, Zhang et al., 2016, Skorina et al., 2016, Lismonde et al., 2017, Wang et al., 2017a, George Thuruthel et al., 2018]. In these models, the robot's shape is described as a spline of circular arcs, resulting in a description which is exact when a set of pure torques are applied to the robot. However, these so-called PCC models have proven to generate good approximations also outside this ideal condition. Other prior work on modeling and control of soft robots includes modeling biological systems [Sareh et al., 2012], automatically designing the soft robot's kinematics [Runge and Raatz, 2017], and developing algorithms for inverse kinematics [Marchese and Rus, 2016, Wang et al., 2017a]. The use of purely kinematic strategies for soft robot control, together with heuristically tuned low-level high gain feedback controllers, work well in static situations with sparse contacts with the environment. However, a dynamic model is required for control strategies for dynamic tasks and continuous interactions with the environment. An issue that slowed down the development of dynamical control strategies is the difficulty of developing reliable yet tractable mathematical models for soft robots. The general formulation of an exact model requires to take the infinite dimensionality of the robot's state space into account [Rubin, 2013, de Payrebrune and O'Reilly, 2016]. However, the theory of infinite state space control is still confined to relatively simple systems [Curtain and Zwart, 2012], and its applications are still preliminary, even if interesting in their own right [Luo et al., 2012, Armanini et al., 2017]. This issue drives the development of simplified models that are capable of describing the robot's behavior through a finite set of variables. For some hybrid soft-rigid systems the rigid part is dynamically dominant, which allows to neglect the soft dynamics in the control design [Skorina et al., 2015, Deutschmann et al., 2017b,a]. Moving to a more general scenario, finite element methods are commonly used in the mechanical design of soft robots [Polygerinos et al., 2015, Chenevier et al., 2018]. However, their high dimensionality limits the practical use of these models for feedback control. Simulations provided in Thieffry et al. [2017] use a linearized finite element model to regulate postures. Prior work on dynamic models with finite dimensions

also includes discrete Kirchhoff-Love models [Bergou et al., 2008, Greco and Cuomo, 2013], and discrete Cosserat models [Gazzola et al., 2016, Renda et al., 2017, Sadati et al., 2018]. We are not aware of any prior work that applies these dynamic models for the control of soft robots. Dynamic models based on the PCC hypothesis were presented in Falkenhahn et al. [2015] and Marchese et al. [2016]. The models presented in these works are merely used for generating purely feedforward actuations. The application of PCC models for regulating the posture of continuous rigid robots is discussed in Kapadia et al. [2010, 2014]. To the best of our knowledge, there has only been little previous work on the design and validation of dynamical feedback controllers for soft robots. Our work on a soft juggling robot proposes a dynamic implicit-surface model that describes the contact of rigid objects colliding with highly deformable soft surfaces. This dynamic model is used experimentally for controlling the trajectory of a fast-sliding puck through an actuated paddle with a surface made of rubber [Katzschmann et al., 2018c]. Our initial conference work [Della Santina et al., 2018] on the dynamic modeling and controlling of a planar soft robotic arm is substantially extended in this thesis.

2.4 Devices and Applications

2.4.1 Soft Locomotory Robots on Land

Natural systems often exceed the performance of rigid robotic systems due to their soft and compliant characteristics, such as the unmatched speed and agility of a cheetah [Wilson et al., 2013, Seok et al., 2015] or the ability of a dead fish to swim upstream [Beal et al., 2006]. In the past years, soft roboticists have made many soft robots intended for land and water locomotion. For example, rolling belts have been produced by Correll et al. [2010] and Marchese et al. [2011]. Trimmer et al. [2006] and Umedachi et al. [2013] emulated the peristaltic locomotion of caterpillars. Shepherd et al. [2011] developed a multi-gait walking robot, and Shepherd et al. [2013a] developed a jumping robot powered by combustion. However, a limitation of the aforementioned locomotory

robots is that they require an electrical and/or pneumatic tether. Soft actuation systems, especially fluidic actuation systems, typically require significant supporting hardware and they often prevent soft locomotory robots from being self-contained. That said, there are a few examples of untethered soft robots: Onal et al. [2011] created a rolling robot, Onal and Rus [2013] emulated the serpentine locomotion of snakes, and Tolley et al. [2014b] developed a quadrupedal walking robot; these are all soft-bodied fluidic elastomer systems. Seok et al. [2010] realize peristaltic locomotion with a self-contained SMA-based inchworm. However, a limitation of all these untethered soft platforms is that performance is severely limited with respect to their rigid-bodied counterparts, and this limitation is due to the constraints imposed by bringing on-board all supporting hardware. More specifically, they all exhibit locomotory speeds of 0.008 to 0.07 body lengths per second.

2.4.2 Soft Locomotory Robots Underwater

The pioneering works in robotic fish were the robotic pike [Kumph, 2000] and the VCUUV [Anderson and Chhabra, 2002], systems using a driven link assembly to perform fish-like swimming. The hydraulic control of tuna fins [Pavlov et al., 2017] served as an inspiration to develop soft robotic fish with hydraulic actuation. Several underwater vehicles using bio-inspired locomotion mechanisms have been proposed since [Chu et al., 2012]. There have been initial steps towards soft robots that mimic fish [Marras and Porfiri, 2012, Marchese et al., 2013, 2014c, Katzschmann et al., 2014, Phamduy et al., 2016, Zhong et al., 2017], mantas [Suzumori et al., 2007, Cloitre et al., 2014, Li et al., 2017], lamprey [Stefanini et al., 2012, Manfredi et al., 2013], and octopi [Calisti et al., 2011, Giorgio-Serchi et al., 2013]. Several simple fish prototypes have been proposed for studying the interaction of robotic fish with real fish in small tanks [Marras and Porfiri, 2012, Polverino et al., 2012, Cianca et al., 2013, Butail et al., 2015, Ruberto et al., 2016, Bonnet et al., 2016, Romano et al., 2017a]. None of the proposed systems have demonstrated autonomous, untethered biomimetic underwater operation in a real environment at several meters of depth [Raj and Thakur, 2016]. Furthermore, none of those systems have observed or interacted with aquatic life in

their natural habitat.

2.4.3 Soft Grippers

There are several hardware examples for soft grippers described in recent literature. The following review is mostly based on our review in Homberg et al. [2018].

Dollar and Howe [2006, 2010] presented one of the earliest examples of underactuated and flexible grippers. Fabricated with stiff links and tendon cables providing underactuated grasping force, the hand was shown to be able to grasp a wide array of objects easily. Deimel and Brock [2013] developed a pneumatically actuated three-fingered hand made of reinforced silicone that is mounted to a hard robot and capable of grasping. More recently, they have developed an anthropomorphic soft pneumatic hand capable of dexterous grasps, which is not mounted to a robot, but instead held by a human [Deimel and Brock, 2014, 2016]. The hand was evaluated grasping a variety of objects with grasps designed as a dexterity test for human hands [Kapandji, 1986]. Using a soft-lithography fabrication, Ilievski et al. [2011] created a pneumatic starfish-like gripper composed of an array of silicone chambers and a PDMS membrane. The authors demonstrated the grasping of an egg. The gripper hangs on a string and grasps objects like an egg or a mouse in an open-loop controlled manner. Stokes et al. [2014] use a soft elastomer quadrupedal robot attached to a wheeled robot to grasp and retrieve objects. A puncture-resistant soft pneumatic gripper is developed by Shepherd et al. [2013b]. An alternative to positive pressure-actuated soft grippers is a robotic gripper that makes use of granular material jamming developed by Brown et al. [2010]. Amend et al. [2012] expanded the work on the jamming gripper, using positive pressure to also throw objects. The soft octopus-inspired arms [Calisti et al., 2010, 2011] are not fluidic powered, but instead use cables to pull rigid fixtures embedded within an elastomer body. These arms were capable of grasping objects like pens or screws. A soft robotic tentacle developed by Martinez et al. [2013] was able to hold a flower and a horseshoe-shaped object. We presented an open-loop controlled soft gripper that performs haptic identification of grasped objects [Homberg et al., 2015, 2018]. Using this soft gripper, Choi et al. [2016] use vision for object localization before

and after a grasp and Choi et al. [2018] use a learning approach to perform repeated grasps of objects. The fast PneuNets design by Mosadegh et al. [2014] and Polygerinos et al. [2013] is similar to the single-finger design presented by Katzschmann et al. [2015]. These finger-like actuators deform with small volume change and can bend to high curvatures.

2.4.4 Soft Manipulator Arms

Recently, continuum manipulators consisting of soft elastic material have been developed. These soft rubber manipulators can be categorized in two primary morphologies. The first type of morphology are tendon-driven manipulators consisting of variable-length tendons, typically cables or shape memory alloy wire, embedded in and anchored to portions of a soft silicone rubber arm. For example, previous work on soft bio-inspired octopus-like arms developed by Calisti et al. [2010] used tendons and demonstrated capabilities like grasping and locomotion [Laschi et al., 2012, Calisti et al., 2011]. Also, Wang et al. [2013] developed a cable-driven soft rubber arm consisting of one large actuated segment that bends bi-directionally. Lastly, McEvoy and Correll [2014a,b] used a programmable stiffness spine in conjunction with tendons to achieve shape change in a soft rubber arm. The second morphology uses fluidic elastomer actuators (see Section 2.1.1.5) distributed inside the manipulator's soft body segments. The primary advantages of using fluidic actuation for soft continuum manipulators is that this energy transmission system (i) can be lightweight, ensuring easy integration into distal locations of the body, (ii) conforms to the time-varying shape of the manipulator, and (iii) does not require rigid components for implementation. There are several examples of soft fluidic grippers described in recent literature. Deimel and Brock [2013] developed a pneumatically actuated three-fingered hand made of fiber-reinforced silicone that is mounted to a hard industrial robot and capable of robust grasping. More recently, they have used similar fiber-reinforced actuation technology to develop an anthropomorphic soft pneumatic hand capable of dexterous grasps [Deimel and Brock, 2014]. Additionally, we have previously shown that planar manipulation is possible with an entirely soft robot. That is, a six-segment planar flu-

idic elastomer robot can be positioned precisely using a closed-loop kinematic controller [Marchese et al., 2014b,a, Katzschmann et al., 2015]. Ilievski et al. [2011] created a pneumatic starfish-like gripper composed of FEAs and demonstrated its capability of grasping an egg. Stokes et al. [2014] used an FEA-based elastomer quadrupedal robot to grasp objects on a hard-soft hybrid robotic platform. A puncture-resistant soft pneumatic gripper has been developed by Shepherd et al. [2013b]. An alternative to positive pressure-actuated soft grippers is the robotic gripper based on the jamming of granular material developed in Brown et al. [2010]. Another relevant piece of work is the manually operated 3D elastomer tentacles developed by Martinez et al. [2013] containing 9 pneumatic crescent-shaped channels embedded within 3 body segments.

Chapter 3

Design and Fabrication of Fluidic Elastomer Robots

For a self-contained soft robot, we need a robotic body that contains actuation, powering, sensing, and computation. This chapter focuses on design and fabrication of a soft body with built-in actuation, and also covers the aspects of powering and state sensing. In particular, in this chapter we discuss the operating principles, actuator morphologies, fabrication processes, sensing approaches, and powering through pressurization of fluidic elastomer actuators. We also present the resulting soft-actuated robots used throughout the rest of this thesis. Most of this chapter is based on work presented in [Marchese et al., 2015, Katzschmann et al., 2015, 2018b] and extends the design and fabrication aspects presented in three previous conference publications, namely Katzschmann et al. [2014], Marchese et al. [2014a,b].

3.1 Overview

This chapter describes new processes for design and fabrication of fluidic elastomer actuators [Correll et al., 2010, 2014, Onal and Rus, 2013] for soft robotic systems. Fluidic elastomer actuators are the fundamental building blocks of the soft robots presented in this thesis. A fluidic elastomer actuator is a body made of polymers with viscoelasticity and shaped in a way that they contain functional inner cavities.

These cavities allow for actuation through pressurization, creating an integrated body that acts both as a continuously deforming joint as well as a structural link. In comparison, revolute or prismatic joints and rigid links are the typical building blocks as we know them from traditional robots. Cavities within the body can be made in different shapes, leading to different actuator morphologies. Each morphology requires its own fabrication method. In this chapter, we describe the design of these morphologies and each fabrication method. Fabrication processes shown here can be used to create actuatable soft modules; these modules can be composed in series or in parallel to create a range of different soft robots. The goal of this chapter is to provide and compare multiple actuator morphologies and multiple fabrication processes for realizing soft autonomous fluidic elastomer robots. Later in this thesis, we experimentally validate these morphologies in form of soft and compliant locomotory robots and manipulators.

3.1.1 Outline of this Chapter

This chapter is organized as follows. We present the design and characterization of three fluidic elastomer actuator morphologies in Section 3.2. These actuator morphologies are differentiated by their internal channel structure, namely: ribbed, cylindrical, and pleated. Next, in Section 3.3 we provide three alternative fabrication approaches for reliably fabricating different morphologies of fluidic elastomer actuators. These processes are lamination-based embedded casting, retractable-pin-based casting, and lost-wax-based casting. Alternative approaches for fluidically pressurizing these actuators are presented in Section 3.4. The closed-circuit fluid control of the actuators is then presented in Section 3.5. To place it in context, in Section 3.6 we provide examples of robots built using the design and fabrication techniques of this chapter. Finally, in Section 3.7 we give a summary of our contributions to the field of design and fabrication of soft robots.

3.2 Actuators

In this section we detail the design and fabrication of three different soft fluidic elastomer body segments. Each type of body segment can serve as a unit-module for composing different soft robot body morphologies. The primary design constraint is that the actuated body segments should almost entirely consist of soft materials. The primary functional specification is that these actuated segments should integrate into an autonomous robotic system. That is, they should be capable of performing tasks such as trajectory tracking in free space, moving dexterously through confined spaces, and/or grasping and placing objects, all of it without human intervention.

3.2.1 Operating Principles

Despite the variability in fluidic elastomer actuator morphologies, their fundamental operating principles are universal. This section provides an overview of these operating principles. Generally, each segment of a fluidic elastomer robot bends and this bending occurs due to material strain. Figure 3-1 illustrates how unidirectional bending arises from material strain. Consider a block of elastomer where the edges of the top and bottom surfaces have equal lengths, L_0. If the top surface is strained in a way that its new edge length is $L_0 + \Delta L$, but the bottom of this block remains unextended, then the elastomer will bend.

Bending is the basic motion primitive of the fluidic elastomer robot.

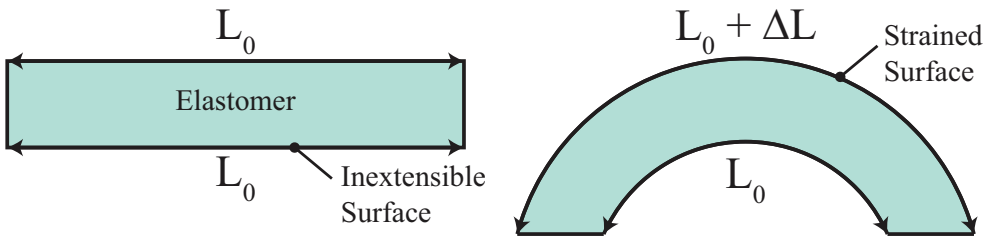

Figure 3-1: Operating principle of a bending elastomer segment: One surface of the elastomer is strained while the opposite side remains unextended. The difference in length produces bending. This figure first appeared in Marchese et al. [2015].

In order to generate strain within the elastomer, this class of actuator uses pres-

surized fluids. Essentially, expandable, fluid-filled chambers are embedded within the elastomer. When these chambers are pressurized, the entrapped fluid generates stress in the material causing the material to strain. This concept is illustrated in Figures 3-2A and 3-2B. Here, the entrapped fluid is shown in yellow and its pressure is p_c. In order to express the relationship between fluid pressure and elastomer deformation, we can use a one-dimensional simplification of an iterative model. Let $\bar{h}$ and $\bar{t}$ be the initial undeformed diameter and wall thickness of a cylindrical elastomer channel, and let $\hat{h}$ and $\hat{t}$ represent the deformed diameter and wall thickness. Algorithm 3.1 expresses how the channel's diameter grows as a function of pressure. Stresses are successively updated based on deformed channel dimensions. Here, $\Delta\mathbf{p}_c$ is a vector of all consecutive incremental pressure increases until the maximum channel pressure $p_c^{\max}$ is reached. Stress and strain in the elastomer are represented by σ_{el} and ϵ_{el}, respectively. The procedure STRAINLOOKUP() provides a nonlinear mapping from stress to strain.

Algorithm 3.1 Iterative channel deformation

Input: $\bar{t}$, $\bar{h}$, $\Delta\mathbf{p}_c$, $p_c^{\max}$

$\hat{h} \leftarrow \bar{h}$.
$\hat{t} \leftarrow \bar{t}$.
$\bar{c} \leftarrow \pi\left(\frac{\bar{t}}{2} + \bar{h} + \frac{\bar{t}}{2}\right)$. ▷ Circumference of Channel
$p_c \leftarrow p_{\text{atm}}$. ▷ Atmospheric Pressure
$i \leftarrow 0$.
repeat
  $\sigma_{\text{el}} \leftarrow p_c \frac{\hat{h}}{2\,\hat{t}}$.
  $\epsilon_{\text{el}} \leftarrow$ STRAINLOOKUP(σ_{el}).
  $\hat{c} \leftarrow \bar{c}\,(1+\epsilon)$.
  $\hat{h}, \hat{t} \leftarrow$ `solve` $\left\{ \begin{array}{l} \textbf{Circumferential Strain:} \\ \hat{h} = \frac{\hat{c}}{\pi} - \hat{t} \\ \textbf{Conservation of Material Volume:} \\ \pi\left[\left(\frac{\hat{h}}{2} + \hat{t}\right)^2 - \frac{\hat{h}^2}{4}\right] = \pi\left[\left(\frac{\bar{h}}{2} + \bar{t}\right)^2 - \frac{\bar{h}^2}{4}\right] \end{array} \right\}$.
  $p_c \leftarrow p_c + \Delta p_{c,i}$.
  $i++$
until $p_c \geq p_c^{\max}$

3.2.2 Actuator Morphologies

This section describes three separate soft elastomer body segments actuated using pressurized fluids. We use a defining structural feature to refer to each of the presented

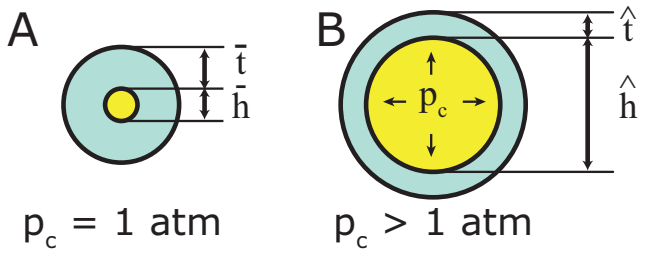

Figure 3-2: Operative principle of producing material strain through fluidic power: (**A**) Fluid, shown in yellow, is entrapped in an elastomer channel. (**B**) When the fluid is pressurized, stress and therefore strain are generated in the material. The algorithm is adapted from [Marchese et al., 2015].

segment morphologies, namely they are (i) ribbed, (ii) cylindrical, and (iii) pleated. Section 3.6 shows examples that use these segments to make a tail of a swimming robot or to form a multi-body manipulator by serial connection. Although similar in material composition and function, differences in internal and external structure and form lead to several distinct differences between the three presented morphologies. First, we present each morphology, examining the structural differences, then we provide a comparative characterization of the segments, highlighting salient performance characteristics.

3.2.2.1 Ribbed Segment

The ribbed fluidic elastomer actuator with its multiple rectangular channels was first implemented and characterized in Correll et al. [2010] followed by Onal et al. [2011], Onal and Rus [2013]. Joining two fluidic elastomer actuators in an agonist-antagonist pairing provides bidirectional bending. This actuator type provided the fundamental segment-level structure of the manipulator developed in Marchese et al. [2014b]. We refer to this three-layer composite here as a ribbed segment. That is, two actuator layers are combined in a pair, but separated by an inextensible constraint layer. An implementation of this segment morphology is shown in both a neutral (Figure 3-3A) and a bent state (Figure 3-3B). Bending is produced through the pressurization of agonist fluidic channels (Figure 3-3b) that are embedded within the actuated layers (Figure 3-3, layers 1 and 3). The structure of the actuated layers is cast of soft

elastomer (Figure 3-3a). When pressurized, the agonist fluidic channels expand and strain the elastomer. This deformation is transferred into bending by means of an inextensible but flexible constraint (Figure 3-3c) embedded within the center layer (Figure 3-3, layer 2). Ribs located between channels (Figure 3-3e) mitigate strain normal to the inextensible neutral axis. At segment level, Marchese et al. [2014b] extended the ribbed segment design to make it suitable for inclusion in a multi-segment manipulator. Specifically, fluidic supply channels (Figure 3-3d) were introduced on both sides of the inextensible constraint and embedded within the center layer. Each segment accommodates multiple, parallel supply channels, two for each body segment within the manipulator. For a detailed model of how a ribbed segment deforms under fluidic pressure input, please refer to Marchese et al. [2014c]. It is important to note that this simplifying static model assumes that ribbed channels deform purely by extending their side and top walls, and that these wall stresses are based on initial channel geometry. In reality, as is shown here in Algorithm 3.1, wall stresses change as a function of the deformed geometry. If needed, Algorithm 3.1 can be used to augment the ribbed model with variable geometry used for the soft robotic fish in Marchese et al. [2014c].

Advantages: The primary benefits of this morphology in relation to alternatives presented in this section are as follows: (1) Ribs between channels mitigate strain normal to the neutral axis. (2) For a fixed fluid energy input, this segment provides greater bending than the cylindrical segment.

Disadvantages: The primary disadvantages of this morphology in relation to alternatives presented in this section are as follows: (1) The three layer structure is prone to delamination and rupture under high strain. (2) Manufacturing this rectangular, layered structure is challenging because all transmission lines must be embedded within the thin constraint layer.

3.2.2.2 Cylindrical Segment

The cylindrical fluidic elastomer segment is an alternative to the ribbed design. We first presented this design in Marchese et al. [2014a]. Design inspiration was drawn from the

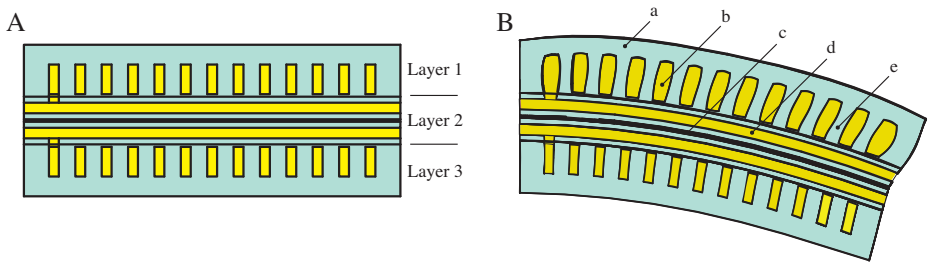

Figure 3-3: A conceptual representation of the ribbed segment morphology: The segment is composed of three layers made of soft elastomer (a), embedded fluidic channels (b), inextensible, but flexible constraint (c), embedded fluid transmission lines (d), and ribbed structures (e). (**A**) The segment in an unactuated, or neutral state. (**B**) The segment in an actuated state where fluid within the agonist channel group is pressurized producing bending about the inextensible axis. This figure first appeared in Marchese et al. [2015].

soft rubber tentacles developed by Martinez et al. [2013] which use embedded crescent-shaped channels in a similar two-layer rubber construction. Although the cylindrical segment morphology is notably different from the ribbed segment, the fundamental operating principles are the same. In the cylindrical morphology (Figure 3-4A and B), we transition from a rectangular, planar-layered composite to a cylindrical, concentric-layered composite. Specifically, the segment consists of three concentric layers: (i) an outer soft layer (Figure 3-4b, *transparent*), (ii) a slightly stiffer inner layer (Figure 3-4d, *green*), and (iii) a hollow core that accommodates a bundle of fluid transmission lines (Figure 3-4f, *white*). Two fluid-filled, and cylinder-shaped channels are embedded laterally within the outermost layer (Figure 3-4c). These channels interface with the transmission lines by means of a stiffer rubber inlet piece (Figure 3-4a, *brown*). When pressurized, the entrapped fluid deforms the embedded channel both circumferentially and longitudinally (Figure 3-4B), but in effect lengthens. Specific to this morphology, the inner tube-like layer composed of slightly stiffer rubber serves as an inextensible constraint, transforming channel deformation into bidirectional segment bending. The segment has rubber endplates which allow multiple segments to be concatenated to a multi-segment manipulator, shown in Section 3.6.6.

Advantages: The primary benefits of this morphology in relation to alternatives presented in this section are: (1) Entirely composed of rubber, the resiliency and

durability of the actuator is increased. (2) The two cylindrical channels make this segment easiest to fabricate. (3) Embedded fluidic channels are not at the interface between fabricated layers, making this morphology robust against delamination under high pressures.

Disadvantages: The primary disadvantages of this morphology in relation to alternatives presented in this section are as follows: (1) The simple channel design exhibits high circumferential strain. Compared to the ribbed and pleated morphologies, more fluid energy is required to produce bending. (2) When the segment bends, an increased volume of rubber on the antagonist side of the actuator has to be compressed. This inhibits a high maximum curvature.

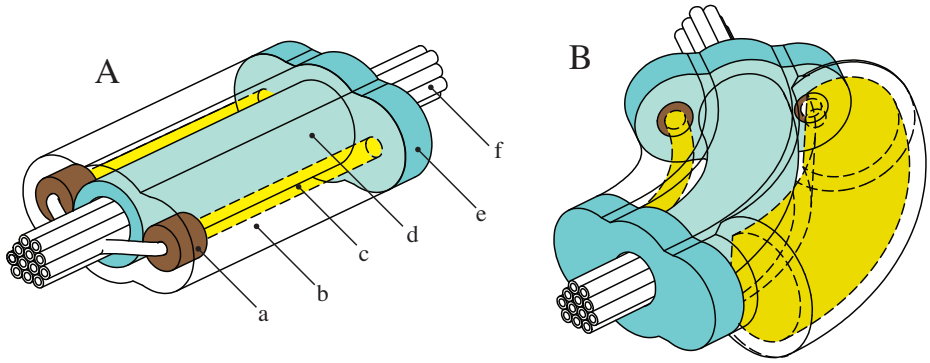

Figure 3-4: A conceptual representation of the cylindrical segment morphology: The segment consists of a soft silicone rubber outer layer (b, *transparent*), a slightly stiffer silicone inner layer (d, *turquoise*), crush resistant silicone inlets (a, brown), expanding embedded fluidic channels (c, *yellow*), and an internal tubing bundle (f, *white*). The segment terminates in soft endplates (e). (**A**) A depiction of the segment in an unactuated state. (**B**) A depiction of the body segment in an actuated state where the expansion of the pressurized fluidic channel is schematically represented. The figure is adapted from Marchese et al. [2014a].

3.2.2.3 Pleated Segment

After we reviewed the previous two approaches, we derived the pleated channel design, which addresses some of the disadvantages of the other two actuator morphologies. The pleated channel design is detailed in Figure 3-5 and consists of evenly spaced, discrete elastomer sections (Figure 3-5d), which are separated by gaps (Figure 3-5c). Embedded within each elastomer section is a hollow channel (Figure 3-5e). Cut views

of the unactuated and actuated states are shown in Figure 3-5A and Figure 3-5B, respectively. This design approach draws inspiration for its pleats from the soft pneumatic gloves developed by Polygerinos et al. [2013] and its homogeneous body design is inspired by the tail design of a soft robotic fish developed by Katzschmann et al. [2014]. The hollow channels within each pleat are connected via a center channel and are accessible through a front inlet (Figure 3-5a). When fluid within these channels is pressurized (Figure 3-5, *yellow*), an individual pleat undergoes a balloon-like expansion of the thin exterior skin both normal and parallel to the neutral axis. Similar to the cylindrical actuator design, a stiffer silicone layer (Figure 3-5, *blue*) serves as an almost inextensible constraint layer. The sum of the balloon-like expanding motions leads to bending of the less extensible center constraint layer.

Advantages: The primary benefits of this morphology in relation to alternatives presented in this section are as follows: (1) A unidirectional pleated actuator is capable of bending to higher curvatures than the ribbed or cylindrical morphology. (2) A bidirectional pleated segment is capable of exerting higher maximum forces because of its ability to accommodate the largest energy input. (3) Using a lost-wax casting approach, the *turquoise* portion of this segment can be cured in a single step, avoiding seams that are prone to delamination.

Disadvantages: The primary disadvantages of this morphology in relation to alternatives presented in this section are as follows: (1) The morphology is more complex to manufacture because it requires a lost-wax casting procedure detailed in Section 3.3.3. (2) The implementation of this morphology requires the most fluid energy to actuate it to appreciable tip forces. This might very well be due to the fact that, when compared to the other implementations, this implementation is larger in size and uses elastomer with a higher shore hardness.

3.2.2.4 Comparative Characterization

To characterize the actuated segments, we first perform bending tests to experimentally determine the relationship between the segment's neutral axis bend angle θ, internal channel pressure p_c, and supplied volume $\mathbb{V}_c$ for each morphology. In these experiments,

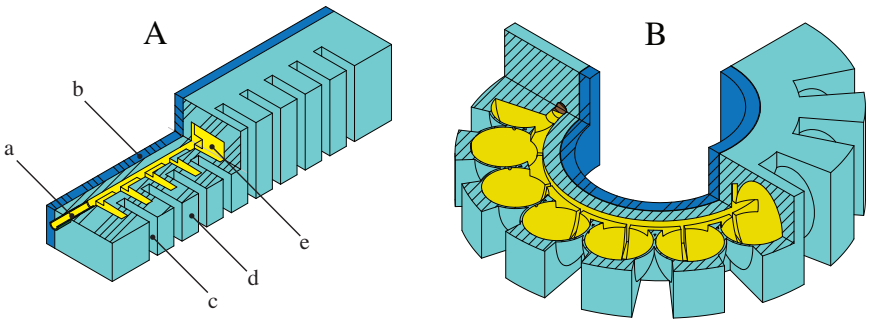

Figure 3-5: A conceptual representation of the pleated segment morphology. The design consists of a channel inlet (a), an almost inextensible constraint layer (b), uniform pleats (d) separated by even gaps (c), and internal channels within each pleat (e). (**A**) depicts the segment in an unactuated state and (**B**) shows the segment in an actuated and therefore bent state. The expansion of the pressurized channels is schematically represented. The figure is adapted from Katzschmann et al. [2015].

the base of each segment is grounded securely in a fixture and the segment's tip is supported vertically with a ball transfer. The setup is shown in the top row of Figure 3-6. The segment's agonist channel is incrementally filled under closed-loop volume control via the displacement of a pneumatic cylinder; please refer to Section 3.4. After each incremental fill, we allow pressure within the cylinder and within the actuated channel to equalize before measurements of the channel's pressure and the segment's curvature are taken. Curvature is assumed to be constant along the length of the segment and is uniquely defined by measuring the cartesian locations of the base and the tip of the segment. From this curvature we compute the segment's bend angle.

Since this is a quasi-static process, fluid pressure and supply volume measurements can be used to determine the elastic potential fluid energy input into the actuation system. The actuation system consists of the elastomeric segment and the internal compressible transmission fluid. The elastic potential fluid energy serves as a comparative metric between the different actuator segment designs. The potential energy is calculated by

$$V_{Elastic} = \int_0^{\mathbb{V}_c} p_c\left(\mathbb{V}\right) \, \mathrm{d}\mathbb{V}. \tag{3.1}$$

Each segment's geometry and cavity volume is different, because each actuator segment was built with a different type of robot prototype in mind. The geometries and the resulting cavity volumes are listed in Table 3.1. The different cavity volumes and the

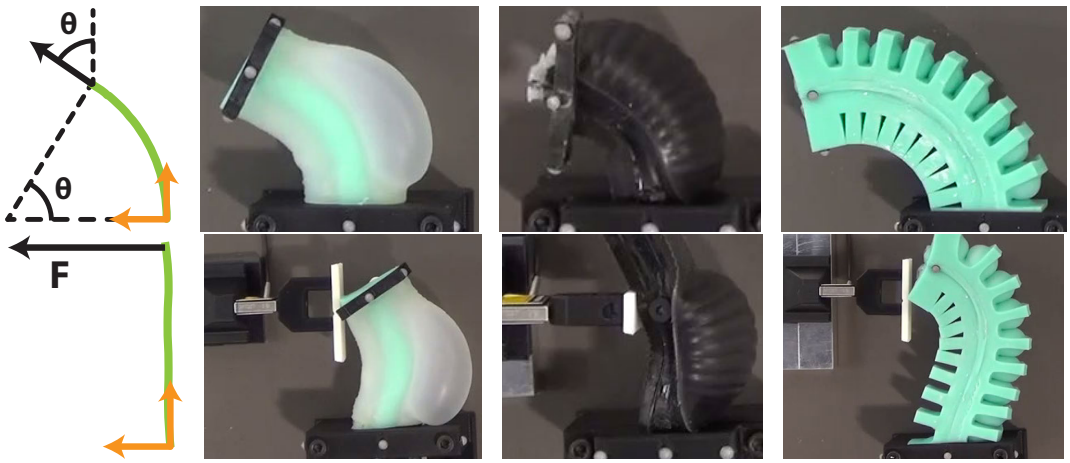

Figure 3-6: Experimental setup of the comparative characterization: Top row shows bend angle measurements, bottom row shows blocking force measurements via a load cell. The figure is adapted from Marchese et al. [2015].

Table 3.1: Geometric parameters of an actuator segment

	Actuator Type		
	Ribbed	Cyl.	Pleated
Actuator Length [mm]	37.8	61.2	107.5
Actuator Width [mm]	32.0	33.5	44.4
Actuator Thick. [mm]	18.5	19.6	25.4
# of Channels per Side	13	1	10
Single Channel Length [mm]	25.4	40.0	12.9
Single Channel Width [mm]	3.1	2.8	12.3
Single Channel Thick. [mm]	1.0	2.8	2.8
Cavity Volume per Side [ml]	1.04	0.31	5.12

different characteristic deformations of each morphology under pressurization require significantly different volumetric displacements.

Additionally, a blocking force test is performed in order to understand the variability in tip force output between the segment morphologies. Again, a similar experimental procedure is used as for the bending characterization; however, during blocking force experiments a plate attached via a force transducer to ground is mounted in contact with the segment's tip, orthogonally to the bending plane. This effectively measures the force required to block the actuator from bending. The setup is shown in the bottom row of Figure 3-6.

Figure 3-7 details the results of these characterization experiments from which

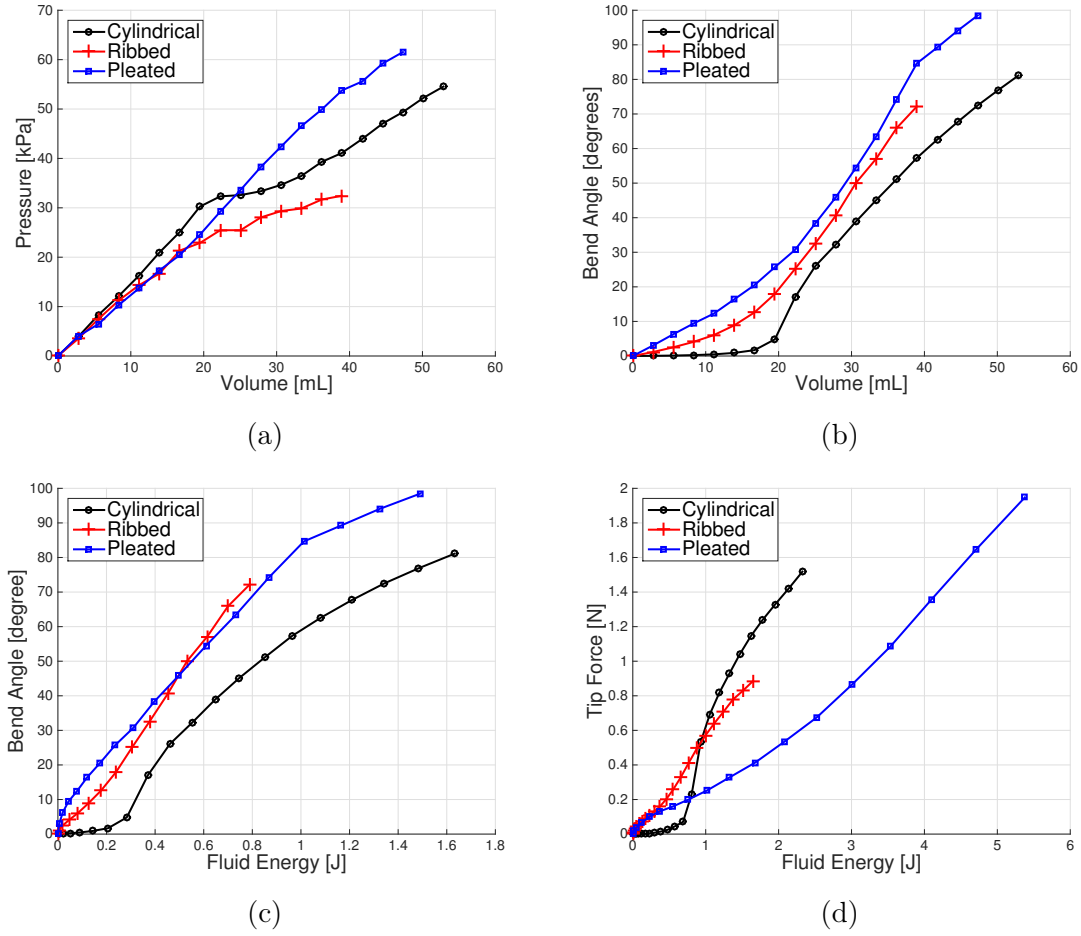

Figure 3-7: Experimental characterizations of three actuated segment morphologies performed by filling each actuator by means of controlled volumetric displacements and measuring internal pressure, neutral axis bend angle under a constant-curvature assumption, and blocking force. The figure is adapted from Marchese et al. [2015].

we can make several observations. First, the relationship $\frac{\partial p_c}{\partial \mathbb{V}_c}$ is similar among the different morphologies for inputs up to approximately 20 mL. In the regime where $\mathbb{V}_c$ is above 25 mL, the pleated morphology has the highest $\frac{\partial p_c}{\partial \mathbb{V}_c}$, followed by the cylindrical, and then the ribbed (Figure 3-7a). Second, the cylindrical morphology has a salient bend angle nonlinearity (Figure 3-7b). More specifically, small volumetric fluid changes of less than 15 mL provide little control authority over the curvature; however, for displacements of more than 25 mL, the control authority is strong and the curvature-volume relationship is approximately linear. This can be explained by the initial, relatively large radial expansion of the segment. Third, for a given fluid energy

input, the bending angle of the cylindrical actuator is the least while the blocking force is the highest. In this morphology, a considerable amount of fluid energy radially expands the actuated channel. This energy does not contribute to axial expansion and therefore does not contribute to the increase of the bend angle. However, the radial expansion causes a considerable increase in area moment of inertia, which stiffens the actuator and causes it to have a higher blocking force than the other designs. Fourth, the cylindrical morphology requires the highest amount of fluid energy to produce a given bend angle and the ribbed and pleated segments require approximately the same amount of fluid energy to generate equivalent bending (Figure 3-7c). This observation holds true over the range of inputs generated during these experiments. Finally, the pleated segment requires more fluid energy than both the ribbed and cylindrical morphologies to produce a given tip force for inputs greater than 1 J. However, the pleated segment can accommodate significantly higher input energies and therefore can reach the highest maximum tip force. Each actuator was inflated either to its maximum before the elastomer plastically deformed or to the highest feasible bend angle. The pleated prototype is larger in scale than the cylindrical and ribbed ones, therefore it can be driven to higher energy inputs.

3.3 Fabrication

Three distinct fabrication techniques for soft actuators are presented in this section. These techniques are *lamination casting with heterogenous embeddings* (Section 3.3.1), *retractable pin casting* (Section 3.3.2), and *lost wax casting* (Section 3.3.3).

3.3.1 Lamination Casting with Heterogenous Embeddings

Lamination-based casting with heterogeneous embeddings is a fabrication technique that extends current soft lithography casting processes. This technique was first introduced in Marchese et al. [2014b] and Marchese et al. [2015]. As detailed in the related work (Section 2.2), the outer layers of a soft robot are often cast separately using soft lithography techniques to inlay channel structures. Then, these layers

are laminated together with a constraint layer to form the actuator. To power the actuation, supply lines are pierced through the actuator's side wall and run external to the mechanism. This approach can be prohibitive in that it creates an unreliable pneumatic interface between the supply lines and the actuated channels. Also, these external supply lines can inhibit the robot's movement or otherwise obstruct it from completing its intended function. By embedding heterogeneous components within the elastomer layers as they are cast, we address both of these challenges. In this section, we show how the idea of soft lithography can be combined with embedding heterogenous components and that it is well-suited for realizing the ribbed body segment morphology. The process steps of lamination casting with heterogenous embeddings are detailed in Process 3.1. Specifically, we illustrate this fabrication process in the context of creating both a soft ribbed manipulator and a soft ribbed fish robot.

Process 3.1: Lamination casting with heterogeneous embeddings (Examples are shown in Figures 3-8 and 3-9)

1: Machine or 3D print constraint supports dividing arm into equal segments.
2: Machine or 3D print mold for the constraint layer.
3: Place constraint supports equally spaced into the mold for the constraint layer.
4: Laser-cut constraint layer from a plastic sheet.
5: Insert constraint layer through the aforementioned constraint supports.
6: Above and below the constraint layer, eight pieces of silicone tubing are threaded through the supports.
7: Rubber is mixed, vacuumed and poured into the mold for the constraint layer. ▷ Tubing, constraint layer, and supports are embedded in the rubber.
8: The uncured rubber inside the mold is again vacuumed and then allowed to cure.
9: Pierce into the embedded tubings to allow each line to independently supply a fluidic channel within a segment.
10: Machine or 3D print mold for creation of elastomer pieces with fluidic channel patterns.
11: Cast and cure elastomer pieces containing fluidic channel patterns.
12: Laminate elastomer pieces to both faces of the constraint layer using a thin layer of silicone rubber.

A ribbed manipulator, like the one detailed in Section 3.6.4, can be fabricated using lamination-based casting with heterogeneous embeddings. The specific approach for fabricating a six segment manipulator is illustrated in Figure 3-8. Here, seven

constraint supports (Figure 3-8d) are 3D printed[1] and placed into a constraint layer mold (Figure 3-8f), which is also 3D printed. The constraint film (Figure 3-8c) is cut from a thin acetal sheet[2] using a laser[3] and inserted through the aforementioned supports. Above and below the constraint film, eight pieces of silicone tubing (Figure 3-8a) are threaded through the supports. Silicone rubber[4] is then mixed and poured into the constraint layer mold, immersing tubing, film, and supports in a layer of elastomer to create the composite constraint layer (Figure 3-8g). The uncured rubber inside the mold is then immediately degassed using a vacuum chamber[5]. Once cured, small holes are created in the constraint layer to pierce the embedded tubing at specific locations, allowing each line to independently address a group of fluidic channels. Elastomer pieces containing channels (Figure 3-8b) are cast and cured separately using a similar molding technique. These cured elastomer pieces (Figure 3-8b) are then carefully attached to both faces of the constraint layer using a thin layer of silicone rubber. Finally, the printed feet (Figure 3-8e) are attached to the constraint supports (Figure 3-8d) to create an attachment point for ball transfers (Figure 3-25ad). These mechanisms help constrain the arm's motion to a plane.

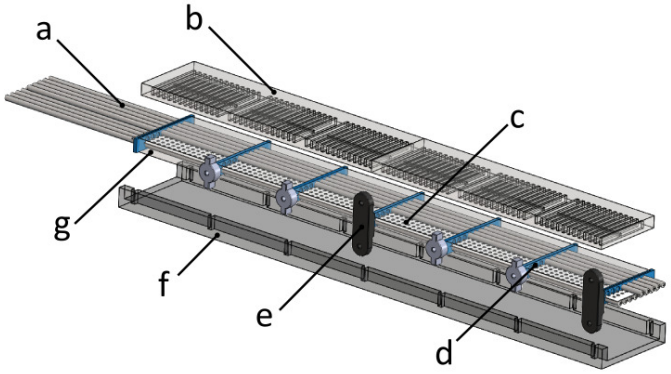

Figure 3-8: Fabrication process for a ribbed manipulator morphology: silicone tubing (a), elastomer pieces containing channels (b), constraint film (c), constraint supports (d), feet (e), constraint layer mold (f), and composite constraint layer (g). The figure is reproduced from Marchese et al. [2015].

[1]Fortus 400mc, Stratasys
[2]PN 5742T51, McMaster
[3]VLS3.50, Universal Laser Systems
[4]Ecoflex 0030, Smooth-On
[5]AL Cube, Abbess Instruments

One version of an anatomically proportioned body of a fish-like robot was also fabricated using a similar lamination-based casting process [Marchese et al., 2014c]. This casting process is detailed in Figure 3-9. Supply lines that connect the posterior actuator pair are embedded within the body during step 2 (Figure 3-9-2).

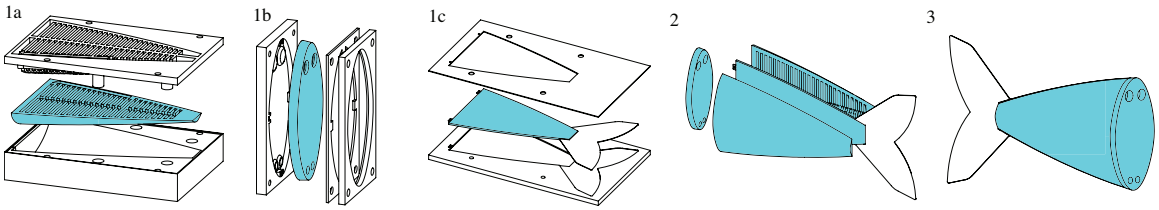

Figure 3-9: Lamination casting of a soft fish tail: (1a) Two halves of the body, (1b) a connector piece, and (1c) a constraint layer are cast of silicone rubber using two molds each. (2) All four cast pieces are bonded together using a thin layer of silicone rubber. (3) The cured fish body is ready for pressurization. The figure is adapted from Marchese et al. [2014c].

3.3.2 Retractable Pin Casting

Retractable pin casting allows the relatively simple channel structure of the cylindrical body segment to be cast without lamination or lost-wax core. This technique was first introduced in Marchese et al. [2014a, 2015]. This fabrication process is advantageous because it eliminates the rupture-prone seems between the channels and constraint layer seem in the ribbed morphology fabricated through lamination-based casting. Additionally, retractable pin casting is well-suited for the modular fabrication of multi-body soft robots. Here, segments are individually cast and then concatenated to form the robot. The process steps of the retractable pin casting are detailed in Process 3.2. Specifically, in this section we demonstrate retractable pin casting in the context of fabricating a cylindrical manipulator.

A cylindrical manipulator, like that detailed in Section 3.6.6, is fabricated through a retractable pin casting using pourable silicone rubber and 3D printed molds[6]. Figure 3-10 details this process. First, each body segment is independently fabricated in steps 1 to 3 and later these segments are joined serially to form the arm in steps 4 and 5.

[6]Fortus 400mc, Stratasys

Process 3.2: Retractable pin casting (Example is shown in Figure 3-10)

1: Outer mold is assembled, consisting of side walls and bottom piece with extruded feature.
2: Pins are inserted into the bottom piece. ▷ Pins will form the cavities for lateral fluidic actuation channels.
3: Cylindrical short tube sections are added at one end of the pins. ▷ Short tube sections are stiffer and form inlets for soft silicone tubes.
4: Center sleeve is slipped over extruded feature of bottom piece. ▷ Center sleeve will produce cavity in the center for later filling with slightly stiffer rubber.
5: Softer rubber is mixed and degassed in vacuum.
6: Uncured mix is poured into outer mold to cure and form soft segment without inner constraint. ▷ The mold's outer piece forms the segment's desired exterior shape.
7: Center sleeve is pulled off the extruded feature of the bottom piece.
8: Stiffer rubber is poured into the center cavity. ▷ The extruded feature of the bottom piece functions as the segment's hollow interior core. ▷ This stiffer rubber forms the segment's partially constraining inner layer.
9: Cured body segments are removed from their molds and each segment receives endplate.
10: Soft silicone tubes are joined to inlets of each embedded channel.
11: Resulting bundle of tubes is passed through each segment's hollow interior core.
12: Multiple body segments are attached at their endplates using adhesive.

To start, a four-piece mold is printed. The mold is then poured in two steps. In step 1, a low elastic modulus rubber[7] is mixed, degassed in a vacuum[8], and poured to form the body segment's soft outer layer shown in *white*. The mold's outer piece, one half of it is shown in *green*, functions to form the segment's exterior. Metal rods shown in *pink* are inserted into the mold and are held in place by the *orange* bottom piece of the mold. These rods will form the cavities for the segment's two lateral fluidic actuation channels. After the outer layer is cured, the *red* rigid sleeve is removed in step 2 from the extruded feature of the *orange* bottom piece of the mold. This produces a cavity into which a slightly stiffer rubber[9] is poured, forming the segment's partially constraining inner layer shown in *turquoise*. The extruded feature of the *orange* bottom piece, shown by its *orange* end tip, functions to produce the segment's hollow interior core. In step 3, the body segments are removed from their molds and joined to rubber[10]endplates shown in *turquoise* using silicone adhesive[11]. The small *yellow* channel inlets were added on one side of the *pink* metal pins during step 1. In

[7]Ecoflex 0030, Smooth-On
[8]AL Cube, Abbess Instruments
[9]Mold Star 15, Smooth-On
[10]Mold Star 15, Smooth-On
[11]Silicone Sealant 732, Dow Corning

step 4, soft silicone tubes[12] are joined to the inlet of each embedded channel. The resulting bundle of tubes is passed through each segment's hollow interior. Lastly, in step 5 multiple body segments are connected to their endplates using the same adhesive[13].

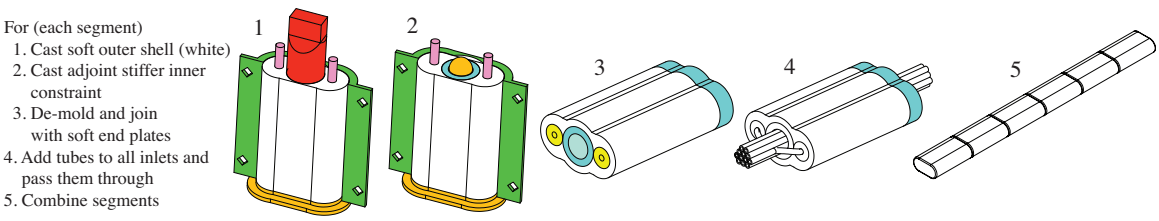

Figure 3-10: Retractable pin casting of a cylindrical manipulator morphology: Each body segment is cast using a two-step process: (1) the outer soft layer and (2) the inner stiffer layer are poured. (3) Once cured, the segments are joined to endplates using silicone adhesive. (4) Silicone tubing is connected to each embedded channel and the resulting bundle of tubes is run through the inside of each segment's hollow interior. (5) The segments are serially connected using silicone adhesive to form a manipulator arm. The figure is adapted from Marchese et al. [2014a].

3.3.3 Lost Wax Casting

In the following, we introduce a method for the fabrication of soft actuators without weakening seams and nearly arbitrary fluidic channel geometries. Existing soft robots are often produced through a multi-step lamination process, which produces seams and is prone to delamination. By abandoning the need for lamination, the retractable pin fabrication process enables seamless channel structures; however, the channel structures are limited to a relatively simple shape. For these reasons, we introduce lost wax casting as another possible fabrication process for soft actuators. With this process, arbitrarily shaped internal channels can be achieved to enable a wider range of applications. This fabrication technique for soft robots was first introduced in Katzschmann et al. [2014] for making soft fish tails and in Katzschmann et al. [2015] for making soft grippers. The process steps of the lost wax casting are detailed in Process 3.3. As examples, in this section we fabricate a pleated uni-directional gripper

[12]PN 51845K52, McMaster
[13]Silicone Sealant 732, Dow Corning

and a ribbed soft fish tail using the lost-wax approach.

Process 3.3: Lost wax casting (Examples are shown in Figures 3-11 and 3-12)

1: Stiffer rubber is mixed and degassed in vacuum.
2: Pour and cure rubber molds using stiffer rubber. ▷ Rubber molds are needed for creation of lost wax cores.
3: Place supportive rods into rubber molds. ▷ Supportive rods are embedded within the wax core for added stability during de-molding.
4: Pour wax into rubber molds to create lost wax core.
5: Combine outer mold elements, plastic constraint layers, and wax cores using alignment pins and screws. ▷ Plastic constraint layers and wax cores will be embedded in the cast soft body.
6: Softer rubber is mixed and degassed in vacuum.
7: Pour rubber into assembled mold.
8: (Optional) Pour stiffer rubber on top of the cured actuator to form a rubber-based constraint layer.
9: Remove cured actuator from mold.
10: Melt out wax core from the actuator using an oven.
11: Cook out in boiling water the remaining wax. ▷ Cooking in boiling water removes wax residues and creates desired actuator cavities.
12: Add silicone plug to outlets using adhesive.
13: Add silicone tubing into inlets using adhesive.

3.3.3.1 Lost-Wax Fabrication of a Pleated Gripper

The complete fabrication process for a pleated actuator consists of eight steps that are depicted in Figure 3-11. In step (A), harder silicone rubber[14] is poured into a mold, which contains a 3D printed model of the wax core. In preparation for step (B), the model is removed and the rubber mold is left inside the outer mold. Next, a rigid rod or tube, for example made of carbon fiber[15], is used as a supportive inlay for the wax core. The rod is laid into the cavity of the rubber mold, supported by the outer mold on both ends. This ensures that the wax core does not break when removed from the rubber mold. Mold release spray is applied to the silicone rubber mold to ease the wax core removal process. The wax[16] is heated until it is fully liquefied. The assembly of the rubber mold and the outer mold is heated for a few minutes to the same temperature as the wax. Using a syringe, the liquid wax is injected into the assembly.

[14]Mold Star 30, Smooth-On
[15]PN 2153T31, McMaster
[16]Beeswax, Jacquard

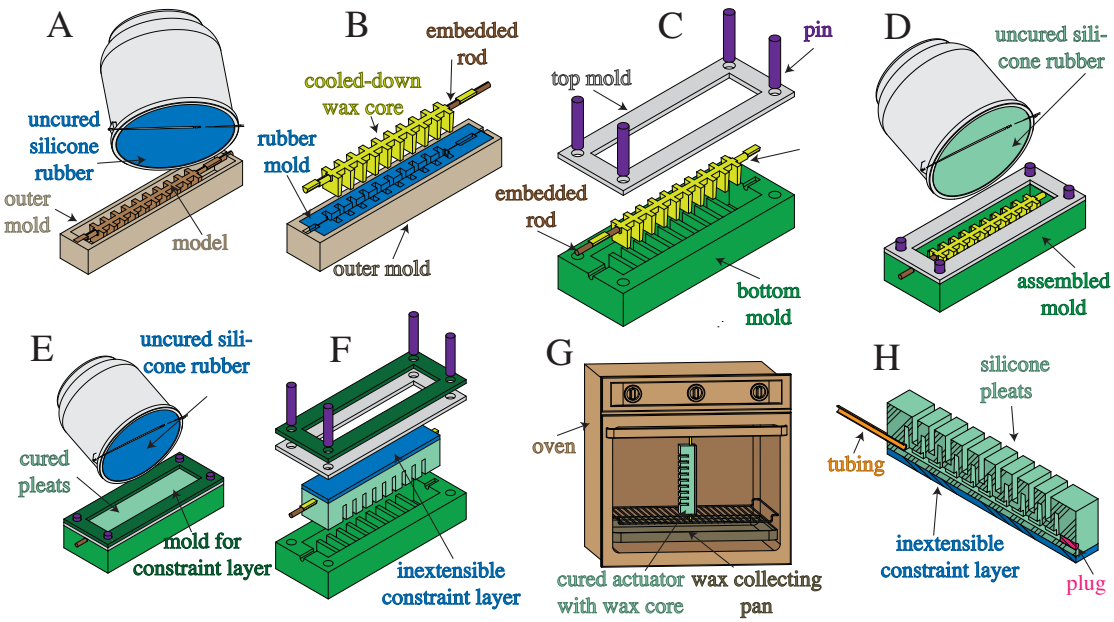

Figure 3-11: Fabrication process for the pleated actuator morphology: (A) Pour and cure a rubber mold, (B) pour wax core with embedded supportive rod, (C) combine bottom mold, top mold and wax core using pins, (D) pour rubber into assembled mold, (E) pour stiffer rubber on top of the cured actuator to form a constraint layer, (F) remove cured actuator from mold, (G) melt out wax core from the actuator using an oven, and (H) add silicone tubing and plug using silicone sealant. The figure is adapted from [Marchese et al., 2015].

Within a few minutes, the injected wax starts to solidify and significantly shrink in volume; this is counteracted by injecting more hot wax into the solidifying wax core during the cooling phase. In step (B), the wax core is first allowed to completely cool down, then it is released from the mold. In step (C), the cooled-down wax core is combined with the bottom mold, which defines the pleated structure of the actuator. The mold assembly is aligned with a top mold using pins. This top mold provides additional volume to cover the wax core. In step (D), low elastic modulus rubber[17] is mixed, degassed in a vacuum[18], and poured to form the pleats and allowed to cure. In step (E), stiffer rubber[19] is poured on top of the cured pleats to form a constraint layer. In step (F), the cured actuator is removed from the mold. In step (G), most of the wax core is melted out by placing the cured actuator into an oven in an upright position.

[17]Mold Star 15, Smooth-On
[18]AL Cube, Abbess Instruments
[19]Mold Star 30, Smooth-On

After this, remaining wax residues are cooked out in a boiling water bath. Finally, in step (H) a silicone tube[20] and a piece of silicone cord[21] are covered with silicone adhesive[22] and inserted into the front and back holes, respectively. The actuator can be used as a unidirectional gripper, see Figure 3-4, or as one agonist-actuated segment within a multiple body manipulator, see Section 3.6.5.

3.3.3.2 Lost-Wax Fabrication of a Ribbed Fish Tail

The actuated body of the hydraulic fish detailed in Section 3.6.1 is also produced via lost-wax casting. The fabrication process is depicted in Figure 3-12. In step (A),

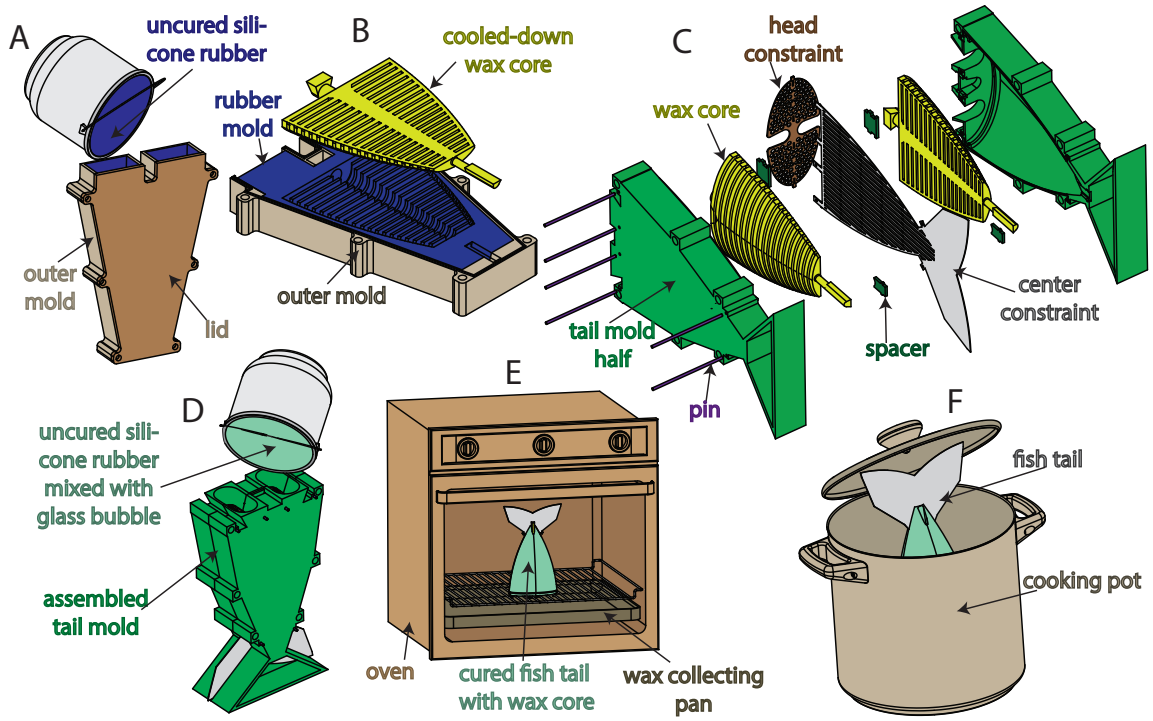

Figure 3-12: Fish tail fabrication process: (A) Pour and cure a rubber mold, (B) pour wax cores with embedded supportive rods, (C) combine head constraint, center constraint and wax cores with tail mold halves, (D) pour rubber mixed with glass bubbles into assembled tail mold, (E) using an oven melt out wax core from the cured fish tail, and (F) cook out remaining wax to create desired actuator cavities. The figure is adapted from [Katzschmann et al., 2014].

the rubber mold is poured and cured inside an assembly consisting of an outer mold

[20] PN 51845K53, McMaster
[21] PN 9808K21, McMaster
[22] Silicone Sealant 732, Dow Corning

with lid and a model for the core inside of it. In preparation for step (B), the lid and the model core are removed and the rubber mold is left inside the outer mold. The rubber mold receives a small carbon fiber tube as an inlay in its center cavity. This ensures that the wax core does not break when being removed from the rubber mold. Mold release spray is applied to the silicone rubber mold to ease the wax core removal process. The wax is heated up until it becomes fully liquefied. The assembly of rubber mold and outer mold is heated for a few minutes to the same temperature as the wax. Using a syringe, the liquid wax is injected into the assembly. Within a few minutes, the injected wax starts to solidify and significantly shrink in volume; this is counteracted by injecting more hot wax into the solidifying wax core during the cooling phase. In step (B), the wax core is first allowed to completely cool down, then it is released from the mold. In step (C), a head constraint, a center constraint, and two wax cores are combined with the surrounding tail mold halves using spacers, positioning pins and screws. In step (D), a mix of silicone rubber[23] with microbubbles[24] is poured into the tail assembly and allowed to cure. In step (E), most of the wax core is melted out by placing the fish tail in an upright position into an oven. Finally, in step (F) the remaining wax residues are cooked out in a boiling water bath.

3.4 Fluidic Power Sources

Fluidic power sources present many challenges for soft robots. There are three major ways to characterize these power sources: by transmission fluid, circuit continuity, and portability.

3.4.1 Transmission Fluids

The actuators detailed in Section 3.2.2 can be powered using either pneumatic or hydraulic systems where gases or liquids are the transmission fluid. Pneumatics are advantageous for powering FEAs because they serve as a power transmission

[23] Dragon Skin 10, Smooth-On
[24] 3M low-density crush resistant microbubbles

medium with low viscosity. High flows can be achieved with relatively low driving pressures. However, gases also introduce compressibility into the power transmission system and these dynamics can be difficult to model and can produce undesirable time delays. Hydraulics are advantageous because liquids are relatively incompressible when compared to gases, meaning power can be transferred almost immediately from the power source to the actuators. However, to achieve comparable volumetric flow rates, liquid drive systems often require high driving pressures and/or low impedance (large diameter) power transmission lines because of the increased viscosity of the transmission medium.

3.4.2 Circuit Continuity

Further, the actuators detailed in Section 3.2.2 can be powered using either open-circuit or closed-circuit power systems. Open-circuit power systems exhaust the transmission fluid to the environment, whereas closed-circuit systems recover fluid delivered to the actuators. Open-circuit systems are advantageous because they do not require mechanisms to re-pressurize and return transmission fluid to the supply. However, they often rely on passively exhausting transmission fluid to ambient/environmental pressure meaning the actuator depressurization is unactuated and a function of the actuator's compliance and the impedance of the exhaust pathway. Examples of open-circuit power systems are a soft robot that uses as its actuators energy-efficient valves controlled by electropermanent magnets [Marchese et al., 2011] and a robotic fish capable of escape maneuvers [Marchese et al., 2014c].

Closed-circuit systems (see Figure 3-13) are advantageous because the amount of transmission fluid is constant and moved around within the system; this means the power system's fluid medium is not required to match the operating environment (e.g., a soft robot fish powered by pneumatics swimming underwater). Furthermore, because the volume of transmission fluid is constant the power system can typically vacuum fluid from the actuator under power; meaning the system has control authority over actuator depressurization. The disadvantage to closed-circuit systems is that they typically require additional plumbing to complete the fluid circuit and supporting

hardware like a revisable pump. The fluidically-driven soft robots in this thesis are examples of closed-circuit power systems [Marchese et al., 2014b, Katzschmann et al., 2014, Marchese et al., 2014a, Katzschmann et al., 2015, 2018b].

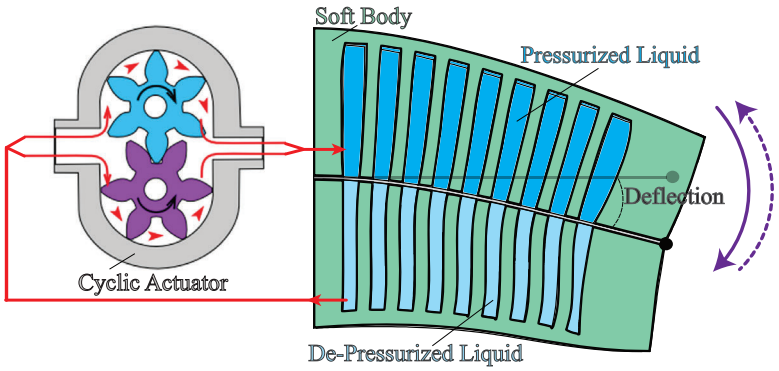

Figure 3-13: Actuation principle of fish's soft tail. A closed-circuit power system is used to drive the pressurization in the soft hydraulic fish. A displacement pump (left) drives a soft fluidic elastomer actuator (right). The figure is from Katzschmann et al. [2016].

3.4.3 Portability

The portability of a power source may be of significant interest to a soft roboticist. For example, locomotory soft robots are typically designed under the constraint of being self-contained, meaning all supporting hardware is located on-board the robot. Additionally, if the untethered robot is intended for high speed maneuvers, then compressed gas [Marchese et al., 2014c] or combustion [Tolley et al., 2014a] are viable power alternatives. However, if prolonged operations are required, then open-circuit pumps [Tolley et al., 2014b, Onal and Rus, 2013] or closed-circuit pumps [Katzschmann et al., 2014, 2018b] are suitable options. A hydraulic closed-circuit pump is detailed in Sections 3.6.1.3 and 4.5.

3.5 Closed-Circuit Fluid Control

The volumetric control provides real-time, closed-circuit adjustment of fluid energy input to a soft arm segment. The power system is used in conjunction with model-free

control algorithms developed in Chapter 5 and model-based controllers developed in Chapter 6 to achieve closed-loop control of a manipulator. The power system interfaces the computational and algorithmic aspects with the physical system.

Fluid power can be achieved by controlling either pressure or volume. For our systems, we choose volumetric control because it offers the ability to: (i) measure the control variable via linear displacement as opposed to pressure transducers, (ii) set a maximum safe displacement limit, and (iii) vary pre-pressurization of segments to accommodate for differences in actuator compliance.

We use an array of motor-powered pneumatic cylinders to independently and bidirectionally actuate the soft arm segments. The pneumatic cylinders provide fluidic power to the arm by producing volumetric changes within a segment's embedded channels. Linear electrical actuators are coupled to and control the positional displacements of the pistons within the cylinders. The linear actuators govern the volumetric displacement of fluid out of the cylinders and into a segment's embedded fluidic channels, and vice versa. Figure 3-14 illustrates the components of a pneumatic cylinder with an attached linear electrical actuator.

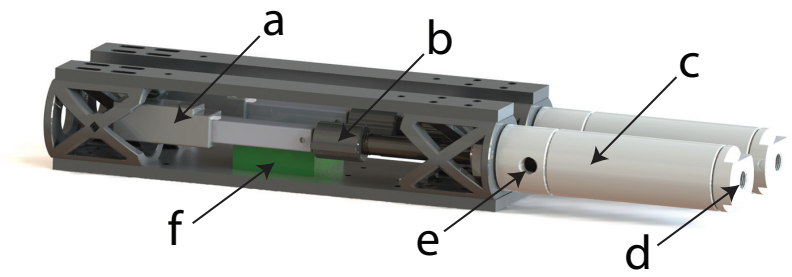

Figure 3-14: An overview of two pneumatic cylinders used to drive the curvature of a bidirectional arm segment. An electric linear actuator (a) is directly attached to the piston of a fluidic cylinder (c) via a 3D-printed coupler (b). Fluid is displaced through the inlet (e) and outlet (d) of the cylinder. A motor controller (f) allows digital command signals to govern fluid movement. The figure is reproduced from Marchese et al. [2014b].

Two pneumatic cylinders are used to control a single bidirectional segment. Although the mapping of either the agonistic or antagonistic channel deformation is monotonically related to a single piston's displacement, when considering bidirectional

segment movement as well as positive and negative curvatures, the two drive cylinders must be controlled synchronously. One piston is moved opposite to the other piston, either forward or reverse, to increase or decrease curvature.

3.6 Soft Robots and Systems

Soft and continuously deformable locomotion systems and manipulators can be made of bending fluidic elastomer segments. We briefly describe how different actuator morphologies presented in Section 3.2.2 are combined with a power system to create soft robotic systems. We show the actuated tail of a soft robotic fish, a soft gripper hand, and multi-segment manipulator arms composed by serially concatenating actuated segments. An overview of the soft robots developed in this thesis is given in Figure 3-15.

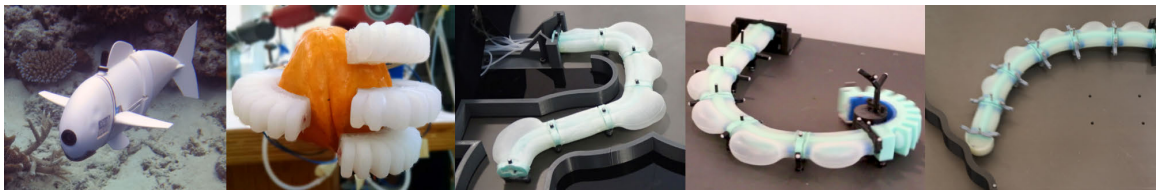

Figure 3-15: Soft robots developed in this thesis. Left to right: soft robotic fish (SoFi) (Section 3.6.1 and Chapter 4), soft gripper hand (Sections 3.6.2, 3.6.3, and 7.1.2), cylindrical multi-segment arm (Sections 3.6.6 and 7.1.1), pleated gripper on multi-segment arm (Sections 3.6.5 and 7.1.3), and soft hemisphere on multi-segment arm (Sections 3.6.8 and 7.2.2). Some of the images are adapted from Katzschmann et al. [2018b], Homberg et al. [2018], Marchese et al. [2014a], and Katzschmann et al. [2015].

3.6.1 Ribbed Fish Tail

3.6.1.1 Undulating Soft Body

The soft hydraulic fish achieves undulating locomotion via a hydraulically actuated soft fish tail with two internal cavities [Katzschmann et al., 2014, 2018b]. The soft fish tail, shown in Figure 3-16, is a fluidic elastomer actuator using one ribbed segment (Section 3.2.2.1). The design mimics the rear portion of a fish, encompassing the posterior peduncle and the caudal fin. The tail can continuously bend along its

vertical center constraint layer by fluidic actuation of two lateral cavity structures. The inextensible and stiffer center constraint layer splits the tail evenly along a vertical plane. The actuator consists of evenly spaced ribs with hollow sections in between, connected by a center channel and accessible by a front inlet. The rib structure allows for expansion or contraction of the thin exterior skin under positive or negative fluidic pressure, respectively. These expanding or contracting motions bend the inextensible center constraint layer. The rib structure is evenly spread along the fin, leading to continuous flexing of the whole body under fluidic pressure. The inherent elasticity of the body forces it back into its neutral state after each pulse of actuation. A fluidic flow alternating into each lateral cavity structure leads to a complex undulating motion of the soft body and enables forward swimming and turning.

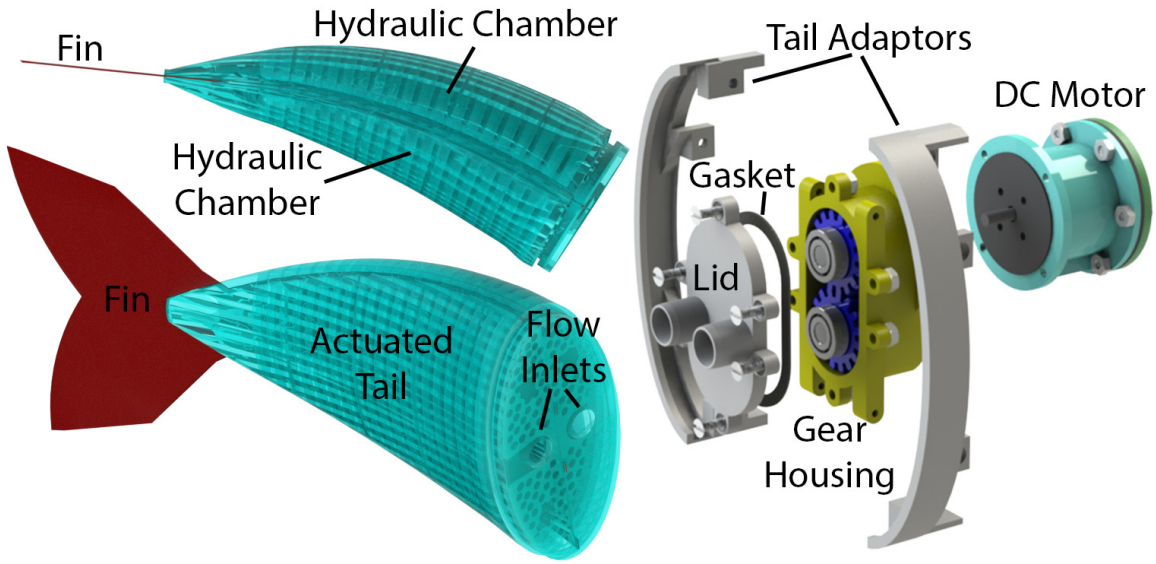

Figure 3-16: Renderings of actuated soft fish tail and custom-made gear pump. Left: Soft fish tail in actuated state (two views). Right: Custom external gear pump in an exploded view. The figure is adapted from Katzschmann et al. [2018b].

3.6.1.2 Tail Fabrication

The fabrication of the soft body with its integrated constraint layers and posterior fins is realized through the lost-wax fabrication process described in its principles in Section 3.3.3.2. Here, we describe in detail how this is actually implemented for the example of a soft fish tail. The interior cavity of the tail body is realized by means

of a lost-wax core. The steps from silicone rubber mold creation to de-molding of the lost-wax core are depicted in Figure 3-17. Outer mold, lid, and model core are 3D-printed. The silicone rubber mold has a Shore hardness of A30. A plastic rod is added in the center for added stability of the core when demolding. Beeswax with a melting point of 63 °C is heated up to 95 °C for pouring into the rubber mold.

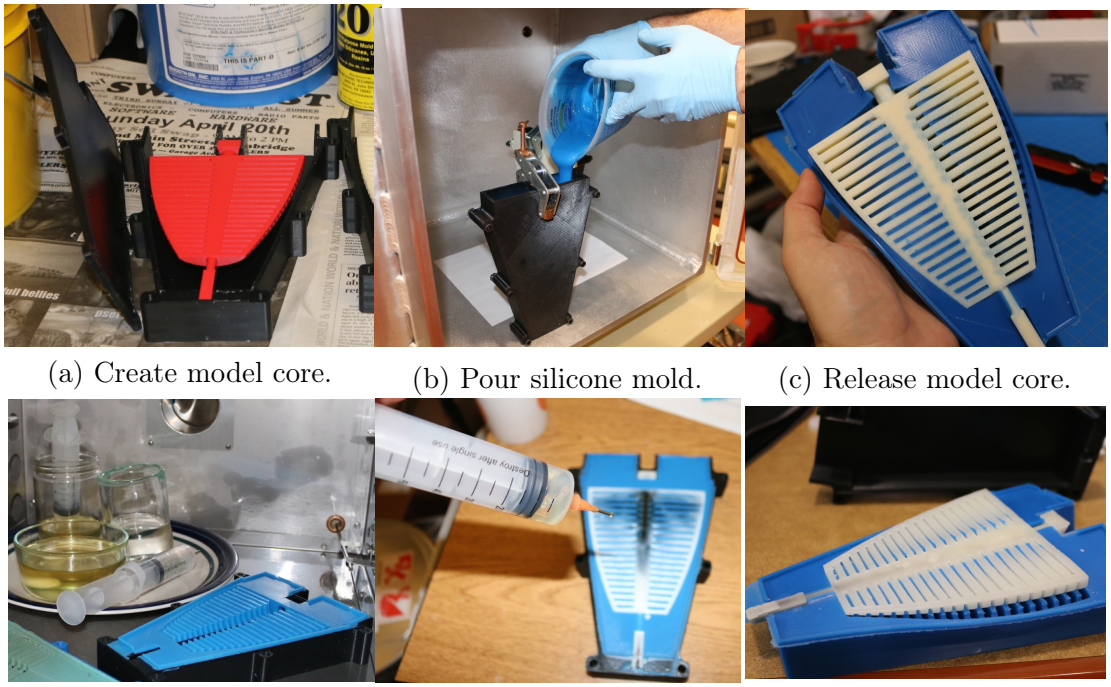

(a) Create model core. (b) Pour silicone mold. (c) Release model core.

(d) Heat wax and mold. (e) Pour wax. (f) Demold wax.

Figure 3-17: Wax core fabrication: (a) 3D print model core; (b) Create silicone mold for wax casting; (c) Release model core; (d) Heat beeswax and mold; (e) Pour wax with syringe; (f) Demold wax core. The figure is adapted from Katzschmann et al. [2014].

The two constraint layers are laser-cut out of a 0.5 mm thick flexible acetal sheet. The center constraint layer also functions as the posterior fin of the fish tail. The surrounding molds are 3D printed. In the final fabrication steps depicted in Figure 3-18, two wax cores and two constraint layers are combined with the fish tail molds. The soft silicone elastomer and microbubbles are mixed at a mass ratio of 40:1 to achieve the desired rubber density of 0.94 g/cm^3, achieving neutral buoyancy in salt water. This additional mixing step is important for achieving overall neutral buoyancy of the robotic fish. Otherwise, the added weight of the tail body has to be compensated with

additional floats around the center of the fish, which also add undesired drag. This mix is filled into the cavity and allowed to cure. Heating the resulting body in an oven and then in a water bath removes the interior wax body and creates the soft body.

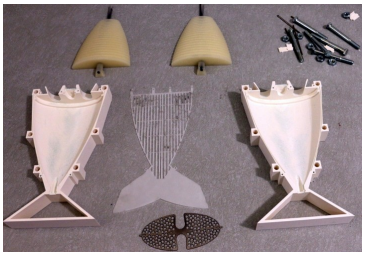

(a) Individual parts.

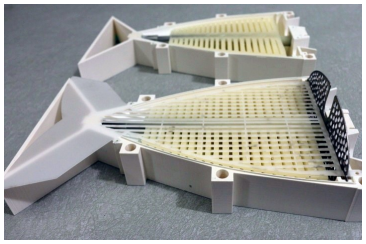

(b) Assembly of parts.

(c) Mix rubber and bubbles.

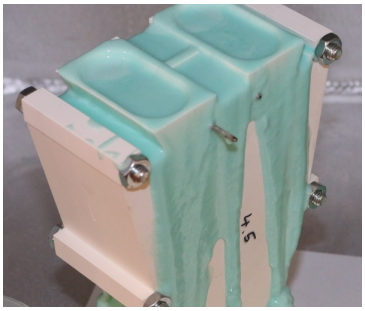

(d) Degas and cure.

(e) Melt wax in oven.

(f) Hot water bath.

Figure 3-18: Fabrication of soft fish tail: (a) Individual parts of the tail mold are (b) assembled; (c) Mix silicone rubber and glass bubbles; (d) Degas and cure silicone rubber fish tail; (e) Melt out the wax core in an oven; (f) Remove residues of wax with hot water bath. The figure is adapted from Katzschmann et al. [2014].

3.6.1.3 Hydraulic Pump

The soft tail is actuated by a hydraulic displacement pump, an example of a closed-circuit power system. The outlets of the hydraulic pump are directly attached to the soft body to allow for water movement between the two inner cavities in a closed-loop fashion.

We dimensioned the custom-designed pump (Figure 3-19) and its attached motor based on the maximum pressure required and the volumetric flow rate. We estimate the effective volumetric flow rate based on the displaced volume of fluid for a single static deflection and the desired flapping frequency. An initial value for the desired flapping frequency and amplitude of the soft tail was determined based on previous

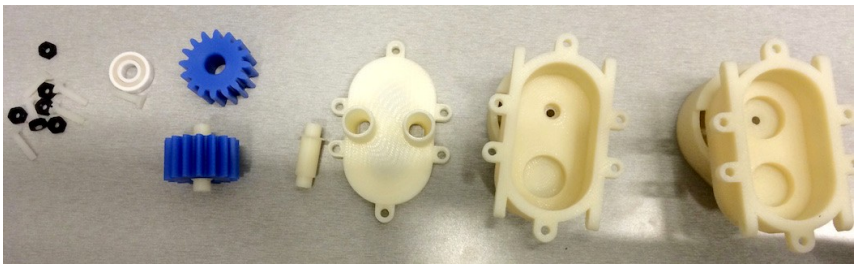

Figure 3-19: Fabricated external gear pump. Disassembled view of the gear pump unit, components from left to right: bearings, gears and shafts; lid with inlets/outlets to fish tail; main body with hole for motor shaft. The figure is adapted from Katzschmann et al. [2016].

studies on self-propelling foils driven by an external actuator [Lauder et al., 2012, Alben et al., 2012]. A custom pump, its attached motor, and a waterproof housing were then specified, designed, and built. The effectiveness of six different self-contained designs based on centrifugal pump, flexible impeller pump, external gear pump, and rotating valves was compared. These hydraulic actuation systems combined with the soft tail were then measured at low and high oscillation frequencies. The propulsive force, deflection characteristics of the soft tail, acoustic noise of the pump, and overall efficiency of the system were recorded. A brushless, centrifugal pump combined with a custom-printed rotating valve performed most efficiently at both test frequencies, producing sufficiently large cyclic body deflections and the least acoustic noise. An external gear pump design produced the largest body deflection and therefore the best swimming performance, but consumed an order of magnitude more power and produced higher noise levels. A detailed study of the various actuation systems for the tail is provided in Katzschmann et al. [2016]. We chose an external gear pump (Figure 3-16) for the fully integrated robotic fish due to its better swimming performance, lower part count, and easier controllability.

3.6.2 Pleated Finger

Another application of soft single actuation is the development of fingers for soft robot hands. In the case of fingers, we need a design that can wrap around the grasped objects and provide contact and curvature feedback during grasping. For these reasons,

we augment the soft actuators with bend and force sensors and arrange them in form of a hand that can be mounted to the end effector of a robotic arm.

The modular fingers can be easily slipped onto a 3D-printed interface. We designed each finger with the goal in mind to have: (a) constant curvature bending when not loaded; (b) partially constant curvature bending under loaded conditions; (c) high compliance and softness in order to be safer when interacting; (d) the capability of internal state sensing; and (e) force contact sensing.

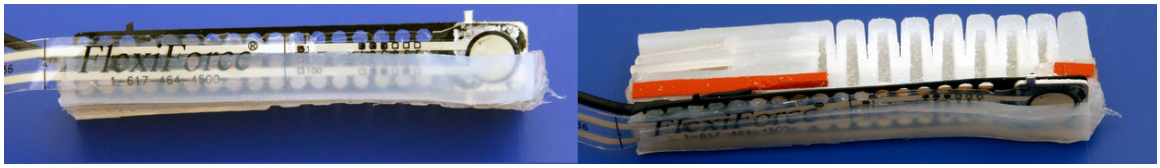

Figure 3-20: A cutaway view of a soft finger, showing the internal air channels, sealed sections, and inserted sensors as well as constraint layer. The figure is adapted from Homberg et al. [2015].

A resistive bend sensor is embedded into the finger by affixing it beneath the finger's inextensible constraint layer, as shown in Figure 3-20. Bending the resistive strip changes the resistance of the sensor. The resistive change can be correlated with the curvature of the finger. A force sensor is added on top of the constraint layer, which is also visible in Figure 3-20. When the finger contacts an object, the resistance of the sensor changes, allowing us to detect the contact.

3.6.2.1 Finger Fabrication

The fabrication of a single finger is based on the lost-wax casting process described in Section 3.3.3. Figure 3-21 shows an adjusted fabrication process of what is shown in Figure 3-11: One additional step is needed to add the bend and force sensors on top of the constraint layer.

Figure 3-20 shows an image of the inside of the finished finger; the constraint layer and the sensors are visible.

The finger is 1.8 cm wide by 2.7 cm tall by 10 cm long, contains both bend and force sensors, and is not prone to popping or leaks. Various views of a completed finger can be seen in Figure 3-22. The new version benefits from shaping of the internal air

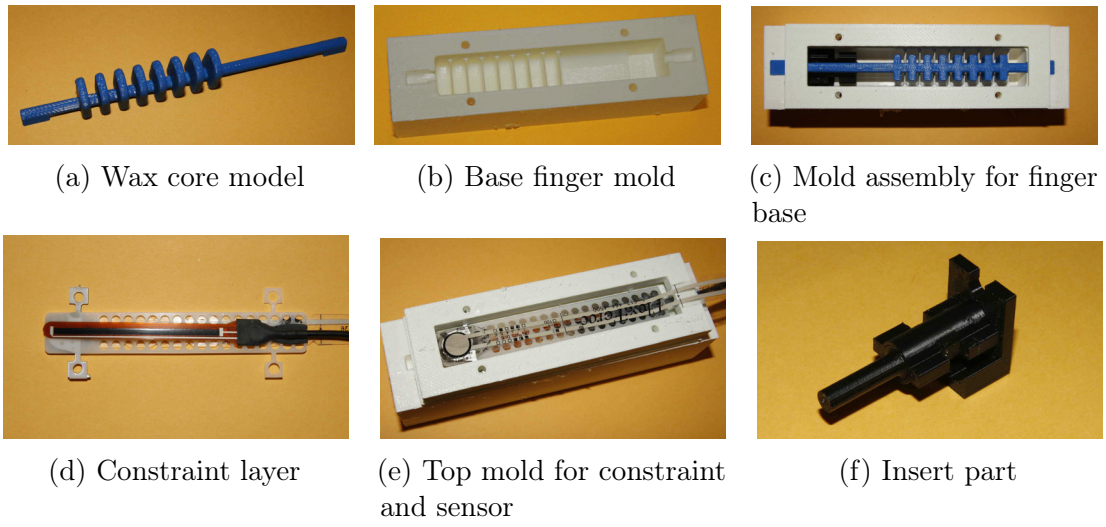

(a) Wax core model (b) Base finger mold (c) Mold assembly for finger base

(d) Constraint layer (e) Top mold for constraint and sensor (f) Insert part

Figure 3-21: Create wax core mold using 3D printed model (a). For each finger create a wax core by pouring wax into the wax core mold. Create mold assembly for finger base (c) using wax core, insert part (f) and white lid. Cast the first layer of the finger using mold assembly (c). Melt the wax core out of the rubber piece and remove the insert piece. Re-insert the rubber piece into the base mold. Glue the sensors onto the constraint layer (d). Place the constraint layer on top of the rubber piece (e). Pour a second layer of softer rubber into the mold. Remove the finger and plug the hole at the finger tip with solid tubing. The figure is adapted from Homberg et al. [2018].

channels and external finger shape to avoid all sharp corners which can be places of stress on the rubber. While the old version of the finger often broke intermittently, sometimes after light use only, the new version of the finger lasts several months and many hundreds of grasps before succumbing to rubber fatigue.

3.6.2.2 Actuation of Finger

Each finger is connected via a tube to a pneumatic piston, an example for a closed-circuit, volumetric control system. Each pneumatic cylinder[25] has its volume changed by a linear actuator. The linear actuators[26] are controlled by motor controllers[27] connected to a PC and controlled via serial messages sent from ROS [Quigley et al., 2009].

[25] 2-1/2" bore Bimba cylinder with a 3" stroke
[26] Pololu LACT2P-12V-20 linear actuators with 2" stroke
[27] Pololu JRK 12v12 motor controllers

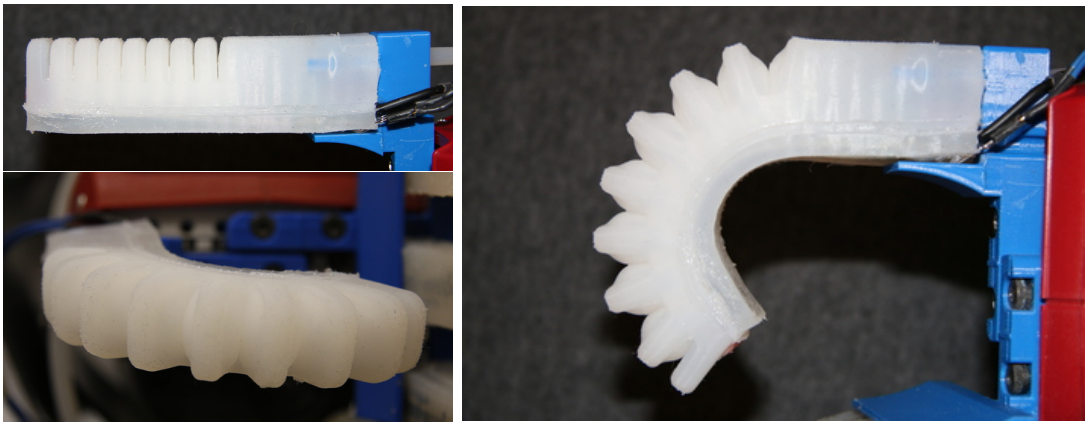

Figure 3-22: Views of an individual pleated finger. The figure is adapted from Homberg et al. [2018].

3.6.2.3 Proprioception in Finger

The proprioception of the finger is achieved through two sensors in each finger: a force sensor[28] at the tip of the finger and a bend sensor[29]. Both sensors are resistive sensors: as the sensor is pressed or bent, the resistance of the sensor changes. The force sensor has a range of 4.5 N, it has an op-amp circuit to lower the range and increase the sensitivity. In order to get accurate results, we place a small metal piece behind the active area of the sensor. This prevents the bending of the finger from affecting the resistance of the sensor so that any sensed measurement comes solely from the contact of the finger with an object.

3.6.2.4 Sensor Characterization

Due to the construction of the sensor, the relative change in resistance increases as the curvature of the sensor increases. Thus, the sensor has better accuracy and resolution as its diameter decreases. The diameter we refer to is the diameter of a circle tangent to the bend sensor at every point, for some constant curvature bend of the sensor. This relation between diameter of the finger and sensor value is shown in Figure 3-23a, where sensor values versus finger curvatures are plotted for the unloaded case.

We also map the diameter values to the linear actuator position: the linear actuator

[28]Flexi-force force sensor, iCubeX
[29]Bendshort-2.0 flex sensor, iCubeX

can be controlled by specifying a fraction of the full range of its range. Thus, for the unloaded case, we know the approximate diameter of the finger's bend even without sensors, as seen in Figure 3-23b.

Due to the inherent changes in variance for the sensor values, we are able to distinguish objects more accurately if they have a smaller diameter.

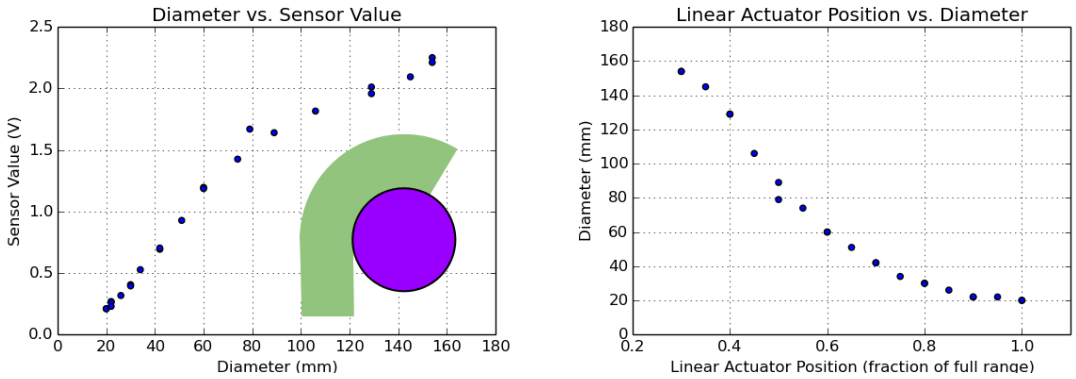

(a) Sensor Value over Diameter.

(b) Diameter over Actuator Position.

Figure 3-23: Sensor Characterization. (a) The diameter of the finger versus the sensor values. (b) The input linear actuator value versus the resulting diameter of the finger bend. The figure is adapted from Homberg et al. [2018].

3.6.3 Pleated Gripper Hand

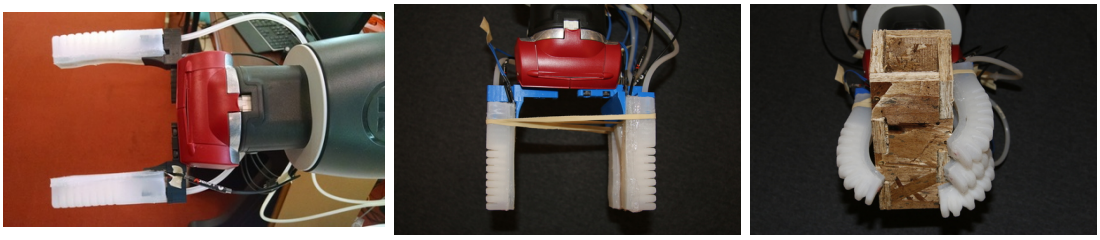

Figure 3-24: Views of the entire composed hand. The figure is adapted from Homberg et al. [2018].

The soft gripper hand has a modular design combining four soft fingers. The soft fingers described in Section 3.6.2 are easily attached and detached via 3D-printed interface parts. We can combine fingers to create different configurations of soft hands with different numbers of fingers. The primary configuration discussed here is a four-fingered hand, an improved version to our previous three-fingered design [Homberg

et al., 2015]. The added finger directly opposes the thumb of the hand, allowing for better enveloping of the object and increased payload capability due to the firmer grasp at the center and the additional contact force. The four-fingered design allows for enveloping and in addition for pinch grasps. Various views of the completed hand can be seen in Figure 3-24.

3.6.4 Ribbed Multi-Segment Arm

Structurally, a ribbed manipulator arm is composed of serially concatenated, homogeneous ribbed body segments. Each body segment is a fluid elastomer actuator. By volume, over 97% percent of the ribbed manipulator is soft silicone rubber, excluding the feet. This manipulator is depicted in Figure 3-25a. The manipulator can theoretically be composed of any number of the aforementioned ribbed segments (Figure 3-25a-e), but practically, we have constructed a six-segment prototype (Figure 3-25b). All twelve fluidic transmission lines as well as channel-to-supply interfaces are embedded within the manipulator's center layer. Markers are located at the interface between segments (Figure 3-25a-b), making segment endpoints identifiable to an external localization system. The starting point of the arm's first segment (Figure 3-25a-a) is grounded to the platform on which the arm moves and we refer to this as the base. Ball transfers (Figure 3-25a-d) are also located at each segment endpoint to allow the arm to move on a two-dimensional plane with minimal friction. In many experiments conducted throughout this work, the pose of the arm's end effector (Figure 3-25a-c) is controlled.

3.6.5 Pleated Multi-Segment Arm

A manipulator can also be composed of pleated fluidic elastomer segments, as shown in Figure 3-26. Just as in the ribbed and cylindrical composition, pleated segments are joined end-to-end. The fluid transmission lines are passed through along the central axis of the segments. A supportive hollow profile can be added to combine two segments. This pleated design allows for modular composition of a manipulator,

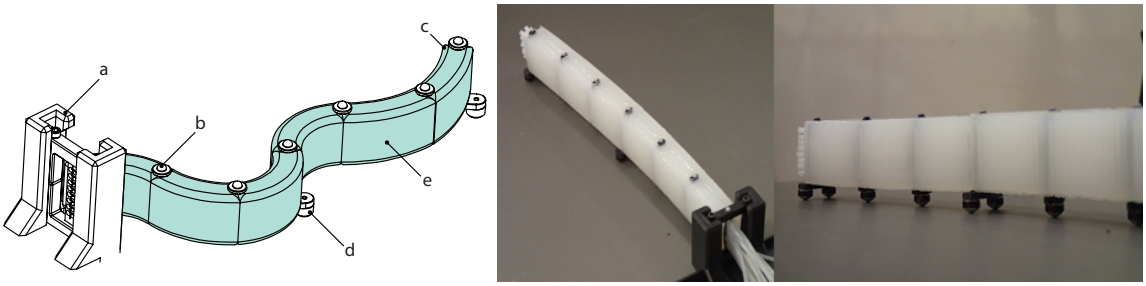

(a) (b)

Figure 3-25: A ribbed soft manipulator prototype. Panel (a): The arm is composed of homogeneous and independently actuated ribbed segments (e). The base of the arm's first segment is fixed (a) and the end of its last segment is the end effector (c). Markers (b) identify the endpoints of each segment and ball transfers (d) mitigate friction. Panel (b): Prototype of the ribbed manipulator arm, shown from two views. The figure is adapted from Marchese et al. [2015].

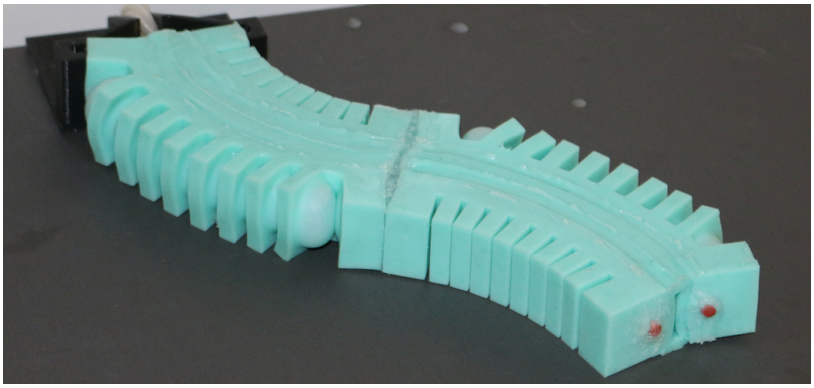

Figure 3-26: A pleated soft manipulator prototype composed of two segments with two degrees of freedom each. The figure is adapted from Marchese et al. [2015].

because transmission lines are not permanently embedded within the elastomer. Additionally, this type of manipulator is, like the cylindrical manipulator, entirely composed of soft silicone rubber.

3.6.6 Cylindrical Multi-Segment Arm

We can also compose a manipulator of cylindrical fluidic elastomer segments, as shown in Figure 3-27. Each segment is capable of bending bidirectionally, has two concentric layers of rubber, a hollow inner core, and distributed pneumatic actuators. As shown through the characterization of various actuator morphologies (Section 3.2.2.4), the concatenation of soft cylindrical segments is most suitable to build up a robotic arm

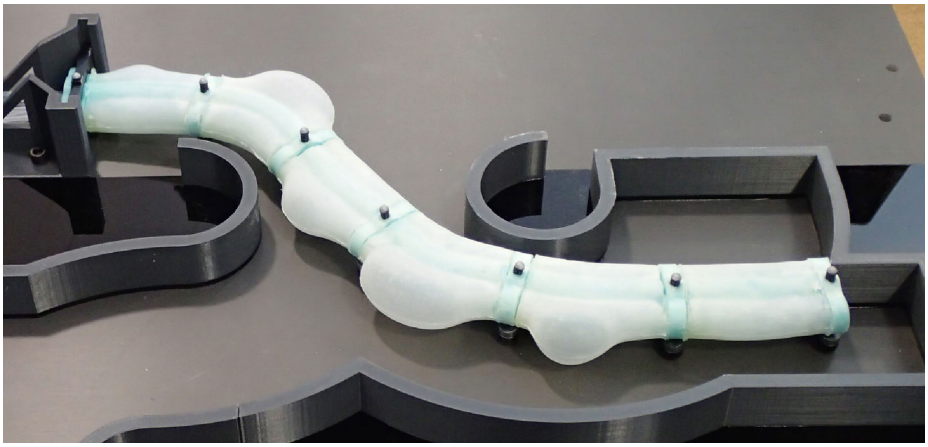

Figure 3-27: A cylindrical soft manipulator prototype with no end effector. The figure is adapted from [Marchese et al., 2014a].

that can create high blocking forces per fluid energy inserted. The cylindrical segments of the arm are fabricated through a retractable pin fabrication technique, which does not require any lost wax cores because of their simple cylindrical cavities. Each cylindrical segment is 6.3 cm long and can be actuated up to a bend angle of about 60°. This requires the combination of several segments to allow the arm to reach a sufficiently large workspace to perform proper manipulation tasks on a plane. Using six segments, the robot is able to touch its base with its tip without interference from the individual joint limits. Just as in the ribbed composition, cylindrical segments are joined end-to-end. Here, fluid transmission lines are passed through the manipulator's hollow center. This feature not only facilitates segment concatenation, but also allows for modular composition of a manipulator, because transmission lines are not permanently embedded within the elastomer. Additionally, this manipulator type is almost only composed of soft silicone rubber as there is no inextensible constraint. The manipulator is highly deformable, as heuristically shown in Figure 3-28. The manipulator is supported vertically off the ground with two roller supports per segment. The rollers minimize frictional forces to the surface, allowing the arm to move with low friction on a level plane. If the arm was moved over a non-slippery surface without rollers, the frictional effects would greatly reduce the agility of the arm and largely increase the stick-slip friction effects with the ground, rendering the arm less useful.

In the following, we further describe two variations of this planar soft manipulator,

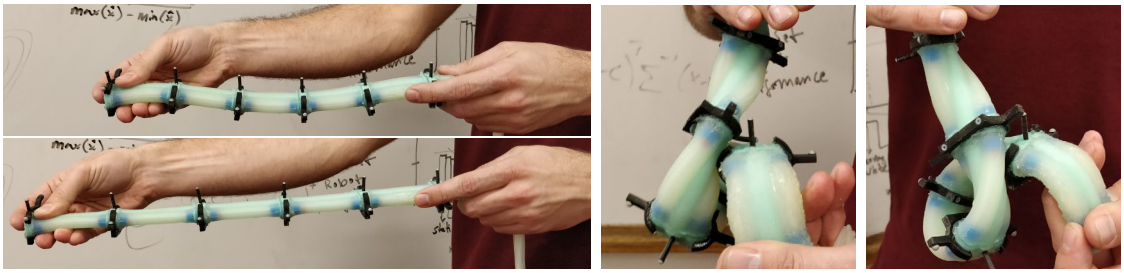

Figure 3-28: The cylindrical soft robot is highly compliant. Top left shows the robot in rest. Bottom left shows the behavior of the soft robot when subjected to a small axial pulling force. The two images to the right show, from different viewing angles, the result of a large torsional wrench applied to the soft robot.

all have the same six segment multi-segment arm in common and only differ by the type of added end effector.

3.6.7 Pleated Gripper on Cylindrical Multi-Segment Arm

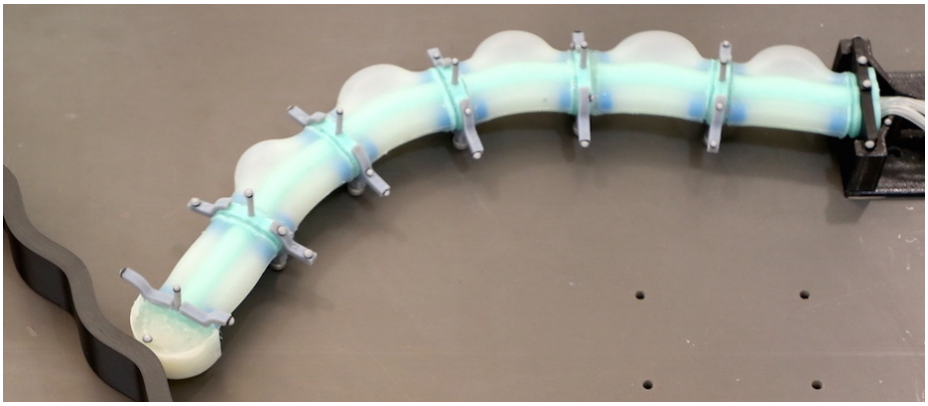

Figure 3-29: A cylindrical soft manipulator prototype with soft hemisphere as end effector.

The soft grasping manipulator shown in Figure 3-30 has six bidirectional segments with cylindrical cavities forming the arm and a single unidirectional soft gripper with pleated shape (Figure 3-5) as the end effector. The cylindrical segment design with its hollow channel in the center has enough space to accommodate not only for the pneumatic tubes to connect all six cylindrical segments, but also to connect a tube to a pleated gripper that is glued to the tip of the manipulator as an end effector. The pleated gripper has to be appropriately sized, just big enough to allow for proper

manipulation without exceeding the payload capacity of the soft arm. The manipulator with gripper is shown in Figure 3-30.

3.6.8 Soft Hemisphere on Cylindrical Multi-Segment Arm

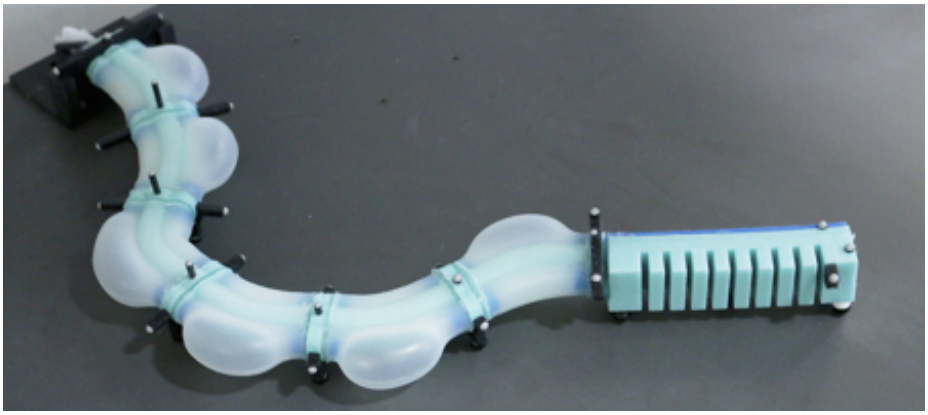

Figure 3-30: A cylindrical soft manipulator prototype with pleated gripper as end effector. The figure is adapted from Katzschmann et al. [2015].

The manipulator with a soft hemisphere as end effector is shown in Figure 3-29. The hemisphere is cast of the same silicone rubber as the material of the cylindrical segments. Additionally, we glue a flexible acetal sheet onto the hemisphere to make a minimal friction surface, which is useful for tracing or following along a wall with minimal tangential friction forces.

3.6.9 Localization and Pneumatic Actuation of Manipulator Arms

Figure 3-31 depicts the aggregate setup of our soft manipulation system and highlights the major subsystems for localization and pneumatic actuation. While the figure shows a setup using the multi-segment manipulator arm (Figure 3-31-C) with gripper (Figure 3-31-E) introduced in Section 3.6.7, also the manipulators described in Sections 3.6.4, 3.6.5, 3.6.6, and 3.6.8 can be installed, actuated, and sensed within this setup. The manipulator with gripper is supported vertically off the ground with two roller supports per segment. The manipulator moves with minimal friction on a

level plane. A localization system (Figure 3-31-A) provides real-time measurements of the end-point positions of each segment along the neutral axis of the manipulator arm. The localization system also provides real-time measurements of the marked points on top of objects (Figure 3-31-D) to be grasped or environments to go in contact with and trace along. This localization data can be provided by an exteroceptive system, for example a motion capture system, or through a proprioceptive system, for example the embedded sensors used within the soft fingers (Sections 3.6.2 and 3.6.3). In our implementation we use an external motion capture system[30] as shown in Figure 3-31-A. This system provides accurate measurements of the robot's posture. A rigid frame (Figure 3-31-B) holds the cameras of the motion capture system in a fixed orientation, providing reliable hardware experiments without the need for frequent recalibration of the cameras. The system provides real-time measurements of groups of reflective markers along the back of the soft arm. Groups of four markers each are placed at the root and the end of each individual segment in order to identify the position and orientation of the segments along their neutral axis. The degree of curvature of a segment is evaluated by measuring the relative rotation between each end of a segment. Two nearby computers (Figure 3-31-G) take the tracking information as input and then run a suite of motion planning algorithms.

The independent pneumatic actuation of the bidirectional arm segments is achieved through an array of 12 pneumatic cylinders driven by linear actuators[31](Figure 3-31-F). The independent pneumatic actuation of the unidirectional soft gripper is achieved through an additional pneumatic cylinder.

Changing the placement of the piston changes the fluid volume and pressure within a bidirectional segment, effectively changing the curvature of a segment. This placement value is regulated by a local PID controller within a motor controller connected to each linear actuator. Each motor controller runs on its own embedded system[32], which is mounted inside the housing of each pneumatic cylinder (Figure 3-31-F). The desired piston placement is the available control input. This control input

[30]Five Flex:V100:R2 cameras, OptiTrack, NaturalPoint, Inc.
[31]Concentric LACT4P-12V-5
[32]Polulu Jrk 12v12

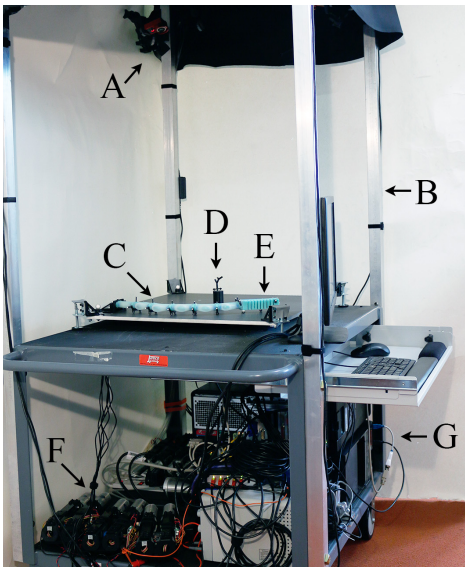

Figure 3-31: Major components of the soft robotic manipulation system including the localization and actuation. The system is composed of (**A**) a motion capture system, (**B**) a rigid frame, (**C**) a soft six-segment planar manipulator, (**D**) an object within the grasp envelope, (**E**) a soft gripper fixed to the manipulator, (**F**) a pneumatic cylinder array to control actuation, and (**G**) computers for real-time processing and control. The figure is adapted from Katzschmann et al. [2015].

is sent to the motor controller expressed as encoder tics, ranging from 0 to 1000 tics.

3.7 Contributions to Design and Fabrication

This chapter covers the following contributions:

1. Classification of three viable fluidic elastomer actuator (FEA) morphologies. That is, an FEA with (i) a seamless ribbed channel structure allowing for heterogeneous embeddings, (ii) a cylindrical channel structure with hollow interior for tubing, (iii) a seamless pleated channel structure. The ribbed design improves over a previous design [Marchese et al., 2014b]; the cylindrical design [Katzschmann et al., 2015, Marchese et al., 2014a] and the pleated design [Katzschmann et al., 2015] are new.

2. Three fabrication processes to reliably manufacture these FEAs. These are (i) a lamination casting process that allows for heterogeneous embedded components, (ii) a retractable pin casting process, (iii) a lost wax casting process.

3. Design of fluidic power sources for FEAs.

4. Hydraulic actuation system for water-filled fluidic elastomer actuators.

5. A set of soft robots for locomotion and manipulation, built using the design and fabrication techniques of this chapter.

Chapter 4

Application for Biomimetic Swimming

In this chapter we describe an application of the design and fabrication techniques in Chapter 3 to a robot swimming in the ocean. The design and fabrication example given in Section 3.6.1 is used for this application. The soft robotic fish (SoFi) is an embedded and self-contained underwater system using a single fluid elastomer actuator for swimming. We show that with a fluid elastomer actuator, we can create a biomimetic soft robotic fish that uses undulating motion to swim in the ocean and has the application of exploring underwater life and structures. This work is based on the robotic fish presented in Katzschmann et al. [2014, 2016, 2018b], and the acoustic communication in DelPreto et al. [2015].

4.1 Goal and Challenge

We want to build and successfully deploy an untethered underwater robotic fish, similar in size and behavior to living fish, that can autonomously execute high-level commands remotely received from a diver. The challenge is to realize biomimetic swimming of a self-contained system in a compact size, with good portability, limited power, and communication capabilities. The robotic fish has to execute 3D trajectories with lifelike undulatory locomotion by using a soft fluidic circulatory actuator and a compact

buoyancy control mechanism. All components of the integrated end-to-end system have to be designed accordingly, including the pump, the soft actuator body, the on-board control, the energy storage, the wide-view video camera, the on-board sensors, the acoustic communication module, and the remote control interface. Two major challenges related to locomotion are: 1) the creation of a hydraulic propulsion system that can carry all crucial components needed for untethered underwater exploration; 2) a low-drag design with appropriate buoyancy and weight distribution that can maintain structural integrity under pressure throughout a suitable depth range. To overcome these challenges and achieve biomimetic propulsion, we had to design a custom low-pressure high-flow pump and an appropriately sized soft fluidic actuator. An adjustable buoyancy unit, oil-filled chambers for electronics, custom seals, and rigid foam-filled compartments all had to fit within the limited volume available. Human interaction with the robot in the challenging underwater environment is also a design constraint. We created an underwater communication module that allows for real-time control of the robot and provides an intuitive interface in a rugged, compact, and low-power package.

4.2 System Overview

The soft robotic fish (SoFi) is open-loop controlled and swims in the ocean by undulating its soft tail. SoFi is designed to swim independently and receives high-level commands from a human diver. An overview of the system is shown in Figure 4-1. The robot measures 0.47 m x 0.23 m x 0.18 m, weighs 1.6 kg, is neutrally buoyant, and swims for about 40 minutes. It propels itself by undulating its soft tail in a cyclic manner, and adjusts this undulation to swim forward or turn (Section 3.6.1.1). The tail is fabricated through lost wax casting (Section 3.6.1.2). The tail motion is created by the cyclic flow of a displacement pump (Section 3.6.1.3), and adjusting the relative amount of liquid pumped into each side of the tail can generate a turning motion. Vertical swimming is achieved via dive planes and a buoyancy control unit. The fish is equipped with a fisheye camera at its tip to observe its environment. An acoustic

transducer, used as receiver, is mounted in front of the rigid dorsal fin, tilted upwards, to receive commands from the human-operated diver interface module. The human remotely controls SoFi through the diver interface module using a custom-designed unidirectional acoustic communication protocol.

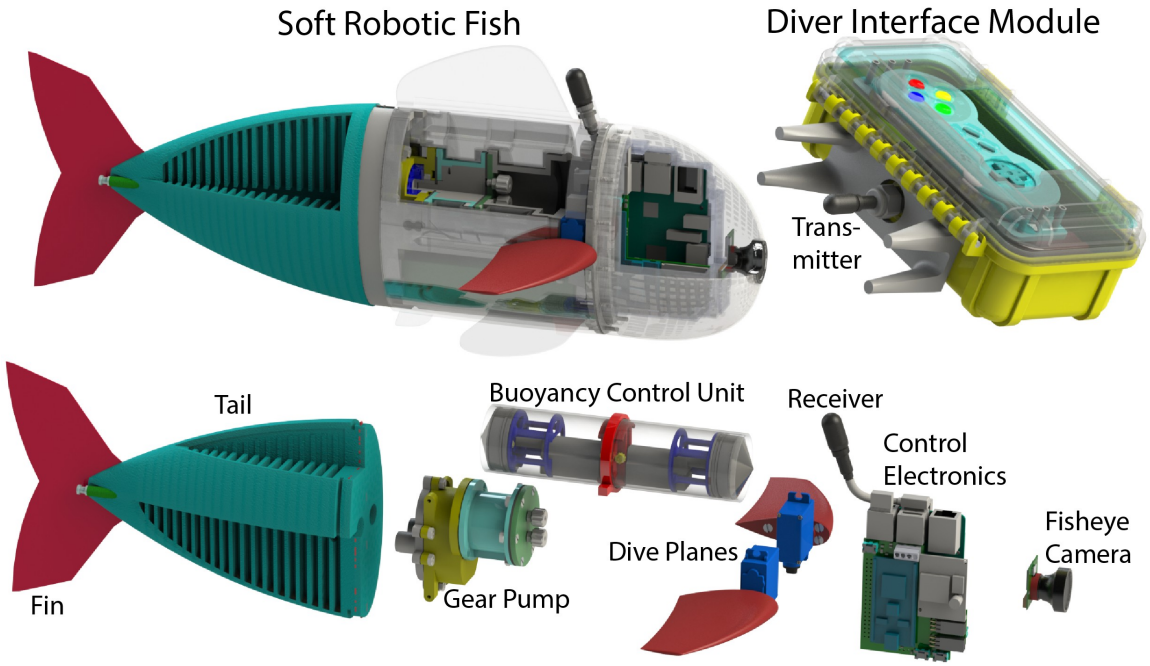

Figure 4-1: System overview of the soft robotic fish (SoFi): Top (left to right): Soft robotic fish and diver interface module. Bottom (left to right): Subcomponents of the system are the elastomer tail (cut view), external gear pump, buoyancy control unit, two dive planes, control electronics including acoustic receiver, and fisheye camera.

4.3 Embedded System for Independent Operation

The embedded system and its major subcomponents are shown in Figure 4-1. The nose of the fish is a waterproof housing for the fisheye camera, microcontroller, computer, motor driver, wireless communication electronics, inertial measurement unit, and depth sensor. The housing is 3D-printed and waterproofed by brush-coating it with pre-heated epoxy paint and subsequent degassing. Behind the nose is the dive plane assembly, consisting of two individually controllable dive plane units. Each unit consists of a dive plane directly mounted onto the lever arm of a waterproof servo

motor. The dive plane assembly is mounted to the end of the gear pump's DC motor. Motor and gear pump unit are directly attached to the soft fish tail. Underneath the gear pump motor is a lithium polymer battery to power all components. Above the gear pump is the buoyancy control unit. The mass of the complete assembly was slightly adjusted to make it almost neutrally buoyant using internal rigid urethane foam chambers and additional magnetic weights placed underneath the robotic fish.

4.4 Control Architecture

The flow of commands within the system is depicted in Figure 4-2. The diver commands a change to the fish state via the gamepad controller within the diver interface module. The command is encoded into an acoustic signal transmitted via the transmitter to the amplifying receiver within the fish. Both the transmitter and receiver use the same acoustic transducer[1]. The microcontroller decodes the received command and adjusts its state accordingly. Changes to the swimming speed or turning motion change the behavior of the displacement pump and therefore the soft tail undulation. Changes in pitch or depth, depending on the mode, are sent to the servos of the dive planes or the buoyancy control unit. Changes to the video recording state are forwarded to the single-board computer, which records from the fisheye camera.

[1] Aquarian Scientific AS-1 hydrophone

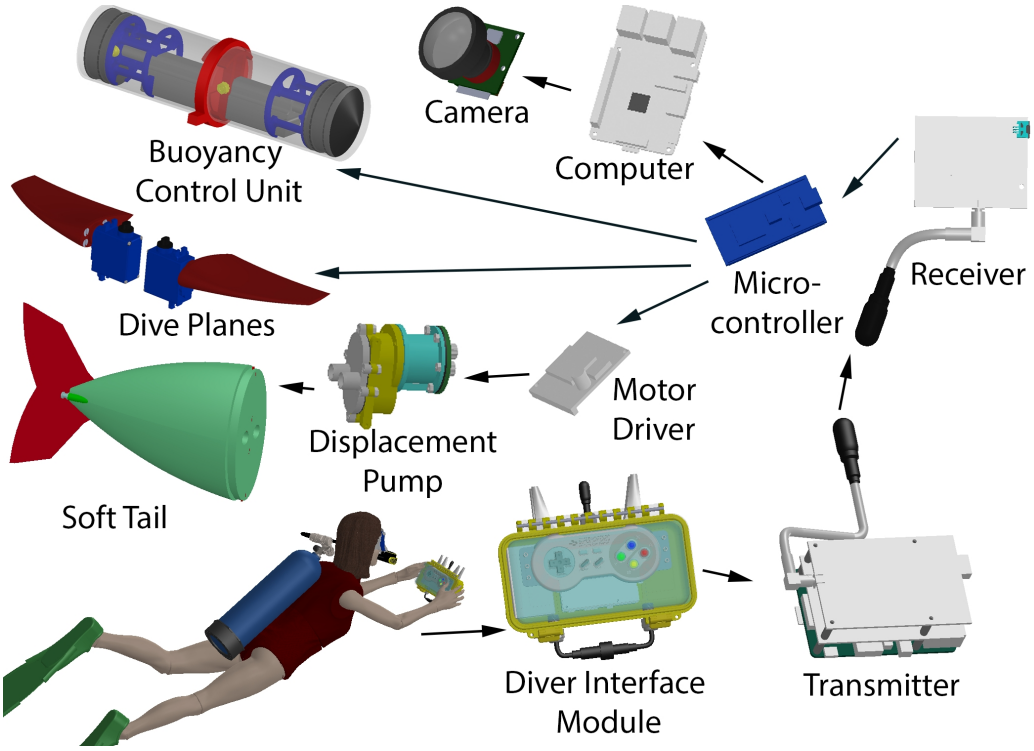

Figure 4-2: Signal flow within the soft robotic fish: The command flow goes from the human diver to the robot. The diver sends acoustic commands such as thrust, left/right and up/down as well as camera modes from the transmitter within the diver interface module. The analog signal travels several meters underwater and is then amplified by the receiver and parsed by the microcontroller. The microcontroller adjusts the pump speed, the dive plane position, the BCU, and the mode of the camera.

4.5 Cyclic Hydraulic Actuation for Swimming

Longevity and endurance are important challenges for self-contained soft robots. Pneumatic energy sources are commonly used for the actuation of terrestrial soft robots [Wehner et al., 2014], but external pneumatic pumps constrain the mobility of a system, limiting autonomy and range. Systems utilizing a compressed-air cartridge as an on-board pressure source can only operate on the order of a few minutes due to the low energy density of compressed-air and the challenge of either recycling or venting the air after the inflation of a cavity [Marchese et al., 2014c]. Constant release of gas causes non-negligible changes in the overall buoyancy of the robotic fish, rendering depth control infeasible. Additionally, a fixed volume of gas limits deployment time.

In contrast, alternately transporting fluid from one chamber to the other, as done in SoFi, does not require an extra storage unit, and the fluid does not need to be exhausted in order to deflate the actuator. Using water instead of air as transmission fluid also eases deployment underwater.

The soft tail (Section 3.6.1.1) is therefore actuated by a hydraulic pump (Section 3.6.1.3) at a desired undulation frequency and amplitude. The outlets of the hydraulic pump are directly attached to the soft body to allow for water movement between the two inner cavities in a closed-loop fashion. Alternating the flow direction leads to a flexing actuation of the soft body in a side-to-side manner, propelling the robot forward. The soft tail has removable plugs at the caudal fin, which are initially removed so that water can fill the actuation chambers by running the self-priming gear pump at a low frequency for a short duration. After all air has been removed, the plugs are inserted to seal the chambers.

The motor controller operates the motor attached to the pump through a trapezoidal voltage profile, alternating from positive to negative voltages after each half cycle. This profile rotates the motor shaft back and forth, causing the pump to create a cyclic hydraulic flow. Asymmetrically varying the flow intensity for each half phase can enable yaw control by creating a pressure bias in the tail.

4.6 Depth Control of the Soft Robotic Fish

There are multiple systems used to control the buoyancy of underwater robots. The major open research problem for these mechanisms is reducing weight, bulk, and noise [Raj and Thakur, 2016]. One system heats and cools wax or oil to change its buoyancy [McFarland et al., 2003, Shibuya et al., 2006]. However, this has a slow response time, especially when cooling the medium. A second system uses a buoyancy chamber that can be filled with air or water; the water is pushed out of the chamber by filling it from a compressed air tank [Laine et al., 1999]. This system is large, and requires refilling of the compressed air tanks. A third system uses electrolysis to create bubbles of 2 ml volume [Guo et al., 2000]. However, as the system is scaled up in size, the realizable

change in volume becomes insufficient. A fourth system, used in large underwater gliders, adjusts buoyancy by compressing or filling an air chamber and adjusts pitch by moving an internal mass [Davis et al., 2002, Detweiler et al., 2009]. While these parts are reliable, the complex actuation mechanisms of the plunger or bladders are intricate, bulky, and difficult to scale down. A fifth mechanism, used in a batoid robot, also compresses air through a piston. While smaller than the fourth system, it still has bulky external actuation parts, such as a lead screw drive that protrudes from the main body of the robot, and is difficult to incorporate in other designs like submarines or robotic fish [Cloitre et al., 2012]. By using similar principles as this fifth mechanism but further miniaturizing the actuation, we designed a modular buoyancy system that is fast, simple, and effective in actuation and control.

The depth of SoFi is controlled by dive planes or the BCU. The dive planes, shown in Figure 4-1, allow the diver to finely control the robot's change in depth through dynamic diving for limited deviations from its baseline depth before a buoyancy adjustment is needed. Each dive plane is attached to an oil-filled waterproof servo. Both dive planes are mounted next to the fish's pectoral fin. Pectoral fins are responsible for the creation of dynamic lifting forces to allow for dynamic diving and therefore depth control. The dive plane profile is designed using a loft limited by two symmetric airfoils. A symmetric profile is chosen so that no lift is produced when held in a horizontal position. Controlling the pitch of the fish and therefore changing the depth is achieved by adjusting the angle of attack of the dive planes.

Manually adding or removing magnetic weights attached to the bottom of the robot adjusts the neutral depth level. This allows the diver to operate the robot over a larger depth range.

Additionally, the diver can remotely adjust the neutral buoyancy of the robot using the BCU. The BCU, shown in Figure 4-1, can simultaneously control the buoyancy and pitch of the robot. The mechanical design of the BCU comprises two mirroring volume control modules by means of two pistons. The BCU is symmetrically oriented at the robot's center of buoyancy. An exploded view of a single unit is presented in Figure 4-3. A single unit contains a micro-linear actuator with potentiometer feedback (PQ12,

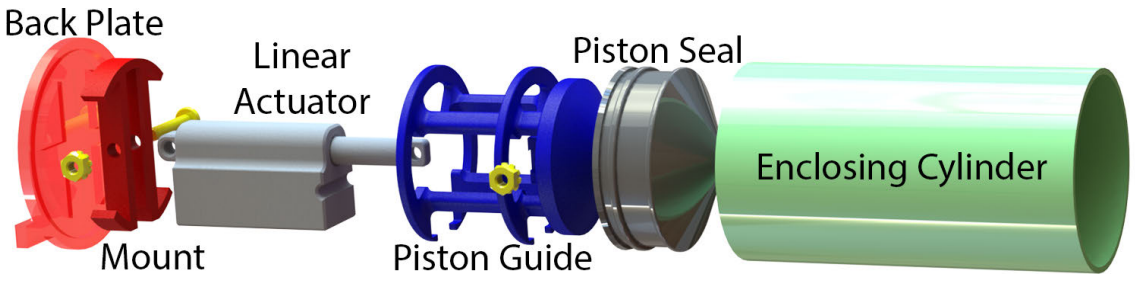

Figure 4-3: Buoyancy Control Unit: One of two identical BCU modules in an exploded view.

Actuonix, Victoria, Canada) that sits within a watertight cylinder and moves a piston. A closed-loop proportional-integral-derivative (PID) controller with pressure feedback from an integrated pressure sensor is used to drive the volume-changing actuators. Ascent, descent, and hovering can be achieved over several meters by symmetrically controlling the pistons. The pitch can also be modified by asymmetrically controlling the two pistons (Figure 4-4).

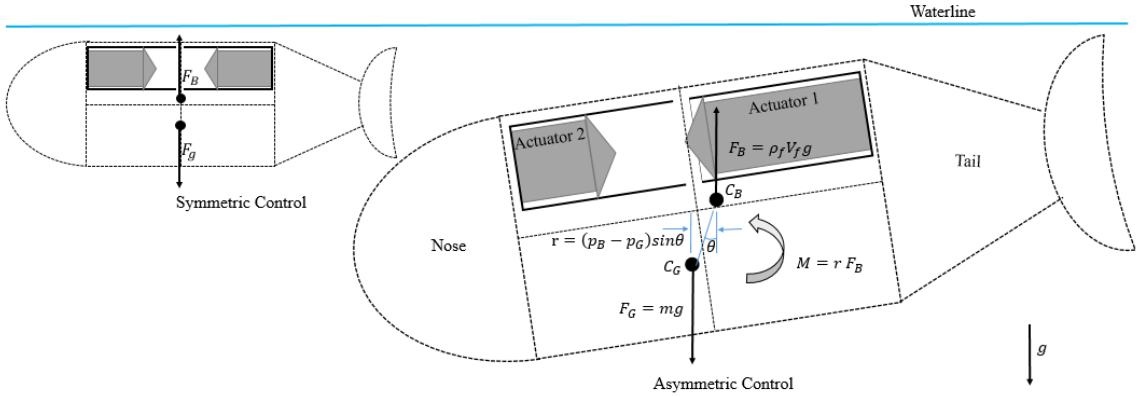

Figure 4-4: Buoyancy control system of SoFi: If the actuators are controlled asymmetrically, gravitational force and buoyant force are shifting and become misaligned. To restore the static equilibrium, a restoring moment is created, pitching the submerged fish robot. If the actuators are controlled symmetrically around the center of buoyancy, the depth can be adjusted without affecting pitch.

4.7 Underwater Communication for Remote-Control

Underwater communication is an essential component for controlling the robot. We designed a compact unidirectional acoustic communication modem to allow SoFi

to support remote-controlled operation. The following provides a summary of the communication, more details can be found in Appendix A as well as in DelPreto et al. [2015], Katzschmann et al. [2018b].

While radio-frequency communications [Liu et al., 2008] are ubiquitous in terrestrial applications, those signals rapidly attenuate in saltwater [Che et al., 2010]. Optical communications [Vasilescu et al., 2005, Doniec et al., 2013a,b] are also challenging underwater, as they are subject to scattering and noise from ambient light. We therefore used acoustic communications, which have been widely adopted for underwater applications [Chitre et al., 2008, Stojanovic and Preisig, 2009, Lacovara, 2008]. While WHOI modems [Johnson et al., 1994, Freitag et al., 2001] can overcome challenges such as multipath effects and Doppler shifts [Akyildiz et al., 2005], their size and power consumption are too large for fish-sized robots. Similarly, other modems [Martins et al., 2014, Sánchez et al., 2012] focus on higher data rates and longer ranges than required for remote-controlled operation by a diver, rendering them too bulky, expensive, and energy-consuming for our present application. Some acoustic modems [Vasilescu et al., 2005] use hardware-defined signal generation and detection, but this limits available processing and reduces versatility. Taking these prior works into account, we designed a lean unidirectional communication protocol with software-defined detection algorithms that enable our system to send short command words while being small and easily integrated into SoFi.

The diver interface module (Figure 4-5 left) contains the transmitter and allows the diver to issue commands, while the receiver is embedded within SoFi's head. Tight volumetric constraints made accommodating of existing underwater modem designs impractical. Thus, we implemented a new low-power, low-cost, software-defined acoustic modem, schematically represented in Figure 4-5 on the right, and described in detail in DelPreto et al. [2015].

We designed a modulation scheme that could be efficiently implemented in software on a microcontroller while still being robust to multipath effects and Doppler shifts. It uses pulse-based Frequency-Shift Keying (FSK) and a computationally-efficient software-defined demodulation approach leveraging the Goertzel algorithm [Goertzel,

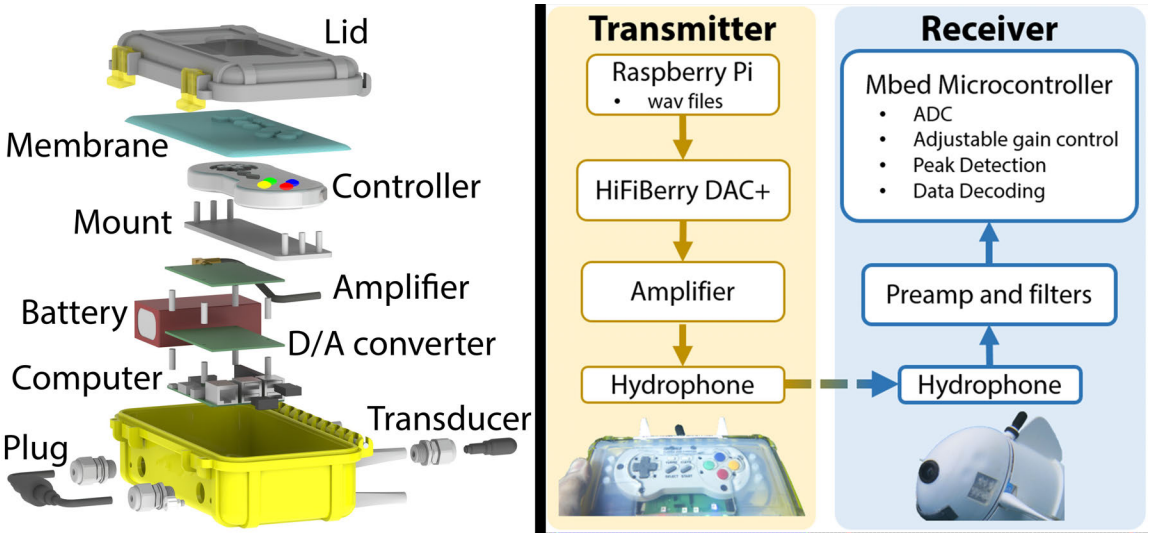

Figure 4-5: Acoustic communication: Left: Exploded view of the Diver Interface Module, containing the transmitter. Right: Schematic view of the Transmitter and Receiver pipelines.

1958] and a custom dynamic peak detection algorithm. The chosen parameters support 2048 distinct messages with a data rate of one message per second at 20 bits/s. Further details on the algorithm can be found in DelPreto et al. [2015].

The desired fish state, encoded as a 16-bit word, is transmitted from the controller once per second. Each command describes a desired state of the fish, including tail oscillation frequency (2 bits), oscillation amplitude (2 bits), pitch or depth (3 bits), yaw (3 bits), and video recording (1 bit). These 11 bits are expanded to a 16-bit word using a [15,11] Hamming encoding with an additional parity bit. This vocabulary of commands can then be used to remotely control the fish.

4.8 Experimental Setting

We tested the complete system in the open ocean, with a diver remotely adjusting the fish's state and navigating it to points of interest in a complex underwater environment. Six dives were conducted over the course of three days, exploring the Somosomo Strait in Taveuni, Fiji (see Table 4.2 for details). This location offers numerous coral reef environments with varying tidal conditions, allowing SoFi to be evaluated in real-world

conditions where the interactions of marine life and the biocenosis of coral reefs can be studied.

The robot conducted about 40 minutes of continuous observation during each dive, totaling approximately 240 minutes of controlled exploration at an average depth of 8.1 m and maximum depth of 18 m. We performed an additional 90 minutes of preparatory swim tests in shallow ocean waters to test control system, communication, and video recording. All of these tests evaluated the effectiveness of SoFi's biomimetic actuation and the usability of the acoustic communication interface for remote control. The distance between the operator and SoFi was typically between 1 and 10 m, and the transmit power of the acoustic modem was 137.3 dB SPL re 1 µPa. The robot's trajectories along the reefs and following other fish were documented by two or more divers using GoPro Hero 3, Canon PowerShot S100, and Olympus Tough TG-1 cameras from a distance of several meters.

Qualitative observations were made during five of the dives, during which SoFi explored the coral reef environments. The magnetic weights were adjusted at the beginning of each dive for neutral buoyancy, then the robot was continuously operated via the acoustic modem. The distance between controller and robot was varied to understand the effective communication range. The fish was steered throughout the coral reefs, going as close as possible to interesting environmental features and marine life. Such dives provided qualitative observations of SoFi's swimming capabilities in constrained and unconstrained areas, of the acoustic communication reliability, and of the effect that SoFi has on nearby fish.

In addition, one dive was dedicated to performing quantitative swimming tests on the ocean floor at a baseline depth of about 7 m. We installed several pre-measured ropes to define a reference volume (4 m x 4 m x 1 m) for measuring and filming the robot's ability to swim straight, turn right, turn left, dive up, and dive down. We performed 3 trials for each ability. During all trials, the thrust was set to maximum and the undulation frequency set to medium (1.15 Hz). For right and left turns, the yaw was set to $\pm 30^\circ$ and the dive planes set to neutral. For up or down swimming, the dive planes were adjusted to $\pm 45^\circ$ and yaw set to neutral. Yaw and pitch were both

neutral for straight swimming. At the beginning of each trial, a diver repositioned the fish to its starting position at the center of one of the bounding planes of the reference volume and then released the fish without pushing it. This diver also took notes during trials. A second diver commanded the desired fish state from the starting position. Two additional divers filmed the trials from the side and from the top, standing or floating at the boundary of the reference volume.

Throughout all sessions, the diver interface module transmitted the desired fish state once per second using a bitrate of 20 bits/s. By recording logs of commands on both the transmitter and receiver, the percentage of commands successfully received and executed by SoFi could be extracted. In addition, qualitative observations were made regarding achievable communication distances, the effect of real-world obstacles such as coral reefs on transmission reliability, the effect of ambient noise such as from marine life, and the effect of the system on surrounding organisms.

We estimated the number of tail strokes at various combinations of thrust and yaw using the logs of the executed fish states. Using the highest commanded undulation frequency, we estimated a conservative total stroke duration. We then weighted according to the thrust level and used the average speed from the quantitative tests to estimate the swimming distance.

4.9 Underwater Communication Tests

We evaluated the acoustic modem for underwater communication in a pool, a fish tank, and the ocean. The system was first evaluated in a tank (1.2 m x 0.3 m x 0.45 m) and a pool (23 m x 12.5 m x 2.2 to 4.2 m) to test the modem under controlled conditions. These environments facilitate multipath reflections due to the enclosed configuration, hard walls, and shallow depth, approximating the types of interference observed in open-ocean deployments.

As described in more detail in Section A.3, tests were performed during development to choose parameters of the modulation scheme and decoding algorithm. Then, to evaluate communication reliability of the completed modem, we transmitted a series of

200 alternating bits at a rate of 20 bits/second over a sequence of increasing distances and depths. For each transmission, the percentage of bits correctly decoded by the receiver and the longest error-free segment of received bits were extracted. After evaluating single-bit transmissions, transmissions of complete words were investigated by sending a predefined series of 250 16-bit data words using 50 ms for each bit and 200 ms between words. The correctness of the decoded sequence was then measured.

Finally, the complete modem integrated within SoFi was used in the open ocean to evaluate performance in real-world operations.

4.10 Buoyancy Control Tests

Vertical diving capabilities using the BCU were quantified in an indoor swimming pool of 4.2 m depth. There were no substantial disturbances in the environment except the pool circulation and swimmers in adjacent lanes. The gains of the PID controller were estimated by averaging the results of two frequency response tests [Åström and Hägglund, 2004]. Before the start of each trial, the robot's weight was adjusted for neutral buoyancy at a desired baseline depth. Desired depth values were then commanded as a step function. Once a set depth was held for 4 s within an error margin of 10 %, the next depth level was commanded. The robot's microcontroller continuously logged the depth by reading a pressure sensor. Each run started at a different depth to investigate varying baselines. We measured depth, speed, duty cycles, and error.

The BCU reliably controlled depth changes of up to 2.8 m. This was repeatedly tested at different baseline depths of 1.6 to 2.7 m by adjusting magnetic weights. The average dive speed up and down was 10.6 cm/s (±1.1 cm/s), equivalent to 0.6 body heights per second. Commanding a step change in a depth of 0.2 m had a 10 % settling time of 17.8 s (±6.6 s). Figure 4-6 shows the depth profile of a vertical dive, where the robot was directed to continuously dive deeper solely by compressing the air in the piston of the BCU. The BCU responded with slight oscillations around the set depth until it settled and the next depth was commanded. The two linear actuators within

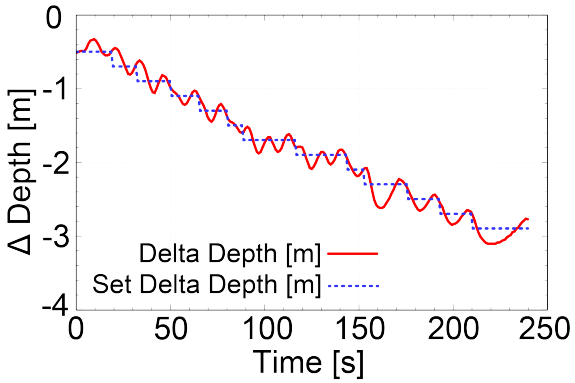

Figure 4-6: Vertical dive experiment: the robot was directed to continuously dive deeper solely by compressing the air in the piston of the BCU. Series of step functions (blue). The BCU followed the commanded values (red).

each of the two modules moved symmetrically to vary the buoyancy while maintaining constant pitch of the robot. Additional buoyancy control experiments are provided in Figure 4-7.

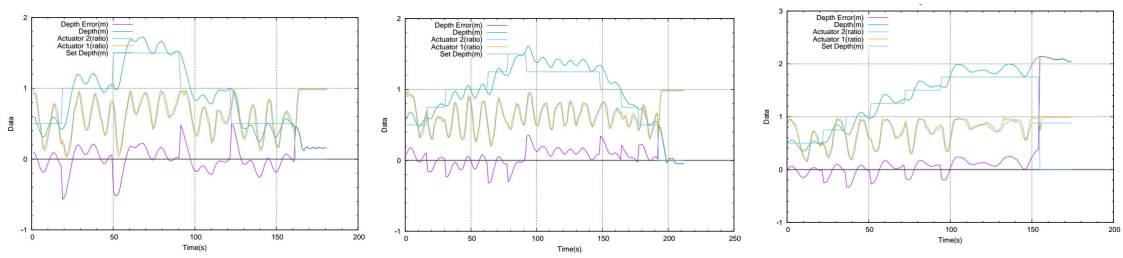

Figure 4-7: Additional buoyancy control experiments: The buoyancy control unit (BCU) was commanded to follow the step function (light blue). The BCU followed the commanded values (cyan). The difference in the set value and actual value is shown by the error function (purple). The plots also display the normalized actuator positions (yellow, blue).

4.11 Swimming along a 3D trajectory

The hydraulic system performed undulating tail actuation at low (0.9 Hz), medium (1.15 Hz), and high (1.4 Hz) frequencies to achieve a range of swimming speeds. The fish executed left and right turns by adjusting the baseline deflection angle of the tail around which the tail undulates. The fish performed three levels of deflection in each direction, with a maximum baseline deflection of about $\pm 30°$. Similarly, the fish

Figure 4-8: Underwater exploration of the soft robotic fish: Snapshots show the fish's trajectory exploring a coral reef. The snapshots of the fish are equally spaced in time by 2.6 s per representation.

could pitch its dive planes at three levels in each direction, with a maximum pitch of ±45°. A sample fish trajectory along a coral reef is shown in Figure 4-8, illustrating the controlled swimming motion as it was commanded by a human diver. The fish changed direction and depth while exploring the reef, with an average swimming speed of 21.7 cm/s (±3.2 cm/s) at depths of 0 to 18 m.

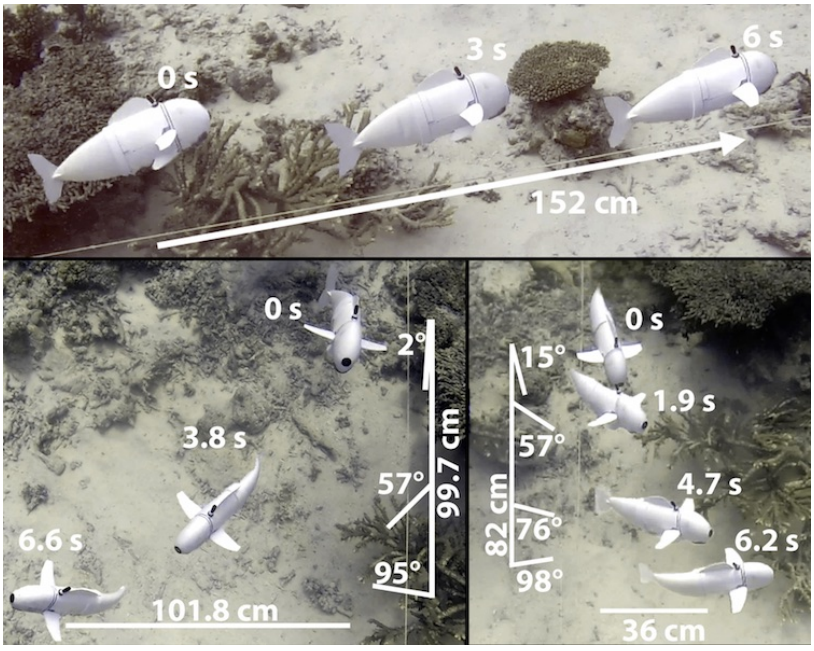

Figure 4-9: Quantitative ocean experiments: Straight swimming (top), left turn (bottom right), and right turn (bottom left) experiments of the robotic fish.

We performed quantitative tests in the ocean to measure the forward and turning

capabilities of the fish (Figure 4-9). The average swimming speed in a straight path was 23.5 cm/s (±0.4 cm/s), equivalent to 0.5 body lengths per second. The average turning speed was 18.3 cm/s (±4.1 cm/s) on an average turning radius of 78.2 cm (±28.6 cm). Dynamic diving using the dive planes was possible within a range of ±0.9 m from its baseline depth at an average speed of about 14.0 cm/s, equivalent to 0.8 body heights per second. During the dive, we changed the robot's baseline depth within 0 to 18 m by manually adjusting attached weights. At deeper depths, the rigid foam flotations experienced too much compression and inhibited rising.

4.12 Human-Robot Interaction

The human remotely controls SoFi through a custom-designed unidirectional acoustic communication modem. This system consists of the diver interface module and the acoustic receiver, both shown in Figure 4-1.

We characterized the reliability of the communication modem by transmitting a series of 200 alternating bits at a rate of 20 bits/s at varying distances and depths in a large pool. The results, shown in Figure A-3, indicate that error-free communication was achieved at 1.8 m depth for ranges up to about 15 m, with over 97 % of the data successfully received at 21 m, and that the effective communication range remains similar when the robot's motor is turned on. In addition, a complete sequence of 250 16-bit data words was successfully received and decoded without errors at distances of about 0.5 m in a fish tank and 10 m in a small pool.

A human diver used the diver interface module to successfully steer the robot through various complex underwater coral reef environments. The diver commanded levels of thrust, tail undulation frequency, depth/pitch, and turning angle; Figure A-5 illustrates the transmitted and received commands for a single dive, and Table 4.1 summarizes the detection rates. During dive 5, the diver remained closer to the fish (within a few meters) and therefore communication was more reliable. Our analysis focused on "steady" commands, which were not immediately followed by a different command within one second; for example, a diver commanding a transition from

lowest to highest pitch would repeatedly press the "up" arrow, resulting in transient intermediate pitch states, but only the final command state is of importance. If the fish did not receive any commands within a timeout period of about 10 seconds, it would return to a neutral state and turn off the motor; this temporary silencing would then facilitate detecting fainter commands.

In the coral reef experiments (at depths ranging from 0 to 18 m), effective communication was established at a range of up to 10 m when the robot's motor was switched off and 5 m when the motor was switched on. The largest factors affecting communications were environmental complexity, noise of the fish motor, and transmission distance. Additional experiments close to the shoreline showed that in a shallow, cluttered underwater environment, the system can communicate up to 10 m, even in the presence of motor noise.

	Dive 3	Dive 4	Dive 5	Dive 6
Total commands obeyed	67	30	111	93
Total commands missed	55	62	46	57
Steady commands obeyed	55	26	75	78
Steady commands missed	25	31	7	21
Percent of steady commands obeyed	**68.8%**	**45.6%**	**91.5%**	**78.8%**
Fish timeouts (reversions to neutral state)	63	34	81	81
Percent of dive spent timed out	**12.3%**	**8.0%**	**7.3%**	**8.1%**

Table 4.1: Communication experiments: Cumulative results of the acoustic communication during four of the six dives, spanning 2 days and averaging about 40 minutes per dive. Note that "steady commands" are commanded states that persisted for at least 1 s. "Timed out" means that the fish did not receive a command within the last 10 s. Observations were made at an average depth of 8.1 m, a maximum depth of 18 m, a range between transmitter and receiver of 0 to 10 m, and an acoustic transmission power of 137.3 dB SPL re 1 µPa.

4.13 Oceanic Experiments

The robotic fish has an on-board fisheye camera that allows a remote human operator to film the underwater exploration. This setup reduces the impact of the diver on marine life being filmed. The fish continuously operated for about 40 minutes during each of six approximately 51-minute dives over 3 days, accumulating 240 minutes of

controlled exploration (Table 4.2). Each dive used a single charge of a 35 Wh battery. The average depth was 8.1 m and the maximum depth was 18 m. We recorded the number of tail strokes performed for an average dive (Table 4.3). Based on the average swimming speed observed during the quantitative tests, for a single dive this would correspond to 296.8 m (±5.1 m) of straight swimming, 17.6 m (±3.9 m) of turning left, and 14.6 m (±3.3 m) of turning right. The ocean experiments showed that the robotic fish is capable of 3D-controllable motions in natural environments, in the presence of currents.

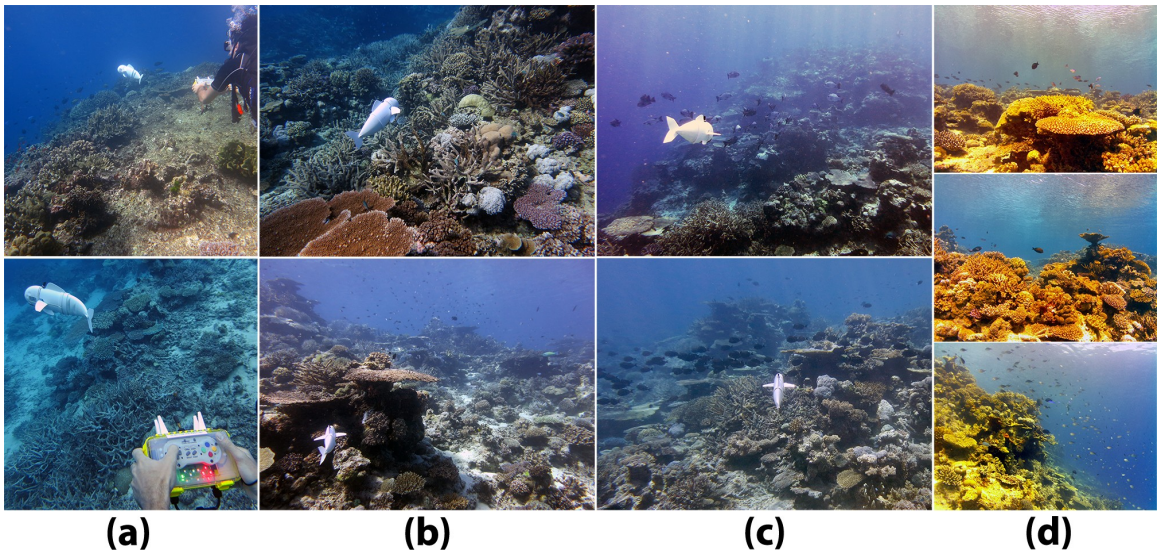

Figure 4-10: Underwater observatory: Column (a) depicts a diver using the acoustic communication modem to remotely control the robotic fish. Column (b) shows the fish exploring complex coral reef environments, and column (c) shows the robotic fish among marine life. Finally, column (d) shows pictures captured by the fish's on-board camera.

During the ocean experiments, we also made preliminary observations of the robot's ability to make close-up observations of marine life and record their responses. Without the intent to imitate any specific species of biological fish, the robotic fish was colored white except for the black lens and acoustic receiver (Table A.1). There were several close-up encounters with underwater life, during which SoFi observed fish and their interactions. During the scope of the ocean experiments, it appeared that SoFi could get close to other fish without causing them to flee. Figure 4-10 shows examples of high-level remote control by a human diver, and depicts some of SoFi's explorations

Figure 4-11: Close-up view SoFi has of marine life: Left panel shows snapshot of the on-board view filming several fish passing by the lens of SoFi. Right panel is a photo taken by a diver from further behind, showing both the robotic fish and the observed biological fish.

and observations: exploring complex coral reef environments, encountering schools of fish, and capturing images with the on-board camera. Figure 4-11 and Movie 1 also show SoFi approaching overhanging reefs and other environments with fish swimming nearby. As the video shows, multiple fish swim parallel to the robot a few centimeters below it and also pass a few centimeters in front of its lens. The fish did not appear to change their swimming trajectory as SoFi approached them in these cases, suggesting that SoFi has the potential to integrate into the natural underwater environment.

Movie 1 Underwater experiments. [`https://youtu.be/z-SHv3aF4lU`] The movie shows multiple sequences of the robotic fish exploring the coral reefs. The robotic fish is shown from different viewing angles. The movie also contains recordings from the robot's perspective using the on-board fisheye camera. We also show the human interaction with the robotic fish through the acoustic diver interface module.

Movie 2 Underwater experiments and a look inside the fish. [`https://youtu.be/Dy5ZETdaC9k`] The movie shows multiple sequences of the robotic fish exploring the coral reefs. The robotic fish is shown from different perspectives, and a brief sequence of the fish's disassembly is shown to allow a look inside. The movie also contains recordings from the robot's perspective using the on-board fisheye camera. Human interaction with the robotic fish through the acoustic diver interface module is also shown, and a close-up is shown of the interface in action.

Dive #	**Day #**	**Location (all in Taveuni, Fiji)**	**Bottom Time (min)**	**Maximum Depth (m)**	**Average Depth (m)**
1	1	Three Sisters, Somosomo Strait	49	13.4	7.9
2	1	Three Sisters, Somosomo Strait	48	15.2	10.7
3	2	Nuku's Reef, Somosomo Strait (Rainbow Reef)	55	14.6	7.3
4	2	Fish Factory, Somosomo Strait (Rainbow Reef)	47	14.9	6.7
5	3	Nuku's Reef, Somosomo Strait (Rainbow Reef)	60	11.0	8.5
6	3	Cabbage Patch, Somosomo Strait (Rainbow Reef)	49	14.3	7.6
			Total: 308	Maximum: 15.2	Average: 8.1

Table 4.2: Dive summaries: Six dives were performed over the course of 3 days, exploring various coral reef environments in Fiji. The depths and times presented were recorded for one of the divers participating in the experiments; while the trajectory of the diver and of SoFi were not the same, the diver was typically within several meters of SoFi and can therefore indicate the type of conditions that SoFi experienced. The experimenters were typically at slightly shallower depths than SoFi.

	No Thrust	Thrust 1	Thrust 2	Thrust 3	TOTAL
Yaw Left	13	2	28	115	158
Straight	1893	195	805	1166	4059
Yaw Right	81	3	81	57	221
TOTAL	1987	201	914	1338	**4439**

Table 4.3: Tail strokes: Summarizing the number of executed tail strokes during an average dive in the open ocean. We estimated the number of tail strokes at various combinations of thrust and yaw using the logs of the executed states of the robotic fish. Note that tail strokes for no thrust are equivalent to the time spent at that state without undulation of the tail.

4.14 Contributions of the Biomimetic Swimming Application

We show the integration of a soft fluidic actuator into an end-to-end system that locomotes underwater in a biomimetic manner, is remote controlled, and can serve as an underwater observatory for the study of marine life. We present a biomimetic soft robotic fish that is able to swim along 3D trajectories with autonomous buoyancy control to observe the biocenosis of coral reefs in the ocean. The soft robotic fish prototype is capable of:

- 3D-controllable motion for prolonged operation underwater;
- autonomous depth control via dive planes and a miniaturized piston-based buoyancy control unit;
- underwater remote control via a miniaturized end-to-end acoustic communication system;
- performing at depths of 0 to 18 m, as evidenced by ocean experiments.

Chapter 5

Model-Free Quasi-Static Feedback Control

5.1 Overview

In this chapter, we provide an approach to model-free closed-loop control for multi-segment manipulator arms made of fluid elastomer actuators, designed and fabricated with the techniques described in Chapter 3. This quasi-static control approach combined with planning algorithms enables free-space motion, grasp-and-place [Katzschmann et al., 2015], and planned continuous motions in confined environments [Marchese et al., 2014a]. The method of closed-loop configuration control for a soft fluidic elastomer robot consists of (i) a kinematic model and an algorithm for estimating the manipulator's configuration in real-time, (ii) a device for providing continuous, closed-circuit adjustment of the manipulator's fluid, and (iii) a cascaded curvature controller. Task-space planning algorithms solve the inverse kinematics (IK) problem and enable these manipulators to autonomously (i) position their end-effector in free-space, (ii) maneuver in confined environments, and (iii) grasp and place objects. The work on the quasi-static control in confined environments was developed in collaboration between Marchese and Katzschmann [Marchese et al., 2014a]. This work is now documented in Marchese [2015] and the thesis here at hand.

5.2 Kinematic Modeling

In this section, we describe a kinematic model of the soft actuators described in Section 3.2, used for the manipulator arms described in Section 3.6.4 and Section 3.6.5. Specifically, we first discuss the application of a piecewise constant curvature modeling assumption [Webster and Jones, 2010] to describe these soft multi-segment arms. Next, we provide a procedure for measuring a configuration-space representation of each segment by means of external localization data. Then, we describe how these measurements can be used to compute the multi-segment manipulator's task-space representation by means of a recursive, integral-based forward kinematics algorithm. Lastly, we provide a method for solving the inverse kinematics problem for this manipulator type, that is a nonlinear optimization-based approach. We provide a summary and extension of the work described in Marchese et al. [2014b].

5.2.1 Piecewise Constant Curvature

Based on the observed deformation characteristics of fluidic elastomer actuators discussed in Section 3.2, we approximate the bending of an arm segment i with a constant curvature (CC) model, expressed by the signed curvature κ_i, and the arc length L_i. The degree of curvature is $q_i = \kappa_i L_i$. For a planar soft arm segment i modeled with CC, the kinematic transformation from the base frame $i-1$ to the tip frame i is

$$T_{i-1}^{i} = \mathrm{R}_z\left(\frac{q_i}{2}\right) \mathrm{P}_y\left(\frac{2\,L_i}{q_i}\sin\left(\frac{q_i}{2}\right)\right) \mathrm{R}_z\left(\frac{q_i}{2}\right), \tag{5.1}$$

where R and P represent coordinate rotations and translations about or along the subscript axes. Note that the base is also the tip of the previous segment $i-1$. This representation is consistent with the literature on continuum manipulation [Webster and Jones, 2010, Marchese et al., 2014b]. The assumption of piecewise constant curvature (PCC) for a planar soft manipulator is defined by cascading the transformations of n single segments together

$$T_0^n = T_0^1\left(q_1\right) \ldots T_{i-1}^{i}\left(q_i\right) \ldots T_{n-1}^{n}\left(q_n\right). \tag{5.2}$$

To account for the orientation of the base described by ϑ, (5.2) is pre-multiplied with a rotation by

$$T^n_{\text{base}} = \mathrm{R}_z(\vartheta) T^n_0. \tag{5.3}$$

5.2.2 Single-Segment Inverse Kinematics

Algorithm 5.1 Single segment inverse kinematics (refer to Figure 5-1). The algorithm is adapted from Marchese et al. [2014b].

procedure SINGLESEGINVKIN(A, B, θ_{i-1})
    Starting tangent vector u_{base} is defined by base orientation θ_{i-1}
    Construct a line aa, orthogonal to the starting tangent vector u_{base} and passing through A.
    Construct a perpendicular bisector pp to the line segment $\overline{\text{AB}}$.
    The intersection of aa and pp forms the center point O of a constant radius arc that connects A and B. The line segment $\overline{\text{AO}}$ is the radius ρ of this arc.
    The curvature is $\kappa_i \leftarrow \frac{1}{\rho}$.
    The degree of curvature is $q_i \leftarrow \angle\text{AOB}$.
    The length of the arc is $L_i \leftarrow \frac{q_i}{\kappa_i}$.
    return κ_i and L_i
end procedure

We control the pose of an arbitrary point along a soft segment i by computing the arm's configuration state κ_i and L_i from the measured base position A, measured base orientation θ_{i-1}, and measured tip position B. This inverse kinematics problem for a single segment has been previously addressed by Hannan and Walker [2003], Jones and Walker [2006a] and Marchese et al. [2014b]. Algorithm 5.1 together with Figure 5-1 summarize the inverse kinematics procedure that independently outputs curvatures and lengths for each segment.

5.2.3 Forward Kinematics

The forward kinematics of a serially connected soft arm with n segments was originally developed by Onal and Rus [2013] and Marchese et al. [2014b]. This algorithm is used for the multi-segment inverse kinematics in Section 5.2.4 and the task-space planners in Section 5.4. The orientation at any point $s \in [0, L_i]$ along the arc of the

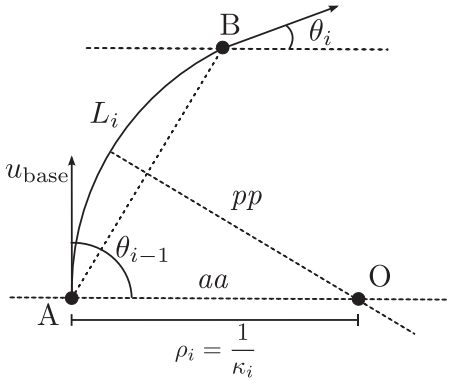

Figure 5-1: Visualization of Algorithm 5.1 used to determine the configuration of a soft arm segment at a given point in time from end point data. The i-th segment's base point (A) and tip point (B) are measured and the initial orientation, θ_{i-1}, of the segment is provided. The i-th segment's curvature κ_i and length L_i are determined. We assume the deformation of each segment at a point in time can be adequately represented by a signed curvature value κ_i (or alternatively by the degree of curvature q_i). The figure is adapted from Marchese et al. [2014b].

i-th segment is expressed by

$$\theta_i(s) = \kappa_i \, s + \theta_i(0) \, . \tag{5.4}$$

All segments are serially and continuously connected, therefore we assume $\theta_i(0)$ $= \theta_{i-1}(L_{i-1})$. The procedure FORWARDKIN() in Algorithm 5.2 uniquely identifies the state of the entire arm by starting at the grounded base segment ($i = 1$) with *a priori* known orientation ϑ and determining the state of each consecutive segment. The position of any point along the arm can be expressed by

$$\mathrm{x}_i(s) = \mathrm{x}_{i-1}(L_{i-1}) + \int_0^s \cos\left[\theta_i(s')\right] \, \mathrm{d}s' \tag{5.5}$$

$$\mathrm{y}_i(s) = \mathrm{y}_{i-1}(L_{i-1}) + \int_0^s \sin\left[\theta_i(s')\right] \, \mathrm{d}s' \tag{5.6}$$

$\forall \, i = 1 \, .. \, n$ [Marchese et al., 2014b]. We will refer to the manipulator's end effector by $w = [\mathrm{x}_n(L_n), \, \mathrm{y}_n(L_n), \, \theta_n(L_n)]$. Algorithm 5.2 recursively determines a point on the arm located at s on segment i, given curvature and length are provided [Marchese et al., 2014b].

Algorithm 5.2 Forward kinematics [Onal and Rus, 2013, Marchese et al., 2014b]

Input:

The inputs κ and L represent the current manipulator configuration determined by running first the Single Segment IK in Algorithm 5.1 $\forall\, i = 1\,..\,n$. The input i is the index of the segment of interest and s is the arc length along the indexed segment.

1: **procedure** FORWARDKIN(κ, L, i, s) ▷ i: segment of interest, s: arc length along segment
2: **if** $i = 1$ **then**
3: $\theta_i(0) \leftarrow \vartheta$. $\Leftarrow$ known *a priori*
4: $\mathrm{x}_i(0) \leftarrow 0$.
5: $\mathrm{y}_i(0) \leftarrow 0$.
6: **else**
7: $[\mathrm{x}_i(0),\, \mathrm{y}_i(0),\, \theta_i(0)] \leftarrow$ FORWARDKIN(κ, L, $i-1$, L_{i-1}).
8: **end if**
9: $\theta \leftarrow \theta_i(0) + \kappa_i s$.
10: $\mathrm{x} \leftarrow \mathrm{x}_i(0) + \frac{\sin\theta}{\kappa_i} - \frac{\sin\theta_i(0)}{\kappa_i}$.
11: $\mathrm{y} \leftarrow \mathrm{y}_i(0) - \frac{\cos\theta}{\kappa_i} + \frac{\cos\theta_i(0)}{\kappa_i}$.
12: **return** $[\mathrm{x},\, \mathrm{y},\, \theta]^{\mathrm{T}}$ or $[\mathrm{x},\, \mathrm{y}]^{\mathrm{T}}$
13: **end procedure**

5.2.4 Multi-Segment Inverse Kinematics

Besides the procedures SINGLESEGINVKIN() (Algorithm 5.1) and FORWARDKIN() (Algorithm 5.2), a critical component to multi-segment manipulation is the arm's inverse kinematics procedure. Given the pose of a point or points along the arm's backbone, this procedure returns the manipulator's arc-space configuration. In the following, we describe a nonlinear optimization-based approach to the inverse kinematics (IK) problem that allows easy encoding of primary task-space and secondary arc-space manipulation objectives in the form of nonlinear constraints and cost functions. The optimization-based approach is used in Section 5.4.1 for the motion of a soft arm through a confined environment [Marchese et al., 2014a], and in Section 5.4.2 for a grasp-and-place task of a soft manipulator arm [Katzschmann et al., 2015].

5.2.4.1 Optimization-based Approach

We can pose the IK problem as a constrained nonlinear optimization. That is, we can find an optimal manipulator configuration κ^* in such a way that a point or point(s)

Algorithm 5.3 Optimization-based inverse kinematics. The algorithm is adapted from Katzschmann et al. [2015].

procedure INVERSEKINOPT(κ, L, w_d, i, s)

  $\varpi \in \mathbb{R}^n$ is a weighting vector.

  $\kappa^* \leftarrow \min_{\kappa} \quad \sum_{i=1}^{n} \varpi_i \, \kappa_i^2.$

  subject to $\quad \mathbf{f} \leftarrow \text{FORWARDKIN}(\kappa, L, i, s).$

$$\begin{bmatrix} x \\ y \\ \theta \end{bmatrix} - \begin{bmatrix} f_1 \\ f_2 \\ f_3 \end{bmatrix} = 0. \Leftarrow \text{linear kinematic constraint}$$

$$h(\kappa) = 0. \quad \Leftarrow \text{nonlinear constraints}$$

$$\kappa_i^{\min} \leq \kappa_i \leq \kappa_i^{\max} \quad \forall \, i = 1 \,..\, n.$$

  return κ^*

end procedure

along the arm have a desired pose while simultaneously minimizing an objective function and considering other nonlinear constraints in the form $h(\kappa) = 0$. This IK approach is suited for soft continuum manipulation where there is typically a primary manipulation task, for example end-effector positioning, as well as a secondary task, for example avoiding collisions, or minimizing material strain.

Algorithm 5.3 details an instantiation of this approach, where the objective is to find a minimal-strain configuration that simultaneously satisfies a pose constraint imposed on a point along the centerline of the arm, and that is within allowable curvature limits.

5.3 Control System

This section provides the design of a control system used to govern the manipulator's position and orientation in real-time. That is, we build on the power system developed in Section 3.4, the closed-circuit fluid control in Section 3.5, and the kinematic algorithms developed in Section 5.2 to develop a controller for the soft manipulator. In subsequent sections, this controller in combination with task-space planning algorithms is used to provide autonomous capabilities for the developed soft machines.

5.3.1 Main Controller

The main controller determines in real-time the curvature adjustments required to move the end-effector or points along the arm through their requested pose trajectory. A state flow diagram describing at a high-level the main controller's sensing, task planning, and execution states is given in Figure 5-2.

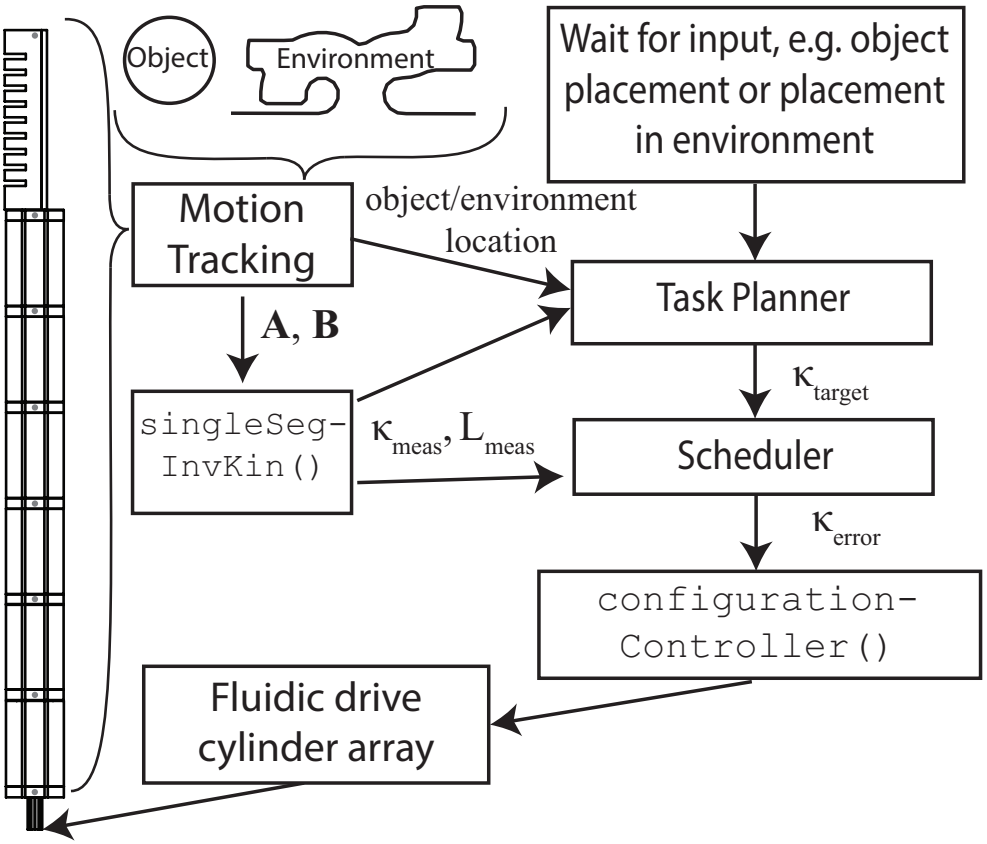

Figure 5-2: State flow diagram of the main controller, describing the flow and processing of information from the motion tracking system to the actuators. The figure is reproduced from Katzschmann et al. [2015].

A task for the soft manipulator could be, for example, free space motion, whole arm planning, or grasping and placing of an object, see also Section 5.4. While the task planner waits for an input that triggers it, the localization system is constantly capturing segment endpoint locations along the soft manipulator, any objects in the workspace, and the environment boundaries at a constant rate. Our experimental implementation uses an external motion capture system to provide this positional data. The localization system recursively calls the SINGLESEGINVKIN() procedure using the

manipulator's segment endpoint locations as input (see Section 5.2.2). The procedure outputs curvatures κ_{meas} and lengths L_{meas} at an update rate of 20 Hz. After the task planner has been triggered, it uses the current location of any objects in the workspace and the environment together with the current curvature values of the manipulator to solve the task at hand. The task planner then passes the target configuration κ_{target} of the manipulator to the scheduler for execution in real-time.

The scheduler has access to a trajectory generation procedure TRAJGEN(), needed for some of the possible tasks. It generates in real-time for each individual degree of freedom velocity profiles with acceleration and velocity constraints. These profiles allow real-time interpolation between the intermediate target configurations of the manipulator and avoid overshoot at the next target configuration. The scheduler also constantly receives the manipulator's measured configuration representation κ_{meas}, L_{meas} from SINGSEGINVKIN() and uses this information in combination with intermediate target configurations determined by TRAJGEN() to determine the curvature error κ_{error} at a given point in time.

The CONFIGURATIONCONTROLLER(), described in Section 5.3.2, receives κ_{error} as an input and accordingly controls the pneumatic cylinder array to achieve the intermediate target configuration.

5.3.2 Configuration Controller

In order to control in real-time the manipulator's configuration, a closed-loop control algorithm CONFIGURATIONCONTROLLER() was adapted from the original implementation by Marchese et al. [2014b]. A block diagram representation of this controller is shown in Figure 5-3. An instance of this controller is instantiated for each segment of the manipulator. This algorithm periodically receives discrepancies κ_{error} between the soft arm's measured and reference curvatures and uses a cascaded control structure to effectively adjust the reference volumetric displacement of the pneumatic cylinders to resolve the manipulator's configuration errors. The controller achieves this by running a proportional-integral (PI) computation on the curvature error in order to generate a set-point for the positional control of the drive cylinder's linear actuator. The outer

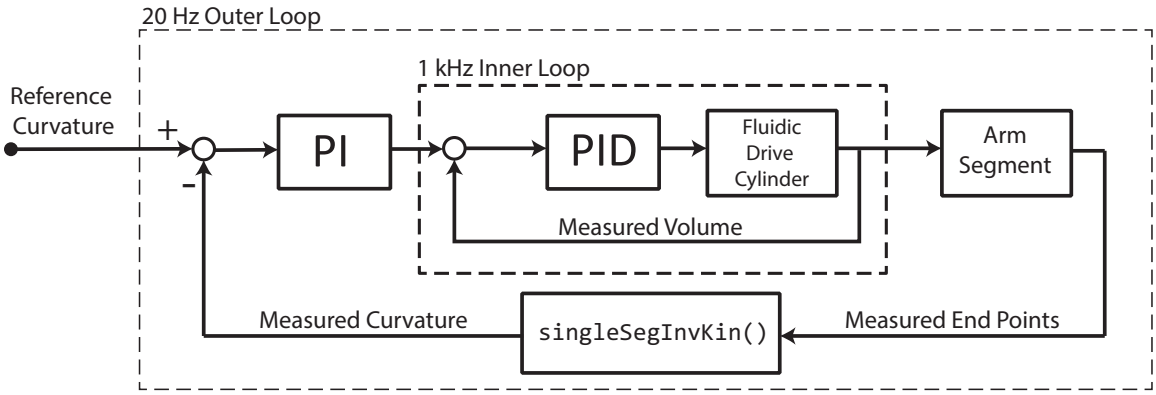

Figure 5-3: Block diagram of the manipulator's configuration controller: A cascaded curvature-volume control structure is used to achieve closed-loop configuration control. The inner volume control loop runs at approximately 1 kHz, which is substantially faster than the outer curvature control loop, which runs at approximately 20 Hz. The figure is adapted from Marchese et al. [2014b].

curvature control loop is triggered by the availability of sensor measurements from the external localization system and runs at approximately 20 Hz. The inner positional control loop runs at 1 kHz and ensures that the cylinder's piston displacement matches the reference displacement determined by the outer control loop. The cylinder's piston displacement is the primary manipulated variable as input fluid volume is monotonically related to the curvature of a manipulator segment (see Section 3.2).

The capability of an individual segment to track a curvature profile varying over time is a fundamental requirement for any free-space motion and more advanced manipulation tasks described in Section 5.4. Marchese et al. [2014b] tested and validated the tracking capabilities of individual fluidic elastomer segments using PID controllers for quasi-static, that is slow, motions. The tuning of the controller was done using the Ziegler-Nichols method [Åström and Hägglund, 2004].

5.4 Task-Space Planning and Control

This section details several task-space planning algorithms for soft fluidic elastomer manipulators. These planners enable quasi-static control in Cartesian space. We discuss maneuvering in a confined pipe-like environment, and grasping and placing of objects.

5.4.1 Whole Arm Planning

We develop a task-space planner to autonomously advance the soft planar multi-segment manipulator through a confined environment. The task-space of the arm consists of the position and orientation of a point $w = [\mathrm{x},\ \mathrm{y},\ \theta]$ or points along the arm (see Section 5.2.3). The goal of this algorithm is to find locally optimal manipulator configurations (curvatures κ) that (1) position the end-effector to points along a path through the confined environment and (2) consider the proximity of the points on the robot's envelope $\mathbf{h} \in \mathbb{H} \subseteq \mathbb{R}^2$ in relation to points on the surrounding environment $\mathbf{e} \in \mathbb{E} \subseteq \mathbb{R}^2$. The envelope $\mathbb{H}$ is modeled by trapezoids linearly scaled according to the measured curvature values. The environment $\mathbb{E}$ is represented as a set of boundary points and is known *a priori*. We assume that initially the arm is always placed in a free space outside the bounded environment we want to enter. Also, a series of task-space waypoints w_t, $\forall\, t = 1\,..\,t_\mathrm{f}$, is predefined by the user, where the first waypoint is placed at the inlet to the environment. All following waypoints describe a path that would lead to a final goal position inside the environment.

The optimization-based whole-arm configuration planning is outlined in Algorithm 5.4, visually supported by Figure 5-4, and explained in further detail in the following.

At the start time $t = 1$, we set the arm segments to a locally optimal κ that places the manipulator's end-effector at the first waypoint w_1 according to the forward kinematics procedure FORWARDKIN() (see Algorithm 5.2). The solution also ensures that each segment does not exceed its curvature limits κ^{min} and κ^{max}. The extreme curvatures are experimentally determined to be either the maximum curvatures achievable given the fixed volumetric displacements of the pneumatic cylinders or the maximum curvatures which would not yet damage the segments due to overinflation, whichever of the two is lower. After the start, we enter a loop until the last waypoint at time step t_f is reached. At the start of the loop, we find the closest environment points left $\mathbf{e}_{1,t}$ and right $\mathbf{e}_{2,t}$ of the arm's body shape. To define the two sides of the arm, we use the arm's approach vector $\mathbf{n}_t$ and the angle $\alpha = \angle(\mathbf{e} - w_t, \mathbf{n}_t)$. The origin

Algorithm 5.4 Whole arm planner outline. The algorithm is adapted from Marchese et al. [2014a].

Input:

$\mathbb{E} \subseteq \mathbb{R}^2 \leftarrow$ environment

$w_t, \quad \forall\, t = 1 \,..\, t_\mathrm{f} \leftarrow$ path waypoints

1: $t \leftarrow 1$ ▷ set first time step to 1

2: $\kappa_\mathrm{meas}, L_\mathrm{meas} \leftarrow$ SINGLESEGINVKIN( )

3: $\kappa_t \leftarrow$ INVERSEKINOPT(κ_meas, L_meas, w_t, n, L_n)

4: **while** $t \leq t_\mathrm{f}$ **do** ▷ loop until last waypoint index t_f is reached

5: $\mathbb{E}_1 \leftarrow \mathbb{E} \mid \sin(\alpha) > 0$ ▷ environment to the left of the arm hull

6: $\mathbf{e}_{1,t} \leftarrow \underset{\mathbf{e} \in \mathbb{E}_1}{\operatorname{argmin}} \{\|\mathbf{e} - w_t\|\}$

7: $\mathbb{E}_2 \leftarrow \mathbb{E} \setminus \mathbb{E}_1$ ▷ environment to the right of the arm hull

8: $\mathbf{e}_{2,t} \leftarrow \underset{\mathbf{e} \in \mathbb{E}_2}{\operatorname{argmin}} \{\|\mathbf{e} - w_t\|\}$

9: $(\mathbb{H}_1, \mathbb{H}_2) \leftarrow$ ARMHULL($\kappa_t, L_\mathrm{meas}$) ▷ left and right hull points

10: **for** $j = 1 \ldots t$ **do** ▷ for all times until t

11: **for** $i = 1 \ldots 2$ **do** ▷ for left and right

12: $\mathbf{h}_{i,j} \leftarrow \underset{\mathbf{h} \in \mathbb{H}_k}{\operatorname{argmin}} \{\|\mathbf{e}_{i,j} - \mathbf{h}\|\}$ ▷ closest hull points

13: $\mathbf{b}_{i,j} \leftarrow \mathbf{e}_{i,j} - \mathbf{h}_{i,j}$ ▷ vector betw. hull and environment

14: $\mathbf{a}_{i,j} \leftarrow$ ENVNORMAL($\mathbf{e}_{i,j}$) ▷ normal to wall

15: **end for**

16: **end for**

17: $\kappa_t \leftarrow \max_{\kappa} \left\{ \sum_{j=1}^{t} \sum_{i=1}^{2} \|\boldsymbol{b}_{i,j}\| \ln\left(\boldsymbol{a}_{i,j} \cdot \boldsymbol{b}_{i,j} + 1\right) \right\}.$

subject to $\mathbf{f} \leftarrow$ FORWARDKIN(κ, L, N, L_n).

$w_t - \mathbf{f} = \mathbf{0}.$

$h(\kappa) = \mathbf{0}.$

$\kappa_n^{\min} \leq \kappa_i \leq \kappa_n^{\max} \quad \forall\, n = 1 \,..\, n.$

18: $t \leftarrow t + 1$

19: **end while**

of the end-effector's approach vector $\mathbf{n}_t$ is defined by the positions x and y and its direction by the angle θ. Positive values for α result in the closest point $\mathbf{e}_{1,t}$ left of w_t and negative values result in $\mathbf{e}_{2,t}$ to the right of w_t. Next, we calculate the arm hulls ARMHULL($\kappa_t, L_\mathrm{meas}$) of both sides by modeling each segment's expanded side with a trapezoid that is linearly scaled in height by the segment's curvature value. The concave side is not vacuumed during the actuation process, so the hull is described by a constant offset from the curved body centerline. For every stored environment

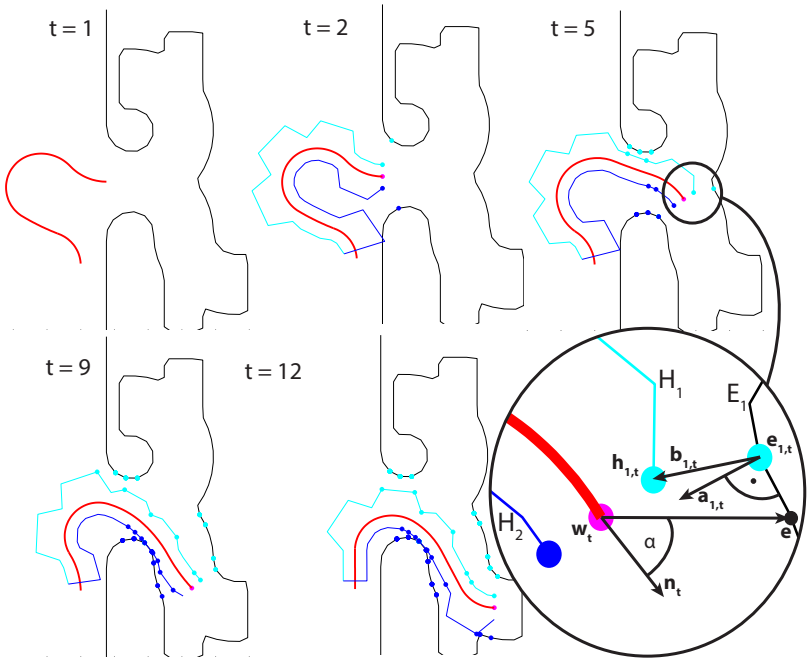

Figure 5-4: Whole arm planner: The soft robot is depicted for several time steps t by a *red* body center line, a *cyan* line for the left body shape and a *blue* line for the right body shape. The *black* line depicts the bounded environment. The *purple* dot at the end of the *red* center line represents the end-effector of the manipulator. At every time step t, the end-effector reaches the planned waypoint by using the controller developed in Section 5.3.1. At timestep $t = t_f = 12$, the last point inside the bounded environment is reached. A close-up view shows the vectors relevant for the whole body planner described in Section 5.4.1 and Algorithm 5.4. The figure is reproduced from [Marchese et al., 2014a].

point $\mathbf{e}_{i,j}$, $\forall\, i = 1 \ldots 2$ and $\forall\, j = 1 \ldots t$, we find the closest hull points, calculate their connection vector, and calculate the normals of the environment $\textsc{envNormal}(\mathbf{e}_{i,j})$. We then perform an optimization to find the curvatures that best fit the hull into the environment with the constraint that the end-effector pose must match the current target waypoint. Finally, the time step is incremented and the loop repeats until the last waypoint is reached.

The optimization algorithm was implemented using Matlab's Optimization Toolbox with the function call *fmincon*, which finds the minimum of a constrained nonlinear multivariable function. Sequential Quadratic Programming was used as the solver with a relative upper bound of 2×10^{-3} on the magnitude of the constraint functions. The maximal function evaluations were bounded by 2000 and the lower bound on

the size of a step was given by 1×10^{-6}. The function *dsearch* was used to find the minimal distant points on the environment and on the hull.

5.4.2 Grasp-and-Place

The robotic manipulation system is supposed to be capable of autonomously performing grasp-and-place operations by encapsulation with uncertainty in position and shape of the object. A planning system is designed around the idea of using the compliance and continuous bending of the soft grasping manipulator to repeatable grasp in the presence of uncertainty. Our approach is to first pre-plan motion waypoints for the soft robot and then control the manipulator along those points.

The problem we are solving is the following. An object of feasible size but unknown geometry is randomly placed within the reachable envelope of the manipulator. The soft manipulation system is supposed to grasp the randomly positioned object within its reachable envelope and move it to a desired location without human intervention.

We build on the path planning algorithm presented in Section 5.4.1. There, we plan the motion of the soft arm without a gripper through a maze at a centerline while taking the arms bulging shape into account. The approach does not work for approaching and grasping of objects, since a tip trajectory for successfully moving towards the object is not known, but needs to be generated by posing and solving a new optimization problem. The manipulator trunk should not push the object away when approaching it.

A state flow diagram describing the grasp-and-place task-space planner is shown in Figure 5-5. As mentioned in Section 5.3.1, a motion tracker constantly captures the position of the object and passes it along to a routine, which checks for the object to settle. After it has settled, the grasp object planner receives the coordinates and radius of the settled object and together with the current curvature values of the arm and gripper, it solves a series of constrained nonlinear optimization problems to generate end-effector poses approaching the object. This is described in more detail in Section 5.4.2.1.

The grasp object planner passes the locally-optimal approach configurations κ_i^*

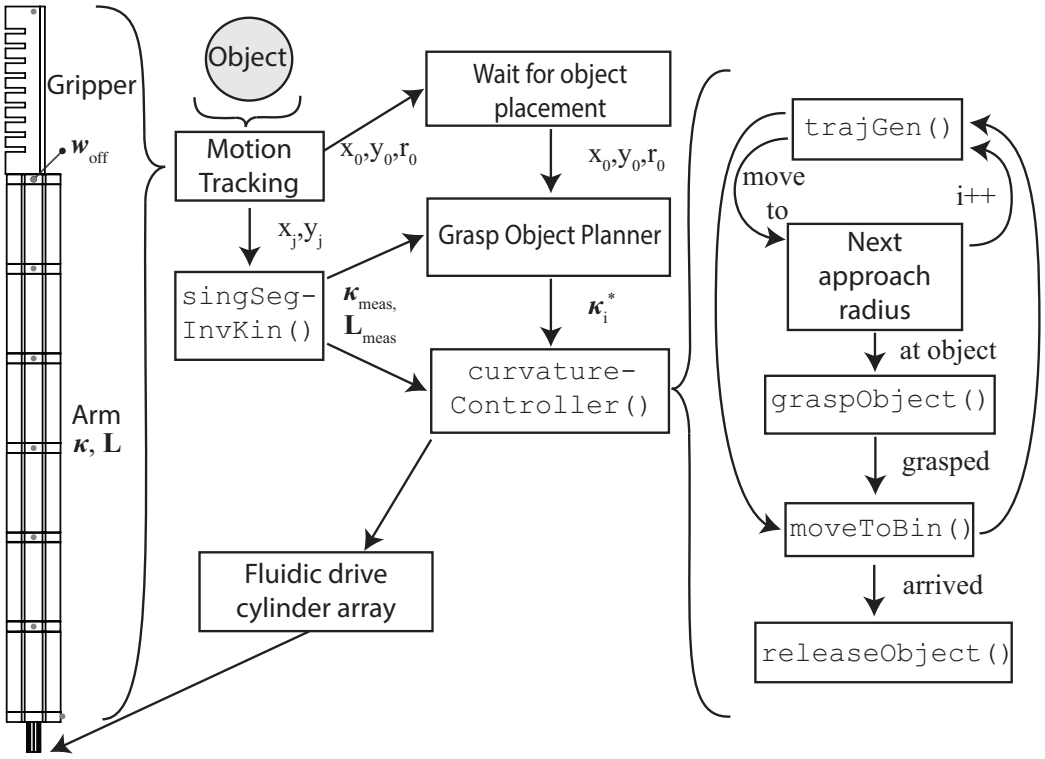

Figure 5-5: State flow diagram of the grasp-and-place planner developed for the autonomous grasp-and-place operation of the manipulator. This diagram describes the flow of information from the motion tracking system to the discrete hardware. The figure is reproduced from Katzschmann et al. [2015].

to the scheduler as κ_{target} for execution in real-time (see Section 5.3.1). To allow for smoother transitions between each approach configuration, the scheduler uses the trajectory generation procedure TRAJGEN() described in Section 5.3.1 to generate velocity profiles with acceleration and velocity constraints for each independent DOF. These velocity profiles allow the scheduler to calculate intermediate manipulator configurations between the given approach configurations by performing a time-based integration. These reference configurations are used to determine κ_{error}, which is sent to the configuration controller. When the arm has arrived at the object, the planner initiates GRASPOBJECT(). After encapsulating the object, MOVETOBIN() is initiated, which also uses TRAJGEN() to generate a trajectory from the current pose to a pre-defined bin location. When the manipulator gets close to the bin location, the procedure RELEASEOBJECT() causes the gripper to open and release the object.

5.4.2.1 Grasp Planner

A fundamental component of the grasp-and-place task planner is the system's ability to plan a feasible approach to the object. That is, given the location (x_o, y_o) and radius r_o of a round object as well as the manipulator's current configuration κ_{meas}, we determine a series of locally optimal manipulator configurations κ_i^*, $\forall i = 1 \ldots numMoves$, that will, if sequentially achieved, bring the manipulator gradually closer to the object while not touching it. We refer to these as approach configurations. The process for determining these approach configurations is detailed in the PLANGRASPAPPROACH() procedure (see Algorithm 5.5).

The planner is visualized in Figure 5-6.

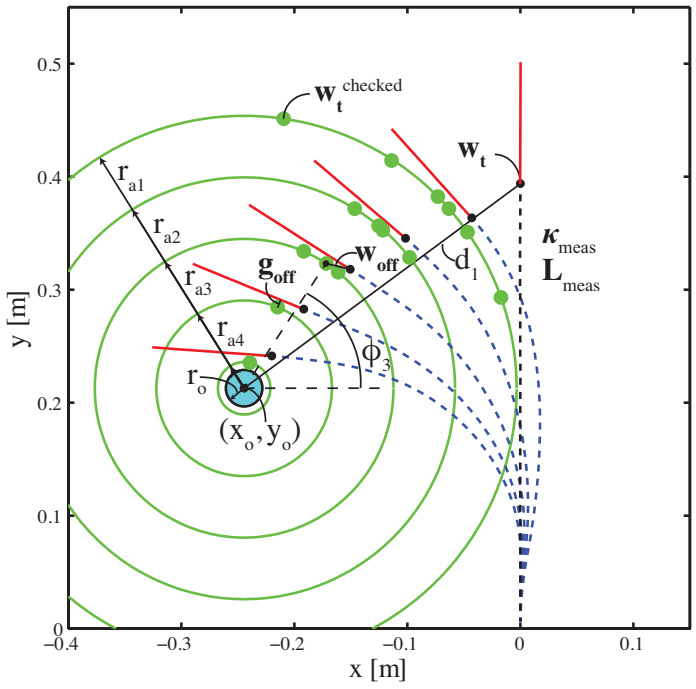

Figure 5-6: Grasp approach planner visualization: Concentric approach circles are shown in *green* and are centered about the object shown in *cyan*. The locally optimal approach configurations are shown in *blue* and the gripper is shown in *red*. The initially measured manipulator configuration is shown in black. The figure is reproduced from Katzschmann et al. [2015].

In short, we define a series of approach radii r_{a_i}, $\forall i = 1 \ldots numMoves$, that define concentric circles shrinking from the manipulator's starting tip pose towards the center of the object. Given actuator limits, we then search for a series of feasible

Algorithm 5.5 Plan grasp. The algorithm is adapted from Katzschmann et al. [2015].

Input:

κ_{meas}, $L_{\text{meas}} \leftarrow$ measured arm configuration
$\kappa_{\text{off}} \leftarrow$ measured manipulator configuration offset at start
$g_{\text{off}} \leftarrow$ gripper offset normal to end-effector
x_o, y_o, $r_o \leftarrow$ object center coordinates and radius
$n \leftarrow$ number of manipulator segments

1: **procedure** PLANGRASPAPPROACH( )
2: $w_t \leftarrow$ FORWARDKIN(κ_{meas}, L_{meas}, N, L_n).
3: $d_1 \leftarrow \|[\mathrm{x}_o,\, \mathrm{y}_o]^{\mathrm{T}} - w_t\|$.
4: $d_2 \leftarrow d_1 - r_o - g_{\text{off}}$.
5: $numMoves \leftarrow \lfloor \frac{d_2}{\Delta d} \rfloor$.
6: $i = 0$.
7: **repeat**
8: $i = i + 1$.
9: $r_{a_i} \leftarrow d_1 - i\,\frac{d_2}{numMoves}$.
10: $\kappa_i^* \leftarrow$ FINDOPTIMALCONFIG(r_{a_i}).
11: **until** $i = numMoves$
12: **return** $\kappa_i^* \quad \forall i = 1..numMoves$
13: **end procedure**
14: **procedure** FINDOPTIMALCONFIG(r_{a_i})

$$\kappa^* \leftarrow \min_{\phi,\,\kappa} \ \varpi\,(\kappa - \kappa_{\text{off}})^2\,.$$

subject to
$$w_t \leftarrow \begin{bmatrix} \mathrm{x}_o + r_{a_i}\cos\phi \\ \mathrm{y}_o + r_{a_i}\sin\phi \\ \phi + \frac{\pi}{2} \end{bmatrix}.$$

15:
$$\mathbf{f} \leftarrow \text{FORWARDKIN}(\kappa,\, L,\, N,\, L_n).$$
$$w_t - w_{\text{off}}\,(r_o,\, \phi) - \mathbf{f} = \mathbf{0}.$$
$$\kappa_n^{\min} \le \kappa_i \le \kappa_n^{\max} \quad \forall\, n = 1\,..\,n.$$

16: **return** κ^*
17: **end procedure**

manipulator configurations κ_i^* that will place the robot's end-effector on approach circles, parameterized by r_a and ϕ, while minimizing manipulator deformation. Minimized manipulator deformation is chosen as the optimization criterion, because it is proportional to the energy consumed by the pneumatic cylinders and it also minimizes the strain to the soft actuators.

The procedure PLANGRASPAPPROACH() in Algorithm 5.5 first determines the manipulator's current tip pose w_t and the Euclidean distance d_1 between the tip and the object's center. The arc length input to the arm's forward kinematics is the

n-th element of the segment lengths L_{meas}. The end effector offset w_{off} describes the distance from the root of the gripper to an offset point close to the lower end of the gripper's palm. It is visualized in the top left corner of Figure 5-5. The minimal tip transit distance d_2 is calculated by considering the object's radius r_o and the gripper's normal offset $\mathbf{g}_{\text{off}}$. The symbol $\mathbf{g}_{\text{off}}$ represents the component of the end effector offset w_{off}, which is normal to end-effector orientation.

Also, the number of approach configurations $numMoves$ is determined as $\lfloor \frac{d_2}{\Delta d} \rfloor$, where Δd is an allowable incremental distance. Using these parameters, approach radii r_a, shown by the green circles, are iteratively calculated and their corresponding locally optimal configurations are found by using the optimization equation and constraints described in procedure FINDOPTIMALCONFIG(r_{a_i}) of Algorithm 5.5. The procedure FINDOPTIMALCONFIG(r_a) is posed as a nonlinear optimization problem. Here, the objective function represents the summation of independently weighted manipulator curvatures $\kappa - \kappa_{\text{off}}$. The weights are set by the matrix ϖ. The variables to optimize for are ϕ and κ. The optimization constraints cause the manipulator's tip to lie on and to be tangent to the approach circle. The constraints also ensure that the manipulator segment curvatures do not exceed the individual soft actuator limits. This process leverages the arm's forward kinematics FORWARDKIN(), or Algorithm 5.2, defined in Section 5.2.3. The optimization becomes over-constrained only if it has to find an arm pose outside of the arm's reachable workspace. That occurs if the object was user-placed outside the workspace. Before performing the optimization, a feasibility check is performed using the arm's forward kinematics.

Chapter 6

Model-Based Dynamic Feedback Control

In this chapter, we describe dynamic model-based feedback controllers for multi-segment soft fluidic manipulator arms. These models and controllers expand on the models and controllers for quasi-static control introduced in Chapter 5.

Soft robots do not have any predictable way of positioning themselves, but this is typically a fundamental ingredient to manipulation with rigid robots. Current robots primarily rely on the concept of morphological control [Nakajima et al., 2014, Cheney et al., 2013] or feedforward control [Falkenhahn et al., 2015, Marchese et al., 2016]. The challenge in controlling the configuration of soft limbs is due to the inherent elasticity, the sensing of the limb's state, the compliance of its fluidic power system, and the interaction of an end-effector with the environment. Models accounting for these aspects, and controllers leveraging these models are needed. In particular, when dynamic manipulations of objects and interactions with the world are required, we use dynamic models to allow for precise model-based control. Without a model, we can not predict the behavior of a soft manipulator and realize reasonably precise motions. Model-based methods for controlling the deformation of fluidic elastomer robots have not been proposed yet, except for our initial work in Della Santina et al. [2018]. In this chapter, we substantially expand our previous work and in Section 7.2 we validate our control approach through simulations and experiments.

6.1 Overview

To the best of our knowledge, there has been no previous work by other researchers on the design and validation of dynamical feedback controllers for multi-segment soft robots. With the goal of making a step towards the proper exploitation of soft robotic potentials, we propose two feedback control architectures and a contact planning algorithm specifically designed for the dynamic control of soft robots (Section 6.3). The first controller aims to achieve dynamic trajectory tracking of curvatures in free space (Section 6.4). The second controller is an impedance controller (Section 6.5) that allows to control the position of the end-effector in free space and to move along a surface, while staying in contact with that surface. The surface tracing is enabled through the combination of the impedance controller with the contact planning algorithm (Section 6.6). Both controllers rely on an *augmented formulation* linking the soft robot to a classic rigid serial manipulator with a parallel elastic mechanism (Section 6.2). Prior tools developed for this classical type of robot model can be exploited under this formulation [Ott, 2008, Sciavicco and Siciliano, 2012]. This augmented formulation allows the development of a dynamic model that is used for both controllers. Within the sections on the controllers, we also assess the effectiveness of the controllers theoretically within the modeling hypotheses. The controllers are applicable to single bending actuators such as the fingers in Section 3.6.2, and to multi-segment arms such as the manipulators presented in Sections 3.6.4, 3.6.5, 3.6.6, 3.6.7, and 3.6.8.

6.2 Model Mapping Rigid to Soft

In this section, we propose a framework for modeling the dynamics of soft robots, linking it to an approximately equivalent rigid body constrained through a set of nonlinear integrable constraints. The key property of the model is to define an appropriate matching under the hypothesis of piecewise constant curvature [Webster and Jones, 2010], enabling the application of control strategies typically used in

rigid-bodied robots onto soft robots. We first introduce the kinematics including an augmented formulation. Leveraging the augmented formulation, we describe the dynamic model and its properties.

6.2.1 Kinematics

In the piecewise constant curvature (PCC) model, the infinite dimensionality of the soft robot configuration is resolved by considering the robot's shape as composed of a fixed number of segments with constant curvature (CC), merged in a way that the resulting curve is differentiable everywhere. This is a fairly good approximation of the actual shape of a soft robot with multiple segment that continuously bend in an arc-shaped manner. In the case of significant external forces applied somewhere along a soft segment, a temporary splitting of a segment into multiple CC segments is recommended to not violate the assumption. Similarly, in the case of a much longer than wide segment, such a segment has to be split into multiple CC segments for the purpose of properly approximating its impedance and dynamics.

Consider a PCC soft robot composed by n CC segments. We introduce n reference frames $\{S_1\}, \ldots, \{S_n\}$ attached at the end of each segment, plus one base frame $\{S_0\}$. Figure 6-1a presents an example of a soft robot composed of four CC segments. Using the constant curvature hypothesis, $\{S_{i-1}\}$ and $\{S_i\}$ fully define the configuration of the i-th segment. Thus, the robot kinematics can be defined by the n homogeneous transformations $T_0^1, \ldots, T_{n-1}^n$, which map each reference system to the subsequent one.

In the interest of conciseness, we consider the planar case. Please refer to Webster and Jones [2010] for more details about the PCC kinematics for the 3D case. Figure 6-2 shows the kinematics of a single CC segment. Under the hypothesis of non-extensibility, one variable is sufficient to describe the segment's configuration. We use the relative rotation between the two reference systems as the configuration variable or generalized coordinate. Let us call this variable q_i for the i-th segment, and $q \in \mathbb{R}^n$ the vector collecting q_i for all the n segments. Note that this angle is directly related to the radius of curvature ρ_i of the segment through the linear relation $q_i \, \rho_i = L_i$, where L_i

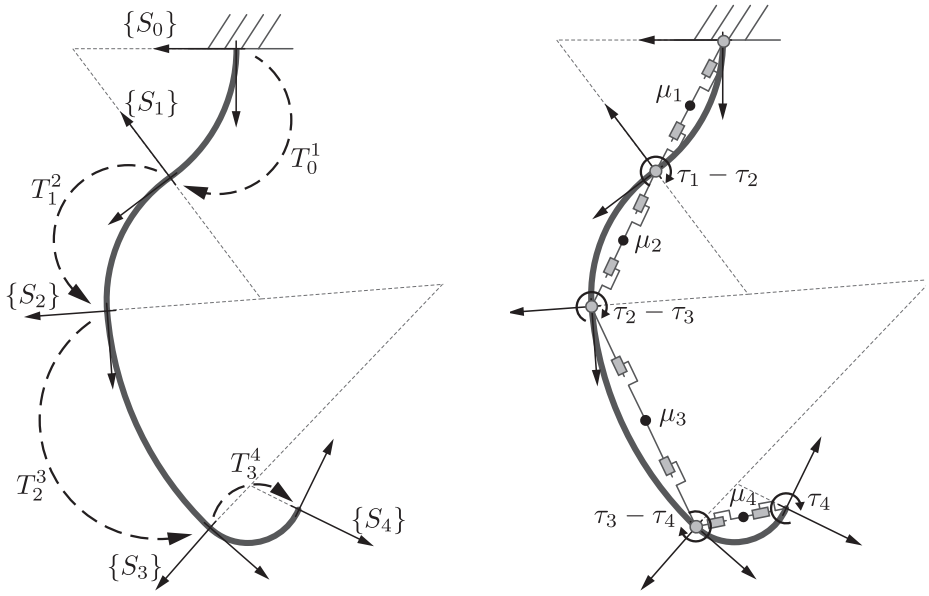

(a) Piecewise constant curvature representation of a soft robot.

(b) Augmented representation between a rigid and a soft robot.

Figure 6-1: Example of a soft robot represented by a piecewise constant curvature model, composed of four constant curvature elements. Panel (a) shows the robot's kinematics. $\{S_0\}$ is the robot's base frame. A reference frame $\{S_i\}$ is attached at the end of each segment. T_{i-1}^i is the homogeneous transformation mapping $\{S_{i-1}\}$ into $\{S_i\}$. Panel (b) presents an augmented representation of the soft robot through a model typically used for rigid robots. Each segment has mass μ_i and is actuated through a torque τ_i.

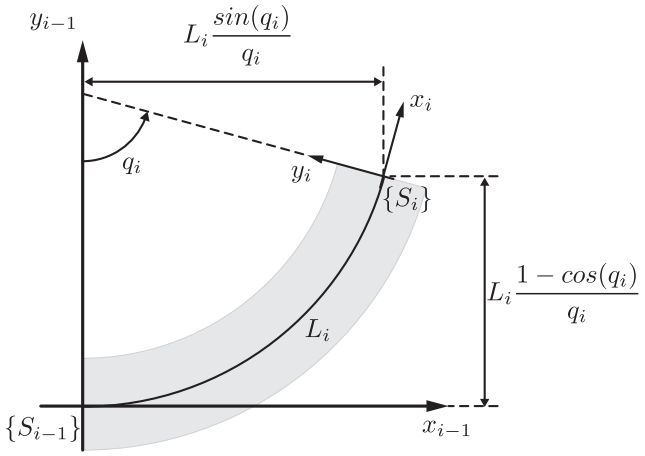

Figure 6-2: Kinematic representation of the i-th planar constant curvature segment. Two local frames are placed at the two ends of the segment, $\{S_{i-1}\}$ and $\{S_i\}$ respectively. The length of the segment is L_i, and q_i is the generalized coordinate, that is the degree of curvature.

is the constant length of a segment. We refer to q_i as the degree of curvature.

The i-th homogeneous transformation can be derived using geometrical considerations as

$$T^i_{i-1}(q_i) = \begin{bmatrix} \cos(q_i) & -\sin(q_i) & L_i \frac{\sin(q_i)}{q_i} \\ \sin(q_i) & \cos(q_i) & L_i \frac{1-\cos(q_i)}{q_i} \\ 0 & 0 & 1 \end{bmatrix} . \tag{6.1}$$

6.2.2 Dynamics

Eq. (6.1) can be reformulated using elemental Denavit-Hartenberg transformations, as described by Hannan and Walker [2003]. Such equivalence implicitly defines a connection between the soft robot and a rigid robot described by the equivalent parametrization. Figure 6-3a,b, shows two examples of rigid robotic structures matching a single CC segment. More complex rigid structures for generic PCC soft robots can be built by interconnecting such basic elements.

From a kinematic point of view, any representation satisfying the condition that the end points of each CC segment coincide with the corresponding reference points of the rigid robot is equivalent. However, as soon as we consider the dynamics of the two robots, another constraint has to be taken into account: the inertial properties of the augmented and the soft robot must be equivalent. One possible solution for this can be obtained by matching the centers of mass of each CC segment by an equivalent point mass attached to the rigid robot structure. Figure 6-3c,d, presents two examples of rigid structures approximately matching a CC segment in its dynamics.

We refer to the state space of the equivalent rigid robot as the augmented state $\xi \in \mathbb{R}^{n\,h}$, with h being the number of joints per CC segment and n being the number of segments. The two configurations are connected through the continuously differentiable map

$$m : \mathbb{R}^n \to \mathbb{R}^{n\,h} . \tag{6.2}$$

The map m is such that the nonlinear constraint $\xi = m(q)$ assures that the end points and the point masses of each CC segment coincide with the corresponding points of the rigid robot in position and orientation.

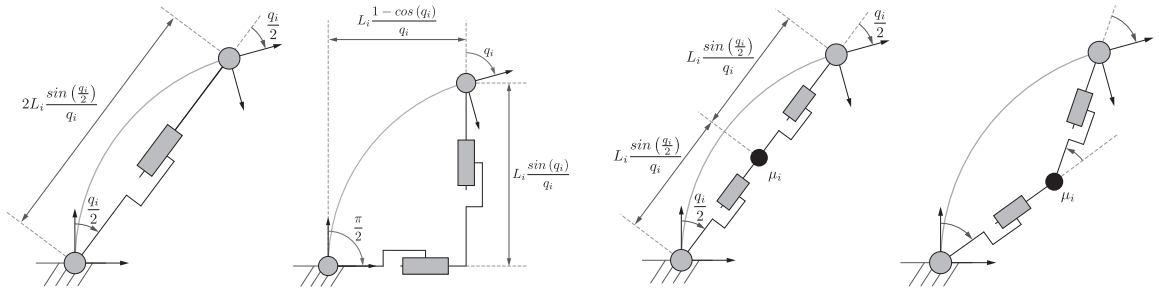

(a) RPR (b) RPPR (kin.) (c) RPPR (dyn.) (d) RPRPR

Figure 6-3: Examples of rigid robots matching a single CC soft segment. A combination of revolute joints R shown as circles and prismatic joints P shown as rectangles achieves the matching. Several of these basic elements can be connected to obtain a representation of a PCC soft robot. Panels a and b show two robots matching the segment's kinematic. Panels c and d show two robots matching the segment's dynamics, with two different hypotheses on the mass distribution. In panel c, the center of mass is in the middle of the chord. In panel d, the added rotational DOF allows the center of mass to be moved to the symmetry axis of the arc.

For example, we consider the middle point of the chord as a suitable approximation of the mass distribution of the CC segment, see Figure 6-3c. For that representation we report the dynamically consistent DH parametrization in Table 6.1. The corresponding map is

$$m_i(q_i) = \begin{bmatrix} \frac{q_i}{2} \\ L_i \frac{\sin(\frac{q_i}{2})}{q_i} \\ L_i \frac{\sin(\frac{q_i}{2})}{q_i} \\ \frac{q_i}{2} \end{bmatrix} . \tag{6.3}$$

Table 6.1: Description of the rigid robot equivalent to a single CC segment. The parameters θ_{DH}, d_{DH}, a_{DH}, α_{DH} refer to the classical DH parametrization, and μ refers to the mass of the CC segment.

Link	θ_{DH}	d_{DH}	a_{DH}	α_{DH}	μ
1	$\frac{q_i}{2}$	0	0	$\frac{\pi}{2}$	0
2	0	$L_i \frac{\sin(\frac{q_i}{2})}{q_i}$	0	0	μ_i
3	0	$L_i \frac{\sin(\frac{q_i}{2})}{q_i}$	0	$-\frac{\pi}{2}$	0
4	$\frac{q_i}{2}$	0	0	0	0

Figure 6-4 presents the CC segment and the corresponding rigid counterpart for five

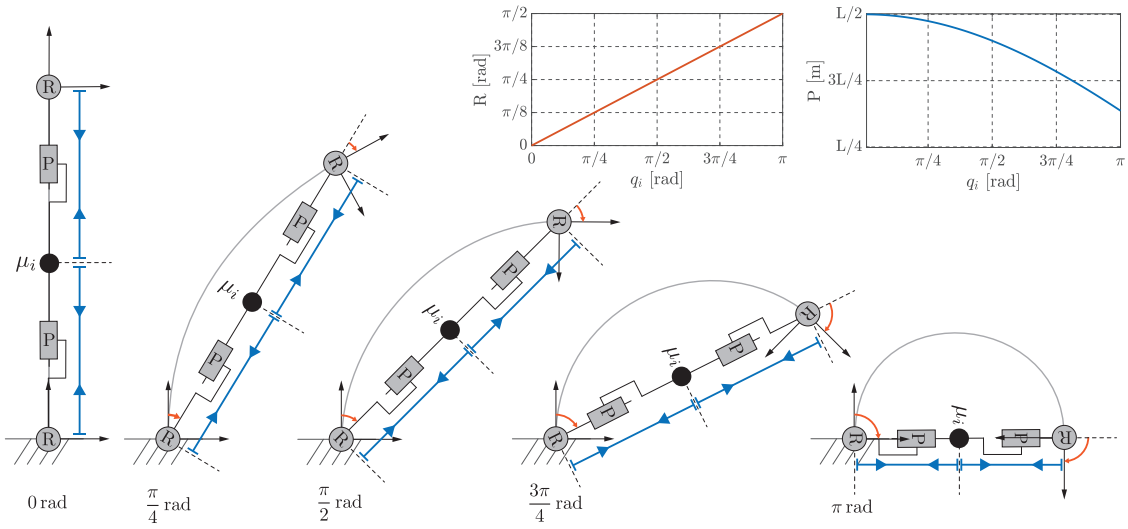

Figure 6-4: Increasing levels of deformation of a dynamically consistent augmented robot (RPPR) matching a single CC segment. We show five different configurations corresponding to the degrees of curvature ranging from $q_i = 0\,\text{rad}$ (straight configuration) to $q_i = \pi\,\text{rad}$ (half circle). The constraints imposed by the map $\xi_i = m_i(q_i)$ in (6.3) assure the correct positioning of the equivalent mass in the middle of the chord and the matching of the reference frames connected to the tip of the segment and at the end of the rigid robot. As q_i changes, the change in angle of the revolute joints R and the change in length of the prismatic joints P are shown in the two plots.

postures ranging from $q_i = 0\,\text{rad}$ to $q_i = \pi\,\text{rad}$. A continuous soft robot represented by the PCC model can be approximately matched to a dynamically consistent rigid robot, built as a sequence of these elements. Figure 6-1b presents an example with four segments. The robot configurations are connected by the map

$$m(q) = \begin{bmatrix} m_1(q_1)^{\mathrm{T}} & \dots & m_n(q_n)^{\mathrm{T}} \end{bmatrix}^{\mathrm{T}} . \tag{6.4}$$

The dynamics of the augmented rigid robot are

$$B_\xi(\xi)\ddot{\xi} + C_\xi(\xi,\dot{\xi})\dot{\xi} + G_\xi(\xi) = J_\xi^{\mathrm{T}}(\xi) f_{\text{ext}}\,, \tag{6.5}$$

where $\xi,\ \dot{\xi},\ \ddot{\xi} \in \mathbb{R}^{nh}$ is the robot configuration with its derivatives, $B_\xi(\xi) \in \mathbb{R}^{nh\times nh}$ is the robot's inertia matrix, $C_\xi(\xi,\dot{\xi})\dot{\xi} \in \mathbb{R}^{nh}$ collects Coriolis and centrifugal terms, $G_\xi(\xi) \in \mathbb{R}^{nh}$ takes into account the effect of gravity on the robot. The robot is subject to a set of external wrenches f_{ext}, mapped through the Jacobian $J_\xi(\xi)$. The Jacobian

$J_\xi(\xi)$ is defined by $\frac{\partial x}{\partial \xi}$. The vector $x \in \mathbb{R}^k$ describes the coordinates of a set of contact points.

The dynamics of the soft robot is thus described by the equation (6.5) expressed on the sub-manifold implicitly defined by the map $\xi = m(q)$. This map describes nonlinear constraints that are scleronomic and holonomic. Therefore, it is possible to integrate them directly into the dynamics of the system. To this end, we evaluate the augmented configuration derivatives ξ, $\dot{\xi}$, $\ddot{\xi}$, w.r.t. q, $\dot{q}$, $\ddot{q}$

$$\begin{cases} \xi &= m(q) \\ \dot{\xi} &= J_m(q)\dot{q} \\ \ddot{\xi} &= \dot{J}_m(q,\dot{q})\dot{q} + J_m(q)\ddot{q} \,. \end{cases} \tag{6.6}$$

where $J_m(q)$: $\mathbb{R}^n \to \mathbb{R}^{n\,h \times n}$ is the Jacobian of $m(\cdot)$, that is $\frac{\partial m}{\partial q}$. When $m_i(q)$ is defined as in (6.3), it is

$$J_{m,i} = \begin{bmatrix} \frac{1}{2} & L_{\mathrm{c},i} & L_{\mathrm{c},i} & \frac{1}{2} \end{bmatrix}^{\mathrm{T}} \tag{6.7}$$

where $L_{\mathrm{c},i} = L_i \, \frac{q_i \, \cos(\frac{q_i}{2}) - 2 \, \sin(\frac{q_i}{2})}{2\, q_i^2}$. By substituting (6.6) into (6.5), it follows

$$\begin{aligned} & B_\xi(m(q))(\dot{J}_m(q,\dot{q})\dot{q} + J_m(q)\ddot{q}) \\ +& C_\xi(m(q), J_m(q)\dot{q})J_m(q)\dot{q} + G_\xi(m(q)) \\ =& J_\xi^{\mathrm{T}}(m(q)) f_{\mathrm{ext}} \,. \end{aligned} \tag{6.8}$$

This generalized balance of forces can be projected by pre-multiplication with $J_m^{\mathrm{T}}(q)$ onto the constraints described by the map $\xi = m(q)$. This yields the compact dynamics

$$B(q)\ddot{q} + C(q,\dot{q})\dot{q} + G(q) = J^{\mathrm{T}}(q) f_{\mathrm{ext}} \,, \tag{6.9}$$

where

$$\begin{cases} B(q) & = J_m^{\mathrm{T}}(q)\, B_\xi(m(q))\, J_m(q) \\ C(q,\dot{q}) & = J_m^{\mathrm{T}}(q)\, B_\xi(m(q))\, \dot{J}_m(q,\dot{q}) \\ & \quad + J_m^{\mathrm{T}}(q)\, C_\xi(m(q), J_m(q)\dot{q})\, J_m(q) \\ G(q) & = J_m^{\mathrm{T}}(q)\, G_\xi(m(q)) \\ J^{\mathrm{T}}(q) & = J_m^{\mathrm{T}}(q)\, J_\xi^{\mathrm{T}}(m(q)) \end{cases} \tag{6.10}$$

Note that the terms in (6.5) can be efficiently formulated in an iterative form, as discussed by Featherstone [2014]. The dynamic model for the soft robot derived in (6.9) inherits this property through (6.10).

We would like to highlight that our dynamics formulation presented in (6.9) and (6.10) differs from the standard manipulator formulation due to the way we model the lumped inertia using the constraints described in (6.6). Our dynamics formulation is used to develop later our curvature controller (Section 6.4) and our Cartesian controller (Section 6.5). In particular, the Theorems 1 and 2 will be demonstrations showing how the existing well-known theorems on closed-loop stability still hold true for our dynamics formulation.

6.2.3 Impedance and Actuation

We complete (6.9) by introducing elastic and dissipative terms. It is convenient to directly evaluate the impedance for the PCC soft robot using the configuration variable q, and its derivative $\dot{q}$. We consider here the planar case described in Figure 6-5. We model the elasticity of a link through a continuous distribution of infinitesimal springs along the cross-sectional area of a segment.

The length of an infinitesimal spring at distance δ_{imp} from the central axis of the segment is

$$L_{\delta_{\mathrm{imp}},i}(q_i) = (\rho_i - \delta_{\mathrm{imp}})\, q_i = \left(\frac{L_i}{q_i} - \delta_{\mathrm{imp}}\right) q_i \,, \tag{6.11}$$

where L_i is the length of the central axis of the segment (constant for every q_i by construction), ρ_i is the radius of curvature, and $L_i = \rho_i\, q_i$. We consider the spring to

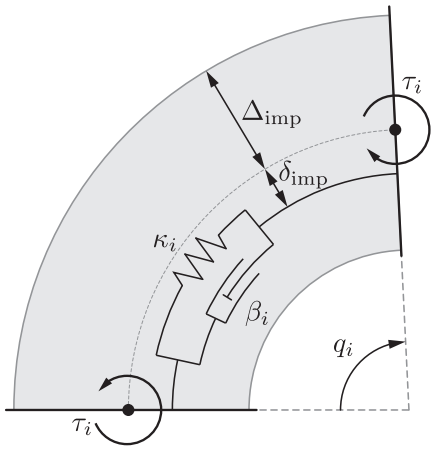

Figure 6-5: Impedance model of a segment with constant curvature. An internal torque τ_i is applied at both ends. The thickness of the segment section is $2\Delta_{\text{imp}}$. We consider a continuous distribution of springs and dampers. An infinitesimal impedance element is connected at a distance δ_{imp} from the center axis of the segment.

be linear with an infinitesimal linear stiffness ϱ. The amount of stored energy is equal to

$$\begin{aligned} E_{\delta_{\text{imp}},i}(q_i) &= \frac{1}{2}\varrho_i \left(L_{\delta_{\text{imp}},i}(0) - L_{\delta_{\text{imp}},i}(q_i)\right)^2 \\ &= \frac{1}{2}\varrho_i \delta_{\text{imp}}^2 q_i^2 \,. \end{aligned} \tag{6.12}$$

Thus, the total energy stored in the segment is

$$E_i(q_i) = \int_{-\Delta_{\text{imp},i}}^{+\Delta_{\text{imp},i}} E_{\delta_{\text{imp}},i}(q_i)\, \mathrm{d}\delta_{\text{imp}} = \frac{1}{3}\, \varrho_i\, \Delta_{\text{imp},i}^3\, q_i^2. \tag{6.13}$$

The elastic force acting on the i-th segment can then be evaluated as

$$\frac{\partial E_i(q_i)}{\partial q_i} = \frac{2}{3}\, \varrho_i\, \Delta_{\text{imp},i}^3\, q_i \,, \tag{6.14}$$

which is linear in the curvature angle q_i.

Similarly, we introduce an infinitesimal linear damper in parallel to each infinitesimal spring. It generates a force equal to $\varsigma\, \dot{L}_{\delta_{\text{imp}},i}$. By exploiting kinetostatic duality and integrating over the cross section, we obtain the total dissipative force produced

at the i-th segment

$$\int_{-\Delta_{\text{imp},i}}^{\Delta_{\text{imp},i}} \varsigma_i \left(\frac{\partial L_{\delta_{\text{imp}},i}}{\partial q_i} \right)^2 \dot{q}_i \, \mathrm{d}\delta_{\text{imp}} = \frac{2}{3} \varsigma_i \Delta_{\text{imp},i}^3 \dot{q}_i \, . \tag{6.15}$$

For the PCC hypothesis, elastic and damping actions can be described by two linear terms: $K\,q$ and $D\,\dot{q}$, respectively. Stiffness K and damping D are two diagonal matrices, with

$$k_i = \frac{2}{3} \varrho_i \Delta_{\text{imp},i}^3 \tag{6.16}$$

and

$$d_i = \frac{2}{3} \varsigma_i \Delta_{\text{imp},i}^3 \tag{6.17}$$

as the i-th diagonal elements, respectively. Note that $K \succ 0$ and $D \succ 0$, since $\varrho_i > 0$, $\varsigma_i > 0$, and $\Delta_{\text{imp},i} > 0$, $\forall i$.

Furthermore, we assume the soft robot is actuated through a pair of internal torques for each segment applied as shown in Figure 6-5. For a soft robot that is fluidically actuated, the forces generated through pressurized cavities generate in sum this pair of internal torques for each segment. This argumentation is based on the insights gained from the development of this actuator morphology in Sections 3.2.1 and 3.2.2.2. We later experimentally identify in Section 7.2.1.2 the mapping from the controlled volumetric actuation to the internal torques of the segments. Furthermore, we show later in our experiments (Section 7.2.2.2), that the hypothesis of linearity in actuation and stiffness holds true despite our volumetric actuation approach. The mapping between actuations and generalized torques can be evaluated using the Jacobians as defined in (6.10). In the planar case the mapping is the identity. For the sake of space we do not report the calculation of these Jacobians.

6.2.4 Complete Model

We combine the model describing the dynamics (Section 6.2.2) and the model describing the impedance and actuation (Section 6.2.3) to get the complete model. The complete

model is

$$B(q)\ddot{q} + (C(q,\dot{q}) + D)\dot{q} + G(q) + K\,q = \tau + J^{\mathrm{T}}(q) f_{\mathrm{ext}}\,. \tag{6.18}$$

6.2.5 Model Properties

The proposed model verifies a set of basic properties of classical rigid robots, of which we report a selection in the following. We acknowledge that these results are specific to our chosen mapping and modeling assumptions. The model is approximate in describing the deformations of a soft bending segment under two core assumptions. These two assumptions are: approximating the bending of a segment through a piecewise constant curvature model and the use of a point mass at the approximate center of mass to describe the mass distribution of a segment. Therefore, the following model properties only hold true as long as a soft segment does not significantly deviate from a constant curvature arc and the mass distribution does not significantly change due to fluidic pressurization. Both assumptions continuously remained true for the experiments we performed with our soft robot in Section 7.2.

The following model properties are of particular interest for the aim of the present work, since they are used to prove the stability of the two proposed controllers in Section 6.4 and Section 6.5. We formulate the following properties for our augmented formulation and later apply it to our serial link robots. These model properties are useful for proofs of convergence and robustness of the most commonly used control strategies in rigid robot torque control [Sciavicco and Siciliano, 2012]. To be specific, the Theorems 1 and 2 will make use of these model properties to demonstrate that the existing well-known theorems on asymptotic stability still hold true for our dynamics formulation in (6.9) and (6.10).

Lemma 1. *If $C_\xi(\xi,\dot{\xi})$ is defined with Christoffel symbols [Murray, 1994, Ch. 4], then the matrix $\dot{B}(q) - 2C(q,\dot{q})$ is skew symmetric.*

Proof. We start by evaluating the time derivative of the inertia matrix, using its

definition in (6.10)

$$\dot{B} = \dot{J}_m^{\mathrm{T}} B_\xi J_m + J_m^{\mathrm{T}} \dot{B}_\xi J_m + J_m^{\mathrm{T}} B_\xi \dot{J}_m \, . \tag{6.19}$$

Note that in this proof we omit arguments for the ease of reading. Combining (6.19) with the expression of C in (6.10) yields

$$\begin{aligned} \dot{B} - 2\,C &= \dot{J}_m^{\mathrm{T}} B_\xi J_m + J_m^{\mathrm{T}} \dot{B}_\xi J_m + J_m^{\mathrm{T}} B_\xi \dot{J}_m \\ &\quad - 2 J_m^{\mathrm{T}} B_\xi \dot{J}_m - 2 J_m^{\mathrm{T}} C_\xi J_m \\ &= J_m^{\mathrm{T}} (\dot{B}_\xi - 2 C_\xi) J_m \\ &\quad + \dot{J}_m^{\mathrm{T}} B_\xi J_m - J_m^{\mathrm{T}} B_\xi \dot{J}_m \, . \end{aligned} \tag{6.20}$$

The skew symmetry of the first term of the sum follows by direct application of the quadratic form definition. Indeed, for every $\nu \in \mathbb{R}^n$ the following holds

$$\nu^{\mathrm{T}} J_m^{\mathrm{T}} (\dot{B}_\xi - 2 C_\xi) J_m \nu = (\nu J_m)^{\mathrm{T}} (\dot{B}_\xi - 2 C_\xi)(J_m \nu) = 0 \, , \tag{6.21}$$

where for the last step we exploit the skew symmetry of $\dot{B}_\xi - 2C_\xi$, see Slotine and Li [1987]. The skew symmetry of matrix $\dot{B} - 2\,C$ then derives by considering that

$$\begin{aligned} (\dot{J}_m^{\mathrm{T}} B_\xi J_m - J_m^{\mathrm{T}} B_\xi \dot{J}_m)^{\mathrm{T}} &= J_m^{\mathrm{T}} B_\xi \dot{J}_m - \dot{J}_m^{\mathrm{T}} B_\xi J_m \\ &= - \left(\dot{J}_m^{\mathrm{T}} B_\xi J_m - J_m^{\mathrm{T}} B_\xi \dot{J}_m \right) \, , \end{aligned} \tag{6.22}$$

and that the sum of skew symmetric matrices is also skew symmetric. □

Remark 1. *If C_ξ is not built through Christoffel symbols, the thesis of Lemma 1 becomes $\dot{q}^{\mathrm{T}} (\dot{B}(q) - 2\,(C(q, \dot{q})))\dot{q} = 0$. This can be proven by following the same steps of the proof above.*

Lemma 2. *The inertia matrix $B(q)$ is positive semidefinite and limited, that is*

$$B(q) \succeq 0 \, , \quad ||B(q)|| < \infty \qquad \forall q \in \mathbb{R}^n \, ,$$

if $-\infty < m_i(q) < +\infty$ *for all* $q \in \mathbb{R}^n$ *and* $\forall i$ *such that the* i*-th joint is prismatic, and* $||J_m|| < \infty$.

Proof. For the first property, we start by considering that $B_\xi(m) \succeq 0$ for every ξ by construction. Note that in this proof we omit the dependencies $q, \dot{q}$ for ease of reading. Thus, recalling that $B = J_m^{\mathrm{T}} B_\xi(m) J_m$, the first property derives from the very definition of positiveness. Indeed, for every $\nu \in \mathbb{R}^n$ the following holds

$$\nu^{\mathrm{T}} J_m^{\mathrm{T}} B_\xi(m) J_m \nu = (\nu J_m)^{\mathrm{T}} B_\xi(m)(J_m \nu) > 0 \,. \tag{6.23}$$

For the second property, the submultiplicative property of the matrix norm of a square matrix tells us that $||B|| < ||J_m^{\mathrm{T}}||\, ||B_\xi(m)||\, ||J_m||$. The limitedness of $||J_m||$ is assured by the hypothesis on J_m. $B_\xi(m)$ is the inertia matrix of a rigid robot. Its norm may tend to infinity only if the length of at least one of its prismatic joints tends to infinity. This possibility is excluded by the hypothesis of m.

□

Corollary 1. *Let* $R(q) \in \mathbb{R}^{nh \times d_{\mathrm{r}}}$ *be such that* $\mathrm{Rank}(B_\xi(m(q))) = d_{\mathrm{r}}$ *and* $\mathrm{Span}(R(q))$ *is the range of* $B_\xi(m(q))$*, and let the hypotheses of Lemma 2 be verified. Then* $\mathrm{Rank}(R^{\mathrm{T}}(q)\, J_m(q)) = n$ *implies that* $B(q) \succ 0$.

Proof. The inertia matrix B_ξ of a rigid robot is symmetric, which assures that it is diagonalizable. Note that in this proof we omit arguments for ease of reading. Since the augmented rigid robot can include massless links, the Kernel of B_ξ is in general not empty. Thus by spectral decomposition the following holds

$$B_\xi = M^{\mathrm{T}} \begin{bmatrix} U & 0 \\ 0 & 0 \end{bmatrix} M \tag{6.24}$$

where $U \in \mathbb{R}^{nh \times nh}$ is the diagonal matrix collecting all the non-null eigenvalues of B_ξ, and

$$M = \begin{bmatrix} R^{\mathrm{T}} \\ N^{\mathrm{T}} \end{bmatrix} \tag{6.25}$$

where $R \in \mathbb{R}^{nh \times d_\mathrm{r}}$ and $N \in \mathbb{R}^{nh \times nh - d_\mathrm{r}}$ have as columns a base of the Range and the Kernel of B_ξ, respectively.

Combining (6.10), (6.24), and (6.25), the following holds

$$\begin{aligned} B &= J_m^\mathrm{T} \, B_\xi(m) \, J_m \\ &= J_m^\mathrm{T} \, R \, U \, R^\mathrm{T} \, J_m \, . \end{aligned} \tag{6.26}$$

The application of the Sylvester inequality [Petersen and Pedersen, 2012] yields

$$\begin{aligned} \mathrm{Rank}(B) \geq \, & \mathrm{Rank}(J_m^\mathrm{T} \, R \, U) \\ & + \mathrm{Rank}(R^\mathrm{T} \, J_m) - d_\mathrm{r} \\ \geq \, & \mathrm{Rank}(U) \\ & + 2 \, \mathrm{Rank}(R^\mathrm{T} \, J_m) - 2 \, d_\mathrm{r} \, . \end{aligned} \tag{6.27}$$

Note that $\mathrm{Rank}(U) = d_\mathrm{r}$ is given by construction, and $\mathrm{Rank}(R^\mathrm{T} \, J_m) = n$ by hypothesis. The latter also implies that $n \geq d_\mathrm{r}$. Therefore

$$\mathrm{Rank}(B) \geq n \, . \tag{6.28}$$

Since B lives in $\mathbb{R}^{n \times n}$, then (6.28) implies that B is full rank. This excludes the semi-definiteness of B, and together with Lemma 2 proves the thesis. □

Remark 2. *The hypotheses on $m(q)$ and on $J_m(q)$ in Lemma 2 and Corollary 1 are verified for the representation described by* (6.3)*,* (6.7) *and Table 6.1.*

6.3 Model-Based Control Design

While it is largely accepted for describing the kinematics, the use of a PCC model in representing the infinite dimensionality of a soft robot can always introduce some mismatch with reference to the real system. The same holds for the introduction of approximations in the inertia distribution. Thus, it is critical to design controllers which are able to exploit the information given by the proposed model, while being

robust to uncertainties. Moreover, the controllers are designed with the aim of achieving a wide exploitation of the intelligence embedded within the robot's mechanics. We thus avoid the use of complete feedback cancellations of robot dynamics [De Luca and Lucibello, 1998], as well as other kinds of control actions that present robustness issues in classic robots, as e.g. pre-multiplications of feedback actions by the inverse of the inertia matrix [Nakanishi et al., 2008].

In the following sections, we present two model-based feedback controllers following the described design principles. The first controller enables dynamic trajectory tracking in curvature space (Section 6.4). The second controller is a Cartesian impedance controller (Section 6.5) that is combined with a contact planning algorithm (Section 6.6) to enable the tracing of a surface under contact with the robot's end-effector.

6.4 Curvature Dynamic Control

We propose the following controller for implementing trajectory tracking in the soft robot's state space q

$$\tau = K\bar{q} + D\dot{\bar{q}} + G(q) + C(q,\dot{q})\dot{\bar{q}} + B(q)\ddot{\bar{q}} \tag{6.29}$$

where $q, \dot{q} \in \mathbb{R}^n$ are the degree of curvature vector and its derivative. $\bar{q}(t), \dot{\bar{q}}(t), \ddot{\bar{q}}(t) \in \mathbb{R}^n$ are the desired evolution and its derivatives expressed in the generalized coordinates, that is the degree of curvature space. $B \in \mathbb{R}^{n\times n}$ is the robot's inertia, $C \in \mathbb{R}^{n\times n}$ is the Coriolis and Centrifugal matrix obtained by computing C_ξ through Christoffel symbols [Murray, 1994, Ch. 4], $K \in \mathbb{R}^{n\times n}$ and $D \in \mathbb{R}^{n\times n}$ are the robot's stiffness and damping matrices, respectively. Figure 6-6 illustrates a block representation of (6.29). It is worth noticing that $K\bar{q} + D\dot{\bar{q}}$ are purely feedforward actions, while $G(q)$, $C(q,\dot{q})$, and $B(q)$ close the feedback loop by depending on q and $\dot{q}$.

The resulting form of the closed loop system is

$$B(q)(\ddot{q} - \ddot{\bar{q}}) + C(q,\dot{q})(\dot{q} - \dot{\bar{q}}) = K(\bar{q} - q) + D(\dot{\bar{q}} - \dot{q})\,. \tag{6.30}$$

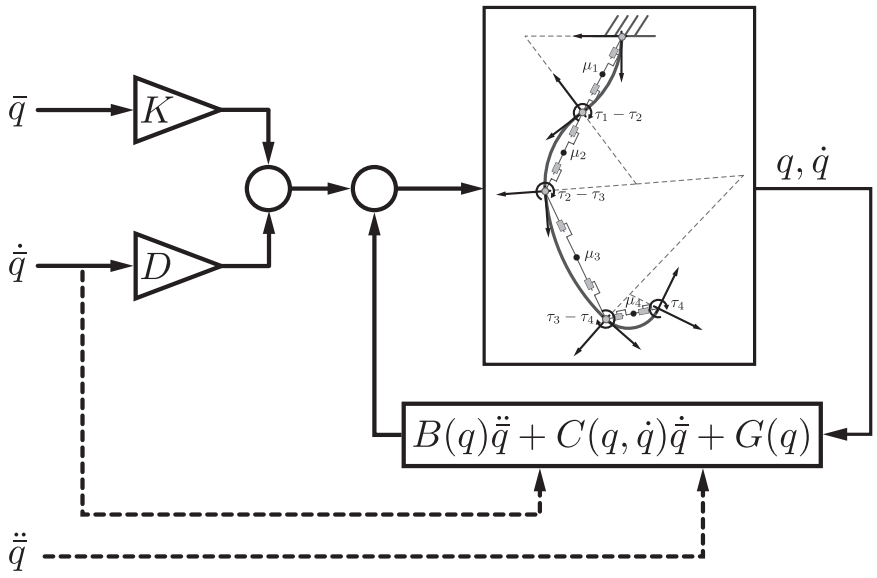

Figure 6-6: Block scheme of the proposed controller (6.29) for trajectory tracking in curvature space. The algorithm is composed of a pure feedforward term $K\bar{q} + D\dot{\bar{q}}$, plus a mixed feedforward-feedback term $B(q)\ddot{\bar{q}} + C(q,\dot{q})\dot{\bar{q}} + G(q)$.

The feedforward action $K\bar{q} + D\dot{\bar{q}}$ is combined with the physical impedance of the system, generating a natural proportional-derivative (PD) action $K(\bar{q} - q) + D(\dot{\bar{q}} - \dot{q})$. In this way the softness of the robot is preserved in sight of possible interactions with the environment. Balancing the feedforward and feedback terms to achieve this natural PD action is inspired by Della Santina et al. [2017] proposing a controller for articulated robots with variable impedance in their joints. Note that the algorithm does not require any tuning, since all the terms are specified by the model.

Let us consider for a moment the case in which $\dot{\bar{q}} \equiv 0$. For simplicity we also consider no gravitational field. For this scenario of a constant reference $\bar{q}$, the control action (6.29) is purely feedforward, and (6.30) becomes a classical rigid robot controlled through a PD, which is well known to be globally asymptotically stable in the reference $\bar{q}$ [Sciavicco and Siciliano, 2012]. This can be regarded as a manifestation of the self-stabilizing properties of soft robotic systems, which have been already recognized in previous works such as Bosi et al. [2016], Thuruthel et al. [2018]. The following theorem will show that the introduction of the dynamic feedback terms $G(q)$, $C(q,\dot{q})\dot{\bar{q}}$, and $B(q)\ddot{\bar{q}}$ enhances this property by also including a non-constant $\bar{q}$ into the range of self-stabilized references. The following theorem demonstrates that the existing well-known

theorems on closed-loop stability still hold true for our dynamics formulation given in (6.9) and (6.10). This theorem shall further exemplify that our dynamic formulation can enable the application of control strategies typically used in rigid-bodied robots to soft robots.

Theorem 1. *The continuously differentiable trajectory $\bar{q}(t)$ is a globally asymptotically stable equilibrium for the closed-loop system* (6.30) *under the hypotheses of Corollary 1.*

Proof. Let us define the error variable $e \doteq q - \bar{q}$. The system (6.30) becomes

$$B(q)\ddot{e} + C(q,\dot{q})\dot{e} + Ke + D\dot{e} = 0\,. \tag{6.31}$$

The thesis can now be proven by considering as radially unbounded Lyapunov candidate the following natural extension of the energy function

$$V(e,\dot{e}) = \frac{1}{2}\dot{e}^{\mathrm{T}}B(q)\dot{e} + \frac{1}{2}e^{\mathrm{T}}Ke\,. \tag{6.32}$$

Note that in order to become a candidate, B has to be positive definite. This is assured by Corollary 1.

The time derivative of V is

$$\dot{V}(e,\dot{e},t) = \frac{1}{2}\dot{e}^{\mathrm{T}}\dot{B}\dot{e} + \dot{e}^{\mathrm{T}}B\ddot{e} + \dot{e}^{\mathrm{T}}Ke\,. \tag{6.33}$$

By substituting (6.31), we obtain:

$$\dot{V}(e,\dot{e}) = \frac{1}{2}\dot{e}^{\mathrm{T}}(\dot{B} - 2C)\dot{e} - \dot{e}^{\mathrm{T}}D\dot{e}\,. \tag{6.34}$$

Using Lemma 1, the first term falls away and we obtain $\dot{V}(e,\dot{e}) = -\dot{e}^{\mathrm{T}}\,D\,\dot{e} \leq 0$. The thesis follows by application of LaSalle's invariance principle [Khalil, 1996]. □

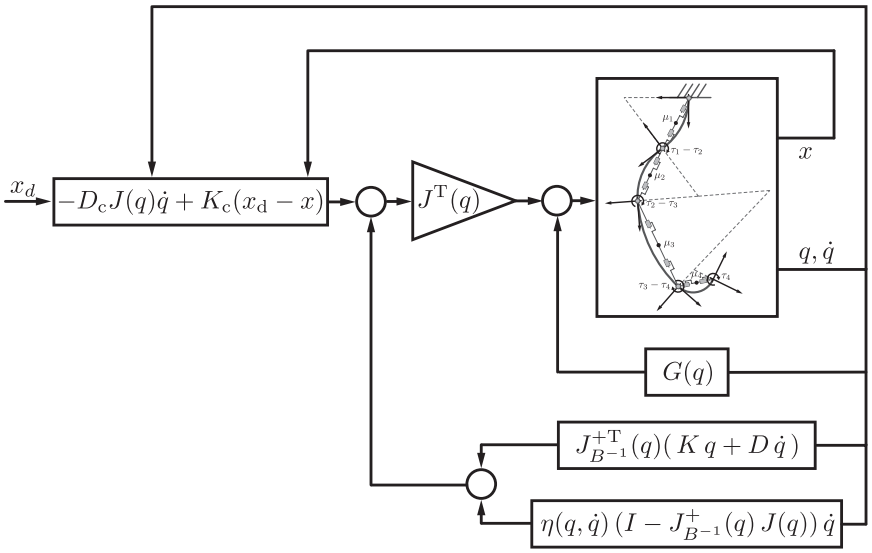

Figure 6-7: Block scheme of the proposed controller (6.35) for Cartesian impedance control. The algorithm is composed of three terms: the actual Cartesian spring-damper system $J^{\mathrm{T}}(q)(K_{\mathrm{C}}(x_{\mathrm{d}} - x) - D_{\mathrm{C}}J(q)\dot{q})$, the non-diagonal stiffness compensation $J^{\mathrm{T}}(q)J_B^{+\mathrm{T}}(q)(\,K\,q + D\,\dot{q}\,) + G(q)$, and the dynamic decoupling $J^{\mathrm{T}}(q)\,\eta(q,\dot{q})\,(I - J_B^{+}(q)\,J(q))\,\dot{q}$.

6.5 Cartesian Impedance Control

We consider a set of contact points with coordinates $x \in \mathbb{R}^k$. Through them, the environment can exert a set of wrenches f_{ext} on the soft robot, mapped through the Jacobian $J(q)$, as described in (6.18).

A correct regulation of the impedance at the contact points is essential to implement robust and reliable end-effector interactions with the environment [Ott, 2008]. We propose to implement the desired compliant behavior through the following dynamic feedback loop

$$\begin{aligned}\tau = {} & J^{\mathrm{T}}(q)J_B^{+\mathrm{T}}(q)(K\,q + D\dot{q}) + G(q) \\ & + J^{\mathrm{T}}(q)\,\eta(q,\dot{q})\,(I - J_B^{+}(q)\,J(q))\,\dot{q} \\ & + J^{\mathrm{T}}(q)(K_{\mathrm{C}}(x_{\mathrm{d}} - x) - D_{\mathrm{C}}J(q)\dot{q})\ ,\end{aligned} \tag{6.35}$$

where $q, \dot{q} \in \mathbb{R}^n$ are the soft robot's degree of curvature vector and its derivative. $J(q) \in \mathbb{R}^{k\times n}$ is the Jacobian, which maps $\dot{q}$ into the end effector velocity $\dot{x}$. $x_{\mathrm{d}} \in \mathbb{R}^k$ is a reference position for the contact point, and x is the configuration of the contact

point. $J_B^+ \in \mathbb{R}^{k\times n}$ is the dynamically consistent pseudo-inverse [Chang and Khatib, 1995] described by

$$J_B^+(q) = B^{-1}(q)\, J^{\mathrm{T}}(q)\, \left(J(q)\, B^{-1}(q)\, J^{\mathrm{T}}(q)\right)^{-1} \ , \tag{6.36}$$

that can be used to map forces in configuration space towards their counterpart in operational space. $\eta(q,\dot{q}) \in \mathbb{R}^{k\times n}$ is the Cartesian Coriolis and centrifugal matrix, defined as

$$\begin{aligned} \eta(q,\dot{q}) &= (J\, B^{-1}\, J^{\mathrm{T}})^{-1}(J\, B^{-1} C - \dot{J}) \\ &= J_B^{+\mathrm{T}} C - \Lambda \dot{J} \end{aligned} \tag{6.37}$$

with the dependencies on $q, \dot{q}$ not reported. $\Lambda(q)$ is the Cartesian inertia matrix [Khatib, 1987], defined as

$$\Lambda(q) = (J(q)\, B^{-1}(q)\, J(q)^{\mathrm{T}})^{-1} \in \mathbb{R}^{k\times k} \tag{6.38}$$

The term $J^{\mathrm{T}}(q)(K_{\mathrm{C}}(x_{\mathrm{d}} - x) - D_{\mathrm{C}} J(q)\dot{q})$ simulates the presence of a spring and a damper connected between x and x_{d}. This imposes the desired Cartesian stiffness K_{C}, and Cartesian damping D_{C}. We will choose these matrices to be diagonal in order to implement a full decoupling within the Cartesian directions. The remaining terms act as a compensation of the non-diagonal Cartesian stiffness $J^{\mathrm{T}}(q) J_B^{+\mathrm{T}}(q)\, K\, q + G(q)$, and as a decoupling of the Cartesian dynamics from the residual dynamics of the redundant degrees of freedom $J^{\mathrm{T}}(q)\left(J_B^{+\mathrm{T}}(q) D + \eta(q,\dot{q})(I - J_B^+(q)\, J(q))\right)\dot{q}$. Figure 6-7 presents a block representation of (6.35).

The following theorem assures that the closed-loop system implements the desired compliant behavior at the contact point. The theorem demonstrates that the existing well-known theorems still hold true for our dynamics formulation given in (6.9) and (6.10). This is done with the goal in mind that our dynamics formulation shall enable the application of control strategies typically used in rigid-bodied robots to soft robots.

Theorem 2. *The closed loop defined by controller* (6.35) *and system* (6.18) *is such that*

$$\lim_{t\to\infty} K_{\mathrm{C}}(x(t) - x_{\mathrm{d}}) = f_{\mathrm{ext}} \ , \tag{6.39}$$

for all $K_{\mathrm{C}} \succ 0$ *and* $D_{\mathrm{C}} \succ 0$, $\dot{x}_{\mathrm{d}} = 0$, $\dot{f}_{\mathrm{ext}} = 0$, *and for every* $x(0) \in \mathbb{R}^k$, *under the hypotheses of Corollary 1.*

Proof. We augment the operational space of the soft robot at the velocity level through a set of complementary velocities $v_{\mathrm{n}} \in \mathbb{R}^{n-k}$

$$\begin{bmatrix} \dot{x} \\ v_{\mathrm{n}} \end{bmatrix} = \begin{bmatrix} J \\ N \end{bmatrix} \dot{q} \,, \tag{6.40}$$

where $N \in \mathbb{R}^{(n-k)\times n}$ is chosen such that the resulting transformation is full rank. Note that the dependencies on $q, \dot{q}$ are not reported in this proof whenever not necessary. The inverse of $[J^{\mathrm{T}},\ N^{\mathrm{T}}]^{\mathrm{T}}$ can be written as $[J_B^+,\ Z^{\mathrm{T}}]$, where Z is an opportunely defined matrix. We do not report the proof here, but it can be found in Ott [2008]. Note that B is invertible, since Corollary 1 holds by hypothesis, a property needed for (6.36).

Thus, (6.40) yields to

$$\dot{q} = J_B^+ \dot{x} + Z^{\mathrm{T}} v_{\mathrm{n}} \,. \tag{6.41}$$

Using the Jacobian from (6.40) we can apply a transformation into operational space [Ott, 2008, Ch. 4] on the system (6.18) to obtain the open-loop operational space dynamics

$$\Lambda\, \ddot{x} + \eta_x\, \dot{x} + \eta_{\mathrm{N}}\, v_{\mathrm{n}} + J_B^{+\mathrm{T}}\, D\, \dot{q} + J_B^{+\mathrm{T}}\, (K\, q + G) = J_B^{+\mathrm{T}}\, \tau + f_{\mathrm{ext}} \,. \tag{6.42}$$

The matrix $J_B^{+\mathrm{T}}$ is the dynamically consistent pseudo-inverse (6.36). The Coriolis and centrifugal terms are collected by $\eta_x = \eta J_B^+ \in \mathbb{R}^{k\times k}$ and $\eta_{\mathrm{N}} = \eta Z^{\mathrm{T}} \in \mathbb{R}^{k\times(n-k)}$, with η defined in (6.37). Λ is defined in (6.38).

Substituting the controller (6.35) into (6.42) yields

$$\begin{aligned} &\Lambda\, \ddot{x} + \eta_x\, \dot{x} + \eta_{\mathrm{N}}\, v_{\mathrm{n}} + J_B^{+\mathrm{T}}\, D\, \dot{q} + J_B^{+\mathrm{T}}\, (Kq + G) \\ &\quad = J_B^{+\mathrm{T}}(K\, q + D\, \dot{q}) + J_B^{+\mathrm{T}} G + \eta\, Z^{\mathrm{T}} v_{\mathrm{n}} + K_{\mathrm{C}}(x_{\mathrm{d}} - x) - D_{\mathrm{C}} J \dot{q} + f_{\mathrm{ext}} \end{aligned} \tag{6.43}$$

where we exploited that $J_B^{+\mathrm{T}} J^{\mathrm{T}} = I$, and that (6.41) yields to

$$Z^{\mathrm{T}} v_{\mathrm{n}} = \dot{q} - J_B^+ \dot{x} = (I - J_B^+\, J)\dot{q} \,. \tag{6.44}$$

Through simple algebraic manipulations, (6.43) yields to

$$\Lambda(q)\,\ddot{x} + \eta_x(q,\dot{q})\,\dot{x} + D_{\mathrm{C}}\,\dot{x} + K_{\mathrm{C}}\,(x - x_{\mathrm{d}}) = f_{\mathrm{ext}}\ . \tag{6.45}$$

Note that the controller left the dynamic terms unchanged and only removed the dynamic coupling with the residual dynamics, as discussed earlier in this section.

We prove the thesis for a generic evolution $q(t)$ in joint space. Under this assumption, (6.45) is rewritten as

$$\Lambda(t)\ddot{e} + \eta(t)\dot{e} + D_{\mathrm{C}}\,\dot{e} + K_{\mathrm{C}}\,e = 0 \tag{6.46}$$

where $e = x - x_{\mathrm{d}} - {K_{\mathrm{C}}}^{-1} f_{\mathrm{ext}}$ and $\dot{e} = \dot{x}$. Thus, proving (6.39) is equivalent to proving the asymptotic stability around the origin of (6.46). We consider the following Lyapunov candidate

$$V(e,\dot{e},t) = \frac{1}{2}\dot{e}^{\mathrm{T}}\Lambda(t)\dot{e} + \frac{1}{2}e^{\mathrm{T}}K_{\mathrm{C}}e\ , \tag{6.47}$$

which is radially unbounded and uniformly positive for each $e, \dot{e}$. Note that this function is a straightforward generalization of the commonly employed total energy of the system [Sciavicco and Siciliano, 2012]. The time derivative of (6.47) is

$$\begin{aligned}\dot{V}(e,\dot{e},t) &= \frac{1}{2}\dot{e}^{\mathrm{T}}\dot{\Lambda}(t)\dot{e} + \dot{e}^{\mathrm{T}}\Lambda(t)\ddot{e} + \dot{e}^{\mathrm{T}}K_{\mathrm{C}}e \\ &= \frac{1}{2}\dot{e}^{\mathrm{T}}(\dot{\Lambda}(t) - 2\eta(t))\dot{e} - \dot{e}^{\mathrm{T}}\,D_{\mathrm{C}}\,\dot{e} \\ &= -\dot{e}^{\mathrm{T}}\,D_{\mathrm{C}}\,\dot{e}\ ,\end{aligned} \tag{6.48}$$

where we used (6.46) for the first step and the skew-symmetry of $\dot{\Lambda}(t) - 2\eta(t)$ for the second step. Note that the latter derives from Lemma 1, combined with standard results in the operational space formulation [Ott, 2008, Ch. 4]. Thus $\dot{V} \leq 0$, since $D_{\mathrm{C}} \succ 0$ by hypothesis.

Invoking the LaSalle-Yoshizawa theorem [Khalil, 1996] yields to $\dot{e} \to 0$. This in turn implies that $e \to 0$ through (6.46), from which the thesis is proven. □

Remark 3. *Eq.* (6.35) *performs a cancellation of only the parts of the elastic field*

and the dissipative forces that act on the operational space dynamics. In this way the redundant degrees of freedom can reach a natural equilibrium without the need to explicitly impose such. This is in contrast to the rigid case where it is necessary to impose the equilibrium [Ott, 2008].

6.6 Contact Planning

For the sake of clarity, in the following we will consider as a single point of contact the soft robot's end effector, that is $x \in \mathbb{R}^2$. The proposed controller (6.35) imposes the dynamics of a simple spring-damper-mass system on the end effector of the soft robot (6.45), albeit with a configuration-dependent inertia. Furthermore, Theorem 2 assures that the equilibrium resulting from an end-effector interaction with the environment is equally expected from such a system.

This allows to write higher level policies in an intuitive way. We define a local frame $(n_\parallel, n_\perp)$ connected to the end effector, as depicted in Figure 6-8. The unit vector $n_\parallel$ is chosen to be always tangent to the environment. The unit vector $n_\perp$ is such that $n_\parallel^{\mathrm{T}}\, n_\perp = 0$, and always points from the inside to the outside of the environment. We assume the knowledge of the following information:

- the coordinate x_0 of a point included within the environment,
- the occurrence of a contact between the end effector and the environment, acquired by isInContact(),
- parallel $n_\parallel$ and perpendicular $n_\perp$ unit vectors at the contact point, which are extracted by the methods readParallelDirection() and readPerpendicularDirection(), respectively,
- the final target x_{t} on the surface of the environment.

We specify the value of x_{d} on-line through a simple planning procedure, described by Algorithm 6.1. It consists of two phases: approaching and exploring. In the first phase (lines 1-3), a generic point inside the environment x_0 is selected as reference for

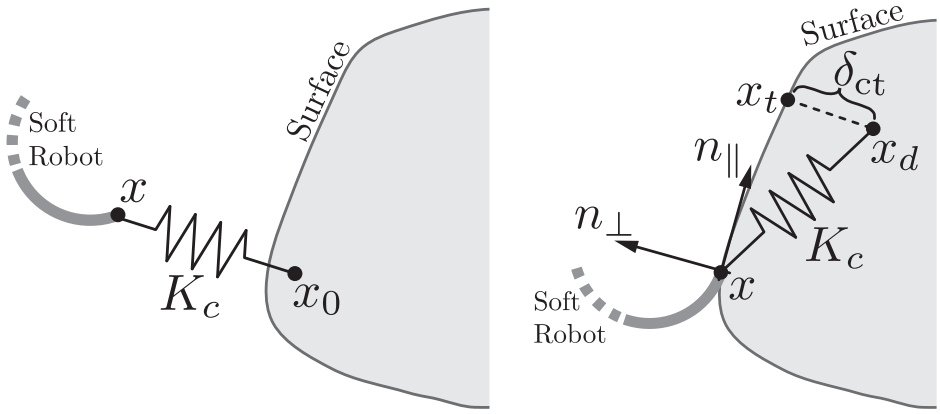

(a) Phase 1: Approaching. (b) Phase 2: Exploring.

Figure 6-8: Contact planner for approaching and exploring surface: The goal of the proposed Cartesian impedance controller is to simulate the presence of a spring and a damper connected between the robot's end effector and a point in space x_{d}. In this way higher level policies can be intuitively defined. Panel (a) and Panel (b) show the two phases of Algorithm 6.1. The frame $(n_{\parallel}, n_{\perp})$ defines the parallel and perpendicular directions to the environment in the contact point.

the impedance controller. When the soft robot makes contact with the environment, the second phase begins (lines 4-8). Here, the desired end effector position is chosen as the final target x_{t}. A constant displacement $-n_{\perp}\delta_{\text{ct}}$ is introduced to ensure that the contact with the environment is maintained during the exploration. δ_{ct} is a small distance going from x_{t} perpendicular into the environment. Algorithm 6.1 terminates when the semi-norm of the error weighted on $n_{\parallel}n_{\parallel}^{\text{T}}$ is below a manually defined threshold ϵ. In this way, only the error along the surface is considered. Figure 6-8 presents a sketch of the two phases of Algorithm 6.1.

Algorithm 6.1 Contact planning for the Cartesian impedance controller

1: **while** isInContact( ) == False **do**
2: $\quad x_{\text{d}} \leftarrow x_0$
3: **end while**
4: **while** $||x - x_{\text{t}}||_{n_{\parallel}n_{\parallel}^{\text{T}}} > \epsilon$ **do**
5: $\quad n_{\parallel} \leftarrow$ readParallelDirection()
6: $\quad n_{\perp} \leftarrow$ readPerpendicularDirection()
7: $\quad x_{\text{d}} \leftarrow x_{\text{t}} - n_{\perp}\delta_{\text{ct}}$
8: **end while**

The environment provides guidance for the end-effector that helps to keep the

error between the desired and the actual position low in the perpendicular direction $n_\perp$. To mitigate the error tangentially, we introduce an integral action acting on the tangential direction $I_{\mathrm{ct}} J^{\mathrm{T}}(q) n_\parallel \int n_\parallel^{\mathrm{T}}(x_{\mathrm{d}} - x)$ when the soft robot is in contact with the environment. Theorem (2) can be extended to consider this term by using a Lyapunov candidate analogous to the one proposed by Kelly [1995].

Chapter 7

Applications on Planar Multi-Link Soft Manipulators

In this chapter we describe applications for soft multi-segment arms. These applications combine the design and fabrication techniques given in Chapter 3 with the model-free control approaches described in Chapter 5, and the model-based dynamic control approaches in Chapter 6.

7.1 Experiments with Model-free Control

In this section, we experimentally validate the proposed model-free controllers outlined in Chapter 5. We hereby demonstrate the planning and control algorithms of Section 5.4. Experiments are performed with multiple fluidic elastomer manipulator prototypes within the experimental setting described in Section 3.6.9.

7.1.1 Confined Environment

To experimentally validate the soft robot's ability to successfully advance through a confined environment, we carry out a series of experiments using a six DOF cylindrical manipulator prototype. The primary goal of these experiments is to see if the whole body planner outlined in Section 5.4.1 can incrementally advance the robot's end

effector pose according to a series of user-specified waypoints, ultimately terminating at the end of one of four distinct pipe-like sections. To achieve this primary goal, the planner also has to successfully accomplish the intermediate task of conforming the whole manipulator's shape to the pipe-like environment. The purpose of these experiments is to show that through a combination of computation (Algorithm 5.4) and design (the inherent softness and compliance of the manipulator) we can successfully accomplish the primary task. If we ignore the manipulator's softness and high compliance, the planar manipulator provides only six DOF and the primary task constrains three degrees of freedom (X-Y position and orientation). In the non-compliant case, this would leave only three DOF for the whole body planner to conform the manipulator's whole body to the environment's interior at any point along the waypoint path. Fortunately, the compliance of the manipulator provides many passive DOF and we leverage this by making occasional, almost frictionless contacts with the rigid environment. Again, the computational solution does not prevent collisions, but simply minimizes their likelihood and magnitude.

Specifically, a rigid pipe-like environment with 3D-printed walls is used in these experiments. To create frictionless collisions, we coat the exterior of the robot with a thin layer of talc powder, reducing the friction between the robot and the wall. In order to constrain the robot's motion to the X-Y plane, reduce friction between the robot and the ground, and prevent segment torsion about the hollow core, small ball transfers are placed underneath each segment's soft endplate.

Before the robot autonomously snakes through the environment, it is reset to an initial near-zero curvature outside the confined environment (Figure 7-1A). Independent of the experiment's targeted final waypoint, the planner finds the same solution to maneuver the manipulator to the pipe-like environment's entrance (Figure 7-1B). As the planner autonomously advances the manipulator's end effector through the environment's center and considers the proximity of the changing envelope to the boundaries, collisions inevitably happen and are highlighted in red in Figure 7-1C. The manipulator successfully reaches one of four goal states depicted in Figure 7-1D-F. Table 7.1 contains data for several successful demonstrations of the manipulator

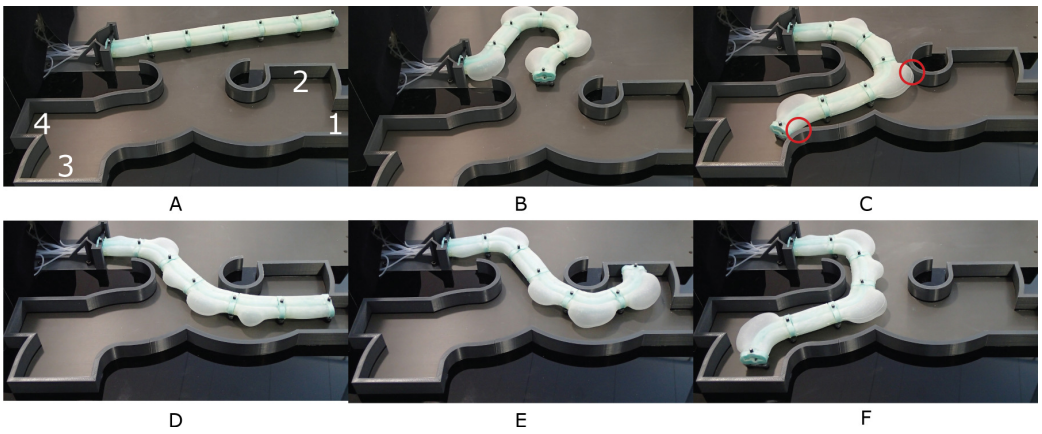

Figure 7-1: Experimental validation of the soft robot's ability to autonomously navigate through a confined environment: (A) The starting point of the robot and the positions of the goal locations, 1-4, are shown. (B) The manipulator advances to the entrance of the environment. (C) Example of the soft robot harmlessly colliding at two points with the boundaries of the environment. (D-F) The final goal points 1-3 are shown. This figure is reproduced from Marchese et al. [2014a].

advancing through the environment to the end goal poses. Approximately twelve waypoints were used along each path. t_{solve} is the average time the planner took to compute a solution at a given path waypoint in simulation. The position and orientation errors between the manipulator's end effector and the goal pose are also listed. t_{task} is the time the manipulator took to advance from the starting location to the goal pose. We have also indicated the number of collisions between the manipulator and the environment for several of these trials. Of thirty path attempts, twenty-four resulted in successful advances to goal locations and six were unsuccessful. The typical failure scenario was that the manipulator became lodged in the environment due to excessive contact friction.

The speed of the manipulator advancing along the path is limited by how quickly the target curvatures determined by the algorithm are realized by the physical system. In the ideal case, the system would realize target curvatures as fast as the algorithm computes them; however, because of the increased compliance of the manipulator and the lack of a dynamic and impedance model for the arm within this model-free approach, the algorithm must halt until the physical system can catch up. In order to improve the speed of the given physical system, the control policy should be optimized

Goal #	t_{solve} [s]	Trial #	Positional Error [cm]	Rotational Error [°]	t_{task} [s]	Collisions #
1	0.9	1	0.9	10.4	44	
		2	0.5	0.1	54	
		3	1.3	1.6	55	6
		4	0.7	1.3	50	4
		5	0.4	0.3	50	2
2	0.9	1	0.7	2.7	44	
		2	0.3	0.6	53	
		3	0.4	0.6	53	4
		4	1.1	5.3	53	2
		5	1.2	4.9	55	3
3	1.0	1	3.1	2.1	42	
		2	3.5	2.5	44	
		3	2.8	0.6	50	8
		4	2.4	4.5	49	6
		5	3.6	3.0	48	12
		6	1.3	1.7	50	
		7	3.5	8.7	52	7
		8	3.4	6.0	53	8
		9	3.4	4.9	50	8
4	1.1	1	4.1	10.7	60	
		2	5.1	17.5	48	4
		3	8.0	25.3	47	12
		4	6.1	21.4	48	7
		5	5.6	17.1	50	6
		6	4.4	14.7	53	13

Table 7.1: Experimental validation

to also consider the manipulator's dynamics as constraints. Our dynamic control approach is described in Chapter 6 and experimentally demonstrated in Section 7.2.

7.1.2 Grasping Delicate Objects

In Section 3.2.2.4 we showed that pleated grippers of similar dimensions like the one used in this work can be continuously actuated in a pressure range of 0 kPa to 60 kPa and create blocking forces in the range of 0 N to 2 N. This fine actuation range and the fact that soft manipulators easily conform to shapes implies that grasping delicate objects should be possible. The manipulator in fact picks up delicate objects such as eggs, shuttlecocks or bakery items without squishing or breaking them.

For example, Figure 7-3 shows how the manipulator approaches and grasps an egg. Delicate objects can be manipulated without requiring a shape or force sensor within

its structure, since the compliant gripper body conforms to the object. Rigid-bodied grippers typically rely on force sensing or another type of sensory feedback to avoid damage caused to the object.

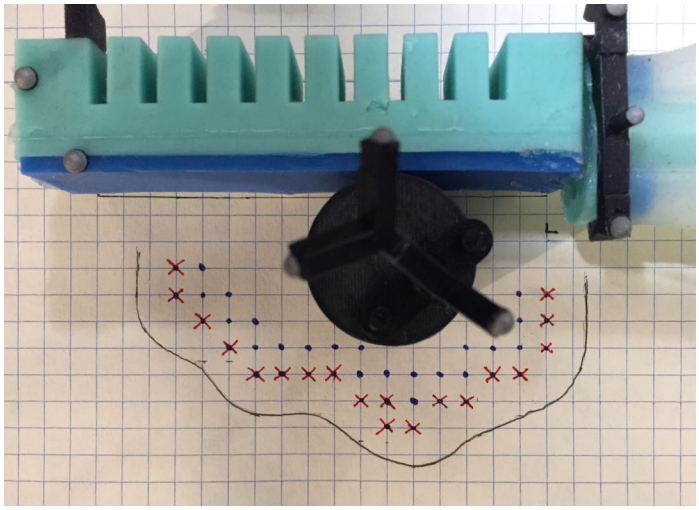

Figure 7-2: Experimental characterization of the pleated gripper's capture region: the allowable positioning uncertainty is determined through repeated placements of the center of a cylindrical object at different points on a 5 mm grid relative to the gripper. Blue dots indicate all object center positions for which a grasp could be performed successfully, red crosses show the positions where a grasp failed. The grey line outlines an area in which the object should be positioned so the gripper can grasp it. The evaluation of the capture region was performed similarly to a method described by Dogar and Srinivasa [2010]. This figure is reproduced from Katzschmann et al. [2015].

7.1.3 Grasp-and-Place

The nonlinear optimization grasp-and-place problem is implemented on a PC using Sequential Quadratic Programming, which iteratively finds the minimum of a constrained nonlinear multivariable function. The solver is run with a relative upper bound of 2×10^{-3} on the magnitude of the constraint functions. The lower bound of the size of a step was given by 1×10^{-6}. The solver takes about 1 s to solve for all waypoints from start to finish.

We implemented the planning algorithm described in Section 5.4.2 on the experimental platform in Section 3.6.9 with the soft manipulator arm of Section 3.6.7 mounted on it. We evaluated the manipulator system for repeatability and ability to

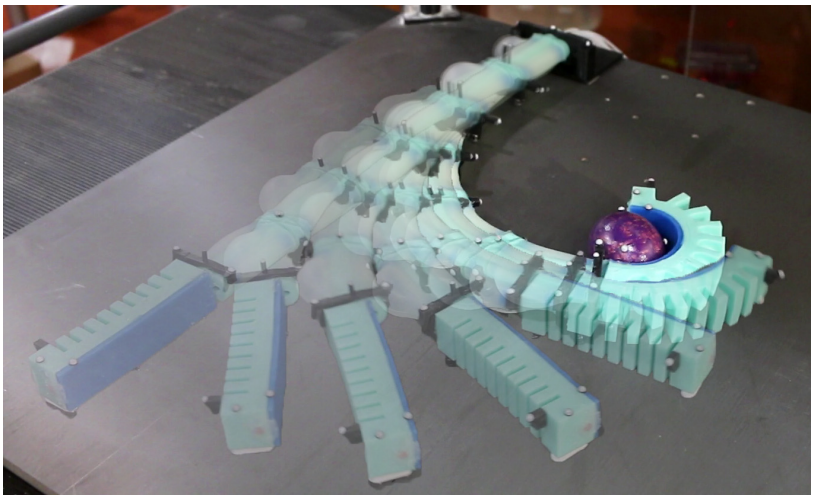

Figure 7-3: The multi-segment arm with an attached pleated gripper is grasping an egg. The robot repeatably approached, grasped and moved this object. This figure is adapted from Katzschmann et al. [2015].

handle uncertainty. The experiments consisted of picking and placing several objects of unknown geometry placed at an unknown location. We measured the execution time and captured the location data during the experiments. Specifically, we performed over 200 experimental grasp-and-place trials at randomly chosen positions within the reachable workspace to demonstrate the capabilities and repeatability of our system. We successfully picked up various objects such as eggs, shuttlecocks, bakery items, cups, light bulbs, and tape holders. An example of picking up an egg is shown in Figure 7-3. The objects had an enclosing diameter with a range of 2 cm to 5 cm. The results of a subset of those experimental trials are shown in Figure 7-4. One representative approaching, grasping, and retracting move is shown in Figure 7-5. In 23 of 25 experimental trials shown, the manipulator successfully achieved the task of grasping an object and placing it at a bin location shown in red. The test object has a weight of 18 g and a diameter of 3.3 cm. The object was placed five times on each of the five points marked on the board. The markers only serve as a reference point for the user to place the object roughly at the same point at every repetition. The user's placing accuracy is not important to the algorithm, since the tracking system re-registers the position of the object every time it is placed. The five points were chosen to approximately represent the major portion of the manipulator's reachable

workspace. As long as the root of the gripper stops so that the object is located within the capture region, the gripper will pick it up through its sweeping closing motion. The capture region is outlined in grey in Figure 7-2.

The evaluation of the capture region is performed similarly to a method described by Dogar and Srinivasa [2010] on determining capture regions for a push-grasp of a classical robotic gripper. Grid paper and fine markings on all four sides of the round object ensure that the placement by the user is accurate within ± 1 mm in relation to the discrete placement locations on the grid. This test serves as a qualitative measure to qualitatively show the relation between object size to gripper size to area of successful grasp. This characterization was repeated two times, resulting in nearly identical capture regions. Despite positioning inaccuracies of the soft manipulator, the gripper can nevertheless successfully perform a grasp of an object. The successful capture region can be characterized by about half a gripper length in diameter.

When the arm reaches its straight pose within a relatively large delta, it drops the object. For these experiments, we focus on showing the capability of picking up objects at various places and moving them around, there is no emphasis set on having to drop off the object at a specific place. To indicate that the arm can move the object after grasping, the arm was controlled to go back to its fully straight pose. When the arm reached the final straight pose within a 1 cm delta, the gripper was set to release and drop the object. It was not ensured by the planner that the arm had to first settle to zero velocity in its final straight pose. As a consequence of this, the experimental data indicates as a red bin a relatively wide drop-off area.

The unsuccessful trials happened due to stick-slip friction between the roller bearings and the table surface. Our kinematic modeling does not account for this non-linear behavior, which acts as a disturbance and can lead to failure to arrive at the next waypoint. To be more specific, in one of the trials, the robot slowed down too much before it almost reached its next waypoint and because of friction the arm halted to a full stop. The proportional gain of the curvature controller was not able to compensate for that small positional delta and since the relatively low saturation level of the integrator portion of the controller was saturated, the arm did

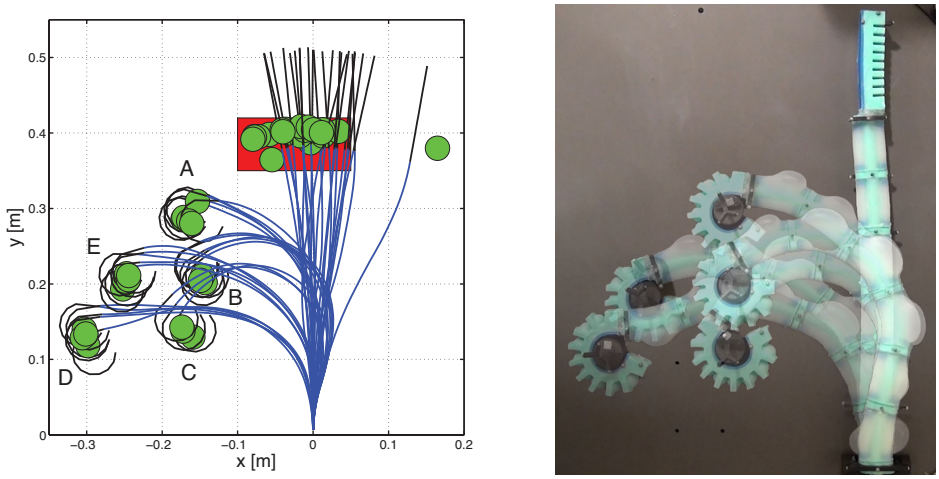

Figure 7-4: Left: Complete set of experimental grasp-and-place trials. In these experiments, the arm moves from an initial straightened configuration to grasp a round object placed in one of five locations (A-E). The arm then returns the object to a bin location shown in red. For each trial, a seven DOF manipulator representation is generated at both the *grasped* and *released* state using experimental data and is shown in blue. The corresponding 1 DOF end-effector representation is shown in black. The round object's measured position at each state is shown in green. In one of the trials, the grasp and return was successfully performed, but an overshoot over the final bin location caused the gripper to drop off the small table it is moving on. Right: Overlaid photographs of the manipulator grasping an object placed at each of the five locations. This figure is reproduced from Katzschmann et al. [2015].

not move to the next waypoint pose. It is to note, that the saturation level for the integrator is defined by a safety limit on the maximal inflation of the robotic arm. In the other unsuccessful trial, the stick-slip friction also caused the arm to halt before a waypoint. The controller built up enough force due to inflation, so that the arm slipped over the next waypoint without having all of its single arm segment curvature within an acceptable epsilon. The controller then tried to swing back to fulfill the missed waypoint, missed it again and that finally caused the whole arm to oscillate back-and-forth and eventually push the object off the table.

7.1.3.1 Experimental Insights and Limitations of Grasp-and-Place

The experiments show that the system was repeatably able to autonomously locate a randomly placed object within its workspace, plan the arm motions, and perform the task of grasping and placing the object. The system can drag payloads of less than 40 g,

higher payloads cause the cylindrical arm segments to stall and possibly lift off the table without moving the payload. There is a trade-off between the reachable workspace and the maximum payload. As the length of the arm increases, more workspace can be reached while less payload can be manipulated. A substantial portion of the payload capability of the arm is already used up by the attached gripper itself. A smaller gripper would allow for larger payloads to get picked up, but consequently only smaller objects can be grasped. The workspace of the manipulator is limited to the top and left by the maximal extension length of the arm, and to the bottom by the maximum bending curvature, which the arm can achieve without over-actuating a single segment. The gripper presented did not only pick up round objects, but also differently shaped objects of similar size, for example a star-shaped object, a tape holder, a shuttlecock, and an egg. Objects were only grasped within the left quadrant of the arm, because of the gripper orientation and an upright initial starting pose. A smoothing of the complete trajectory with several intermediate waypoints was found to be necessary. The amount of intermediate waypoints is determined by the variable Δd, which we found to be about the length of one arm segment. A new waypoint is sent to the controller immediately after arriving within a small delta of the previous waypoint, the controllers for each arm segment then compensate for the new delta in curvature as quickly as possible to come to the new pose κ_i^*. The unsuccessful grasps can in future be avoided by loosening the constraints on the planner. The planner could allow the arm controller to have the arm pass over each intermediate waypoint without having to get to a full stop within an arbitrarily chosen delta of curvature values. As a measure of progress, the planner could take a decreasing Cartesian distance of the gripper to its final target pose.

We developed an end-to-end system that can approximately locate an object placed at an a priori unknown location and move it to a desired location. The external localization system is a convenient way to approximately identify the location of the object and to track how the object is moved around. The exteroceptive tracking system has the disadvantage that the full occlusion of one or more markers can cause the tracking system to temporarily loose track of a measured arm segment. In this

case, the control loop cannot function properly until the occlusion is removed. The external localization system could be replaced with another method for localizing the manipulator and the object in the workspace. For example, adding proprioceptive sensors within the segments would partially solve this issue. Proprioceptive sensing was done for three soft fingers arranged as a hand in Section 3.6.2.

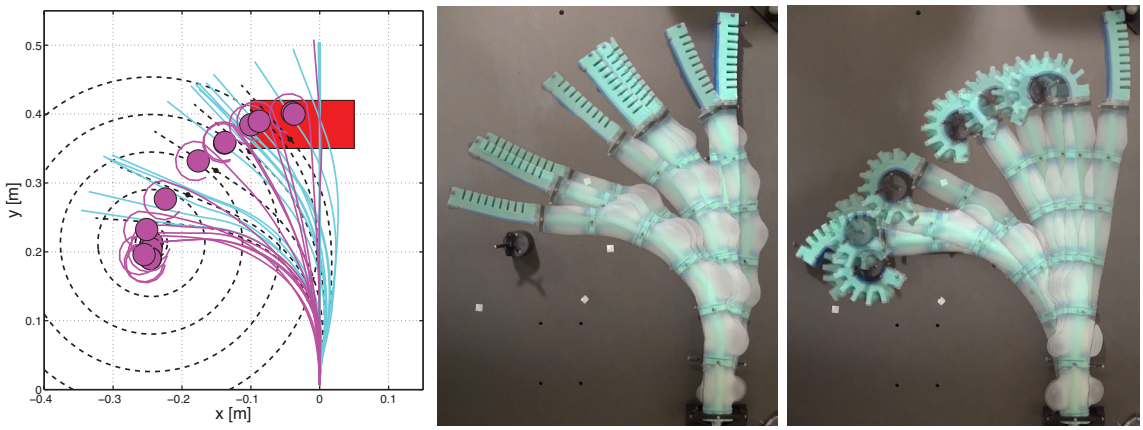

Figure 7-5: Left: A time series representation of an experimental grasp-and-place trial for an object located at point E of Figure 7-4. Here, the locally optimally planned manipulator configurations as well as planned sequential approach circles are shown as black dotted curves. Arm and gripper are shown in their experimentally determined configuration representations in 1 second intervals. The cyan configurations represent the manipulator prior to grasping the object, that is moving from its initial configuration to the object's location. Depending on where the object is placed, the manipulator takes between 17 s to 35 s to approach it. After grasping the object, the magenta configurations represent the manipulator moving from the object's location back to the bin location shown in red. This task of moving back to the bin takes between 10 s to 20 s. Right: Overlaid photographs of the manipulator moving from its initial pose to the object and from the object to the release location, respectively. This figure is reproduced from Katzschmann et al. [2015].

The experiments were performed for picking up objects on the left quadrant of the manipulator. Grasping objects on both sides of the manipulator could be achieved in various ways, including

1. replacing the large gripper at the end of the arm with two smaller grippers next to each other,

2. mounting roller supports on the top face of the manipulator and then rotating the manipulator at its root by 180°,

3. increasing the reachable workspace through starting the soft arm at an extreme curvature configuration within the right quadrant.

In order to improve the speed of the given physical system, the control policy should be optimized by also considering the manipulator's dynamics as constraints. We propose a dynamic control approach given in Chapter 6 and experimentally demonstrated in Section 7.2.

7.2 Experiments with Model-Based Dynamic Control

The validation of the model-based curvature and Cartesian impedance controllers is done through extensive simulations and experiments with a soft robotic arm (Section 3.6.6) using a soft hemisphere as end-effector (Section 3.6.8).

7.2.1 Simulations with a finite element model

In this section, we present the simulations done for the model-based dynamic feedback controller. We first introduce the finite element model (FEM) used for the simulation, followed by a description of the considered identification procedure. We then introduce the benchmark controller, which we then use for comparisons with our proposed curvature and Cartesian impedance controllers.

7.2.1.1 Finite element model

In this section we validate the proposed control strategies outside the design hypothesis of piecewise constant curvature. The control algorithms are applied to a planar soft manipulator that is simulated through a finite element model (FEM).

The total length of the arm is 1 m and is divided into six actuated segments with a length of 0.175 m. Each segment is discretized into 10 rigid links, connected through revolute joints with parallel axes. We refer to the joint angles as $q_{\mathrm{FEM}} \in \mathbb{R}^{60}$. Each link weighs 13 g and is connected to the subsequent element through a linear torsional

spring-damper system. The stiffness is $5\,\mathrm{N\,m\,rad^{-1}}$ and the damping is $20\,\mathrm{N\,m\,s\,rad^{-1}}$. The base frame is rotated so that in the rest position, that is $q_{\mathrm{FEM}} = 0$, the tip of the soft arm is pointing downwards and the soft arm is aligned with the direction of the gravitational field.

The state $q_{\mathrm{FEM}}, \dot{q}_{\mathrm{FEM}} \in \mathbb{R}^{60}$ of the soft robot is mapped in real-time to an equivalent vector of constant curvatures $q \in \mathbb{R}^6$ and their derivatives $\dot{q} \in \mathbb{R}^6$. The equivalent vector is then used by the controller. The mapping is done by matching the orientation of the end of each actuated segment with the corresponding element in the PCC model. In this particular example, this can be accomplished by summing up for all finite elements in one segment their angles and their angular velocities, respectively.

7.2.1.2 Identification

The model (6.18) has several free parameters, which are masses μ_i, lengths L_i, stiffnesses k_i, and damping d_i. We directly measure lengths L_i and masses μ_i. The data used for the identification are collected through a simulated experiment. A constant input torque of a magnitude of $1\,\mathrm{N\,m}$ is applied to each segment. The initial condition is $q_{\mathrm{FEM}} = 0\,\mathrm{rad}$, $\dot{q}_{\mathrm{FEM}} = 0\,\mathrm{rad\,s^{-1}}$.

The remaining parameters are identified by minimizing the $2-$norm of the error between the estimated and measured evolutions. This can be done by rewriting the dynamics as a balance between the known dynamical forces and the product of unknown parameters and their regressor [Ljung, 1998]. We use the More-Penrose pseudo-inversion to extract the solution

$$\begin{bmatrix} \hat{k} \\ \hat{d} \end{bmatrix} = \begin{bmatrix} \mathrm{diag}\{q_{\mathrm{meas}}(t_0)\} & \dots & \mathrm{diag}\{q_{\mathrm{meas}}(t_{\mathrm{f}})\} \\ \mathrm{diag}\{\dot{q}_{\mathrm{meas}}(t_0)\} & \dots & \mathrm{diag}\{\dot{q}_{\mathrm{meas}}(t_{\mathrm{f}})\} \end{bmatrix}^{+\mathrm{T}} f_{\mathrm{kn}}(q_{\mathrm{meas}}, \dot{q}_{\mathrm{meas}}, \ddot{q}_{\mathrm{meas}}) \qquad (7.1)$$

where $q_{\mathrm{meas}}(t)$, $\dot{q}_{\mathrm{meas}}(t)$, and $\ddot{q}_{\mathrm{meas}}(t)$ are the measured evolutions of q, $\dot{q}$, and $\ddot{q}$ at time t. Note that $\dot{q}_{\mathrm{meas}}$ and $\ddot{q}_{\mathrm{meas}}$ are computed through a polynomial fit of q_{meas}. The hat on $\hat{k}$ and $\hat{d}$ indicates that these are estimated values. With $f_{\mathrm{kn}}(q_{\mathrm{meas}}, \dot{q}_{\mathrm{meas}}, \ddot{q}_{\mathrm{meas}})$ we

refer to the set of known forces

$$f_{\mathrm{kn}}(q_{\mathrm{meas}}, \dot{q}_{\mathrm{meas}}, \ddot{q}_{\mathrm{meas}}) = -B\ddot{q} - C\dot{q} - G + \tau \tag{7.2}$$

evaluated for each element of q_{meas}, $\dot{q}_{\mathrm{meas}}$, and $\ddot{q}_{\mathrm{meas}}$.

The identified stiffness and damping are

$$\hat{k} = [0.499; 0.499; 0.499; 0.500; 0.498; 0.510]\mathrm{N\,m\,rad^{-1}},$$
$$\hat{d} = [2.00; 2.01; 2.02; 2.01; 2.03; 1.84]\mathrm{N\,m\,s\,rad^{-1}}.$$

7.2.1.3 Benchmark Controller

We compare the simulated results against state-of-the-art benchmarks in soft continuum robot manipulators. More specifically, for regulating the robot's configuration q we consider a proportional–integral–derivative (PID) controller as discussed in Bajo et al. [2011], Marchese and Rus [2016], George Thuruthel et al. [2018] and described by

$$\tau = k_{\mathrm{P}}\,(\bar{q} - q) + k_{\mathrm{I}} \int (\bar{q} - q) + k_{\mathrm{D}}\,(\dot{\bar{q}} - \dot{q})\,, \tag{7.3}$$

where $\bar{q}$ and $\dot{\bar{q}}$ are a reference curvature and its derivative, for example defined by (7.5). k_{P}, k_{I}, k_{D} are the PID gains to be tuned.

In the state of the art, we could not find any insight about tuning the PID gains for soft robots. In order to have a standard comparison, we consider the well-known Skogestad Internal Model Control (SIMC) tuning rule [Skogestad, 2003], which can be regarded as the state of the art in PID tuning. Using the SIMC-PID tuning, the resulting gains are

$$\begin{aligned} k_{\mathrm{P}} &= \mathrm{diag}\{7.2,\ 3.6,\ 9.3,\ 11.2,\ 9.0,\ 7.2\}\mathrm{N\,m\,rad^{-1}}, \\ k_{\mathrm{I}} &= \mathrm{diag}\{2.8,\ 3.2,\ 3.4,\ 3.6,\ 3.7,\ 4.0\}\mathrm{N\,m\,rad^{-1}\,s^{-1}}, \\ k_{\mathrm{D}} &= \mathrm{diag}\{0.9,\ 1.3,\ 1.4,\ 1.8,\ 1.8,\ 1.8\}\mathrm{N\,m\,rad^{-1}\,s}. \end{aligned} \tag{7.4}$$

To regulate the end effector for this comparison, we use the kinematic inversion

algorithm

$$\dot{\bar{q}} = J^{+}(q)(x_{\mathrm{d}} - x) \ , \tag{7.5}$$

where q is the robot's configuration, x_{d} is the desired end effector position and x is the actual end effector position. $\dot{\bar{q}}$ and $\bar{q}$, obtained by direct integration, are then commanded to the PID controller (7.3)-(7.4) to regulate towards x_{d}. The use of the kinematic inversion algorithm in continuous soft robots is discussed for example by Webster and Jones [2010], Zhang et al. [2016], George Thuruthel et al. [2018].

7.2.1.4 Trajectory tracking in joint space

We test the ability of the curvature controller (6.29) to produce an accurate trajectory tracking in curvature space q with the following trajectory

$$\bar{q}(t) = \begin{bmatrix} \frac{\pi}{12} & \dots & \frac{\pi}{12} \end{bmatrix}^{\mathrm{T}} \sin(\omega t) \ . \tag{7.6}$$

We consider 20 logarithmically distributed frequencies ω, from $0.1\,\mathrm{rad\,s^{-1}}$ to $10\,\mathrm{rad\,s^{-1}}$, with both our proposed controller (6.29) and the benchmark controller (7.3)-(7.4). The robot starts in the initial condition $q_{\mathrm{FEM}} = 0\,\mathrm{rad}$, $\dot{q}_{\mathrm{FEM}} = 0\,\mathrm{rad\,s^{-1}}$. For each trial, we simulate 120 s to properly capture the steady state behavior. The performance is evaluated through the L_2 norm defined as

$$p_{\mathrm{L2}} = \sqrt{\int_0^{t_{\mathrm{f}}} \frac{|\bar{q} - q|_2^2}{t_{\mathrm{f}}}} \ , \tag{7.7}$$

where $t_{\mathrm{f}} = 120\,\mathrm{s}$, and $|\cdot|_2$ is the Euclidean norm. Figure 7-6 presents the results of these simulations. The proposed controller (6.29) outperforms the benchmark controller (7.3)-(7.4) for almost all the considered frequencies. While for quasi-static conditions the two controllers have comparable performances, the PID performance monotonically decreases with an increase in frequency. On the contrary, the performance of the proposed controller is even better in dynamic conditions than in static conditions. Figure 7-7 shows the evolution of the curvature q in time, for $\omega = 1\,\mathrm{rad\,s^{-1}}$. The PID controller is able to track with sufficient accuracy only the

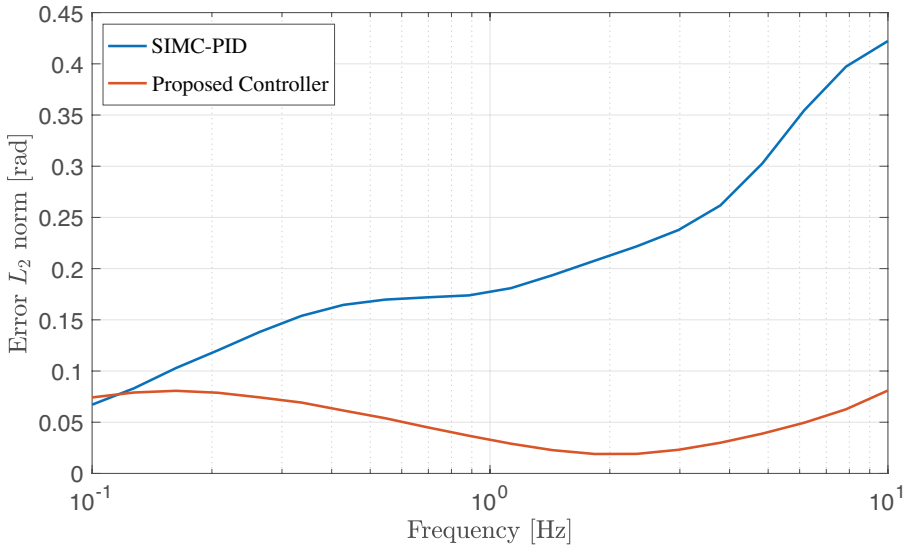

Figure 7-6: Simulation results of the tracking of a sinusoidal reference are shown in curvature space. The task is repeated by varying the frequency ω of the reference trajectory (7.6). The proposed curvature controller (6.29) outperforms the classic SIMC-PID controller in almost all the considered frequencies. In quasi-static conditions the two controllers have comparable performance.

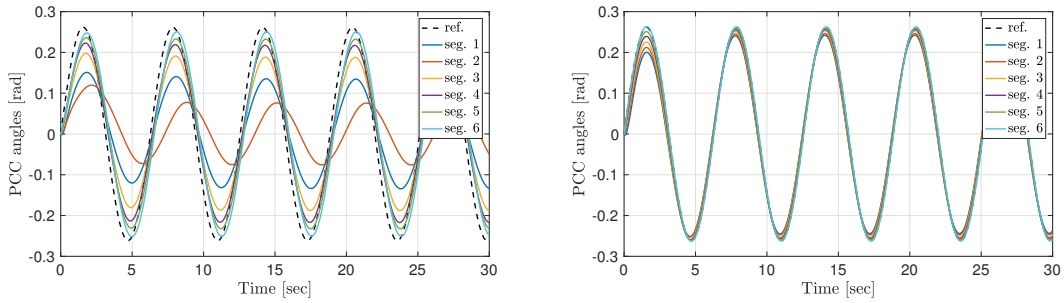

(a) SIMC-PID

(b) Proposed Controller

Figure 7-7: Evolution in curvature space q shown for the trajectory tracking of (7.6), with $\omega = 1\,\mathrm{rad\,s^{-1}}$. The SIMC-PID performs poorly in the segments closer to the base. The proposed curvature control algorithm (6.29) is able to exploit the knowledge of the robot's dynamics to achieve good tracking performance.

reference curvatures of those segments that are close to the tip of the robot. The dynamic effects are less relevant for these elements close to the tip of the robot. On the contrary, the proposed controller is able to correctly regulate with good precision all degrees of curvature q on the desired trajectory.

7.2.1.5 Cartesian Impedance Control and Surface Tracing

We consider the task of reaching a point on a planar surface. The surface is placed vertically at a 0.4 m distance from the robot's rest position, as shown in Figure 7-8. The surface is simulated as a repelling force field with sigmoidal characteristics described as

$$f_{\mathrm{ct}} = \frac{f_{\mathrm{mag}}}{1 + \exp(-a_{\mathrm{Gain}}\delta_{\mathrm{pen}})} \tag{7.8}$$

where $a_{\mathrm{Gain}} = 10^4$ is the gain, $f_{\mathrm{mag}} = 10\,\mathrm{N}$ is the force magnitude, and δ_{pen} is the penetration depth relative to the surface. As before, two control strategies are considered: the benchmark (7.3)-(7.5), and the proposed Cartesian impedance controller (6.35). The desired Cartesian stiffness is $K_{\mathrm{C}} = \mathrm{diag}\{3,\ 3\}\mathrm{N\,m^{-1}}$, and the desired Cartesian damping is $D_{\mathrm{C}} = \mathrm{diag}\{3,\ 3\}\mathrm{N\,s\,m^{-1}}$. For both controllers the reference x_{d} is planned as described in Section 6.6. For phase 1, we consider the point inside the environment $x_0 = [1\ \ -0.5]^{\mathrm{T}}\mathrm{m}$. The control algorithm tries to regulate the end effector to that point, that is $x_{\mathrm{d}} = x_0$, until a contact with the environment is established. The magnitude of the displacement δ_{ct} in Algorithm 6.1 for this simulation is chosen to be equal to 0.5 m. Each closed-loop system is then simulated for a duration of 30 s.

Figure 7-8 shows the resulting behavior of the soft robot for each of the two controllers. The benchmark (Panel (a)) behaves well until contact with the environment is established. After that, it starts moving the end effector in the wrong direction, away from the target. This is due to the non-diagonal form of the Cartesian stiffness matrix. A horizontal force generates a vertical displacement due to the non-diagonal coupling terms. The robot ends up stuck in an undesired equilibrium while pushing towards the wall. On the contrary, the proposed controller produces a desired impedance

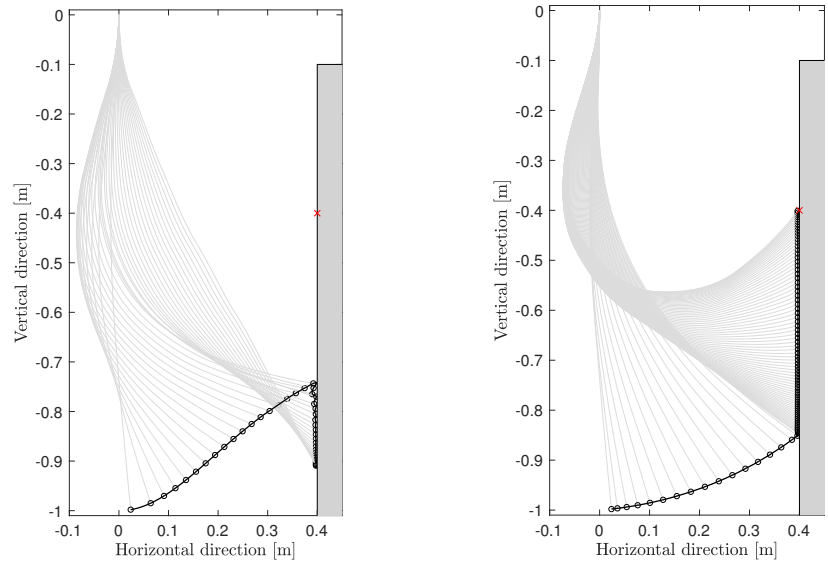

(a) SIMC-PID (b) Proposed Control

Figure 7-8: Two sequences represent the robot's behavior during a full simulation for the two considered controllers: benchmark controller (7.3)-(7.4) in panel (a), and proposed curvature controller (6.29) in panel (b). The trajectory of the end effector is represented by the black solid line. In the first phase, the soft robot approaches the environment, which is represented by a gray rectangle. After that follows the second phase, where the controller tries to move the tip of the robot along the surface to the target point, which is represented by a red cross. The benchmark controller moves in the wrong direction and then remains stuck in an undesired configuration, while the proposed controller reaches the desired configuration with negligible error.

behavior at the end effector and does not manifest this problem. Figure 7-9 presents the evolution over time for the position of the end effector.

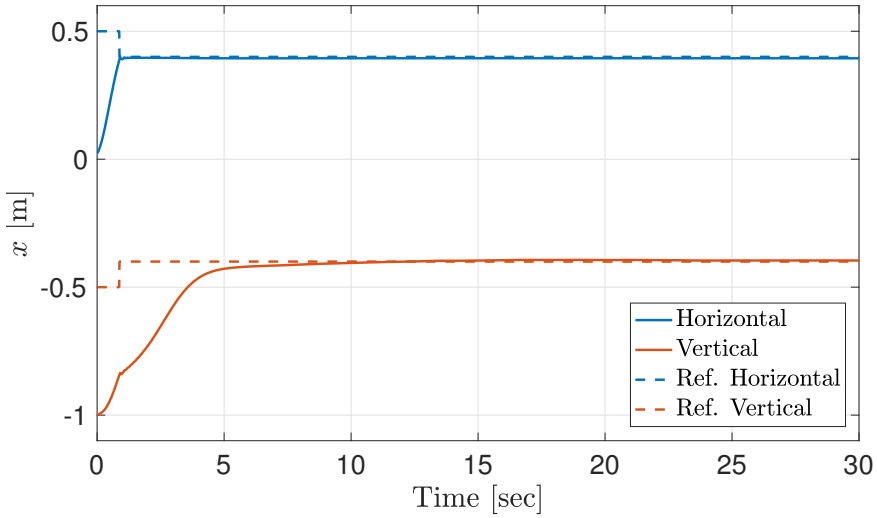

Figure 7-9: The evolution of the soft robot's tip is shown in Cartesian space. The horizontal direction is orthogonal to the surface, and thus after the contact it remains constant.

In Figure 7-10 we present the evolution of full configuration q_{FEM} and equivalent degree of curvature q for the six segments comprising the soft robot. It is interesting to note that the algorithm works properly despite the fact that the actual local curvatures, represented as dotted lines, are widely spread around the equivalent PCC curvature, shown as a solid line.

Repeating the two simulations for 30 targets equally distributed between $[0.4, -0.8]$m and $[0.4, -0.2]$m, the benchmark (7.3)-(7.5) always presents the same poor behavior. The proposed controller in contrast is always able to regulate the tip of the soft robot onto the desired position, with an average error over all repetitions of $2\,10^{-3}$m (minimum $2.0\,10^{-5}$m, maximum $9.5\,10^{-3}$m).

7.2.2 Physical Experiments

A planar soft robotic arm with a soft hemisphere as end-effector as described in Section 3.6.8 is used to validate the effectiveness of the model-based dynamic controllers. Figure 7-11 shows the arm while tracing along a wall.

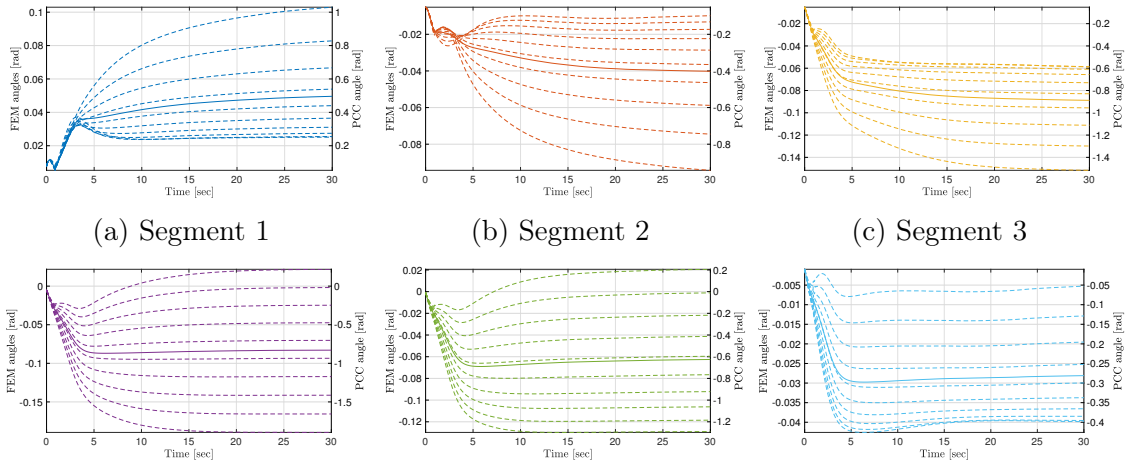

(a) Segment 1 (b) Segment 2 (c) Segment 3

(d) Segment 4 (e) Segment 5 (f) Segment 6

Figure 7-10: The evolution of the curvature of each segment is shown over time. The equivalent PCC curvature q is presented as a solid line, while the corresponding angles of the FEM are presented as dotted lines. In each segment the actual local curvatures of each finite element are widely spread around the PCC curvature q, showing that the FEM simulation is outside the simplifying hypothesis of constant curvature per segment.

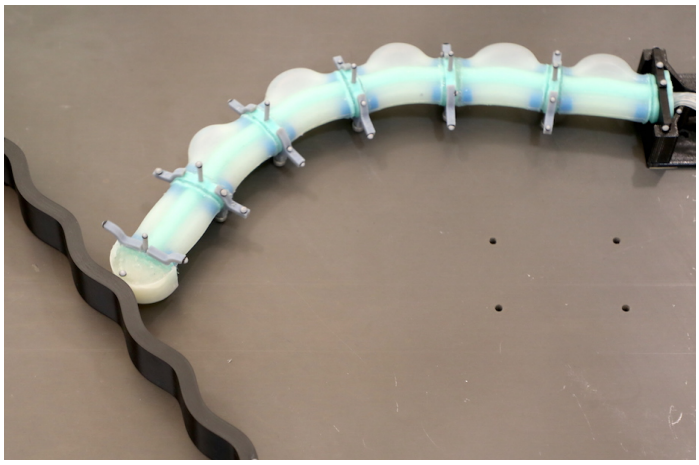

Figure 7-11: A dynamically controlled soft robot approaches and then traces along an environment. The robot has six actuated soft segments and is controlled through a model-based Cartesian impedance regulator, one of two control architectures presented in this paper.

In this section, we start by briefly describing the experimental setup, followed by the identification procedure. Using these identified parameters, we then validate on the physical prototype the proposed curvature controller and the Cartesian impedance controller with surface tracing.

7.2.2.1 Experimental Setup

The available inputs to our soft robot are the desired placements of the pistons within the cylinders. They are expressed in encoder tics, ranging from 0 to 1000 tics. This value is regulated by a local PID controller on the motor controller board[1] of each linear actuator. The relationship between the desired placement of the piston and the exerted force by a chamber can be approximated as linear through the ideal gas law and by the hypothesis of homogeneous pressure distribution over the segment's interior chamber and the volume in the cylinder. When a positive torque within a segment is required by the controller, the right chamber of a segment is inflated and the left chamber is deflated by the same amount. Vice versa, an inflation of the left chamber is required for creating a negative torque. In order to avoid a dead zone effect that otherwise would be present in case of low actuation pressures, we pre-load each chamber. The amount of pre-loading is heuristically defined as the lowest value for which a sinusoidal oscillation with an amplitude of 100 tics is visually perceivable. The resulting linear characteristics between the desired torque τ_i and the corresponding placement of the i-th piston l_i is

$$\tau_i = \zeta_i \, l_i \tag{7.9}$$

where the static gain ζ_i collects all the previously described effects, and it is identified through data fitting in the following Section 7.2.2.2. Figure 7-12 supports the hypothesis of linearity in actuation and stiffness by showing the steady state reached by a single segment for a set of inputs l_i.

Groups of four motion capture markers (Section 3.6.9) are placed at the root and at the end of each segment in order to identify the reference frames $\{S_0\}, \ldots, \{S_6\}$.

[1] Polulu Jrk 12v12

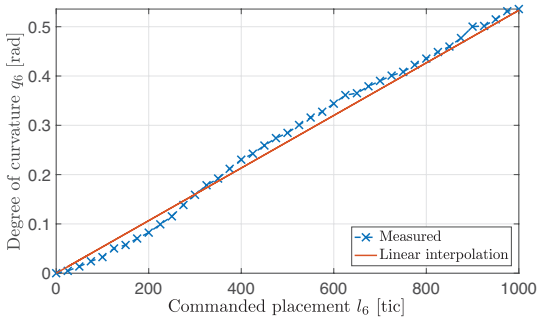

Figure 7-12: Steady state in degree of curvature q_6 is reached by the tip segment in response to a set of inputs l_6. The relation is close to a straight line, as graphically shown by the linear least squares fitting shown as a solid line. This experiment validates (7.9) and (6.14), according to which the graph would have been a straight line with slope $\frac{3\,\zeta_6}{2\,\varrho_6 \Delta_{\text{imp},6}^3}$.

The degree of curvature q is evaluated by measuring the relative rotation between the frames, and the derivative $\dot{q}$ is obtained through numerical derivation of q.

The software architecture is executed on two PC workstations (Figure 3-31-G). The first workstation acquires in real-time data from the motion capture system, evaluates the control action, and communicates it to the second workstation via User Datagram Protocol (UDP). The code is implemented in MATLAB [Matlab, 2017]. We use Peter Corke's robotics toolbox [Corke, 1996] to evaluate B_ξ, C_ξ, G_ξ, and J_ξ in (6.10). In the experiments that we present in the next sections, the code runs with a control loop period of $0.0169 \pm 0.0023\,\text{s}$ for the curvature controller (6.29), and with a control loop period of $0.0199 \pm 0.0089\,\text{s}$ for the Cartesian impedance controller (6.35). The second workstation receives the messages and interfaces with the motor control boards of the linear actuators.

7.2.2.2 Identification

The identification procedure is analogous to the one introduced in Section 7.2.1.2. In addition to stiffness k and damping d, we account here for the presence of the actuators by introducing a set of gains ζ_i statically mapping the placement of the piston within its pneumatic cylinder l_i into corresponding segment torques τ_i, as in (7.9). To prevent over-fitting we hypothesize the same damping value $d = [d_1 \dots d_1]$

for each segment of the robot. The resulting estimation is

$$\begin{bmatrix} \hat{\zeta} \\ \hat{k} \\ \hat{d}_1 \end{bmatrix} = \begin{bmatrix} -\mathrm{diag}\{l_{\mathrm{meas}}(t_0)\} & \dots & -\mathrm{diag}\{l_{\mathrm{meas}}(t_{\mathrm{f}})\} \\ \mathrm{diag}\{q_{\mathrm{meas}}(t_0)\} & \dots & \mathrm{diag}\{q_{\mathrm{meas}}(t_{\mathrm{f}})\} \\ \dot{q}_{\mathrm{meas}}(t_0)^{\mathrm{T}} & \dots & \dot{q}_{\mathrm{meas}}(t_{\mathrm{f}})^{\mathrm{T}} \end{bmatrix}^{+\mathrm{T}} f_{\mathrm{kn}}(q_{\mathrm{meas}}, \dot{q}_{\mathrm{meas}}, \ddot{q}_{\mathrm{meas}}) \,, \quad (7.10)$$

where $q_{\mathrm{meas}}(t)$, $\dot{q}_{\mathrm{meas}}(t)$, and $\ddot{q}_{\mathrm{meas}}(t)$ are the measured evolutions of q, $\dot{q}$, and $\ddot{q}$ at time t. $l_{\mathrm{in}}(t)$ is the generated input at time t. With f_{kn} we refer to the set of known forces $-B\ddot{q} - C\dot{q} - G$ evaluated for each element of q_{meas}, $\dot{q}_{\mathrm{meas}}$, and $\ddot{q}_{\mathrm{meas}}$. Note that for the planar motion on a horizontal surface, we set $G = 0$.

The identification data are collected in three experiments. In each one a saturated ramp is injected into each pneumatic cylinder. The amplitudes are 500 tics, 700 tics, and 900 tics, respectively. We choose a ramp with a slope equal to 166 tics s^{-1} for all the experiments, manually fixed to be under the saturation threshold of the velocity of the motors. We run the whole identification procedure at the beginning of each session of experiments. The identified parameters across 10 runs of the algorithm are

$$\begin{aligned} k &= [6.0,\ 6.5,\ 6.5,\ 6.6,\ 5.7,\ 3.7]^{\mathrm{T}}\, 10^{-2} \\ &\quad \pm [0.24,\ 0.32,\ 0.43,\ 0.55,\ 0.84,\ 0.52]^{\mathrm{T}}\, 10^{-2} \mathrm{N\,m\,rad}^{-1} \\ d &= [0.0119 \dots 0.0119] \\ &\quad \pm [0.0025 \dots 0.0025] \mathrm{N\,m\,s\,rad}^{-1} \\ \zeta &= [2.4,\ 3.4,\ 2.7,\ 2.8,\ 3.4,\ 2.3]^{\mathrm{T}}\, 10^{-5} \\ &\quad \pm [5.0,\ 7.2,\ 6.0,\ 9.0,\ 7.6,\ 6.4]^{\mathrm{T}}\, 10^{-7} \mathrm{N\,m\,tics}^{-1} \,. \end{aligned} \quad (7.11)$$

The lengths $L = [0.06 \dots 0.06]$m and the masses $\mu_i = [0.334 \dots 0.334]$kg are directly measured.

7.2.2.3 Curvature Control

To test the curvature controller (6.29), we start by considering the tracking of a sinusoidal trajectory

$$\begin{aligned} \bar{q}_i(t) = \alpha\,(1+\cos(\omega\,t)) \quad & \forall i \in \{1,\dots,6\}\ , \quad t \in [0,20)\text{s} \\ & \forall \alpha \in \frac{\pi}{180}\{7,10,13\}\text{rad} \\ & \forall \omega \in \frac{2\pi}{20}\{7,8,9,10\}\text{rad}\,\text{s}^{-1}\ , \end{aligned} \tag{7.12}$$

thus testing the effectiveness of the proposed controller for an exhaustive range of frequencies and amplitudes. Note that the control action τ is mapped to the desired piston length l through division by the identified static gains ζ.

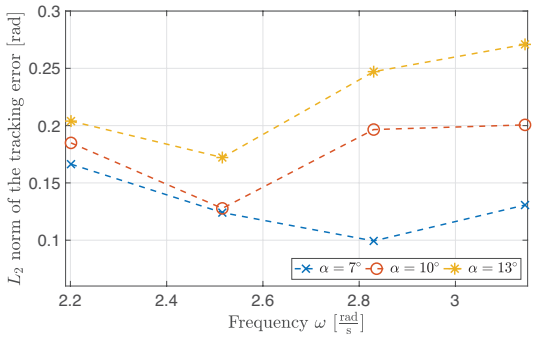

Figure 7-13: Experimental performance of the curvature controller (6.29) is shown for tracking the sinusoidal trajectory (7.12). We consider twelve pairs with varying amplitude α and frequency ω. For each pair we report the L_2 norm p_{L2} (7.7) as our performance metric. Note that the best tracking performance is reached for intermediate values of the frequency ω. This is mainly due to unmodeled static friction at low frequencies, and saturations in the control action for high frequency.

Figure 7-13 presents tracking performances expressed in L_2 norm of the tracking error (7.7), with $t_{\text{f}} = 20\,\text{s}$. The algorithm is able to produce a stable oscillation close to the commanded one for all considered trajectories.

Note that the best performances are obtained for intermediate values of the frequency ω. This can be explained by considering that for low frequencies the quality is diminished by the presence of static friction between the robot and the plane, while for higher frequencies the required torque is often above the saturation limits.

Figure 7-14 shows the evolution of degrees of curvature q and commanded torques τ

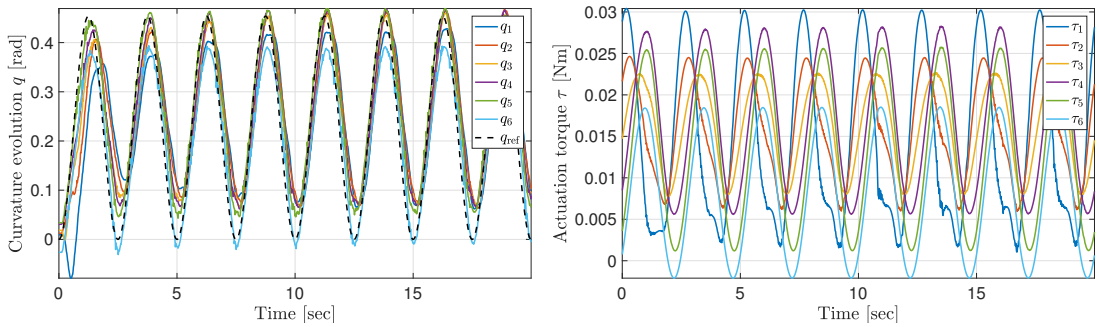

(a) Curvature (b) Torques

Figure 7-14: Experimental evolutions over time resulting from the application of the curvature controller (6.29) in tracking the trajectory (7.12) for $\alpha = 13°$ and $\omega = 2.5133\text{rad}\,\text{s}^{-1}$. Panel (a) shows the evolution of the degree of curvature q for the tracking experiment, while panel (b) presents the corresponding actuation torques τ.

for a case with average performances, that is $\alpha = 13°$ and $\omega = 2.5133\text{rad}\,\text{s}^{-1}$.

In Figure 7-15 a-e, we report the photo sequence of one of the resulting oscillations for the same trajectory.

In Figure 7-16 we present the tracking of

$$\bar{q}_i(t) = \begin{cases} +13\frac{\pi}{180}\left(1+\cos(8\frac{2\pi}{20}\,t)\right) & \text{if } i \in \{1,2,3\} \\ -13\frac{\pi}{180}\left(1+\cos(8\frac{2\pi}{20}\,t)\right) & \text{if } i \in \{4,5,6\}\ , \end{cases} \tag{7.13}$$

with $t \in [0, 20)$s, and Figure 7-15 f-j shows the photo sequence of one of the resulting oscillations.

Finally, in Figure 7-17 we present the tracking of

$$\bar{q}_i(t) = \begin{cases} 0 & \text{if } i \in \{1,2\} \\ 13\frac{\pi}{180}\left(1+\cos(10\frac{2\pi}{20}\,t)\right) & \text{if } i \in \{3,4,5,6\}\ , \end{cases} \tag{7.14}$$

with $t \in [0, 20)$s, and Figure 7-15 k-o shows the photo sequence of one of the resulting oscillations. Relying on the knowledge about the model, the algorithm is able to anticipate the necessary control action to maintain the first two segments still, despite the large oscillation of the remaining four segments. This is evident from the evolution

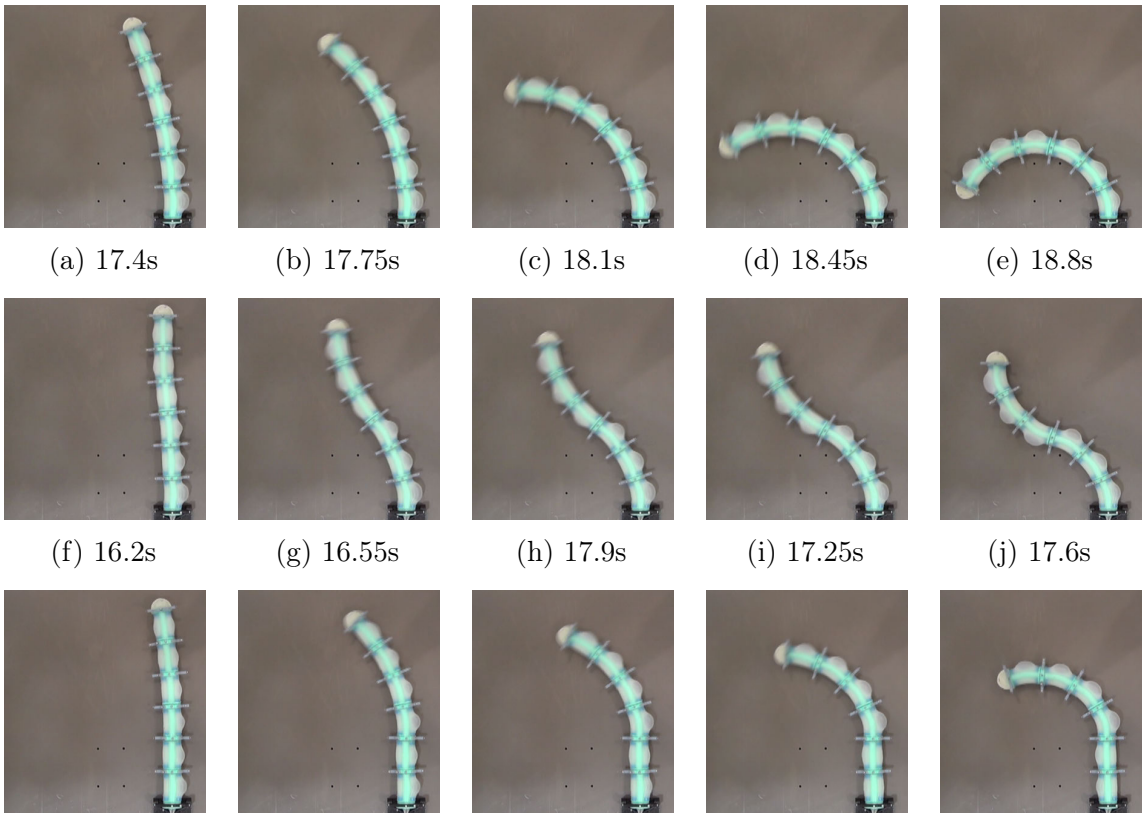

(a) 17.4s (b) 17.75s (c) 18.1s (d) 18.45s (e) 18.8s

(f) 16.2s (g) 16.55s (h) 17.9s (i) 17.25s (j) 17.6s

(k) 17s (l) 17.25s (m) 17.5s (n) 17.75s (o) 18s

Figure 7-15: Photo sequence of one oscillation resulting from the application of the curvature controller (6.29). Panels a-e show how the arm is tracking trajectory (7.12), with $\alpha = 13^\circ$ and $\omega = 2.5133\text{rad}\,\text{s}^{-1}$. Panels f-j show the tracking of trajectory (7.13). Panels k-o show the tracking of trajectory (7.14).

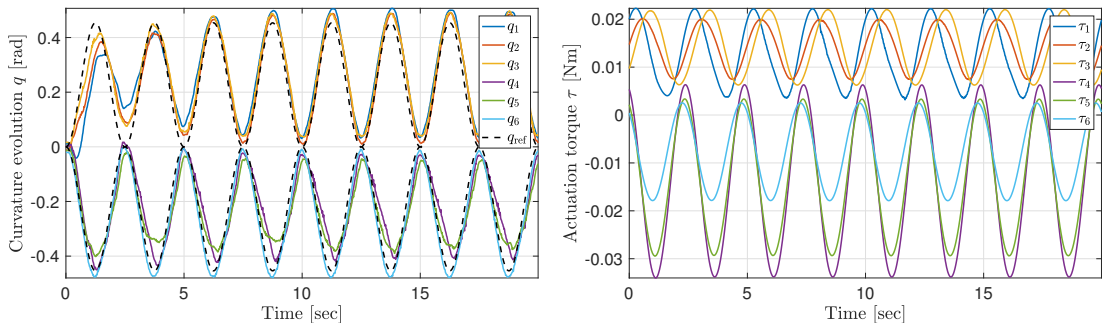

(a) Curvature (b) Torques

Figure 7-16: Experimental evolutions resulting from the application of controller (6.29) in tracking trajectory (7.13). Panel (a) shows the degree of curvature q evolution for the tracking experiment, while panel (b) presents the corresponding actuation torques τ.

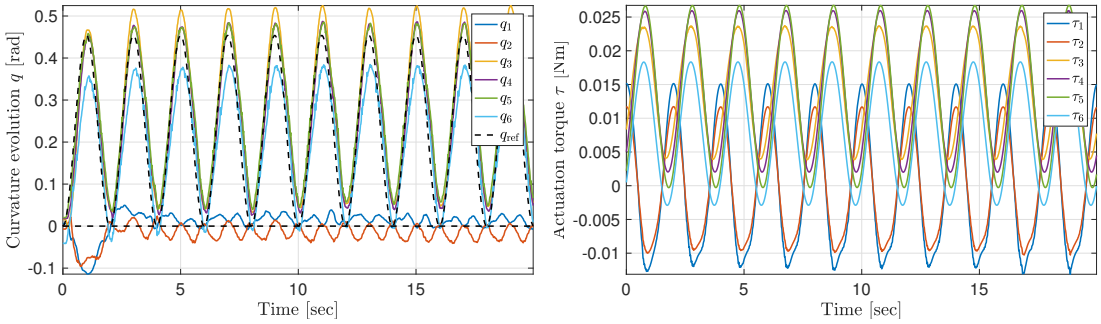

(a) Curvature (b) Torques

Figure 7-17: Experimental evolutions resulting from the application of the curvature controller (6.29) in tracking trajectory (7.14). Panel (a) shows the degree of curvature q evolution for the tracking experiment, while panel (b) presents the corresponding actuation torques τ.

of τ_1 and τ_2 in Figure 7-17b, which have a larger amplitude and a phase shift of about half a period relative to τ_3, τ_4, τ_5, τ_6.

7.2.2.4 Cartesian Impedance Control and Surface Following

Figure 7-18 presents the evolutions resulting from the application of (6.35) in regulating the soft robot's end effector position.

The input to the pistons l is produced through division of τ (Figure 7-18c) by the identified static gains ζ. We approximate here $D \simeq 0$. The desired impedance at the end effector is

$$
\begin{aligned}
K_{\mathrm{C}} &= \begin{bmatrix} 0.825 & 0 \\ 0 & 0.825 \end{bmatrix} \mathrm{N\,m^{-1}}, \\
D_{\mathrm{C}} &= \begin{bmatrix} 0.25 & 0 \\ 0 & 0.25 \end{bmatrix} \mathrm{N\,m^{-1}\,s}\,.
\end{aligned}
\tag{7.15}
$$

The desired end effector position is $x_{\mathrm{d}} = [0.2637,\ 0.2196]^{\mathrm{T}}\mathrm{m}$, and it was manually defined to be approximately in the center of the robot's reachable space. Figure 7-18a shows the evolution of end effector position x expressed in Cartesian coordinates. The system reaches the correct steady state after an oscillatory transient, coherent with the imposed behavior. Such oscillations reflect into more complex non-linear oscillations

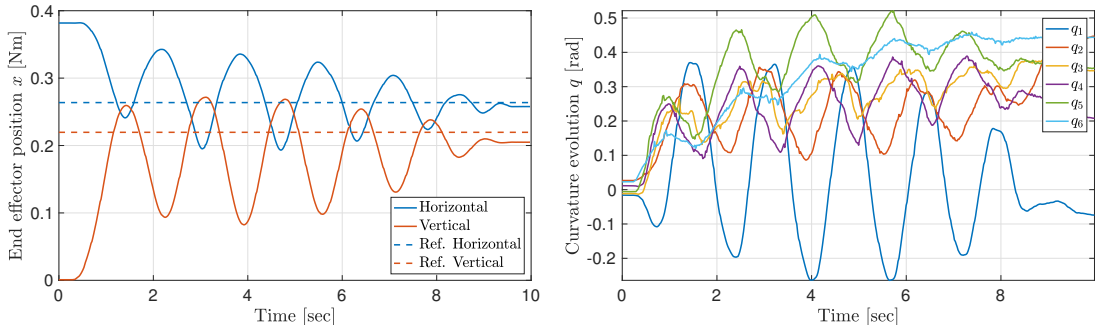

(a) End Effector (b) Curvature

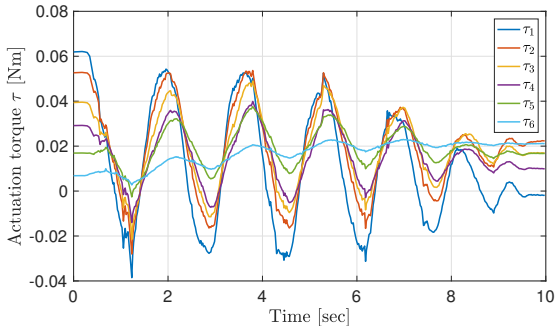

(c) Torques

Figure 7-18: Experimental evolutions resulting from the application of the Cartesian impedance controller (6.35) in regulating the end effector position. Panel (a) shows the evolution of the end effector x, dashed lines indicate the desired steady state, solid lines show the resulting evolution. Panel (b) shows the degree of curvature q evolution for the tracking experiment, while panel (c) presents the corresponding actuation torques τ.

of the degrees of curvature q presented in Figure 7-18b.

However, the main feature of the Cartesian impedance regulator is to generate reliable interactions with an unstructured environment. We thus test (6.35) in combination with Algorithm 6.1, in implementing the desired surface tracing behavior.

At the beginning of each experiment, a surface is placed in front of the robot, as shown in Figure 7-19 a, f, k, p, and u. Remember that the robot is not aware of the exact shape of the surface, nor its position. The only information that Algorithm 6.1 uses are the presence of a contact, a measure of the local tangent direction $n_{\|}$, and the coordinates of a point included in the surface; for further details see Section 6.6. This set of information is produced through geometric considerations and the measurement of the environment's location through the motion capture system. The robot's target is to first reach the surface and then slide along it until the desired position is reached.

Note that we are not interested in a precise regulation of the contact forces. Instead, the constraint imposed by the environment is purposefully exploited in combination with the decoupled compliance imposed by the control, to naturally generate the interaction forces and guide the end effector towards the desired position.

As described in Algorithm 6.1, the experiment is divided into two phases. In the first phase, the end effector of the soft robot is attracted toward a point within the environment, which is manually defined. After contact is established, it triggers the execution of the second phase. The end effector is now pulled toward a new target while staying in contact with the environment.

We repeat the experiment for five different locations of the environment. For all the experiments $\delta_{\mathrm{ct}} = 0.05\,\mathrm{m}$, and K_{C} and D_{C} are as given in (7.15). We collect in Figure 7-19 the photo sequences of the robot successfully performing the task of approaching and tracing along the environment. Figure 7-20 presents the evolutions over time of the end effector position x, degrees of curvature q, and commanded torques τ for the sequence shown in Figure 7-19 a-e. Here, the initial target is $x_0 = [0.3637, 0.1406]^{\mathrm{T}}\mathrm{m}$ and the final target is $x_{\mathrm{d}} = [0.2307, 0.2576]^{\mathrm{T}}\mathrm{m}$. The first contact with the environment is detected around 1.1 s after the beginning of the experiment, happening just after Figure 7-19b. This is evident in the change of reference position in Figure 7-20a. The tracing occurs between $t = 1.1\,\mathrm{s}$ and $t = 3.8\,\mathrm{s}$. Note how the traced folds of the environment can be recognized in the shape of the evolution in end effector position.

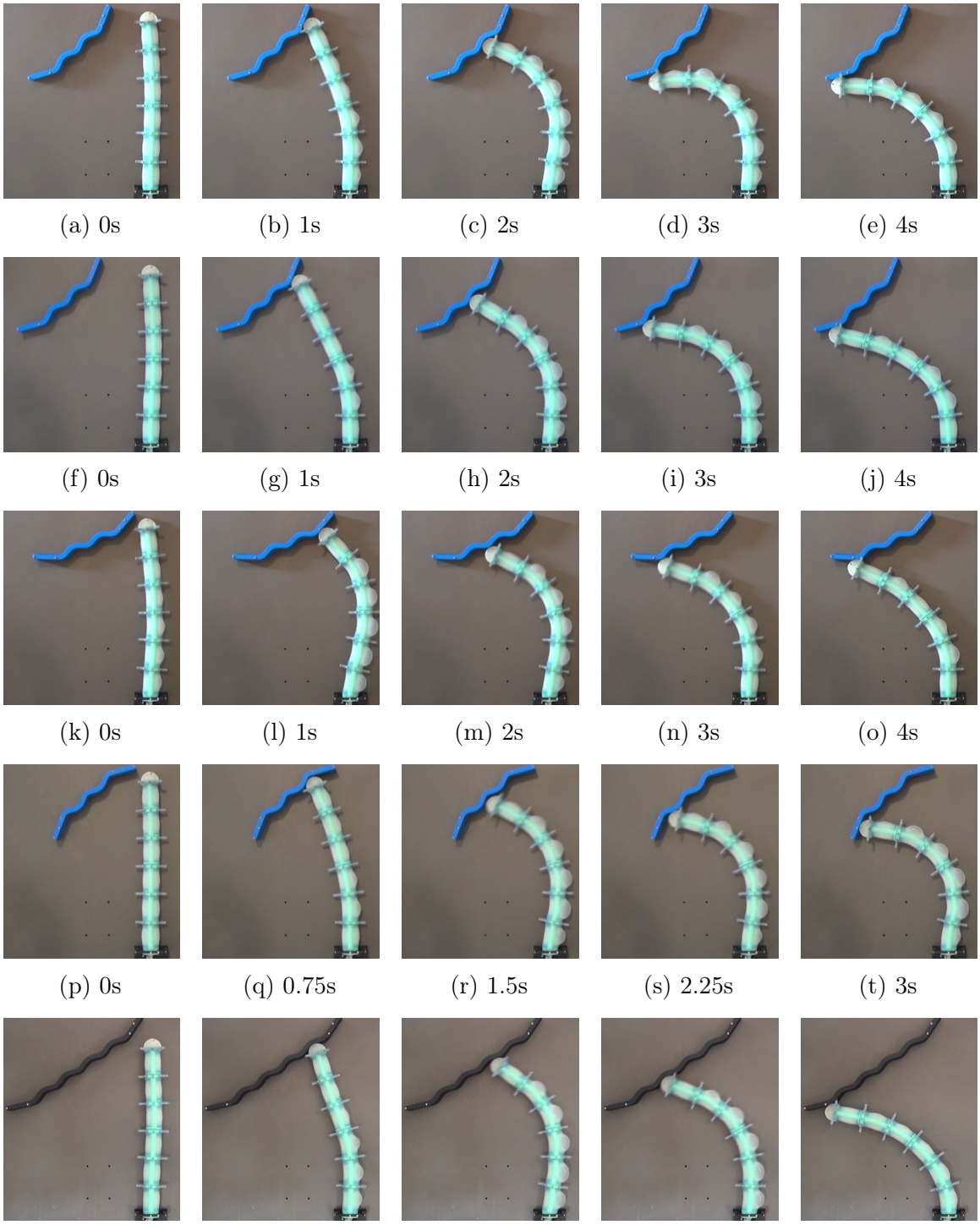

(a) 0s (b) 1s (c) 2s (d) 3s (e) 4s

(f) 0s (g) 1s (h) 2s (i) 3s (j) 4s

(k) 0s (l) 1s (m) 2s (n) 3s (o) 4s

(p) 0s (q) 0.75s (r) 1.5s (s) 2.25s (t) 3s

(u) 0s (v) 1s (w) 2s (x) 3s (y) 4s

Figure 7-19: Five photo sequences of the soft robot controlled to reach the surface of an environment, trace along the surface, and then reach a desired end position at the other end of the surface. The Cartesian impedance controller (6.35) and Algorithm 6.1 are used to realize this behavior. The system is able to reach the goal position on the surface for each of the considered placements of the environment.

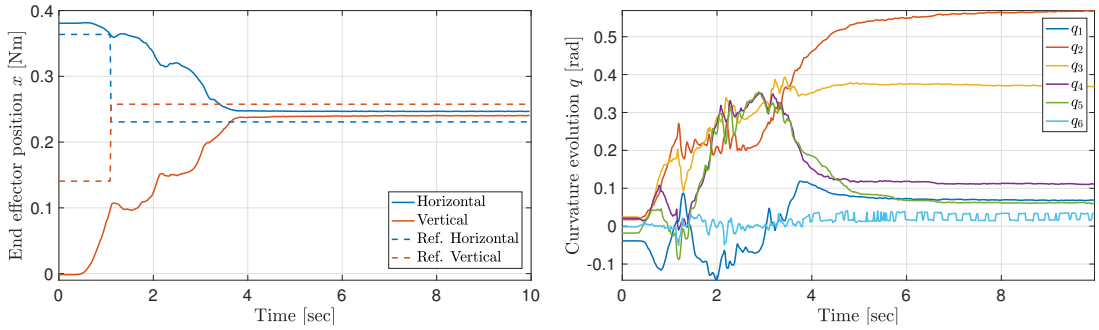

(a) End Effector

(b) Curvature

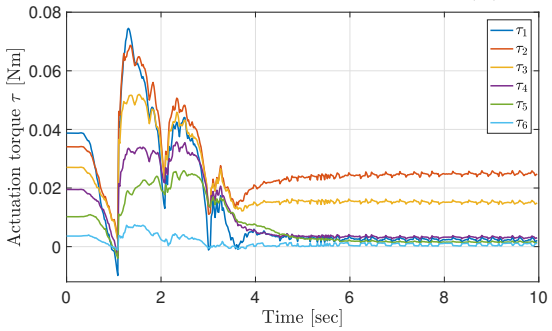

(c) Torques

Figure 7-20: Experimental evolutions resulting from the application of the Cartesian impedance controller (6.35) in tracing a surface towards a desired end effector position. Algorithm (6.1) is used to command a desired end effector evolution. Panel (a) shows the evolution of the end effector x. Panel (b) shows the degree of curvature q evolution for the tracking experiment, while panel (c) presents the corresponding actuation torques τ.

Chapter 8

Conclusion

We yet have to see robots that can safely and smoothly interact with the surrounding world. While we already have autonomous vehicles made up of tons of metal driving among us, we still cannot replicate truly animal-like robots. Animals have evolved over millions of years to become particularly good at doing certain sets of tasks, replicating their capabilities and behaviors in a robotic system can enable us to achieve those capabilities for our own use in transportation, material handling, scientific studies of natural life, and other areas. This motivated us to dive deeper into creating biomimetic robots using soft materials.

Our society has been pushing robots into buildings for tasks such as cleaning or for moving items around, but we yet have a long way to go until we will see robots that can help us with problems that are particularly intensive in interaction and manipulation. Robots are still notoriously bad in interacting with unstructured environments or manipulating arbitrarily shaped objects. Limitations concerning mechanisms, control, and autonomy all equally contribute to this lack in capability. For example, a robot shall be somewhat soft and adaptive to take care of and interact with elderly people, lift them up, feed them, or just generally provide for them through means of physical interaction and care. Touching a human requires the ability of a robot to be compliant and perceive the world fully, but the robot also has to have some insight on how and where to do that within a dynamic context. The daily increasing needs for better robots are found in many sectors, not only in healthcare or building

services. For example, automating material handling is a huge, ever-growing industry in an era where people tend not to leave their homes anymore, but do everything online, including shopping. To meet those logistical demands, picking-and-placing of objects requires high adaptability and dexterity while dealing with millions of items. It is not desirable for humans to run through warehouses and pick up objects and sort them into packages. Adding softness into the equation for the design of grippers and manipulator arms was one of the driving motivations to further improve material handling. These insights motivated us to look deeper into building, modeling, and controlling compliant manipulator arms.

In the following, we summarize the achievements made within the scope of this thesis and discuss those achievements with a view to the more long-term goals of increasing capabilities for robotic systems.

8.1 Summary of the Thesis

We have presented new processes for designing fluidically-driven actuators and created several self-contained soft robots using these soft actuators. Our focus was on two types of soft systems to demonstrate and validate our approach to design, fabrication, modeling and control. Those systems were a self-contained soft robotic fish for underwater exploration and an autonomously controlled soft manipulator consisting of multiple soft segments. We proposed and validated our models on the fluidic powering, the dynamic models, the motion planners, and the closed-loop controllers that enable open-loop locomotion, quasi-static manipulation, and dynamic manipulation. We developed models for the powering, kinematics, impedance, and dynamic characteristics of continuously deformable soft manipulators. We leveraged the kinematic models for the motion planning of soft manipulators under quasi-static closed-loop control. We then extended our insights from the quasi-static control and developed models for dynamic closed-loop feedback control in order to achieve dynamic motions and interactions with an environment. This was particularly enabled by our augmented formulation mapping rigid robots with soft robots and allowed us to make use of

insights from classical control techniques.

8.1.1 Design and Fabrication of Soft Robots

The actuator designs and their fabrication methods described in this thesis provide for the fabrication of modular soft robots with body morphologies useful for various tasks.

For the design, we presented three actuator morphologies and discussed their advantages and disadvantages in use. All three viable actuator morphologies entirely made of soft silicone rubber were explored, and these morphologies were differentiated by their internal channel structure, namely: ribbed, cylindrical, and pleated. To be specific, we showed designs such as a ribbed channel structure with embedded constraint layers and transmission lines, a cylindrical channel structure with a hollow interior, as well as a seamless pleated channel structure with embedded constraint layers. For all the actuator morphologies, we also showed the corresponding fabrication processes.

For the fabrication, we showed three fundamentally different processes and discussed their strengths and weaknesses when using them to build completely soft modules that can be concatenated into multi-segment manipulators or be used for locomotion. The lamination and the lost-wax casting processes allow for the embedding of heterogeneous functional elements like constraint layers or tubes into a soft actuator. This facilitates the interfacing to pressure sources or other system components. The simplicity of the retractable pin fabrication method allows for rapid prototyping of simple fluidic elastomer actuators without the risk of failed lamination, or need for a wax core that adds to the complexity in fabrication. The lost-wax casting allows for almost arbitrarily shaped pressurizable cavity structures, created as a monolithic body without weakening seams caused by a lamination technique. This fabrication approach has the potential of general use beyond just the fabrication of a soft gripper or multi-segment arm. The new approach is advantageous because it allows for arbitrary designs of internal fluidic cavities and the casting of a homogeneous soft segment. It removes the need for laminating several parts together that first had to be cast separately. A

homogeneous soft segment would allow for better performance and longevity of a soft robot made this way, especially since it is less prone to manufacturing inconsistencies and rupture at the seams. We explored two ways of fabricating a multiple DOF robot: casting the complete robot as a whole and casting single body segments with subsequent concatenation.

An experimental characterization of each segment morphology was presented, analyzing and comparing the effects of fluid energy onto a segment's bend angle and tip force. It was seen that the pleated segment morphology is the stiffest, followed by the cylindrical, and then the ribbed. The cylindrical morphology has a prominent bend angle nonlinearity for low input volumes, but its behavior becomes almost linear for higher inflations. Based on this insight, easier control of this morphology can be achieved through pre-pressurization of a cylindrical segment. Furthermore, the cylindrical morphology requires the highest amount of fluid energy to produce a given bend angle. The ribbed and pleated morphology both behave very similar in bending. The pleated segment generally requires more fluid energy than both the ribbed and cylindrical morphologies to produce a tip force. However, the pleated segment can accommodate significantly higher input energies and therefore can reach the highest maximum tip force. This is useful when more powerful manipulation is required.

We showed the use of closed-circuit pneumatic and hydraulic powering methods to actuate the soft fluidic elastomer actuator. We chose volumetrically controlled pneumatic cylinders to power the soft manipulator arms in real-time. We presented a plant model describing the system's input-output relationship and characterized its dynamic parameters. Although this plant model was not used for the control of the cylinders, it served to identify the impact design decisions had on the system's input-output relationships.

With a modular design approach, we then combined these soft actuator morphologies into several robotic systems. We created a soft gripper that is capable of grasping objects under uncertainty and identify a set of objects based on data from internal bend and force sensors. Internal sensing addresses one of the primary disadvantages of soft hands compared to hard hands: the final configuration of the fingers and the final

pose of the object are unknown. Our design allows us to maintain the positive aspects of soft hands, including increased compliance leading to greater ability to pick up various objects with arbitrary shapes without the need for complicated grasp planning. We also created a self-contained soft robotic fish for underwater exploration and a soft manipulator arm consisting of multiple soft segments with different end-effectors attached to it. We focused on the robotic fish to validate our approach to design, fabrication and fluidic powering and created a fully self-contained underwater system. For the validation of our approaches to modeling and control, we focused on the soft manipulator arms as the experimental setup.

8.1.2 Application to Biomimetic Swimming

We created an untethered soft-bodied robotic fish for underwater locomotion and exploration of marine environments. The robotic fish uses a soft hydraulic actuator as its deformable tail to perform open-loop controlled swimming motions through cyclic undulation. The swimming movement of the robotic fish is enabled by a custom-made hydraulic displacement pump and a custom-made buoyancy control unit, all embedded within a fish-like underwater system. The hydraulic pump system can perform low to high frequency actuation of the soft tail to achieve a range of swimming speeds. The pump system can also execute turns by adjusting the baseline deflection around which the tail undulates. A set of dive planes, a buoyancy control unit compressing air, and a set of removable weights enabled vertical diving. The fish robot receives high-level control commands via acoustic signals to move in marine environments. Specifically for this application, we developed this acoustic communication system with a compact, software-defined modulation scheme, able to transmit data robust to substantial noise and interference from complex underwater environments. In open-ocean coral reefs with obstacles, sources of noise, and multipath effects, the acoustic system was able to reliably transmit high level commands once per second over a distance of up to 10 m. A camera was mounted at the tip of the robot, allowing a diver to remotely explore and capture close-up recordings of marine life and environments. While most soft robots are pneumatically powered and tethered, our hydraulically-driven soft actuator

enables prolonged untethered swimming over several hundred meters for 40 minutes on a single battery charge. Divers using the system were able to send high-level commands and navigate the robotic fish, observing the marine life and exploring their surroundings.

8.1.3 Model-Free Quasi-Static Control

We wanted to address the problem of maneuvering a soft planar manipulator through a confined environment and perform manipulation tasks with a similar soft manipulator. To address this control problem, we started by developing geometric models describing the kinematics and changing envelopes of these actuators. We used the piecewise constant curvature assumption to describe the single-segment forward and inverse kinematics, and then presented, based on those formulations, a kinematics algorithm for the multi-segment arm. Using those kinematics, we proposed a model-free feedback controller that works in combination with geometric motion planners to enable a soft manipulator arm to move in confined spaces, and to enable a soft arm with attached gripper to autonomously perform pick-and-place operations of objects.

An approach motion with minimal strain and without collisions towards an object of interest can be achieved by posing the grasp motion plan as a series of constrained nonlinear optimization problems.

8.1.4 Model-Based Dynamic Control

Using the model-free controllers, we were able to show accurate but slow quasi-static control of the soft manipulator arms. To achieve dynamic arm motions as well as interactions with an environment, we developed dynamic models that extend the kinematic descriptions and now also account for the structural impedance, actuation torques, external forces, and inertial effects. We then presented two model-based control algorithms that achieve dynamic closed-loop control of a soft robotic arm and enable interactions between the soft robot and an environment. Both algorithms leverage on the idea of connecting the soft robot to an equivalent augmented rigid robot

in such a way that the matching is exact under the common hypothesis of constant curvature [Webster and Jones, 2010], and under the introduced hypothesis on the distribution of mass. We provided a detailed analysis of this augmented formulation mapping a rigid robot to a soft robot. Analytical proofs of convergences within the approximations of our modeling hypotheses are provided.

8.1.5 Experiments and Applications

We created multi-segment arms for the use in object manipulation and interaction with an environment. To realize these applications, we applied our proposed models and control algorithms to the soft manipulator arms.

We showed in experiments that planar manipulation tasks, such as grasping-and-placing objects and whole arm movement through a confined space, are possible with our soft and highly compliant multi-segment arms entirely made of soft materials. As inputs we used the volumetric displacements of the pneumatic cylinders and as measured feedback we used the positions of the ends of each soft segment to control the soft arms. In experiments we achieved closed-loop configuration control of our soft manipulators despite their low structural impedance. This control strategy is an advantageous alternative to open-loop or morphological control in that we can achieve repeatable and precise task-space positioning for reaching tasks and grasping tasks in confined space without trial and error.

We showed that the planar soft manipulator is capable of pick-and-place operations under high uncertainty concerning position and shape of the object. This control approach of the soft manipulator is suitable for performing delicate tasks with low payloads, for example grasping objects that should not be squeezed and/or should not break during manipulation. The ability to successfully and repeatedly perform object manipulation using a fully soft, multiple DOF arm suggests that despite their extreme compliance, soft robots are capable of reliable and robust object manipulation while simultaneously providing inherently safe interactions with the environment. We also demonstrated the manipulator's ability to autonomously grasp an object, which leads to many potential applications for fully soft robotic manipulation. In a manufacturing

setting, this could resemble a soft robot stretched widely to pick up and place objects appearing at various locations. In a human-centric environment, this concept of soft grasping manipulation enables soft robots to interact safely with humans due to the compliant actuation and enveloping of the gripper.

We also demonstrated the ability of an entirely soft manipulator to autonomously maneuver through a pipe-like environment, which leads to many potential applications. In a manufacturing setting, this could resemble a soft robot executing tasks requiring high dexterity when handling delicate objects. In a human-centric environment, whole arm manipulation may enable soft robots to interact safely with humans. Furthermore, in a surgical setting, highly compliant soft robots under whole body control may assist with operations in sensitive environments.

We also showed simulations of our model-based controllers to validate and demonstrate the effectiveness of our proposed dynamic control strategies. We tested our controllers on a finite element model representing the soft manipulator arm. We compared the performance of our controllers with a state-of-the-art SIMC-PID controller using a Jacobian pseudoinverse-based kinematic inversion. These simulations extensively tested the performance of the controllers outside the modeling hypotheses. In physical experiments we also demonstrated the tracking of several trajectories in curvature space. We achieved high-accuracy tracking of several trajectory profiles. We also tested the Cartesian impedance controller together with the proposed contact planner and achieved compliant and dynamic tracing along a surface. We showed that our model-based closed-loop control approach allows for dynamic motions with a completely soft fluidic manipulator arm, something we could not do with the model-free closed-loop control approach.

8.2 Summary of Contributions

In the following we provide a brief summary of the major contributions of the work presented in this thesis.

8.2.1 Design and Fabrication of Soft Robots

We contributed to the design and fabrication techniques by the following:

- Three viable fluidic elastomer actuator morphologies: ribbed, cylindrical, and pleated channel structure.
- Three fabrication processes: lamination casting with heterogeneous embeddings, retractable-pin casting, lost-wax casting.
- Design, powering, and fluidic control of soft robots built for locomotion and manipulation.
- Modular design approach to create soft systems: A soft robotic fish with an undulating soft tail, a proprioceptive soft hand, soft multi-segment manipulator arms.

8.2.2 Applications for Biomimetic Swimming

We presented a robotic fish as an application of our design and fabrication techniques:

- Biomimetic undulation of a soft fish tail.
- Self-contained, end-to-end system with embedded actuated soft tail.
- 3D controllable and prolonged underwater motion using undulation and buoyancy control.
- Underwater remote control using a miniaturized acoustic system.
- Ocean experiments characterizing the swim performance of the robot and filming of marine life at depths of 0 to 18 m.

8.2.3 Model-Free Quasi-Static Control

We enabled planar manipulation with our completely soft fluidic elastomer manipulator arm:

- Closed-loop control consisting of a kinematic model, closed-circuit fluidic control, and cascaded curvature controller for the execution of motion plans.
- Whole-body motion planner and controller for a continuous motion avoiding collisions within a confined environment.
- Grasp-and-place planner and controller for picking up randomly positioned objects on a planar surface.

8.2.4 Model-Based Dynamic Control

Extending the quasi-static control approaches, we realized dynamic model-based control of our soft robot:

- Dynamics and impedance model derived from augmented formulation linking a soft robot to a rigid-bodied serial manipulator.
- Model allows for application of classical control techniques to the control of soft robots.
- Closed-loop dynamic feedback controller dynamically tracking desired segment deformations over time.
- Closed-loop dynamic feedback controller for moving in Cartesian space and compliantly tracking a surface.

8.2.5 Applications of our Models and Controls to Soft Manipulation

We successfully deploy our models and controllers to our soft multi-segment arms for the use in object manipulation and interaction with the environment. We performed repeated autonomous manipulation experiments that showed:

- End-effector control of a soft finger attached to a soft arm using a motion tracking system.

- Precise control of the end effector's pose while minimizing collisions between the arm's changing envelope and a confined environment.
- Grasping and placing of various objects of unknown geometry placed randomly in the work space without force sensing.
- Dynamically controlled motions with minimal tracking error, both in simulations and real experiments.
- Dynamically controlled motions in Cartesian space for compliant tracking of the end-effector along a curved surface.

8.3 Limitations

8.3.1 Design and Fabrication of Soft Fluidic Actuators

Our actuator morphologies cover a variety of ways in making deformable fluidic elastomer actuators, with the limitation that all these actuators require pneumatic or hydraulic pressurization. In the related work Section 2.1.1 we discussed alternative ways of actuation such as Shape Memory Alloys, cable actuators or Pneumatic Artificial Muscles. Due to the softness of the materials we chose for our actuators, we ran into limitations in terms of strength and payload capacity. While we compensated for these shortcomings in design by suspending our manipulators on a horizontal surface through roller supports, those limitations became particularly apparent in an application of fluidic elastomer actuators by Marchese et al. [2016]. In that application, a pendent fluidic elastomer actuator arm made was feedforward-actuated on a plane to perform a dynamic swing up motion, overcoming gravitational forces that the arm statically could not overcome. We focused on the use of rubbers with fairly low elastic modulus, because it closely matched the softness of real fish, octopus arms, and elephant trunks. We were inspired by the skeletons of those natural systems when embedding constraint layers made of flexible plastic or by adding stiffer rubber sections within the designs. While this constraint design already provided us with

functional motion constraints to create the undulating motion of a fish tail or the continuous bending of an octopus or elephant trunk, we did not further investigate the addition of string or fiber reinforcements at the outer surface of the soft actuators. The fabrication methods offer a set of different approaches to make soft robots, but even the most versatile method, that is the lost wax casting, is restricted by the limitations in casting of the lost wax core. Furthermore, the added fabrication steps of pouring the wax core within a soft mold increases the amount of molds and time needed to iterate over a design. The fabrication of a single fluidic elastomer actuator requires first the creation of the required lost wax cores and the subsequent removal through application of heat. An alternative fabrication method to casting-based methods is 3D printing of the soft actuators using the method of Printable Hydraulics [MacCurdy et al., 2016] or direct printing of a mixed elastomer [Morrow et al., 2017].

8.3.2 Biomimetic Swimming of a Single Actuator

The soft robotic fish (SoFi) can be created at different scales, but its swimming behavior depends on its size. Smaller robotic fish can barely overcome ocean currents and need external power [Zhao et al., 2015], while larger robotic fish are more difficult to prototype and to handle by a diver. SoFi can currently swim up to 0.51 body lengths per second, which is comparable to other robotic fish prototypes [Mazumdar et al., 2008, Valdivia y Alvarado and Youcef-Toumi, 2006]. Note that those fish prototypes were not capable of controlled swimming in three dimensions. Nevertheless, the current swimming speed leaves plenty of room for improvement when aiming for imitating real fish swimming at 2 to 10 body lengths per second [Katz et al., 2001, Videler, 1993]. Further optimizations of the pump system, the tail geometries, and the exterior profile of SoFi may improve the swimming efficiency.

The dive planes provide only fine-tuned control at a limited depth range. Once the range is exceeded, the compression of the fish's flotation becomes so strong that inverting the pitch of the dive planes won't allow returning to the original depth; the diver must manually adjust the weight during the dive to change to another depth range. Using asynchronous control of the BCU modules would enable increased pitch

control (see Figure 4-4 for details), although the BCU is still limited in its diving speed and range. The speed and range can be increased by enlarging the body to allow for larger dive planes or BCU pistons, while balancing against the tradeoff of increased drag. Upgrading the tail design to four instead of two fluidic chambers, with one chamber per quadrant, would also allow steering in vertical direction through biased undulation of the tail in the vertical plane.

Improving the acoustic modem could allow a diver to be further away. Optimizing the modulation parameters, implementing different protocols, such as frequency hopping, refining the transducer, and amplifier circuitry, and reducing the motor noise could increase data rates and detector robustness. Additionally, the modem can be extended to control multiple robots or to be bidirectional and provide the diver with real-time feedback.

The integrated camera enables more autonomous surveying capabilities [Maldonado-Ramírez et al., 2015]. Monocular self-localization would enable the fish to build maps of the underwater environment and explore it further. Instead of using acoustic communication for lower-level settings, such as thrust and depth, a diver could remotely command higher-level mission parameters such as regions to explore or specific marine life to follow.

8.3.3 Manipulation using Quasi-Static Model-free Control

The obvious limitation of the model-free quasi-static controller was that the manipulator's dynamics and impedance are not modeled, only the kinematics were considered for the closed-loop control of the manipulator. Although we were able to demonstrate whole-body motion in a confined environment and grasp-and-place manipulation, the execution speed can certainly be increased and its settling time decreased if a dynamics-based control strategy is used. This limitation was addressed in Chapter 6 and validated in the experiments in Section 7.2. Further, in conducting these experiments it was observed that the soft manipulator can harmlessly collide with its environment, and this contact can be potentially leveraged to either increase primary task precision or its likelihood of success. However, a method for detecting

these collisions is not provided, and the modeling assumption of piecewise constant curvature is becoming imprecise under environmental contact. Accordingly, this is strictly a passive feature but future work could provide strategies for incorporating and/or exploiting collisions into the task-space planner. More advanced kinematic models are needed to understand the deformation of soft manipulators constrained by environmental contacts. These experiments were limited in the sense that we only validated our approach for planar manipulation on a surface. Next steps are to validate our kinematic models and controllers on soft manipulator arms capable of moving in three dimensions. The experiments also bring to attention the need for proprioceptive self-localization within soft robots. Feedback for our controller currently comes from an exteroceptive localization system. This is a reasonable method for indoor, laboratory, or factory environments where sufficient line of sight to the manipulator can be expected. However, this sensing approach is prohibitive in that the environment must be equipped with cameras and the tasks cannot occlude the view of these cameras onto the manipulator. Adding bend and force sensors into the soft manipulator arms, just as we did it for our pleated soft fingers (Section 3.6.2), is one of the next steps to take in order to address the limitation in proprioceptive sensing.

8.3.4 Manipulation using Dynamic Model-Based Control

The dynamic feedback controllers have been evaluated in the context of exploring a two-dimensional surface using a soft planar robotic arm, validation in three dimensions has to be done in future work. The controllers were effective for both tracking accurately the arm's desired curvature as well as having the end-effector follow the environment. The potential for this work is actually much broader. Experimental validations of our control have so far been limited to the plane and we have only showed interactions with the environment using the end-effector. We have not experimentally tested our control when another part of the manipulator's body, other than the end-effector, makes contact with the environment. However, our control algorithms are formulated to be applicable for other tasks as well. The algorithms have the potential to enable a

wide range of dynamic tasks, ranging from exploring three-dimensional spaces through contact, learning the geometry of the world, picking up delicate objects, moving heavy objects, and enabling dynamic interactions with the world.

8.4 Lessons Learned

8.4.1 Practical Insights First

When developing soft robots, it works well to quickly start to prototype a new idea in a physical experiment instead of trying to accurately simulate all the relevant physics. Soft robots are fairly easy to build and modify, at least when it comes to fabricating single actuator units. Much can be learned from testing these units in different environments. We were able to gain many unexpected insights and develop intuition for the systems. If we actually tried to properly simulate a soft robot using a volumetric finite element method, it was particularly surprising that only few tools are actually available for this task. Many physics simulation engines are not designed for robotics purposes including proper motion studies and interactions between multiple objects. Most simulation quickly give up if the robot's geometry is a bit more complex like a pleated or ribbed single segment design. Trying to simulate a multi-segment system was so far not easily feasible. Duriez et al. [2016] are working on design tools to remedy this lack.

Printing soft robots seemed very hopeful in the start, but turned out to be not ready yet for practical purposes due to the limitations in UV-curable material properties. Some researchers have been taking initial steps towards the creation of practical printers that can create promising soft actuators that allow for repeatable high deformations without quickly becoming brittle or fatigued [Morrow et al., 2017]. But until there are commercially available multi-material printers using platinum-cured silicone elastomers or other useful rubber-like materials, it is best to stay with casting techniques when making soft robots.

Design, control, and task definition is a repetitive process and usually starts off with

a very primitive and preliminary design that one quickly tries to make controllable for a task that is not yet properly defined. In this first iteration, one quickly comes to realize that the initial design has not enough actuation force and reachable workspace. With that limitation, there is not much value in trying to further sophisticate the control approach – instead one goes back and starts over with a better design, motivated and inspired by the failures and insights from the first iteration. Effectively, one has to go through this iterative process multiple times until one can start solving useful tasks with soft robots. For example, we had to build half a dozen robotic fish prototypes before we could successfully deploy the robot in the ocean. All iterations up to that level were done either in aquariums or swimming pools.

Initial assumptions of being able to swim in the ocean without a buoyancy unit quickly showed many limitations. Having a robot maintain depth at various levels is hard to realize for soft robots that substantially compress as the robot dives down. Properly sized buoyancy control helps with these limitations, but also a structurally sane design with rigid floatation units is key to success.

8.4.2 Leverage Natural Impedance for Complex Tasks

The completely soft manipulator morphologies we proposed are well-suited, provided the payload is low, for tasks requiring: (i) safe interactions between humans and environments, (ii) mitigations of uncertainty at the hardware level through the body's impedance, (iii) continuous and dexterous deformation, and/or (iv) hardware to take an unstructured form. For example, by making robots of soft elastic materials, with no sharp edges, and with relatively low link inertia, a robot's reliance on sensors and software for safety is reduced. The prospects for safe integrations between a robot and human are generally increased when the compliance of the material composing the machine matches that of soft biological materials [Van Ham et al., 2009], and this feature is inherent to robots made of soft silicone elastomer [Rus and Tolley, 2015]. Additionally, current autonomous systems rely on computational tools like state-estimation, Bayesian models, and robust controllers to effectively mitigate uncertainty, but these approaches can be computationally intensive. As we learned, an alternative

approach is to allow resilient soft machines to handle some uncertainty through their structural impedance in order to reduce the burden on the computational system. For example, consider how the soft arm passively conforms to the environment's boundary. The planner is unaware of this complex interaction, but the primary task can still be successfully executed. Further, modern inspection tasks as well as invasive surgery [Cianchetti et al., 2014b] require devices with redundant degrees of freedom and high dexterity and often impose the constraint of navigating around sensitive objects. As demonstrated in this thesis, soft robotic manipulators are well-suited for these future applications.

8.4.3 Building Blocks for Variety of Soft Robotic Designs

We only showed a selected subset (Section 3.6) of soft robots one can imagine to build using our actuator morphologies and fabrication techniques. For example, the pleated gripper not only served as the template for fingers in the soft hand (Section 3.6.2), but was also easily attached to the end-effector of a long manipulator arm and brought to use for autonomous manipulation (Section 3.6.7). We were even able to combine several of these pleated grippers in series to make a planar manipulator arm (Section 3.6.5) as an alternative to our cylindrical multi-segment arm (Section 3.6.6) used for most of the experiments in this thesis. Similarly, the ribbed design of the soft fish tail (Section 3.6.1) can also be used as the base design for a three dimensional manipulator arm which we are planning to build in future work. That arm uses three wax cores per segment to achieve three dimensional deformations. The Soft Robotics Toolkit [Holland et al., 2014, 2017] is a shared resource to allow for the development of many more future designs. These designs may be based on the fluidic elastomer actuators we presented in this thesis or other design approaches that also incorporate fiber-reinforcements [Deimel and Brock, 2016] or make use of electroactive polymers [Kim and Tadokoro, 2007, Carpi et al., 2011].

8.4.4 Curse of Softness: Always Operating Close at Actuation Limits

Despite all the benefits of soft-bodied robots, such as safe interactions, mitigations of uncertainty, continuous deformations, and enabling amorphous forms, it also comes with a curse of constantly running into actuation limits. There is a direct trade-off between the body's softness and maximum actuation strength, the softer the robot is the less force it can apply. Gravity does not allow us to make very soft robots for use on land or for flying, those only find use underwater. Even underwater the robot can not be too soft despite the supporting buoyancy forces, the robot just won't be able to propel itself or pick up larger objects. For the manipulation work we focused on in this thesis, we demonstrated our models and controllers for manipulation on planar surfaces in order to remove gravity from the equations. Even then, the robot was often at its limits when trying to follow along rigid surfaces, reaching into remote corners of the workspace, or picking up objects firmly. Future work will further improve on the right balance between required minimal softness and desired maximal fluidic actuation strength. There are various possibilities for trying alternative actuation approaches in the future, we listed some of them in Section 2.1.1. The challenge will always be to get enough force out of the prototype.

8.4.5 Classical Control Techniques Applicable to Soft Robots

We learned that we can apply classical control techniques to soft robots by developing an appropriate map. Our dynamic controllers in Sections 6.4 and 6.5 rely on an *augmented formulation*, linking the soft robot to a classic rigid serial manipulator with a parallel elastic mechanism. Our augmented formulation maps the dynamics of a soft robot to an equivalent rigid-bodied robot constrained through a set of nonlinear integrable constraints. The key property of the augmented formulation is to define a perfect matching under the hypothesis of piecewise constant curvature for the soft continuum arm. This insight enabled us to apply control strategies typically used in rigid-bodied robots onto soft robots. Prior tools developed for classical robot models

can be exploited under this formulation [Ott, 2008, Sciavicco and Siciliano, 2012].

8.4.6 Natural Proportional-Derivative Control

We learned to leverage the natural self-stabilizing properties of soft robotic systems for the design of our dynamic controllers. A natural proportional derivative control can be achieved by identifying the impedance of the controlled soft manipulator arm and use those identified values for stiffness and damping in the feedforward terms of our proposed curvature controller (Section 6.4). The resulting closed-loop behavior of the system is a natural proportional-derivative (PD) control. As we know from classical control techniques, a classical rigid robot controlled through a proportional-derivative control is well known to be globally asymptotically stable for the commanded reference trajectory [Sciavicco and Siciliano, 2012].

8.4.7 Intentional Use of Contact with Environment

Since we are dealing with inherently compliant robots made of soft elastomer, we do not have to be concerned about contacting the environment. Instead, we are intentionally making use of the environment to move and advance through a confined space or to explore by tracing along the environment with the manipulator's end effector. In the experiment described in Section 7.1.1, we accounted for the continuously changing envelope of our inflatable arm to fit its whole body into a confined environment. When the robot's bubbles contacted and sort of braced on the wall, it helped the arm to push itself off. When we validated our dynamic Cartesian impedance controller in Section 7.2.2.4, we deliberately spanned a virtual spring-damper element between the soft arm's end effector and a point within the environment we wished to explore. Just like an elephant uses its trunk to explore the world, we waited for the arm to touch the surface and then re-spanned the virtual spring-damper to the new target point on the surface of the environment. As described in our contact planner (Section 6.6), the tip of the arm then followed and pushed against the surface to perform the exploration. The inherent compliance of the arm enabled us to do this compliant interaction with

the surface. In the future, we wish to further expand this idea to three dimensions to explore the world without vision, just through the natural compliance of the soft arm.

8.5 Supplementary Materials Online

The supplementary materials to this thesis can be found online[1]. These materials include the raw files of this thesis document, the presentation slides of the thesis defense, mechanical and electrical design documents, bill of materials, control and planning code, and experimental videos.

8.6 Related Projects by the Author

There are a few related projects that the author of this thesis worked on during his doctoral studies. Those projects extend the scope of this thesis by proposing alternative fabrication techniques through 3D printing, a soft jumping robot, a soft juggling robot, a wearable system with embedded computer vision, and an underwater communication module. Printable hydraulics is an alternative method for fabricating robots by 3D printing solids and liquids to create robots with embedded hydraulic actuation channels [MacCurdy et al., 2016]. A soft jumping cube demonstrates the use of soft elastomer as the surrounding body of a spring-driven jumping robot that is capable of repeated bounces after landing to move further forward compared to a rigid jumping cube [Li et al., 2015]. The soft juggler is a model-based control system capable of juggling a puck on an inclined air hockey table. A dynamic implicit-surface model describes the contact of rigid objects colliding with highly deformable soft surfaces. The model is used for controlling the trajectory of a fast-sliding puck through an actuated paddle with a surface made of rubber [Katzschmann et al., 2018c]. A wearable navigation system was developed to help users with visual impairments to safely navigate through environments by the use of a time-of-flight sensor and a haptic feedback device for directional signaling [Katzschmann et al., 2018a]. In the same

[1] http://people.csail.mit.edu/rkk/phdthesis/

project we also enabled independent navigation and object localization for people with visual impairment through a vision-based system using a depth camera combined with haptic feedback and a Braille display [Wang et al., 2017b]. A compact acoustic communication module allows for underwater communication between robots and humans [DelPreto et al., 2015].

8.7 Future Work

8.7.1 Soft Robotic Fish

We demonstrated that the soft robotic fish can navigate in natural environments. The next steps are to use SoFi as an instrument to 1) study the behavior of marine life over long periods of time without human interference with the scene, 2) study if SoFi can be used to influence the behavior of marine life, and 3) create robotic swarms. These research directions are enabled by SoFi and are the subject of future work.

There are many potential future applications of the robotic fish in the emerging field of ethorobotics [Krause et al., 2011, Miklósi and Gerencsér, 2012]. We are inspired by previous work that considered robot-animal interactions, including research on robot-cockroach societies [Halloy et al., 2007], remote-controlled cow gathering [Butler et al., 2006], pet care robots [Kim et al., 2009a], honeybee robots [Landgraf et al., 2011], and guinea fowl robots [Romano et al., 2017b]. More recently, studies in small fish tanks began to specifically investigate interactions between robotic fish lures and natural fish, such as golden shiners [Marras and Porfiri, 2012, Butail et al., 2015], zebrafish [Abaid et al., 2012, Polverino et al., 2012, Cianca et al., 2013, Ruberto et al., 2016, Bonnet et al., 2016, 2018], or Siamese fighting fish [Romano et al., 2017a]. This previous work considers controlled studies in laboratory environments, conducted in tanks with unactuated fish replicas or primitive robotic fish prototypes with servo-actuated tails. These previous studies showed that the appearance or biomimetic locomotion of the robotic device does not ensure integration within a school of fish, since acceptance depends on multiple signals. It was also found that a robotic fish

can be differently perceived in terms of attractiveness by real fish [Abaid et al., 2012, Phamduy et al., 2014, Cianca et al., 2013, Romano et al., 2017a]. These aspects should be taken into account when designing future robot-fish studies with our fish prototype.

In contrast to previous robot-fish studies, our robot prototype provides the opportunity to perform studies of the biocenosis of coral reefs and other marine environments within natural habitats. In the future, researchers could use the soft robotic fish and easily change its size, color, and shape to emulate various types of fish with different dynamic behaviors. The integrated camera and the ability to remotely control the robot in three dimensions at a variety of depths allow the system to observe and approach marine life.

The soft fish can be rapidly fabricated to create a swarm of robotic fish. Such a swarm could enable studies of schools of fish and their interactions in the presence of varying ocean dynamics [Kalantar and Zimmer, 2007, Schmickl et al., 2011, Read et al., 2013, Jaffe et al., 2017].

8.7.2 Manipulation

In future work we will redesign the manipulator arm to move in three dimensions with enough actuation to pick and place objects and to explore environments through touching and tracing. Integrating proprioceptive sensing within all segments will improve the use of our manipulators in occluded environments where exteroceptive localization is not available. Sensors just like we used for the soft fingers in Section 3.6.2.3 are needed for more accurate feedback while grasping. With additional sensor data next to the motion capture, we would be able to create a more robust and accurate prediction of the configuration of the arms, the identity of the grasped object, the pose of the grasped object, or the contact location with an environment. This additional sensing knowledge is useful in creating a system which can use objects and interact with environments in more complex ways: rather than just performing pick-and-place operations, robots should be able to conform to the environment while getting accurate proprioceptive feedback, so they can explore the space without cameras, and approach and pick up a variety of objects. The additional sensor data will enable the system

to identify where contact was made and when objects are not grasped robustly and enable them to re-grasp accordingly.

Additionally, the data provided by the sensors have the potential of enabling even more capabilities. The proprioceptive feedback is necessary for the in-hand manipulation of objects, extending pick-and-place operations to complex manipulation in 3D. These data will be useful for enabling robots to use tools, picking up objects intended for use with a certain grasp and orientation, identifying the object and confirming that the orientation of the object is correct, and then planning the interaction of the grasped object with the environment to robustly use tools.

We will further expand on our piecewise constant curvature parametrization for the three-dimensional space and present the application of the proposed dynamic controllers on the soft robotic arms moving in three dimensions and interacting with the world. We will need to overcome major challenges such as the design of appropriate actuator stiffness and the development of dynamic fluidic power sources to overcome gravitational and frictional contact forces. We cannot make the new prototypes too stiff, otherwise we would lose most of the desirable characteristics we attribute to soft robots. Also, integrating not only proprioceptive bend sensors but also contact force sensors into the soft arm will enable the exploration of and interaction with a three dimensional environment.

We intend to take our lab prototypes and make use of them in applications of the material handling industry. Immediate applications within an industrial environment are the use of the soft grippers mounted to traditional robotic arms for pick-and-place tasks. We intend to use teleoperation and machine learning to enable this hybrid rigid-soft system for solving many manipulation challenges the material handling industry faces when trying to become more automated.

Manipulation skills are also crucial to enable grasping robots to leave the laboratory and the automated factory to engage in work alongside humans in factories, homes, and workplaces. Anywhere robots will need to interact in human environments, robots will need to be able to have the dexterity and flexibility of grasping that humans do. We envision a future where soft manipulators such as hands and arms enable that

fluidity of interaction.

Appendix A

Appendix: Soft Robotic Fish

We provide additional information on the appearance of the robotic fish and the design of the acoustic modem for the robotic fish.

A.1 Color of Exposed Parts

The colors of all exposed parts of the soft robotic fish are detailed in Table A.1. The color of the robotic fish is useful when studying the effect of the robot's appearance as observed by real fish.

Exposed Parts (listed from tip to tail)	**L***	**a***	**b***
Fisheye Lens (metal, black)	3.05	30	111
Head (3D-printed, epoxy coated, white)	90.52	-1.51	7.21
Acoustic Transducer (rubber, black)	38.95	0.18	1.12
Center Hull (3D-printed, epoxy coated, white)	92.74	-0.52	4.82
Dive Plane (3D-printed, epoxy coated, white)	93.38	-1.23	6.48
Back Floatation (3D-printed, epoxy coated, white)	90.99	-1.39	3.76
Tail (silicone rubber with glass fillers, off-white)	68.69	-0.79	2.92
Fin (acteal, transparent white)	65.97	1.17	2.53

Table A.1: Color measurements of the exposed parts of the soft robotic fish: Color measurements were performed using CIELAB (Commission internationale de l'éclairage) color coordinates (L*,a*,b*) with a D50 Illumination source and a D50 filter. Bolded parts represent the biggest exposed surfaces. Recorded with spectrophotometer i1 Basic Pro 2, X-Rite Pantone, Grand Rapids, Michigan, USA.

A.2 Acoustic Modem Design

A compact unidirectional acoustic communication modem was created to enable remote operation of SoFi by a diver. Additional information on the design, implementation, operation, and evaluation of the communication system is detailed by DelPreto et al. [2015].

A.2.1 Transmitter

The acoustic modem's transmitter is housed in the diver interface module, which incorporates an oil-filled rigid outer shell (22 cm x 22 cm x 6 cm) with a transparent flexible membrane on one face. The membrane, a soft cast-molded silicone rubber (Sorta-Clear 40, Smooth-On), retains non-conductive mineral oil within the housing and allows for pressure equalization underwater. The flexibility and molded shape of the membrane allow the control buttons within the module to be pressed by the diver when selecting a desired fish state. These commands are read by a Raspberry Pi single-board computer via USB and are encoded as a specific sequence of ultrasonic acoustic tones, which are then converted to audio signals by a digital-to-analog converter (HiFiBerry). The analog signals are amplified via a Class G differential audio amplifier (MAX9788) and are then impedance-matched to the output ceramic transducer (Aquarian Scientific AS-1 hydrophone) via a step-up transformer (Pico Electronics 32146). The hydrophone has a transmit sensitivity of 116 dB relative to (re) $1\,\mathrm{V\,\mu Pa^{-1}}$ ($1\,\mathrm{V_{rms}}$ input at 1-m range) at 30 kHz and was driven at 32.8 V peak-to-peak, yielding a transmit sound pressure level (SPL) of 137.3 dB re 1 µPa.

A.2.2 Signal Transmission

The hydrophone has a transmit sensitivity of 116 dB re $1\,\mathrm{V\,\mu Pa^{-1}}$ ($1\,\mathrm{V_{rms}}$ input at 1 m range) at 30 kHz and can be driven at up to 70 V peak-to-peak, yielding a maximum transmit sound pressure level of 143 dB re 1 µPa. A spherical spreading model predicts that the received signal level at 10 m range will be $70\,\mathrm{\mu V_{rms}}$, requiring 80 dB of gain to saturate the ADC. The hydrophone has a typical voltage-mode receive sensitivity of

$-207\,\mathrm{dB}$ re $1\,\mathrm{V\,\mu Pa^{-1}}$. We designed a multi-stage amplification board that employs a low-noise JFET common-source amplifier to buffer the hydrophone and provide 17 dB of gain. The signal is then bandpass-filtered and amplified by 40 dB using a Quad OpAmp circuit in a Sallen-Key topology. The passband is 20 kHz wide, centered at 30 kHz, and employs a Bessel response to provide uniform group delay. Finally, the signal passes through a variable gain amplifier (VGA) capable of controlling the gain from 0 to 40 dB in 7 increments distributed linearly-in-db. Audio signals often span many decades of intensity, and the VGA stage allows the detector to ensure that the limited dynamic range of the 12-bit ADC is matched to the strength of the received signal.

A.2.3 Receiver

The modem's receiver, housed within an oil-filled chamber in SoFi's head (see Figure 4-1), occupies less than $30\,\mathrm{cm^3}$. Audio signals are transduced by a hydrophone (Aquarian Scientific AS-1) with a voltage-mode receive sensitivity of $-207\,\mathrm{dB}$ re $1\,\mathrm{V\,\mu Pa^{-1}}$, amplified and filtered by a custom JFET preamplifier with 17 dB gain, filtered and amplified by a bandpass filter with a 20 kHz to 40 kHz passband and a gain of 40 dB , and digitized by an Mbed microcontroller. A variable-gain amplifier controlled by the Mbed allows dynamic signal equalization with a gain from 0 dB to 40 dB. The modulation and demodulation are both defined in software for versatility, facilitating alternate modulation protocol implementations. The receiver consumes 815 mW, with the Mbed using about 740 mW of that power.

A.2.4 Communication Frequency

Communication frequencies were chosen by considering typical ranges of human hearing, frequency-dependent attenuation in underwater channels [Stojanovic and Preisig, 2009], Doppler effects, SoFi's motor noise, the microcontroller's sampling capabilities, parameters of the receiver's detection algorithm, expected sources of environmental noise such as wind and waves [Tucholski, 2006, Cato, 1997], and marine

life. Noise produced by fish is typically below 10 kHz [Cato, 1978], and the hearing ranges of common aquatic species decay significantly above 10 kHz [Amundsen, 2011, Popper et al., 2004] although some cetaceans and pinnipeds can hear well above this range [Southall et al., 2007]. Taking into account all of these considerations, 36 kHz was chosen for a logical 0 and 30 kHz was chosen for a logical 1.

A.2.5 Modulation and Encoding

A modulation scheme was designed based on binary frequency-shift keying (FSK). To address multipath reflections, each bit is represented as a brief pulse of the appropriate frequency followed by a period of silence called a guard interval. The receiver can therefore detect leading edges of pulses then wait for any reflections to decay. Based on experiments in a fish tank and in a pool, a pulse width of 5 ms followed by a guard interval of 45 ms was chosen to enable reliable detection of pulses and allow significant multipath reflections to decay.

Given the encoding of single bits, words were encoded as a series of 16 bits. The data word consists of 11 bits that describe the desired fish state: 4 possible settings for thrust, 4 possible settings for frequency, 7 possible states for yaw, 7 possible states for pitch or depth (depending on the preset mode), and 2 possible states for video recording. This 11-bit word is then expanded to a 16-bit word using a [15,11] Hamming encoding with an additional parity bit. These bits are encoded and transmitted as described above, followed by an inter-word guard interval that is longer than the inter-bit guard interval. This interval was chosen to be 200 ms. Combined with the pulse timing defined above, this indicates that a single 16-bit word can be transmitted in 1.0 s.

A.2.6 Detection Algorithm

The receiver's detection algorithm is implemented on an Mbed microcontroller based on the NXP LPC1768 with a 32-bit ARM Cortex-M3 core running at 96 MHz. The on-board 12-bit ADC is used to sample the transmitted acoustic signal, which is

preprocessed by custom amplification and filtering PCBs. The sampling rate was set to 250 kHz, and a Direct Memory Access (DMA) chain was configured to fill a buffer of 125 samples using hardware; this process of filling a buffer with samples therefore does not consume processor resources.

Although implementing a Fast Fourier Transform has high processing demands for a low-power consumer microcontroller, individual terms of the Discrete Fourier Transform (DFT) can be computed quickly using the Goertzel Algorithm [Goertzel, 1958]. The chosen sampling rate and buffer length yield an effective bin width of 2 kHz. Since pulses are being transmitted followed by guard intervals, peaks are expected in the computed Goertzel outputs within the specified bins. To detect these peaks while accounting for multipath and environmental interference, an adaptive peak detection algorithm was designed and implemented. It uses a circular buffer of Goertzel outputs and a priori knowledge about the expected shape of a peak to detect received bits. To account for noise, obstacles, and changing patterns of constructive interference when evaluating whether a tone is present on one of the two FSK channels, the algorithm uses the remaining frequency channel as an estimate of ambient noise level. This algorithm was implemented entirely using fixed-point arithmetic in order to increase computational efficiency, and all constant factors were chosen such that bit-shifts could be used instead of explicit multiplication or division.

As individual bits are decoded using this adaptive peak detection, words are decoded using a state machine based on the chosen timing parameters. The long guard interval at the end of each word, along with the expected per-bit timing, allows a state machine to detect if bits were erroneously inserted or omitted from a received word. In addition, a [15,11] Hamming encoding with an additional parity bit was employed to help detect or correct bit flips.

A.2.7 Adjustable Gain Control

To compensate for varying levels of received signal strength, the amplification PCB provides a programmable gain of 1, 2, 5, 10, 20, 50, or 100. The microcontroller continuously evaluates the average received signal strength over a 10 s period, and

chooses a desired gain to maintain an ADC-input signal level of approximately 2 V Peak-to-Peak.

A.3 Acoustic Tests

The acoustic communication modem was tested in controlled conditions as well as in the open ocean. This facilitated exploring the design space during development as well as evaluating its performance in real-world scenarios.

A.3.1 Acoustic Communication Characterization for Design

To test the acoustic communication under a variety of controlled conditions, the system was evaluated in a fish tank, a small pool, and a large pool. The fish tank was 1.2 m x 0.3 m x 0.45 m, the small pool was 12.5 m x 5.5 m x 1.2 m, and the large pool was 23.0 m x 12.5 m x 3.0 m. These environments facilitate multipath reflections due to their enclosed configuration, hard walls, and shallow depth; they therefore provide challenging conditions that can approximate the types of interference that would be observed in open-ocean deployments. The tests aim to evaluate the robustness of the communication with respect to multipath effects and to determine feasible data rates. As such, we investigated acoustic reflections, ambient noise, and the efficiency of the demodulation algorithm to appropriately choose timing and frequency parameters for the modulation protocol.

To characterize the multipath reflections, isolated pulses of the frequencies used by the acoustic modem were transmitted while the transmitter and receiver were submerged in a fish tank and in a pool. As seen in Figure A-1, reflections are more sustained in the fish tank than in the pool; dominant reflections decay after about 20 ms in the fish tank and after about 3 ms in the pool. Based on these measurements, we chose a conservative guard interval of 45 ms for the modulation scheme

To characterize the noise injected into the environment from the robot itself, we recorded its noise as received by the modem's hydrophone when the robot's motor was running continuously. Taking the Fast Fourier Transform of this noise,

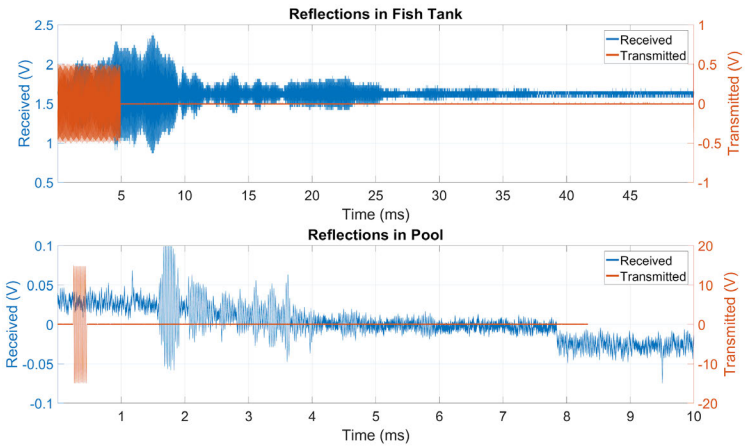

Figure A-1: Acoustic reflections in fish tank (top) and pool (bottom), used to determine appropriate parameters for the acoustic modulation protocol. Transmitted signals are shown in red, and received signals are shown in blue.

as shown in Figure A-2, indicates that the motor produces broad-spectrum noise that is strongest at approximately 5 kHz to 20 kHz and attenuates slowly towards 70 kHz. This then facilitated choosing effective tone frequencies and bin sizes for the FSK-based modulation scheme and decoding algorithm; the tone detection frequencies, 30 kHz and 36 kHz, are higher than the strongest band of motor noise while still accommodating other considerations such as microcontroller sampling rate and marine life. The effective bin size of the algorithm was 2 kHz.

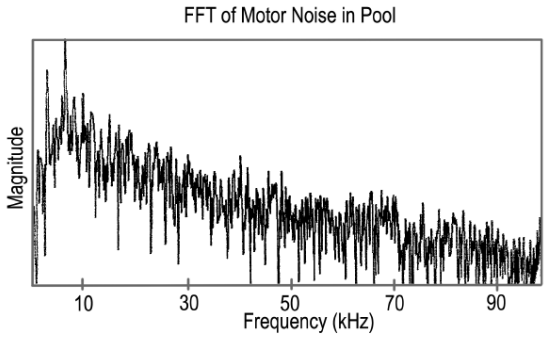

Figure A-2: Motor's broad spectrum noise: A Fast Fourier Transform of received noise recorded by the receiver's hydrophone while SoFi's motor was running continuously nearby, used to determine appropriate communication frequencies for the FSK-based modulation scheme.

Once the parameters of the modulation scheme were chosen, the performance

of the software-defined demodulation algorithm was evaluated by measuring the computational time required to process a buffer of acoustic samples. The algorithm was able to process a complete buffer of 125 audio samples in 120 µs including Goertzel filtering, dynamic peak detection, demodulation, and computations for the adjustable gain control. At a sampling rate of 250 kHz, this is sufficient to run the algorithm in real time.

A.3.2 Acoustic Modem Evaluation in Controlled Environments

The complete transmitter-receiver system was operated in controlled environments to evaluate robustness and feasible data rates for transmitting and decoding individual bits. To do this, a series of 200 alternating bits was transmitted at a rate of 20 bits/s. This was repeated over a sequence of increasing distances and at varying levels of depth. For each transmission, the percentage of bits correctly decoded by the receiver and the longest error-free segment of received bits were extracted during post-processing. In the fish tank, the receiver and transmitter were submerged to approximately 0.25 m and separated as far as possible. In the large pool, the depth of the receiver and transmitter was adjusted from 0.2 m to 1.8 m and the separation was adjusted from 0.9 m to 24.3 m. At the 1.8 m depth, results were recorded both with the robot's motor on and with the motor off. These tests can therefore indicate how the performance of the system is affected by distance, depth, and ambient noise; the results are illustrated in Figure A-3.

The complete transmitter-receiver system was again operated in controlled environments to evaluate the transmission and decoding of complete data words. While the previous tests can indicate reliable parameters for receiving sequential bits, transmitting complete data words can evaluate the state machine algorithm and timing parameters for collecting bits into complete words that indicate desired fish states. To do this, a series of 250 16-bit data words was transmitted, using 50 ms for each bit and 200 ms between words. The data rate was therefore 1 word/s. This experiment was performed in the fish tank and in the small pool; the receiver and transmitter were separated as far as possible in the fish tank and by approximately 10 m in the

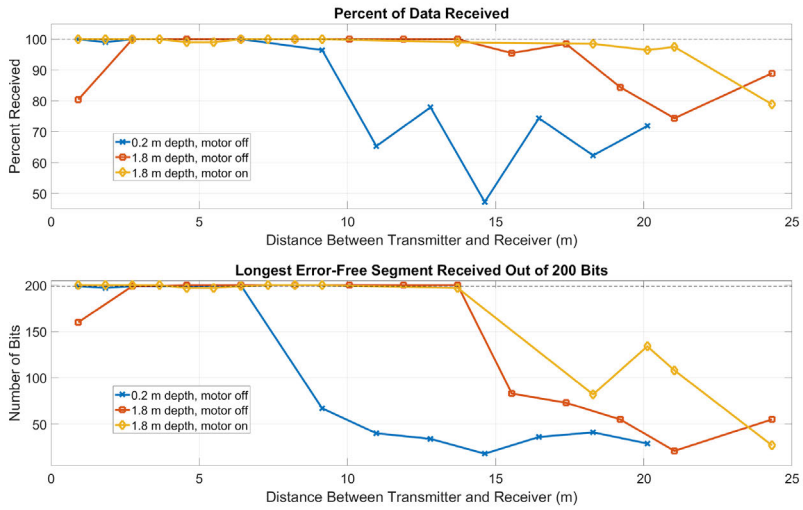

Figure A-3: Acoustic range tests: Results of transmitting a sequence of 200 alternating bits at 20 bits/s at various depths and distances, in order to characterize the acoustic communication performance.

small pool.

The received signals, outputs of the Goertzel algorithm, and decoded bits were also visualized to investigate the detector's performance under increasingly challenging conditions. Figure A-4 provides sample results from the tank and pool, both with the motor on and off. The motor noise interferes substantially with the transmitted tones and causes substantial noise in the output of the Goertzel algorithm. Nevertheless, the overlaid output of the dynamic peak detector algorithm indicates that the data is successfully decoded despite the noise and rapid variability of the received signals.

A.3.3 Acoustic Ocean Experiments

During the open-ocean experiments, the acoustic communication was evaluated by logging transmitted and received commands. Sample results of post-processing this data are presented in Figure A-5, where the red traces indicate desired fish states selected by the diver and blue traces indicate states executed by the fish. The repeated jumps back to neutral demonstrated by the blue traces represent timeouts of the fish, which are marked on the bottom of each plot by black stars. Timeouts occur when no command has been received for a specified duration of about 10 s, at which point

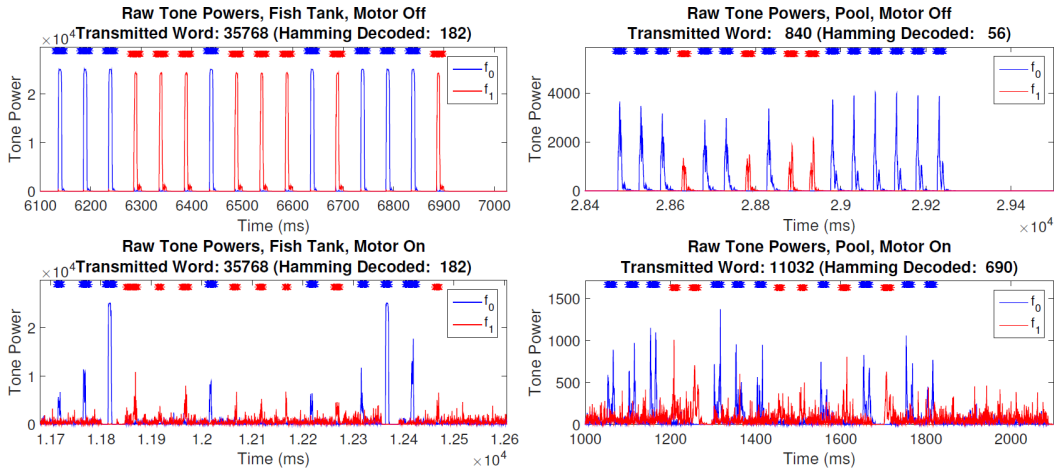

Figure A-4: Performance of tone detection algorithm: Complete command words were transmitted in a tank and a pool with the robot's motor on and off, in order to evaluate the modem's performance. Blue and red traces indicate data for each frequency channel of the FSK scheme, and stars at the top of each plot indicate decoded bits as detected by the real-time demodulation algorithm. Despite substantial noise and signal variations, all data is successfully decoded.

the fish returns to a neutral state and turns off the motor. The resulting silence often allows a faint transmitted command to be received, allowing the fish to return to desired operation.

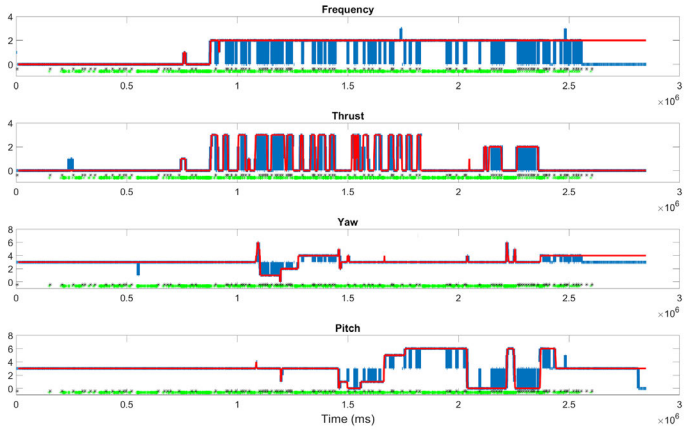

Figure A-5: Ocean communication tests: The sequences of transmitted and received fish states, shown here for dive 5, are used to evaluate the effectiveness of communication in the open ocean. The red lines show what desired fish state the transmitter commanded, and the blue lines show what the fish executed. Green dots indicate successful transmission, while black stars show time-outs of the fish. Each plot represents a separate control dimension exposed by the diver interface module.

Bibliography

Nicole Abaid, Tiziana Bartolini, Simone Macrì, and Maurizio Porfiri. Zebrafish responds differentially to a robotic fish of varying aspect ratio, tail beat frequency, noise, and color. *Behav. Brain Res.*, 233(2):545–553, August 2012. doi: 10.1016/j.bbr.2012.05.047.

Ian F Akyildiz, Dario Pompili, and Tommaso Melodia. Underwater acoustic sensor networks: research challenges. *Ad hoc networks*, 3(3):257–279, 2005. doi: 10.1016/j.adhoc.2005.01.004.

Silas Alben, Charles Witt, T Vernon Baker, Erik Anderson, and George V Lauder. Dynamics of freely swimming flexible foils. *Physics of Fluids*, 24(5):51901–51901, 2012. doi: 10.1063/1.4709477.

John Amend, Eric Brown, Nicholas Rodenberg, Heinrich Jaeger, and Hod Lipson. A positive pressure universal gripper based on the jamming of granular material. *Robotics, IEEE Transactions on*, 28(2):341–350, 2012. doi: 10.1109/tro.2011.2171093.

Martin Landrø Lasse Amundsen. Marine seismic sources part VIII: Fish hear a great deal. *GEO ExPro*, 8(3):42–46, April 2011.

Jamie M Anderson and Narender K Chhabra. Maneuvering and stability performance of a robotic tuna. *Integr. Comp. Biol.*, 42(1):118–126, February 2002. doi: 10.1093/icb/42.1.118.

Russell L Andersson. Aggressive trajectory generator for a robot ping-pong player. *IEEE Control Systems Magazine*, 9(2):15–21, 1989. doi: 10.1109/37.16766.

C Armanini, F Dal Corso, D Misseroni, and D Bigoni. From the elastica compass to the elastica catapult: an essay on the mechanics of soft robot arm. In *Proc. R. Soc. A*, volume 473, page 20160870. The Royal Society, 2017. doi: 10.1098/rspa.2016.0870.

K J Åström and T Hägglund. Revisiting the Ziegler–Nichols step response method for PID control. *J. Process Control*, 14(6):635–650, September 2004. doi: 10.1016/j.jprocont.2004.01.002.

Andrea Bajo, Roger E Goldman, and Nabil Simaan. Configuration and joint feedback for enhanced performance of multi-segment continuum robots. In *Robotics and*

Automation (ICRA), 2011 IEEE International Conference on, pages 2905–2912. IEEE, 2011. doi: 10.1109/icra.2011.5980005.

D N Beal, F S Hover, M S Triantafyllou, J C Liao, and G V Lauder. Passive propulsion in vortex wakes. *J. Fluid Mech.*, 549:385–402, February 2006. doi: 10.1017/s0022112005007925.

Miklós Bergou, Max Wardetzky, Stephen Robinson, Basile Audoly, and Eitan Grinspun. Discrete elastic rods. *ACM transactions on graphics (TOG)*, 27(3):63, 2008. doi: 10.1145/1508044.1508058.

Antonio Bicchi and Giovanni Tonietti. Fast and" soft-arm" tactics [robot arm design]. *IEEE Robotics & Automation Magazine*, 11(2):22–33, 2004. doi: 10.1109/MRA.2004.1310939.

Elaine Biddiss and Tom Chau. Electroactive polymeric sensors in hand prostheses: Bending response of an ionic polymer metal composite. *Medical Engineering and Physics*, 28(6):568–578, 2006. URL `http://www.sciencedirect.com/science/article/pii/S1350453305002122`.

Joshua Bishop-Moser, Girish Krishnan, Charles Kim, and Sridhar Kota. Design of soft robotic actuators using fluid-filled fiber-reinforced elastomeric enclosures in parallel combinations. In *Intelligent Robots and Systems (IROS), 2012 IEEE/RSJ International Conference on*, pages 4264–4269. IEEE, 2012. doi: 10.1109/iros.2012.6385966.

Robert Bogue. Underwater robots: a review of technologies and applications. *Industrial Robot: the international journal of robotics research and application*, 42(3):186–191, 2015. doi: 10.1108/ir-01-2015-0010.

Frank Bonnet, Yuta Kato, José Halloy, and Francesco Mondada. Infiltrating the zebrafish swarm: design, implementation and experimental tests of a miniature robotic fish lure for fish–robot interaction studies. *Artif. Life Robot.*, 21(3):239–246, September 2016. doi: 10.1007/s10015-016-0291-8.

Frank Bonnet, Alexey Gribovskiy, JosÃ© Halloy, and Francesco Mondada. Closed-loop interactions between a shoal of zebrafish and a group of robotic fish in a circular corridor. *Swarm Intelligence*, 11(36), 2018. doi: 10.1007/s11721-017-0153-6.

Federico Bosi, Diego Misseroni, Francesco Dal Corso, Sébastien Neukirch, and Davide Bigoni. Asymptotic self-restabilization of a continuous elastic structure. *Physical Review E*, 94(6):063005, 2016. doi: 10.1103/physreve.94.063005.

Eric Brown, Nicholas Rodenberg, John Amend, Annan Mozeika, Erik Steltz, Mitchell R Zakin, Hod Lipson, and Heinrich M Jaeger. Universal robotic gripper based on the jamming of granular material. *Proceedings of the National Academy of Sciences*, 107(44):18809–18814, 2010. doi: 10.1073/pnas.1003250107.

Rob Buckingham. Snake arm robots. *Industrial Robot: An International Journal*, 29 (3):242–245, 2002. doi: 10.1108/01439910210425531.

Sachit Butail, Nicole Abaid, Simone Macrì, and Maurizio Porfiri. Fish–Robot interactions: Robot fish in animal behavioral studies. In *Robot Fish*, Springer Tracts in Mechanical Engineering, pages 359–377. Springer, Berlin, Heidelberg, 2015. doi: 10.1007/978-3-662-46870-8_12.

Zack Butler, Peter Corke, Ron Peterson, and Daniela Rus. From robots to animals: Virtual fences for controlling cattle. *Int. J. Rob. Res.*, 25(5-6):485–508, May 2006. doi: 10.1177/0278364906065375.

Darwin G Caldwell, N Tsagarakis, and GA Medrano-Cerda. Bio-mimetic actuators: polymeric pseudo muscular actuators and pneumatic muscle actuators for biological emulation. *Mechatronics*, 10(4):499–530, 2000. doi: 10.1016/s0957-4158(99)00071-9.

M Calisti, A Arienti, ME Giannaccini, M Follador, M Giorelli, M Cianchetti, B Mazzolai, C Laschi, and P Dario. Study and fabrication of bioinspired octopus arm mockups tested on a multipurpose platform. In *Biomedical Robotics and Biomechatronics (BioRob), 2010 3rd IEEE RAS and EMBS International Conference on*, pages 461–466. IEEE, 2010. doi: 10.1109/biorob.2010.5625959.

M Calisti, M Giorelli, G Levy, B Mazzolai, B Hochner, C Laschi, and P Dario. An octopus-bioinspired solution to movement and manipulation for soft robots. *Bioinspiration & biomimetics*, 6(3):036002, 2011. doi: 10.1088/1748-3182/6/3/036002.

David B Camarillo, Christopher R Carlson, and J Kenneth Salisbury. Configuration tracking for continuum manipulators with coupled tendon drive. *Robotics, IEEE Transactions on*, 25(4):798–808, 2009. doi: 10.1109/tro.2009.2022426.

Federico Carpi, Danilo De Rossi, Roy Kornbluh, Ronald Edward Pelrine, and Peter Sommer-Larsen. *Dielectric elastomers as electromechanical transducers: Fundamentals, materials, devices, models and applications of an emerging electroactive polymer technology*. Elsevier, 2011.

Douglas H Cato. Marine biological choruses observed in tropical waters near Australia. *J. Acoust. Soc. Am.*, 64(3):736–743, 1978. doi: 10.1121/1.382038.

Douglas H Cato. Features of ambient noise in shallow water. *Shallow water acoustics*, pages 385–390, 1997.

Jorge G Cham, Sean A Bailey, Jonathan E Clark, Robert J Full, and Mark R Cutkosky. Fast and robust: hexapedal robots via shape deposition manufacturing. *The International Journal of Robotics Research*, 21(10-11):869–882, 2002. doi: 10.1177/027836402128964125.

Kyong-Sok Chang and Oussama Khatib. Manipulator control at kinematic singularities: A dynamically consistent strategy. In *Intelligent Robots and Systems 95.'Human Robot Interaction and Cooperative Robots', Proceedings. 1995 IEEE/RSJ International Conference on*, volume 3, pages 84–88. IEEE, 1995.

Xianhui Che, Ian Wells, Gordon Dickers, Paul Kear, and Xiaochun Gong. Re-evaluation of RF electromagnetic communication in underwater sensor networks. *Communications Magazine, IEEE*, 48(12):143–151, 2010. doi: 10.1109/mcom.2010.5673085.

G. Chen, Minh Tu Pham, and T. Redarce. Development and kinematic analysis of a silicone-rubber bending tip for colonoscopy. In *Intelligent Robots and Systems, 2006 IEEE/RSJ International Conference on*, pages 168–173, 2006. doi: 10.1109/IROS.2006.282129.

Jean Chenevier, David González, J Vicente Aguado, Francisco Chinesta, and Elías Cueto. Reduced-order modeling of soft robots. *PloS one*, 13(2):e0192052, 02 2018. doi: 10.1371/journal.pone.0192052. URL `https://doi.org/10.1371/journal.pone.0192052`.

Nick Cheney, Robert MacCurdy, Jeff Clune, and Hod Lipson. Unshackling evolution: evolving soft robots with multiple materials and a powerful generative encoding. In *Proceeding of the fifteenth annual conference on Genetic and evolutionary computation conference*, pages 167–174. ACM, 2013. doi: 10.1145/2661735.2661737.

N. Cheng, G. Ishigami, S. Hawthorne, H. Chen, M. Hansen, M. Telleria, R. Playter, and K. Iagnemma. Design and analysis of a soft mobile robot composed of multiple thermally activated joints driven by a single actuator. In *2010 IEEE International Conference on Robotics and Automation*, pages 5207–5212, May 2010. doi: 10.1109/ROBOT.2010.5509247.

Nadia G Cheng, Arvind Gopinath, Lifeng Wang, Karl Iagnemma, and Anette E Hosoi. Thermally tunable, self-healing composites for soft robotic applications. *Macromolecular Materials and Engineering*, 299(11):1279–1284, 2014. doi: 10.1002/mame.201400017.

Mandar Chitre, Shiraz Shahabudeen, and Milica Stojanovic. Underwater Acoustic Communications and Networking: Recent Advances and Future Challenges. *Mar. Technol. Soc. J.*, 42(1):103–116, 2008. doi: 10.4031/002533208786861263.

Kyu-Jin Cho, Je-Sung Koh, Sangwoo Kim, Won-Shik Chu, Yongtaek Hong, and Sung-Hoon Ahn. Review of manufacturing processes for soft biomimetic robots. *International Journal of Precision Engineering and Manufacturing*, 10(3):171–181, 2009. doi: 10.1007/s12541-009-0064-6.

Changhyun Choi, Joseph Del Preto, and Daniela Rus. Using vision for pre-and post-grasping object localization for soft hands. In *International Symposium on Experimental Robotics*, pages 601–612. Springer, 2016. doi: 10.1007/978-3-319-50115-4_52.

Changhyun Choi, Wilko Schwarting, Joseph DelPreto, and Daniela Rus. Learning object grasping for soft robot hands. *IEEE Robotics and Automation Letters*, 2018. doi: 10.1109/lra.2018.2810544.

Jean-Baptiste Chossat, Hee-Sup Shin, Yong-Lae Park, and Vincent Duchaine. Design and manufacturing of soft tactile skin using an embedded ionic liquid and tomographic imaging. *Journal of Mechanisms and Robotics*, 2014.

Ching-Ping Chou and Blake Hannaford. Measurement and modeling of mckibben pneumatic artificial muscles. *Robotics and Automation, IEEE Transactions on*, 12 (1):90–102, 1996. doi: 10.1109/70.481753.

Won-Shik Chu, Kyung-Tae Lee, Sung-Hyuk Song, Min-Woo Han, Jang-Yeob Lee, Hyung-Soo Kim, Min-Soo Kim, Yong-Jai Park, Kyu-Jin Cho, and Sung-Hoon Ahn. Review of biomimetic underwater robots using smart actuators. *Int. J. Precis. Eng. Manuf.*, 13(7):1281–1292, July 2012. doi: 10.1007/s12541-012-0171-7.

Meng Yee Chuah and Sangbae Kim. Enabling force sensing during ground locomotion: A bio-inspired, multi-axis, composite force sensor using discrete pressure mapping. *Sensors Journal, IEEE*, 14(5):1693–1703, 2014. doi: 10.1109/jsen.2014.2299805.

Valentina Cianca, Tiziana Bartolini, Maurizio Porfiri, and Simone Macrì. A robotics-based behavioral paradigm to measure anxiety-related responses in zebrafish. *PLoS One*, 8(7):e69661, July 2013. doi: 10.1371/journal.pone.0069661.

Matteo Cianchetti, Alessia Licofonte, Maurizio Follador, Francesco Rogai, and Cecilia Laschi. Bioinspired soft actuation system using shape memory alloys. In *Actuators*, volume 3, pages 226–244. Multidisciplinary Digital Publishing Institute, 2014a. doi: 10.3390/act3030226.

Matteo Cianchetti, Tommaso Ranzani, Giada Gerboni, Thrishantha Nanayakkara, Kaspar Althoefer, Prokar Dasgupta, and Arianna Menciassi. Soft robotics technologies to address shortcomings in today's minimally invasive surgery: the stiff-flop approach. *Soft robotics*, 1(2):122–131, 2014b. doi: 10.1089/soro.2014.0001.

Radoslaw Cieslak and Adam Morecki. Elephant trunk type elastic manipulator-a tool for bulk and liquid materials transportation. *Robotica*, 17(1):11–16, 1999. doi: 10.1017/s0263574799001009.

A Cloitre, V Subramaniam, N Patrikalakis, and P V y Alvarado. Design and control of a field deployable batoid robot. In *2012 4th IEEE RAS & EMBS International Conference on Biomedical Robotics and Biomechatronics (BioRob)*, pages 707–712, 2012. doi: 10.1109/biorob.2012.6290739.

Audren Cloitre, Bruce Arensen, Nicholas M Patrikalakis, Kamal Youcef-Toumi, and Pablo Valdivia Y Alvarado. Propulsive performance of an underwater soft biomimetic batoid robot. In *The Twenty-fourth International Ocean and Polar Engineering Conference*, volume 3, pages 326–333, 2014.

Fionnuala Connolly, Conor J Walsh, and Katia Bertoldi. Automatic design of fiber-reinforced soft actuators for trajectory matching. *Proceedings of the National Academy of Sciences*, 114(1):51–56, 2017.

Peter I Corke. A robotics toolbox for matlab. *IEEE Robotics & Automation Magazine*, 3(1):24–32, 1996. doi: 10.1109/100.486658.

Nikolaus Correll, Cagdas D. Onal, Haiyi Liang, Erik Schoenfeld, and Daniela Rus. Soft autonomous materials - using active elasticity and embedded distributed computation. In *12th International Symposium on Experimental Robotics (ISER)*, New Delhi, India, 2010. doi: 10.1007/978-3-642-28572-1_16.

Nikolaus Correll, Çağdaş D Önal, Haiyi Liang, Erik Schoenfeld, and Daniela Rus. Soft autonomous materials—using active elasticity and embedded distributed computation. In *Experimental Robotics*, pages 227–240. Springer, 2014. doi: 10.1007/978-3-642-28572-1_16.

Matthew Csencsits, Bryan A Jones, William McMahan, Vikram Iyengar, and Ian D Walker. User interfaces for continuum robot arms. In *IEEE/RSJ International Conference on Intelligent Robots and Systems (IROS)*, pages 3123–3130. IEEE, 2005. doi: 10.1109/iros.2005.1545434.

Ruth F Curtain and Hans Zwart. *An introduction to infinite-dimensional linear systems theory*, volume 21. Springer Science & Business Media, 2012.

Mark R Cutkosky and Imin Kao. Computing and controlling compliance of a robotic hand. *IEEE Transactions on Robotics and Automation*, 5(2):151–165, 1989. doi: 10.1109/70.88036.

Frank Daerden and Dirk Lefeber. Pneumatic artificial muscles: actuators for robotics and automation. *European journal of mechanical and environmental engineering*, 47(1):11–21, 2002.

Lee Danisch, Kevin Englehart, and Andrew Trivett. Spatially continuous six degree of freedom position and orientation sensor. *Sensor Review*, 19(2):106–112, 1999. doi: 10.1108/02602289910266142.

R E Davis, C C Eriksen, and C P Jones. Autonomous Buoyancy-Driven underwater gliders. *. . . Applications of Autonomous Underwater. . .*, pages 1–11, 2002. doi: 10.1201/9780203522301.ch3.

Alessandro De Luca and Pasquale Lucibello. A general algorithm for dynamic feedback linearization of robots with elastic joints. In *Robotics and Automation, 1998. Proceedings. 1998 IEEE International Conference on*, volume 1, pages 504–510. IEEE, 1998.

Kristin M de Payrebrune and Oliver M O'Reilly. On constitutive relations for a rod-based model of a pneu-net bending actuator. *Extreme Mechanics Letters*, 8: 38–46, 2016. doi: 10.1016/j.eml.2016.02.007.

Agostino De Santis, Bruno Siciliano, Alessandro De Luca, and Antonio Bicchi. An atlas of physical human–robot interaction. *Mechanism and Machine Theory*, 43(3): 253–270, 2008. doi: 10.1016/j.mechmachtheory.2007.03.003.

Raphael Deimel and Oliver Brock. A compliant hand based on a novel pneumatic actuator. In *2013 IEEE International Conference on Robotics and Automation*, pages 2047–2053, May 2013. doi: 10.1109/ICRA.2013.6630851.

Raphael Deimel and Oliver Brock. A novel type of compliant, underactuated robotic hand for dexterous grasping. In *Robotics: Science and Systems*, 2014. doi: 10.15607/rss.2014.x.018.

Raphael Deimel and Oliver Brock. A novel type of compliant and underactuated robotic hand for dexterous grasping. *The International Journal of Robotics Research*, 35(1-3):161–185, 2016. doi: 10.1177/0278364915592961. URL `http://ijr.sagepub.com/content/35/1-3/161.abstract`.

Cosimo Della Santina, Matteo Bianchi, Giorgio Grioli, Franco Angelini, Manuel Catalano, Manolo Garabini, and Antonio Bicchi. Controlling soft robots: balancing feedback and feedforward elements. *IEEE Robotics & Automation Magazine*, 24(3): 75–83, 2017. doi: 10.1109/mra.2016.2636360.

Cosimo Della Santina, Robert K. Katzschmann, Antonio Bicchi, and Daniela Rus. Dynamic control of soft robots interacting with the environment. In *Proceedings of the 1st International Conference on Soft Robotics*, 2018.

Joseph DelPreto, Robert K Katzschmann, Robert MacCurdy, and Daniela Rus. A compact acoustic communication module for remote control underwater. In *WUWNET '15: Proceedings of the 10th International Conference on Underwater Networks & Systems*, New York, NY, USA, oct 2015. ACM. ISBN 9781450340366. doi: 10.1145/2831296.2831337.

Carrick Detweiler, Stefan Sosnowski, Iuliu Vasilescu, and Daniela Rus. Saving energy with buoyancy and balance control for underwater robots with dynamic payloads. *Springer Tracts Adv. Robot.*, 54:429–438, 2009. doi: 10.1007/978-3-642-00196-3_49.

Bastian Deutschmann, Alexander Dietrich, and Christian Ott. Position control of an underactuated continuum mechanism using a reduced nonlinear model. In *Decision and Control (CDC), 2017 IEEE 56th Annual Conference on*, pages 5223–5230. IEEE, 2017a. doi: 10.1109/cdc.2017.8264433.

Bastian Deutschmann, Christian Ott, Concepcion A Monje, and Carlos Balaguer. Robust motion control of a soft robotic system using fractional order control. In *International Conference on Robotics in Alpe-Adria Danube Region*, pages 147–155. Springer, 2017b. doi: 10.1007/978-3-319-61276-8_17.

Mehmet R Dogar and Siddhartha S Srinivasa. Push-grasping with dexterous hands: mechanics and a method. In *Intelligent Robots and Systems (IROS), 2010 IEEE/RSJ*

International Conference on, pages 2123–2130. IEEE, Oct 2010. doi: 10.1109/IROS.2010.5652970.

Aaron M Dollar and Robert D Howe. A robust compliant grasper via shape deposition manufacturing. *Mechatronics, IEEE/ASME Transactions on*, 11(2):154–161, 2006. doi: 10.1109/tmech.2006.871090.

Aaron M Dollar and Robert D Howe. The highly adaptive sdm hand: Design and performance evaluation. *The International Journal of Robotics Research*, 29(5): 585–597, 2010. doi: 10.1177/0278364909360852.

M Doniec, M Angermann, and D Rus. An End-to-End Signal Strength Model for Underwater Optical Communications. *IEEE J. Oceanic Eng.*, 38(4):743–757, October 2013a. doi: 10.1109/joe.2013.2278932.

Marek Doniec, Iulian Topor, Mandar Chitre, and Daniela Rus. Autonomous, Localization-Free Underwater Data Muling Using Acoustic and Optical Communication. In *Experimental Robotics*, pages 841–857, 2013b. doi: 10.1007/978-3-319-00065-7_56.

Kevin J Dowling. Limbless locomotion: learning to crawl with a snake robot. *Ph. D Thesis, The Robotics Institute, Carnegie Mellon University*, 5000, 1996.

Christian Duriez and Thor Bieze. Soft robot modeling, simulation and control in real-time. In *Soft Robotics: Trends, Applications and Challenges*, pages 103–109. Springer, 2017.

Christian Duriez, Eulalie Coevoet, Frédérick Largilliere, T Morales-Bieze, Zhongkai Zhang, Mario Sanz-Lopez, Bruno Carrez, Damien Marchal, Olivier Goury, and Jérémie Dequidt. Framework for online simulation of soft robots with optimization-based inverse model. In *Simulation, Modeling, and Programming for Autonomous Robots (SIMPAR), IEEE International Conference on*, pages 111–118. IEEE, 2016. doi: 10.1109/simpar.2016.7862384.

Valentin Falkenhahn, Alexander Hildebrandt, Rüdiger Neumann, and Oliver Sawodny. Model-based feedforward position control of constant curvature continuum robots using feedback linearization. In *Robotics and Automation (ICRA), 2015 IEEE International Conference on*, pages 762–767. IEEE, 2015. doi: 10.1109/icra.2015.7139264.

Roy Featherstone. *Rigid body dynamics algorithms*. Springer, 2014.

Lee Freitag, Mark Johnson, Matthew Grund, Sandipa Singh, and James Preisig. Integrated acoustic communication and navigation for multiple UUVs. In *OCEANS, 2001. MTS/IEEE Conference and Exhibition*, volume 4, pages 2065–2070, 2001.

Kevin C Galloway, Panagiotis Polygerinos, Conor J Walsh, and Robert J Wood. Mechanically programmable bend radius for fiber-reinforced soft actuators. In

Advanced Robotics (ICAR), 2013 16th International Conference on, pages 1–6. IEEE, 2013. doi: 10.1109/icar.2013.6766586.

Mattia Gazzola, Levi H Dudte, Andrew G McCormick, and L Mahadevan. Dynamics of soft filaments that can stretch, shear, bend and twist. *arXiv preprint arXiv:1607.00430*, 2016.

Thomas George Thuruthel, Yasmin Ansari, Egidio Falotico, and Cecilia Laschi. Control strategies for soft robotic manipulators: A survey. *Soft robotics*, 2018. doi: 10.1089/soro.2017.0007.

Francesco Giorgio-Serchi, Andrea Arienti, Ilaria Baldoli, and Cecilia Laschi. An elastic pulsed-jet thruster for soft unmanned underwater vehicles. In *2013 IEEE International Conference on Robotics and Automation*, pages 5103–5110. IEEE, 2013. doi: 10.1109/icra.2013.6631306.

Gerald Goertzel. An Algorithm for the Evaluation of Finite Trigonometric Series. *Am. Math. Mon.*, 65(1):34–35, 1958. doi: 10.2307/2310304.

Ian A Gravagne and Ian D Walker. Uniform regulation of a multi-section continuum manipulator. In *Robotics and Automation, 2002. Proceedings. ICRA'02. IEEE International Conference on*, volume 2, pages 1519–1524. IEEE, 2002.

Ian A Gravagne, Christopher D Rahn, and Ian D Walker. Large deflection dynamics and control for planar continuum robots. *Mechatronics, IEEE/ASME Transactions on*, 8(2):299–307, 2003. doi: 10.1109/tmech.2003.812829.

Leopoldo Greco and Massimo Cuomo. B-spline interpolation of kirchhoff-love space rods. *Computer Methods in Applied Mechanics and Engineering*, 256:251–269, 2013. doi: 10.1016/j.cma.2012.11.017.

Guo, K Sugimoto, S Hata, Jianliang Su, and K Oguro. A new type of underwater fish-like microrobot. In *Proceedings. 2000 IEEE/RSJ International Conference on Intelligent Robots and Systems*, volume 2, pages 867–872, 2000.

Sami Haddadin, Alessandro De Luca, and Alin Albu-Schäffer. Robot collisions: A survey on detection, isolation, and identification. *IEEE Transactions on Robotics*, 33(6):1292–1312, 2017. doi: 10.1109/tro.2017.2723903.

J Halloy, G Sempo, G Caprari, C Rivault, M Asadpour, F Tâche, I Saïd, V Durier, S Canonge, J M Amé, C Detrain, N Correll, A Martinoli, F Mondada, R Siegwart, and J L Deneubourg. Social integration of robots into groups of cockroaches to control self-organized choices. *Science*, 318(5853):1155–1158, November 2007. doi: 10.1126/science.1144259.

Michael W Hannan and Ian D Walker. Kinematics and the implementation of an elephant's trunk manipulator and other continuum style robots. *Journal of Field Robotics*, 20(2):45–63, 2003. doi: 10.1002/rob.10070.

Kazuo Hirai, Masato Hirose, Yuji Haikawa, and Toru Takenaka. The development of honda humanoid robot. In *Robotics and Automation, 1998. Proceedings. 1998 IEEE International Conference on*, volume 2, pages 1321–1326. IEEE, 1998.

Shigeo Hirose, Peter Cave, and Charles Goulden. *Biologically inspired robots: serpentile locomotors and manipulators*. Oxford University Press, 1993.

Dónal P Holland, Evelyn J Park, Panagiotis Polygerinos, Gareth J Bennett, and Conor J Walsh. The soft robotics toolkit: Shared resources for research and design. *Soft Robotics*, 1(3):224–230, 2014. doi: 10.1089/soro.2014.0010.

Donal Padraic Holland, Colette Abah, Marielena Velasco-Enriquez, Maxwell Herman, Gareth J Bennett, Emir Augusto Vela, and Conor James Walsh. The soft robotics toolkit: Strategies for overcoming obstacles to the wide dissemination of soft-robotic hardware. *IEEE Robotics & Automation Magazine*, 24(1):57–64, 2017. doi: 10.1109/mra.2016.2639067.

Bianca Homberg, Robert K Katzschmann, Mehmet Dogar, and Daniela Rus. Haptic identification of objects using a modular soft robotic gripper. In *Intelligent Robots and Systems (IROS), 2015 IEEE/RSJ International Conference on*. IROS, Sept 2015. doi: 10.1109/iros.2015.7353596.

Bianca S. Homberg, Robert K. Katzschmann, Mehmet R. Dogar, and Daniela Rus. Robust proprioceptive grasping with a soft robot hand. *Autonomous Robots (in press)*, 2018. doi: 10.1007/s10514-018-9754-1.

Youngsuk Hong, Jinkyu Kim, and Frank C Park. Comparative analysis of energy-based criteria for dynamics-based robot motion optimization. In *Control Technology and Applications (CCTA), 2017 IEEE Conference on*, pages 175–180. IEEE, 2017. doi: 10.1109/ccta.2017.8062459.

Filip Ilievski, Aaron D Mazzeo, Robert F Shepherd, Xin Chen, and George M Whitesides. Soft robotics for chemists. *Angewandte Chemie*, 123(8):1930–1935, 2011. doi: 10.1002/anie.201006464.

Jules S Jaffe, Peter J S Franks, Paul L D Roberts, Diba Mirza, Curt Schurgers, Ryan Kastner, and Adrien Boch. A swarm of autonomous miniature underwater robot drifters for exploring submesoscale ocean dynamics. *Nat. Commun.*, 8:14189, January 2017. doi: 10.1038/ncomms14189.

Mark Johnson, David Herold, and Josko Catipovic. The design and performance of a compact underwater acoustic network node. In *OCEANS'94.'Oceans Engineering for Today's Technology and Tomorrow's Preservation.'Proceedings*, volume 3, pages III–467, 1994.

Bryan A Jones and Ian D Walker. Kinematics for multisection continuum robots. *Robotics, IEEE Transactions on*, 22(1):43–55, 2006a. doi: 10.1109/tro.2005.861458.

Bryan A Jones and Ian D Walker. Practical kinematics for real-time implementation of continuum robots. *Robotics, IEEE Transactions on*, 22(6):1087–1099, 2006b. doi: 10.1109/tro.2006.886268.

Shahab Kalantar and Uwe R Zimmer. Distributed shape control of homogeneous swarms of autonomous underwater vehicles. *Auton. Robots*, 22(1):37–53, January 2007.

Kenji Kaneko, Kensuke Harada, Fumio Kanehiro, Go Miyamori, and Kazuhiko Akachi. Humanoid robot hrp-3. In *Intelligent Robots and Systems, 2008. IROS 2008. IEEE/RSJ International Conference on*, pages 2471–2478. IEEE, 2008. doi: 10.1109/iros.2008.4650604.

Rongjie Kang, David T Branson, Tianjiang Zheng, Emanuele Guglielmino, and Darwin G Caldwell. Design, modeling and control of a pneumatically actuated manipulator inspired by biological continuum structures. *Bioinspiration & biomimetics*, 8(3):036008, 2013. doi: 10.1088/1748-3182/8/3/036008.

Apoorva D Kapadia, Ian D Walker, Darren M Dawson, and Enver Tatlicioglu. A model-based sliding mode controller for extensible continuum robots. In *Proceedings of the 9th WSEAS international conference on Signal processing, robotics and automation*, pages 113–120. World Scientific and Engineering Academy and Society (WSEAS), 2010.

Apoorva D Kapadia, Katelyn E Fry, and Ian D Walker. Empirical investigation of closed-loop control of extensible continuum manipulators. In *Intelligent Robots and Systems (IROS 2014), 2014 IEEE/RSJ International Conference on*, pages 329–335. IEEE, 2014. doi: 10.1109/iros.2014.6942580.

A Kapandji. Cotation clinique de l'opposition et de la contre-opposition du pouce. In *Annales de Chirurgie de la Main*, volume 5, pages 67–73. Elsevier, 1986. doi: 10.1016/s0753-9053(86)80053-9.

S L Katz, D A Syme, and R E Shadwick. High-speed swimming. enhanced power in yellowfin tuna. *Nature*, 410(6830):770–771, April 2001. doi: 10.1038/35071170.

Robert K Katzschmann, Andrew D. Marchese, and Daniela Rus. Hydraulic autonomous soft robotic fish for 3d swimming. In *International Symposium on Experimental Robotics (ISER)*, volume 109, pages 405–420, Marrakech, Morocco, 2014. ISBN 9783319237787. doi: 10.1007/978-3-319-23778-7_27.

Robert K Katzschmann, Andrew D. Marchese, and Daniela Rus. Autonomous Object Manipulation Using a Soft Planar Grasping Manipulator. *Soft Robotics*, 2(4): 155–164, dec 2015. ISSN 2169-5172. doi: 10.1089/soro.2015.0013. URL `http://online.liebertpub.com/doi/10.1089/soro.2015.0013`.

Robert K Katzschmann, Austin de Maille, David L Dorhout, and Daniela Rus. Cyclic hydraulic actuation for soft robotic devices. In *2016 IEEE/RSJ International*

Conference on Intelligent Robots and Systems (IROS), 2016. doi: 10.1109/iros.2016.7759472.

Robert K. Katzschmann, Brandon Araki, and Daniela Rus. Safe local navigation for visually impaired users with a time-of-flight and haptic feedback device. *IEEE Transactions on Neural Systems and Rehabilitation Engineering*, pages 1–1, 2018a. ISSN 1534-4320. doi: 10.1109/TNSRE.2018.2800665. URL `http://ieeexplore.ieee.org/document/8276628/`.

Robert K. Katzschmann, Joseph DelPreto, Robert MacCurdy, and Daniela Rus. Exploration of underwater life with an acoustically controlled soft robotic fish. *Science Robotics*, 3(16), 2018b. doi: 10.1126/scirobotics.aar3449. URL `http://robotics.sciencemag.org/content/3/16/eaar3449`.

Robert K Katzschmann, Aykut Satici, Daniela Rus, and Russ Tedrake. The soft juggler: Model-based control of a dynamically dexterous soft robot under large deformations. *The International Journal of Robotics Research (under review)*, 2018c.

Rafael Kelly. A tuning procedure for stable pid control of robot manipulators. *Robotica*, 13(2):141–148, 1995. doi: 10.1017/s0263574700017641.

Hassan K Khalil. Nonlinear systems. *Prentice-Hall, New Jersey*, 2(5):5–1, 1996.

Oussama Khatib. A unified approach for motion and force control of robot manipulators: The operational space formulation. *IEEE Journal on Robotics and Automation*, 3(1):43–53, 1987. doi: 10.1109/jra.1987.1087068.

J H Kim, S H Choi, D Kim, J Kim, and M Cho. Animal-Robot interaction for pet caring. In *2009 IEEE International Symposium on Computational Intelligence in Robotics and Automation - (CIRA)*, pages 159–164, December 2009a. doi: 10.1109/cira.2009.5423214.

Kwang J Kim and Satoshi Tadokoro. Electroactive polymers for robotic applications. *Artificial Muscles and Sensors (291 p.), Springer: London, United Kingdom*, 23, 2007.

Kyunam Kim, Adrian K Agogino, Deaho Moon, Laqshya Taneja, Aliakbar Toghyan, Borna Dehghani, Vytas SunSpiral, and Alice M Agogino. Rapid prototyping design and control of tensegrity soft robot for locomotion. In *Robotics and Biomimetics (ROBIO), 2014 IEEE International Conference on*, pages 7–14. IEEE, 2014. doi: 10.1109/robio.2014.7090299.

Sangbae Kim, Elliot Hawkes, Kyujin Cho, Matthew Joldaz, Joe Foleyz, and Robert Wood. Micro artificial muscle fiber using niti spring for soft robotics. In *Intelligent Robots and Systems, 2009. IROS 2009. IEEE/RSJ International Conference on*, pages 2228–2234. IEEE, 2009b. doi: 10.1109/iros.2009.5354178.

Sangbae Kim, Cecilia Laschi, and Barry Trimmer. Soft robotics: a bioinspired evolution in robotics. *Trends in Biotechnology*, 31(5):287–294, may 2013. ISSN 0167-7799. doi: http://dx.doi.org/10.1016/j.tibtech.2013.03.002. URL `http://www.sciencedirect.com/science/article/pii/S0167779913000632`.

Je-Sung Koh and Kyu-Jin Cho. Omega-shaped inchworm-inspired crawling robot with large-index-and-pitch (lip) sma spring actuators. *Mechatronics, IEEE/ASME Transactions on*, 18(2):419–429, 2013. doi: 10.1109/tmech.2012.2211033.

Jens Krause, Alan F T Winfield, and Jean-Louis Deneubourg. Interactive robots in experimental biology. *Trends Ecol. Evol.*, 26(7):369–375, July 2011. doi: 10.1016/j.tree.2011.03.015.

Scott Kuindersma, Robin Deits, Maurice Fallon, Andrés Valenzuela, Hongkai Dai, Frank Permenter, Twan Koolen, Pat Marion, and Russ Tedrake. Optimization-based locomotion planning, estimation, and control design for the atlas humanoid robot. *Autonomous Robots*, 40(3):429–455, 2016.

John Muir Kumph. *Maneuvering of a robotic pike*. PhD thesis, Massachusetts Institute of Technology, 2000.

S. Kusuda, S. Sawano, and S. Konishi. Fluid-resistive bending sensor having perfect compatibility with flexible pneumatic balloon actuator. In *Micro Electro Mechanical Systems, 2007. MEMS. IEEE 20th International Conference on*, pages 615–618, Jan 2007. doi: 10.1109/MEMSYS.2007.4433082.

Philip Lacovara. High-Bandwidth underwater communications. *Mar. Technol. Soc. J.*, 42(1):93–102, 2008. doi: 10.4031/002533208786861326.

Jennifer L Laine, Scott A Nichols, David K Novick, Patrick D O'Malley, Daniel Copeland, and Michael C Nechyba. Subjugator: a highly maneuverable, intelligent underwater vehicle. Technical report, Technical report, Machine Intelligence Laboratory, University of Florida, Gainesville, FL, 1999.

Tim Landgraf, Raúl Rojas, Hai Nguyen, Fabian Kriegel, and Katja Stettin. Analysis of the waggle dance motion of honeybees for the design of a biomimetic honeybee robot. *PLoS One*, 6(8):e21354, August 2011. doi: 10.1371/journal.pone.0021354.

Cecilia Laschi, Matteo Cianchetti, Barbara Mazzolai, Laura Margheri, Maurizio Follador, and Paolo Dario. Soft robot arm inspired by the octopus. *Advanced Robotics*, 26(7):709–727, 2012. doi: 10.1163/156855312x626343.

Cecilia Laschi, Barbara Mazzolai, and Matteo Cianchetti. Soft robotics: Technologies and systems pushing the boundaries of robot abilities. *Sci. Robot.*, 1(1):eaah3690, December 2016. doi: 10.1126/scirobotics.aah3690.

George V Lauder, Brooke Flammang, and Silas Alben. Passive robotic models of propulsion by the bodies and caudal fins of fish. *Integrative and Comparative Biology*, 52(5):576–587, 2012. doi: 10.1093/icb/ics096.

Joel Lehman and Kenneth O Stanley. Evolving a diversity of virtual creatures through novelty search and local competition. In *Proceedings of the 13th annual conference on Genetic and evolutionary computation*, pages 211–218. ACM, 2011. doi: 10.1145/2001576.2001606.

Daniel Leidner, Alexander Dietrich, Florian Schmidt, Christoph Borst, and Alin Albu-Schäffer. Object-centered hybrid reasoning for whole-body mobile manipulation. In *Robotics and Automation (ICRA), 2014 IEEE International Conference on*, pages 1828–1835. IEEE, 2014. doi: 10.1109/icra.2014.6907099.

Changquing Li and Christopher D Rahn. Design of continuous backbone, cable-driven robots. *Journal of Mechanical Design*, 124:265, 2002. doi: 10.1115/1.1447546.

Jinglin Li and Jing Xiao. A general formulation and approach to constrained, continuum manipulation. *Advanced Robotics*, 29(13):889–899, 2015. doi: 10.1080/01691864.2015.1052846.

Shuguang Li, Robert K. Katzschmann, and Daniela Rus. A soft cube capable of controllable continuous jumping. In *2015 IEEE/RSJ International Conference on Intelligent Robots and Systems (IROS)*, pages 1712–1717, sep 2015. doi: 10.1109/IROS.2015.7353598.

Tiefeng Li, Guorui Li, Yiming Liang, Tingyu Cheng, Jing Dai, Xuxu Yang, Bangyuan Liu, Zedong Zeng, Zhilong Huang, Yingwu Luo, Tao Xie, and Wei Yang. Fast-moving soft electronic fish. *Sci Adv*, 3(4):e1602045, April 2017. doi: 10.1126/sciadv.1602045.

Yu Lianzhi, Lu Yuesheng, Hu Zhongying, and Cheng Jian. Electro-pneumatic pressure servo-control for a miniature robot with rubber actuator. In *Digital Manufacturing and Automation (ICDMA), 2010 International Conference on*, volume 1, pages 631–634, 2010. doi: 10.1109/ICDMA.2010.158.

Hod Lipson. Challenges and opportunities for design, simulation, and fabrication of soft robots. *Soft Robotics*, 1(1):21–27, 2014. doi: 10.1089/soro.2013.0007.

Arthur Lismonde, Valentin Sonneville, and Olivier Brüls. Trajectory planning of soft link robots with improved intrinsic safety. *IFAC-PapersOnLine*, 50(1):6016–6021, 2017.

Andrea J Liu and Sidney R Nagel. Nonlinear dynamics: Jamming is not just cool any more. *Nature*, 396(6706):21–22, 1998.

Lanbo Liu, Shengli Zhou, and Jun-Hong Cui. Prospects and problems of wireless communication for underwater sensor networks. *Proc. Int. Wirel. Commun. Mob. Comput. Conf.*, 8(8):977–994, 2008. doi: 10.1002/wcm.654.

Lennart Ljung. System identification. In *Signal analysis and prediction*, pages 163–173. Springer, 1998. doi: 10.1201/b10384-67.

Ming Luo, Mahdi Agheli, and Cagdas D Onal. Theoretical modeling and experimental analysis of a pressure-operated soft robotic snake. *Soft Robotics*, 1(2):136–146, 2014. doi: 10.1089/soro.2013.0011.

Zheng-Hua Luo, Bao-Zhu Guo, and Ömer Morgül. *Stability and stabilization of infinite dimensional systems with applications*. Springer Science & Business Media, 2012.

Robert MacCurdy, Robert K. Katzschmann, Youbin Kim, and Daniela Rus. Printable hydraulics: A method for fabricating robots by 3d co-printing solids and liquids. In *2016 IEEE International Conference on Robotics and Automation (ICRA)*, pages 3878–3885, Stockholm, may 2016. doi: 10.1109/ICRA.2016.7487576. URL `http://arxiv.org/abs/1512.03744`.

Carmel Majidi. Soft robotics: A perspective - current trends and prospects for the future. *Soft Robotics*, 1(1):5–11, 2014. doi: 10.1089/soro.2013.0001.

A Maldonado-Ramírez, L A Torres-Méndez, and F Rodríguez-Telles. Ethologically inspired reactive exploration of coral reefs with collision avoidance: Bridging the gap between human and robot spatial understanding of unstructured environments. In *2015 IEEE/RSJ International Conference on Intelligent Robots and Systems (IROS)*, pages 4872–4879, 2015. doi: 10.1109/iros.2015.7354062.

L Manfredi, T Assaf, S Mintchev, S Marrazza, L Capantini, S Orofino, L Ascari, S Grillner, P Wallén, O Ekeberg, C Stefanini, and P Dario. A bioinspired autonomous swimming robot as a tool for studying goal-directed locomotion. *Biol. Cybern.*, 107 (5):513–527, October 2013. doi: 10.1007/s00422-013-0566-2.

Andrew D. Marchese. *Design, fabrication, and control of soft robots with fluidic elastomer actuators*. PhD thesis, Massachusetts Institute of Technology, 2015.

Andrew D. Marchese and Daniela Rus. Design, kinematics, and control of a soft spatial fluidic elastomer manipulator. *The International Journal of Robotics Research*, 35 (7):840–869, 2016.

Andrew D. Marchese, Cagdas D Onal, and Daniela Rus. Soft robot actuators using energy-efficient valves controlled by electropermanent magnets. In *Intelligent Robots and Systems (IROS), 2011 IEEE/RSJ International Conference on*, pages 756–761. IEEE, 2011. doi: 10.1109/iros.2011.6095064.

Andrew D. Marchese, Cagdas D. Onal, and Daniela Rus. Towards a self-contained soft robotic fish: On-board pressure generation and embedded electro-permanent magnet valves. In Jaydev P. Desai, Gregory Dudek, Oussama Khatib, and Vijay Kumar, editors, *International Symposium on Experimental Robotics*, volume 88 of *Springer Tracts in Advanced Robotics*, pages 41–54. Springer International Publishing, 2013. ISBN 978-3-319-00064-0. doi: 10.1007/978-3-319-00065-7_4.

Andrew D. Marchese, Robert K. Katzschmann, and Daniela Rus. Whole arm planning for a soft and highly compliant 2D robotic manipulator. *IEEE International*

Conference on Intelligent Robots and Systems, pages 554–560, 2014a. ISSN 21530866. doi: 10.1109/IROS.2014.6942614.

Andrew D. Marchese, Konrad Komorowski, Cagdas D Onal, and Daniela Rus. Design and control of a soft and continuously deformable 2d robotic manipulation system. In *Robotics and Automation (ICRA), 2014 IEEE International Conference on*. IEEE, 2014b. doi: 10.1109/icra.2014.6907161.

Andrew D. Marchese, Cagdas D Onal, and Daniela Rus. Autonomous soft robotic fish capable of escape maneuvers using fluidic elastomer actuators. *Soft Robotics*, 1 (1):75–87, March 2014c. doi: 10.1089/soro.2013.0009.

Andrew D. Marchese, Robert K. Katzschmann, and Daniela Rus. A recipe for soft fluidic elastomer robots. *Soft Robotics*, 2(1):7–25, 2015. ISSN 2169-5172. doi: 10.1089/soro.2014.0022. URL `http://online.liebertpub.com/doi/10.1089/soro.2014.0022`.

Andrew D. Marchese, Russ Tedrake, and Daniela Rus. Dynamics and trajectory optimization for a soft spatial fluidic elastomer manipulator. *The International Journal of Robotics Research*, 35(8):1000–1019, 2016.

S Marras and M Porfiri. Fish and robots swimming together: attraction towards the robot demands biomimetic locomotion. *Journal of The Royal Society ...*, 9(73): 1856–1868, August 2012. doi: 10.1098/rsif.2012.0084.

Ramses V Martinez, Jamie L Branch, Carina R Fish, Lihua Jin, Robert F Shepherd, Rui Nunes, Zhigang Suo, and George M Whitesides. Robotic tentacles with three-dimensional mobility based on flexible elastomers. *Advanced Materials*, 25(2): 205–212, 2013.

M S Martins, Nicolas Pinto, G Rocha, J Cabral, and S Laceros Mendez. Development of a 1 Mbps low power acoustic modem for underwater communications. In *Ultrasonics Symposium (IUS), 2014 IEEE International*, pages 2482–2485, 2014. doi: 10.1109/ultsym.2014.0619.

Matlab. *Version R2017b*. The MathWorks Inc., Natick, MA, 2017.

Anirban Mazumdar, Pablo Valdivia y Alvarado, and Kamal Youcef-Toumi. Maneuverability of a robotic tuna with compliant body. *IEEE Int. Conf. Robot. Autom.*, pages 683–688, May 2008. doi: 10.1109/robot.2008.4543284.

Michael Andrew McEvoy and Nikolaus Correll. Shape change through programmable stiffness. In *International Symposium on Experimental Robotics (ISER)*, Marrakech, Morocco, 2014a. Springer Verlag. doi: 10.1007/978-3-319-23778-7_59.

Michael Andrew McEvoy and Nikolaus Correll. Thermoplastic variable stiffness composites with embedded, networked sensing, actuation, and control. *Journal of Composite Materials*, page 0021998314525982, 2014b. doi: 10.1177/0021998314525982.

Michael Andrew McEvoy and Nikolaus Correll. Materials that couple sensing, actuation, computation, and communication. *Science*, 347(6228):1261689, 2015. doi: 10.1126/science.1261689.

David McFarland, Ian Gilhespy, and Ehsan Honary. DIVEBOT: A diving robot with a whale-like buoyancy mechanism. *Robotica*, 21(4):385–398, August 2003. doi: 10.1017/s026357470300496x.

William McMahan, Bryan A Jones, and Ian D Walker. Design and implementation of a multi-section continuum robot: Air-octor. In *Intelligent Robots and Systems, 2005.(IROS 2005). 2005 IEEE/RSJ International Conference on*, pages 2578–2585. IEEE, 2005. doi: 10.1109/iros.2005.1545487.

William McMahan, V Chitrakaran, M Csencsits, D Dawson, Ian D Walker, Bryan A Jones, M Pritts, D Dienno, M Grissom, and Christopher D Rahn. Field trials and testing of the octarm continuum manipulator. In *Robotics and Automation, 2006. ICRA 2006. Proceedings 2006 IEEE International Conference on*, pages 2336–2341. IEEE, 2006.

Á Miklósi and L Gerencsér. Potential application of autonomous and semi-autonomous robots in the study of animal behaviour. In *2012 IEEE 3rd International Conference on Cognitive Infocommunications (CogInfoCom)*, pages 759–762, December 2012. doi: 10.1109/coginfocom.2012.6421952.

Stephen A Morin, Robert F Shepherd, Sen Wai Kwok, Adam A Stokes, Alex Nemiroski, and George M Whitesides. Camouflage and display for soft machines. *Science*, 337 (6096):828–832, 2012. doi: 10.1126/science.1222149.

John Morrow, Samantha Hemleben, and Yigit Menguc. Directly fabricating soft robotic actuators with an open-source 3-d printer. *IEEE Robotics and Automation Letters*, 2(1):277–281, 2017. doi: 10.1109/lra.2016.2598601.

Bobak Mosadegh, Panagiotis Polygerinos, Christoph Keplinger, Sophia Wennstedt, Robert F Shepherd, Unmukt Gupta, Jongmin Shim, Katia Bertoldi, Conor J Walsh, and George M Whitesides. Pneumatic networks for soft robotics that actuate rapidly. *Advanced Functional Materials*, 24(15):2163–2170, 2014. doi: 10.1002/adfm.201303288.

Richard M Murray. *A mathematical introduction to robotic manipulation*. CRC press, Boca Raton, FL, USA, 1st edition, 1994. ISBN 0849379814.

Kohei Nakajima, Tao Li, Helmut Hauser, and Rolf Pfeifer. Exploiting short-term memory in soft body dynamics as a computational resource. *Journal of The Royal Society Interface*, 11(100):20140437, 2014. doi: 10.1098/rsif.2014.0437.

Jun Nakanishi, Rick Cory, Michael Mistry, Jan Peters, and Stefan Schaal. Operational space control: A theoretical and empirical comparison. *The International Journal of Robotics Research*, 27(6):737–757, 2008. doi: 10.1177/0278364908091463.

Dragomir N Nenchev. Redundancy resolution through local optimization: A review. *Journal of Robotic Systems*, 6(6):769–798, 1989. doi: 10.1002/rob.4620060607.

Srinivas Neppalli, Matthew A Csencsits, Bryan A Jones, and Ian D Walker. Closed-form inverse kinematics for continuum manipulators. *Advanced Robotics*, 23(15): 2077–2091, 2009. doi: 10.1163/016918609x12529299964101.

Cagdas D Onal and Daniela Rus. Autonomous undulatory serpentine locomotion utilizing body dynamics of a fluidic soft robot. *Bioinspiration & biomimetics*, 8(2): 026003, 2013. doi: 10.1088/1748-3182/8/2/026003.

Cagdas D Onal, Xin Chen, George M Whitesides, and Daniela Rus. Soft mobile robots with on-board chemical pressure generation. In *International Symposium on Robotics Research (ISRR)*, 2011. doi: 10.1007/978-3-319-29363-9_30.

Christian Ott. *Cartesian impedance control of redundant and flexible-joint robots*. Springer, 2008.

Yong-Lae Park, Carmel Majidi, Rebecca Kramer, Phillipe Bérard, and Robert J Wood. Hyperelastic pressure sensing with a liquid-embedded elastomer. *Journal of Micromechanics and Microengineering*, 20(12):125029, 2010. doi: 10.1088/0960-1317/20/12/125029.

Yong-Lae Park, Bor-Rong Chen, and Robert J Wood. Design and fabrication of soft artificial skin using embedded microchannels and liquid conductors. *Sensors Journal, IEEE*, 12(8):2711–2718, 2012. doi: 10.1109/jsen.2012.2200790.

Yong-Lae Park, Bor-rong Chen, Néstor O Pérez-Arancibia, Diana Young, Leia Stirling, Robert J Wood, Eugene C Goldfield, and Radhika Nagpal. Design and control of a bio-inspired soft wearable robotic device for ankle–foot rehabilitation. *Bioinspiration & biomimetics*, 9(1):016007, 2014. doi: 10.1088/1748-3182/9/1/016007.

Vadim Pavlov, Benyamin Rosental, Nathaniel F Hansen, Jody M Beers, George Parish, Ian Rowbotham, and Barbara A Block. Hydraulic control of tuna fins: A role for the lymphatic system in vertebrate locomotion. *Science*, 357(6348):310–314, July 2017. doi: 10.1126/science.aak9607.

Kaare Brandt Petersen and Michael Syskind Pedersen. The matrix cookbook, nov 2012. URL `http://www2.imm.dtu.dk/pubdb/p.php?3274`. Version 20121115.

Rolf Pfeifer, Max Lungarella, and Fumiya Iida. The challenges ahead for bio-inspired'soft'robotics. *Communications of the ACM*, 55(11):76–87, 2012. doi: 10.1145/2366316.2366335.

P Phamduy, G Polverino, R C Fuller, and M Porfiri. Fish and robot dancing together: bluefin killifish females respond differently to the courtship of a robot with varying color morphs. *Bioinspir. Biomim.*, 9(3):036021, September 2014. doi: 10.1088/1748-3182/9/3/036021.

Paul Phamduy, Miguel Vazquez, Alessandro Rizzo, and Maurizio Porfiri. Miniature underwater robotic fish for Animal-Robot interactions. In *Volume 2: Mechatronics; Mechatronics and Controls in Advanced Manufacturing; Modeling and Control of Automotive Systems and Combustion Engines; Modeling and Validation; Motion and Vibration Control Applications; Multi-Agent and Networked Systems; Path Planning and Motion Control; Robot Manipulators; Sensors and Actuators; Tracking Control Systems; Uncertain Systems and Robustness; Unmanned, Ground and Surface Robotics; Vehicle Dynamic Controls; Vehicle Dynamics and Traffic Control*, page V002T17A009. ASME, October 2016. doi: 10.1115/dscc2016-9857.

G Polverino, N Abaid, V Kopman, S Macrì, and M Porfiri. Zebrafish response to robotic fish: preference experiments on isolated individuals and small shoals. *Bioinspir. Biomim.*, 7(3):036019, September 2012. doi: 10.1088/1748-3182/7/3/036019.

Panagiotis Polygerinos, Stacey Lyne, Zheng Wang, Luis Fernando Nicolini, Bobak Mosadegh, George M Whitesides, and Conor J Walsh. Towards a soft pneumatic glove for hand rehabilitation. In *Intelligent Robots and Systems (IROS), 2013 IEEE/RSJ International Conference on*, pages 1512–1517. IEEE, IEEE, November 2013. ISBN 978-1-4673-6358-7. doi: 10.1109/IROS.2013.6696549.

Panagiotis Polygerinos, Zheng Wang, Johannes TB Overvelde, Kevin C Galloway, Robert J Wood, Katia Bertoldi, and Conor J Walsh. Modeling of soft fiber-reinforced bending actuators. *IEEE Transactions on Robotics*, 31(3):778–789, 2015. doi: 10.1109/tro.2015.2428504.

Panagiotis Polygerinos, Nikolaus Correll, Stephen A Morin, Bobak Mosadegh, Cagdas D Onal, Kirstin Petersen, Matteo Cianchetti, Michael T Tolley, and Robert F Shepherd. Soft robotics: Review of fluid-driven intrinsically soft devices; manufacturing, sensing, control, and applications in human-robot interaction. *Advanced Engineering Materials*, 2017. doi: 10.1002/adem.201700016.

A Popper, D Plachta, D Mann, and D Higgs. Response of clupeid fish to ultrasound: a review. *ICES J. Mar. Sci.*, 61(7):1057–1061, 2004. doi: 10.1016/j.icesjms.2004.06.005.

Gill A. Pratt and Matthew M. Williamson. Series elastic actuators. In *Proceedings 1995 IEEE/RSJ International Conference on Intelligent Robots and Systems. Human Robot Interaction and Cooperative Robots*, volume 1, pages 399–406 vol.1, Aug 1995. doi: 10.1109/IROS.1995.525827.

Michael B Pritts and Christopher D Rahn. Design of an artificial muscle continuum robot. In *Robotics and Automation, 2004. Proceedings. ICRA'04. 2004 IEEE International Conference on*, volume 5, pages 4742–4746. IEEE, 2004. doi: 10.1109/robot.2004.1302467.

Morgan Quigley, Ken Conley, Brian P. Gerkey, Josh Faust, Tully Foote, Jeremy Leibs, Rob Wheeler, and Andrew Y. Ng. Ros: an open-source robot operating system. In *ICRA Workshop on Open Source Software*, 2009.

Marc H Raibert. *Legged robots that balance*. MIT press, 1986. doi: 10.1109/mex.1986.4307016.

Aditi Raj and Atul Thakur. Fish-inspired robots: design, sensing, actuation, and autonomy- a review of research. *Bioinspir. Biomim.*, 11:31001, 2016. doi: 10.1088/1748-3190/11/3/031001.

Mark Read, Christoph Möslinger, Tobias Dipper, Daniela Kengyel, James Hilder, Ronald Thenius, Andy Tyrrell, Jon Timmis, and Thomas Schmickl. Profiling underwater swarm robotic shoaling performance using simulation. In *Towards Autonomous Robotic Systems*, Lecture Notes in Computer Science, pages 404–416. Springer, Berlin, Heidelberg, August 2013. doi: 10.1007/978-3-662-43645-5_42.

Federico Renda, Frédéric Boyer, Jorge Manuel Miranda Dias, and Lakmal D. Seneviratne. Discrete Cosserat Approach for Multi-Section Soft Robots Dynamics. *CoRR*, abs/1702.03660, 2017. URL `http://arxiv.org/abs/1702.03660`.

DB Reynolds, DW Repperger, CA Phillips, and G Bandry. Modeling the dynamic characteristics of pneumatic muscle. *Annals of Biomedical Engineering*, 31(3):310–317, 2003. doi: 10.1114/1.1554921.

Thomas J Roberts. Contribution of elastic tissues to the mechanics and energetics of muscle function during movement. *Journal of Experimental Biology*, 219(2):266–275, 2016. doi: 10.1242/jeb.124446.

Thomas J Roberts and Emanuel Azizi. Flexible mechanisms: the diverse roles of biological springs in vertebrate movement. *Journal of Experimental Biology*, 214(3):353–361, 2011. doi: 10.1242/jeb.038588.

Ellen T. Roche, Robert Wohlfarth, Johannes T. B. Overvelde, Nikolay V. Vasilyev, Frank A. Pigula, David J. Mooney, Katia Bertoldi, and Conor J. Walsh. A Bioinspired Soft Actuated Material. *Advanced Materials*, 26(8):1200–1206, 2014. doi: 10.1002/adma.201304018.

Donato Romano, Giovanni Benelli, Elisa Donati, Damiano Remorini, Angelo Canale, and Cesare Stefanini. Multiple cues produced by a robotic fish modulate aggressive behaviour in siamese fighting fishes. *Sci. Rep.*, 7(1):4667, July 2017a. doi: 10.1038/s41598-017-04840-0.

Donato Romano, Giovanni Benelli, and Cesare Stefanini. Escape and surveillance asymmetries in locusts exposed to a guinea fowl-mimicking robot predator. *Sci. Rep.*, 7(1):12825, October 2017b. doi: 10.1038/s41598-017-12941-z.

Tommaso Ruberto, Violet Mwaffo, Sukhgewanpreet Singh, Daniele Neri, and Maurizio Porfiri. Zebrafish response to a robotic replica in three dimensions. *R Soc Open Sci*, 3(10):160505, October 2016. doi: 10.1098/rsos.160505.

Mordecai B Rubin. *Cosserat theories: shells, rods and points*, volume 79. Springer Science & Business Media, 2013.

Gundula Runge and Annika Raatz. A framework for the automated design and modelling of soft robotic systems. *CIRP Annals-Manufacturing Technology*, 2017. doi: 10.1016/j.cirp.2017.04.104.

Daniela Rus and Michael T Tolley. Design, fabrication and control of soft robots. *Nature*, 521(7553):467–475, 2015. doi: 10.1038/nature14543.

SM Hadi Sadati, S Elnaz Naghibi, Ian D Walker, Kaspar Althoefer, and Thrishantha Nanayakkara. Control space reduction and real-time accurate modeling of continuum manipulators using ritz and ritz–galerkin methods. *IEEE Robotics and Automation Letters*, 3(1):328–335, 2018. doi: 10.1109/lra.2017.2743100.

Antonio Sánchez, Sara Blanc, Pedro Yuste, Angel Perles, Juan José Serrano, Instituto Itaca, Universitat Politècnica De València, and Camino De Vera. An ultra-low power and flexible acoustic modem design to develop energy-efficient underwater sensor networks. *Sensors*, 12(6):6837–6856, 2012. doi: 10.3390/s120606837.

Sina Sareh, Jonathan Rossiter, Andrew Conn, Knut Drescher, and Raymond E Goldstein. Swimming like algae: biomimetic soft artificial cilia. *Journal of the Royal Society Interface*, page rsif20120666, 2012. doi: 10.1098/rsif.2012.0666.

T Schmickl, R Thenius, C Moslinger, J Timmis, A Tyrrell, M Read, J Hilder, J Halloy, A Campo, C Stefanini, L Manfredi, S Orofino, S Kernbach, T Dipper, and D Sutantyo. CoCoRo – the Self-Aware underwater swarm. In *2011 Fifth IEEE Conference on Self-Adaptive and Self-Organizing Systems Workshops*, pages 120–126, October 2011. doi: 10.1109/sasow.2011.11.

Lorenzo Sciavicco and Bruno Siciliano. *Modelling and control of robot manipulators*. Springer Science & Business Media, 2012.

S Seok, A Wang, M Y (michael) Chuah, D J Hyun, J Lee, D M Otten, J H Lang, and S Kim. Design principles for Energy-Efficient legged locomotion and implementation on the MIT cheetah robot. *IEEE/ASME Trans. Mechatron.*, 20(3):1117–1129, June 2015. doi: 10.1109/tmech.2014.2339013.

Sangok Seok, Cagdas Denizel Onal, Robert Wood, Daniela Rus, and Sangbae Kim. Peristaltic locomotion with antagonistic actuators in soft robotics. In *Robotics and Automation (ICRA), 2010 IEEE International Conference on*, pages 1228–1233. IEEE, 2010. doi: 10.1109/robot.2010.5509542.

Sangok Seok, Cagdas Denizel Onal, Kyu-Jin Cho, Robert J Wood, Daniela Rus, and Sangbae Kim. Meshworm: a peristaltic soft robot with antagonistic nickel titanium coil actuators. *IEEE/ASME Transactions on mechatronics*, 18(5):1485–1497, 2013. doi: 10.1109/tmech.2012.2204070.

Wanliang Shan, Tong Lu, and Carmel Majidi. Soft-matter composites with electrically tunable elastic rigidity. *Smart Materials and Structures*, 22(8):85005, 2013. doi: 10.1088/0964-1726/22/8/085005.

Robert F Shepherd, Filip Ilievski, Wonjae Choi, Stephen A Morin, Adam A Stokes, Aaron D Mazzeo, Xin Chen, Michael Wang, and George M Whitesides. Multigait soft robot. *Proceedings of the National Academy of Sciences*, 108(51):20400–20403, 2011. doi: 10.1073/pnas.1116564108.

Robert F Shepherd, Adam A Stokes, Jacob Freake, Jabulani Barber, Phillip W Snyder, Aaron D Mazzeo, Ludovico Cademartiri, Stephen A Morin, and George M Whitesides. Using explosions to power a soft robot. *Angewandte Chemie*, 125(10): 2964–2968, 2013a. doi: 10.1002/anie.201209540.

Robert F Shepherd, Adam A Stokes, Rui Nunes, and George M Whitesides. Soft machines that are resistant to puncture and that self seal. *Advanced Materials*, 25 (46):6709–6713, 2013b. doi: 10.1002/adma.201303175.

K Shibuya, Y Kado, S Honda, T Iwamoto, and K Tsutsumi. Underwater robot with a buoyancy control system based on the spermaceti oil hypothesis. In *2006 IEEE/RSJ International Conference on Intelligent Robots and Systems*, pages 3012–3017, 2006. doi: 10.1109/iros.2006.282236.

Sigurd Skogestad. Simple analytic rules for model reduction and pid controller tuning. *Journal of process control*, 13(4):291–309, 2003. doi: 10.4173/mic.2004.2.2.

Erik H Skorina, Ming Luo, Selim Ozel, Fuchen Chen, Weijia Tao, and Cagdas D Onal. Feedforward augmented sliding mode motion control of antagonistic soft pneumatic actuators. In *Robotics and Automation (ICRA), 2015 IEEE International Conference on*, pages 2544–2549. IEEE, 2015. doi: 10.1109/icra.2015.7139540.

Erik H Skorina, Weijia Tao, Fuchen Chen, Ming Luo, and Cagdas D Onal. Motion control of a soft-actuated modular manipulator. In *Robotics and Automation (ICRA), 2016 IEEE International Conference on*, pages 4997–5002. IEEE, 2016. doi: 10.1109/icra.2016.7487706.

Jean-Jacques E. Slotine and Weiping Li. On the adaptive control of robot manipulators. *The International Journal of Robotics Research*, 6(3):49–59, 1987. doi: 10.1177/027836498700600303. URL `https://doi.org/10.1177/027836498700600303`.

Brandon L Southall, Ann E Bowles, William T Ellison, James J Finneran, Roger L Gentry, Charles R Greene, Jr, David Kastak, Darlene R Ketten, James H Miller, Paul E Nachtigall, W John Richardson, Jeanette A Thomas, and Peter L Tyack. Overview. *Aquatic Mammals; Moline*, 33(4):411–414, 2007. doi: 10.1578/am.33.4.2007.411.

C Stefanini, S Orofino, L Manfredi, S Mintchev, S Marrazza, T Assaf, L Capantini, E Sinibaldi, S Grillner, P Wallén, and P Dario. A novel autonomous, bioinspired swimming robot developed by neuroscientists and bioengineers. *Bioinspir. Biomim.*, 7(2):025001, June 2012. doi: 10.1088/1748-3182/7/2/025001.

Erik Steltz, Annan Mozeika, Nick Rodenberg, Eric Brown, and Heinrich M Jaeger. JSEL: Jamming skin enabled locomotion. In *Intelligent Robots and Systems, 2009. (IROS) 2009. IEEE/RSJ International Conference on*, pages 5672–5677. IEEE, October 2009. doi: 10.1109/IROS.2009.5354790.

M Stojanovic and J Preisig. Underwater acoustic communication channels: Propagation models and statistical characterization. *Communications Magazine, IEEE*, 47 (1):84–89, 2009. doi: 10.1109/mcom.2009.4752682.

Adam A Stokes, Robert F Shepherd, Stephen A Morin, Filip Ilievski, and George M Whitesides. A hybrid combining hard and soft robots. *Soft Robotics*, 1(1):70–74, 2014. doi: 10.1089/soro.2013.0002.

Koichi Suzumori, Shoichi Iikura, and Hiroshisa Tanaka. Applying a flexible microactuator to robotic mechanisms. *Control Systems, IEEE*, 12(1):21–27, 1992. doi: 10.1109/37.120448.

Koichi Suzumori, Satoshi Endo, Takefumi Kanda, Naomi Kato, and Hiroyoshi Suzuki. A bending pneumatic rubber actuator realizing soft-bodied manta swimming robot. In *Robotics and Automation, 2007 IEEE International Conference on*, pages 4975–4980. IEEE, 2007. doi: 10.1109/robot.2007.364246.

Maxime Thieffry, Alexandre Kruszewski, Olivier Goury, Thierry-Marie Guerra, and Christian Duriez. Dynamic control of soft robots. In *IFAC World Congress*, 2017.

Thomas George Thuruthel, Egidio Falotico, Mariangela Manti, and Cecilia Laschi. Stable open loop control of soft robotic manipulators. *IEEE Robotics and Automation Letters*, 2018. doi: 10.1109/lra.2018.2797241.

Michael T Tolley, Robert F Shepherd, Michael Karpelson, Nicholas W Bartlett, Kevin C Galloway, Michael Wehner, Rui Nunes, George M Whitesides, and Robert J Wood. An untethered jumping soft robot. In *Intelligent Robots and Systems (IROS 2014), 2014 IEEE/RSJ International Conference on*, pages 561–566. IEEE, 2014a. doi: 10.1109/iros.2014.6942615.

Michael T Tolley, Robert F Shepherd, Bobak Mosadegh, Kevin C Galloway, Michael Wehner, Michael Karpelson, Robert J Wood, and George M Whitesides. A resilient, untethered soft robot. *Soft Robotics*, 2014b. doi: 10.1089/soro.2014.0008.

Bertrand Tondu and Pierre Lopez. Modeling and control of mckibben artificial muscle robot actuators. *Control Systems, IEEE*, 20(2):15–38, 2000. doi: 10.1109/37.833638.

Giovanni Tonietti, Riccardo Schiavi, and Antonio Bicchi. Design and control of a variable stiffness actuator for safe and fast physical human/robot interaction. In *Proceedings of the 2005 IEEE International Conference on Robotics and Automation*, pages 526–531. IEEE, April 2005. doi: 10.1109/ROBOT.2005.1570172.

Barry Trimmer. A journal of soft robotics: Why now? *Soft Robotics*, 1(1):1–4, 2014. doi: 10.1089/soro.2013.0003.

Barry A Trimmer, Ann E Takesian, Brian M Sweet, Chris B Rogers, Daniel C Hake, and Daniel J Rogers. Caterpillar locomotion: a new model for soft-bodied climbing and burrowing robots. In *7th International Symposium on Technology and the Mine Problem*, volume 1, pages 1–10. Mine Warfare Association Monterey, CA, 2006.

Deepak Trivedi, Christopher D. Rahn, William M. Kier, and Ian D. Walker. Soft robotics: Biological inspiration, state of the art, and future research. *Applied Bionics and Biomechanics*, 5(3):99–117, July 2008. ISSN 1176-2322. doi: 10.1080/11762320802557865. URL `http://dx.doi.org/10.1080/11762320802557865`.

E J Tucholski. Underwater Acoustics and Sonar. SP411 Handouts and Notes. Fall 2006. *US Naval Academy, Annappolis, MD*, 12:11–1 to 11–8, 2006.

T. Umedachi, V. Vikas, and B.A. Trimmer. Highly deformable 3-d printed soft robot generating inching and crawling locomotions with variable friction legs. In *Intelligent Robots and Systems (IROS), 2013 IEEE/RSJ International Conference on*, pages 4590–4595, Nov 2013. doi: 10.1109/IROS.2013.6697016.

Pablo Valdivia y Alvarado and Kamal Youcef-Toumi. Design of machines with compliant bodies for biomimetic locomotion in liquid environments. *Journal of dynamic systems, measurement, and control*, 128:3, 2006. doi: 10.1115/1.2168476.

Ronald Van Ham, Thomas G Sugar, Bram Vanderborght, Kevin W Hollander, and Dirk Lefeber. Compliant actuator designs. *IEEE Robotics & Automation Magazine*, 16(3), 2009. doi: 10.1109/mra.2009.933629.

Bram Vanderborght, Alin Albu-Schäffer, Antonio Bicchi, Etienne Burdet, Darwin G Caldwell, Raffaella Carloni, M Catalano, Oliver Eiberger, Werner Friedl, Ganesh Ganesh, et al. Variable impedance actuators: A review. *Robotics and Autonomous Systems*, 61(12):1601–1614, 2013. doi: 10.1016/j.robot.2013.06.009.

Iuliu Vasilescu, Keith Kotay, Daniela Rus, Matthew Dunbabin, and Peter Corke. Data collection, storage, and retrieval with an underwater sensor network. In *Proceedings of the 3rd international conference on Embedded networked sensor systems*, pages 154–165, 2005. doi: 10.1145/1098918.1098936.

John J. Videler. *Fish Swimming*. Springer Science & Business Media, July 1993. doi: 10.1007/978-94-011-1580-3.

Daniel Vogt, Yong-Lae Park, and Robert J. Wood. Design and characterization of a soft multi-axis force sensor using embedded microfluidic channels. *IEEE Sensors Journal*, 13(10):4056–4064, October 2013. doi: 10.1109/jsen.2013.2272320.

Michaël De Volder and Dominiek Reynaerts. Pneumatic and hydraulic microactuators: a review. *Journal of Micromechanics and Microengineering*, 20(4):43001, 2010. doi: 10.1088/0960-1317/20/4/043001. URL `http://stacks.iop.org/0960-1317/20/i=4/a=043001`.

Hesheng Wang, Weidong Chen, Xiaojin Yu, Tao Deng, Xiaozhou Wang, and Rolf Pfeifer. Visual servo control of cable-driven soft robotic manipulator. In *Intelligent Robots and Systems (IROS), 2013 IEEE/RSJ International Conference on*, pages 57–62. IEEE, Nov 2013. doi: 10.1109/IROS.2013.6696332.

Hesheng Wang, Bohan Yang, Yuting Liu, Weidong Chen, Xinwu Liang, and Rolf Pfeifer. Visual servoing of soft robot manipulator in constrained environments with an adaptive controller. *IEEE/ASME Transactions on Mechatronics*, 22(1):41–50, 2017a. doi: 10.1109/tmech.2016.2613410.

Hsueh-Cheng C Wang, Robert K. Katzschmann, Brandon Araki, Santani Teng, Laura Giarre, and Daniela Rus. Enabling independent navigation for visually impaired people through a wearable vision-based feedback system. In *2017 IEEE International Conference on Robotics and Automation (ICRA)*, pages 6533–6540, may 2017b. doi: 10.1109/ICRA.2017.7989772.

Robert J Webster and Bryan A Jones. Design and kinematic modeling of constant curvature continuum robots: A review. *The International Journal of Robotics Research*, 29(13):1661–1683, June 2010. ISSN 0278-3649. doi: 10.1177/0278364910368147. URL `http://ijr.sagepub.com/cgi/doi/10.1177/0278364910368147`.

Michael Wehner, Michael T Tolley, Yiğit Mengüç, Yong-Lae Park, Annan Mozeika, Ye Ding, Cagdas Onal, Robert F Shepherd, George M Whitesides, and Robert J Wood. Pneumatic energy sources for autonomous and wearable soft robotics. *Soft Robotics*, 1(4):263–274, October 2014. doi: 10.1089/soro.2014.0018.

Karsten Weiß and Heinz Worn. The working principle of resistive tactile sensor cells. In *Mechatronics and Automation, 2005 IEEE International Conference*, volume 1, pages 471–476. IEEE, 2005.

A M Wilson, J C Lowe, K Roskilly, P E Hudson, K A Golabek, and J W McNutt. Locomotion dynamics of hunting in wild cheetahs. *Nature*, 498(7453):185–189, June 2013. doi: 10.1038/nature12295.

Sebastian Wolf and Gerd Hirzinger. A new variable stiffness design: Matching requirements of the next robot generation. In *Robotics and Automation, 2008. ICRA 2008. IEEE International Conference on*, pages 1741–1746. IEEE, 2008. doi: 10.1109/robot.2008.4543452.

Robert J Wood. The first takeoff of a biologically inspired at-scale robotic insect. *IEEE transactions on robotics*, 24(2):341–347, 2008. doi: 10.1109/tro.2008.916997.

Keenan A. Wyrobek, Eric H. Berger, H. F. Machiel Van der Loos, and J. Kenneth Salisbury. Towards a personal robotics development platform: Rationale and design of an intrinsically safe personal robot. In *2008 IEEE International Conference on Robotics and Automation (ICRA)*, pages 2165–2170. IEEE, 2008. doi: 10.1109/ROBOT.2008.4543527.

Younan Xia and George M Whitesides. Soft lithography. *Annual review of materials science*, 28(1):153–184, 1998. doi: 10.1002/(sici)1521-3773(19980316)37:5<550::aid-anie550>3.3.co;2-7.

Jing Xiao and Rayomand Vatcha. Real-time adaptive motion planning for a continuum manipulator. In *2010 IEEE/RSJ International Conference on Intelligent Robots and Systems (IROS)*, pages 5919–5926. IEEE, 2010. doi: 10.1109/iros.2010.5648888.

Zhongkai Zhang, Jeremie Dequidt, Alexandre Kruszewski, Frederick Largilliere, and Christian Duriez. Kinematic modeling and observer based control of soft robot using real-time finite element method. In *Intelligent Robots and Systems (IROS), 2016 IEEE/RSJ International Conference on*, pages 5509–5514. IEEE, 2016. doi: 10.1109/iros.2016.7759810.

Yang Zhao, Masaaki Fukuhara, Takahiro Usami, and Yogo Takada. Performance of very small robotic fish equipped with CMOS camera. *Robotics*, 4(4):421–434, October 2015. doi: 10.3390/robotics4040421.

Yong Zhong, Zheng Li, and Ruxu Du. A Novel Robot Fish With Wire-Driven Active Body and Compliant Tail. *IEEE/ASME Transactions on Mechatronics*, 22(4): 1633–1643, Aug 2017. ISSN 1083-4435. doi: 10.1109/TMECH.2017.2712820.